KYOTO UNIVERSITY

DOCTORAL THESIS

Modern Approaches to Radio Supernovae

Author:
Tomoki MATSUOKA

Supervisor:
Dr. Keiichi MAEDA

A thesis submitted in fulfillment of the requirements
for the degree of Doctor of Philosophy

20, December, 2022

Declaration of Authorship

I, Tomoki MATSUOKA, declare that this thesis titled, "Modern Approaches to Radio Supernovae" and the work presented in it are my own. I confirm that:

- This work was done wholly or mainly while in candidature for a research degree at Kyoto University.
- Where any part of this thesis has previously been submitted for a degree or any other qualification at Kyoto University or any other institution, this has been clearly stated.
- Where I have consulted the published work of others, this is always clearly attributed.
- Where I have quoted from the work of others, the source is always given. With the exception of such quotations, this thesis is entirely my own work.
- I have acknowledged all main sources of help.
- Where the thesis is based on work done by myself jointly with others, I have made clear exactly what was done by others and what I have contributed myself.

Signed: Tomoki Matsuoka

Date: 20, December, 2022

"There are no facts, only interpretations."

Friedrich Wilhelm Nietzsche

KYOTO UNIVERSITY

Abstract

Graduate School of Science
Department of Astronomy

Doctor of Philosophy

Modern Approaches to Radio Supernovae

by Tomoki MATSUOKA

Core-collapse supernovae (SNe) are explosive phenomena of massive stars and clarifying the properties of SNe can help us understand the stellar evolution of massive stars. Particularly, radio emission from SNe is a unique tool to directly trace not only the information on particle acceleration but also the mass-loss histories of massive stars based on the inferred physical properties of the circumstellar medium (CSM) around the SN progenitor. This thesis summarizes the results of the examinations by some modern approaches described as follows. First is the systematic investigations on radio SNe; we conduct the Markov chain Monte Carlo analysis on tens of radio SNe, and show that the astrophysical parameters such as the physical structure of the CSM density distribution and the ejecta gradient could depend on the degree of the stripping of the outer layer in the SN progenitors. Concretely, red supergiants as progenitors of Type II SNe experience mild but increasing mass-loss activity towards the core collapse, while Wolf-Rayet stars, progenitors of Type Ib, Ic, and broad-lined Ic SNe, would undergo more intense but weakening mass-loss episode. As for the plasma physics, we testify that the soft spectral index of the relativistic electrons would be preferred in a large samples of radio SNe, except for some broad-lined Ic SNe. The efficiencies of the acceleration of electrons and the amplification of magnetic field can be hardly constrained through the modeling of radio SNe. We also present some outlier objects of radio SNe showing a possible peculiar characteristics of stellar evolutionary path or explosion. Second is on the ultra-stripped SN, a transient leading to the formation of the binary neutron star; we show that bright radio emission from ultra-stripped SNe can be diagnostics for the possibility of the remnant DNS merger within the cosmic age. We also propose the plausible observational time and frequency windows for detecting radio emission from ultra-stripped supernovae. Third is the evolution of a supernova remnant (SNR) hosting a binary neutron star which can be regarded as an appearance of the ultra-stripped supernova evolving for a long period; we prove that this type of an SNR expands into the CSM characterized by the inhomogeneous density distribution and the hot plasma shaped by the pre-SN mass-loss activity driven by the binary interaction, and its whole evolution would be totally influenced by such a CSM.

Acknowledgements

The author thanks his supervisor Keiichi Maeda for his various kinds of continuous guidance during my life as a Ph.D. student. The author also appreciates Herman Lee who have given thoughtful supports continuously as a second supervisor. The author thanks Tomoya Takiwaki, Takashi J. Moriya, Shigeo S. Kimura, and Masaomi Tanaka for their academic advises and fruitful suggestions as the co-authors, as well as Nozomu Tominaga for his constructive comments on my studies. In addition, the author appreciates my friends Hidetoshi Omiya, Kazutaka Kimura, Kota Hayashi, Hiroki Okino, Hajime Ogane, and Kengo Tachibana for their heartful encouragements. The studies described in this dissertation are supported by Iwadare Foundation and JSPS Grant No. 21J12145. Finally I express my best gratitude to my parents, grandparents, and sister and her husband for their usual cheering up.

Contents

Declaration of Authorship iii

Abstract vii

Acknowledgements ix

1 General introduction 1
- 1.1 Roles of stars in the universe . . . 1
- 1.2 Stellar evolution of massive stars . . . 1
  - 1.2.1 Thermodynamical evolution of stars . . . 1
  - 1.2.2 Nuclear evolution . . . 4
- 1.3 At the moment of the death: supernova explosion . . . 5
  - 1.3.1 Core collapse . . . 5
  - 1.3.2 Shock breakout . . . 5
- 1.4 Exploding stars . . . 7
  - 1.4.1 Spectra and SN types . . . 7
  - 1.4.2 Light curves . . . 9
- 1.5 Expanding into the interstellar space: supernova remnant . . . 12
  - 1.5.1 Free expansion phase . . . 12
  - 1.5.2 Ejecta-dominated phase . . . 12
  - 1.5.3 Sedov phase . . . 12
  - 1.5.4 Radiative cooling and snow-plow phase . . . 13
- 1.6 Other fates of massive stars . . . 13
  - 1.6.1 Electron capture supernovae . . . 13
  - 1.6.2 Failed SNe . . . 14
  - 1.6.3 (Pulsational) Pair instability SN . . . 15
- 1.7 Type Ia SNe . . . 15
- 1.8 What is the "modern" approach? The objectives in this dissertation . . . 17
  - 1.8.1 Statistical properties . . . 18
  - 1.8.2 New frontier of the research on transients . . . 18
  - 1.8.3 Structure of the dissertation . . . 18

2 Radio emission from supernovae: interaction with circumstellar medium 19
- 2.1 A concept of the interaction with circumstellar medium . . . 19
- 2.2 Hydrodynamics . . . 19
- 2.3 Particle acceleration and magnetic field amplification . . . 23
  - 2.3.1 Parametrizations . . . 23
  - 2.3.2 Energy density distribution of accelerated electrons . . . 24
- 2.4 Radiative process . . . 26
- 2.5 $L_p - t_p$ relation . . . 28
- 2.6 Time and frequency dependences of optically thin and thick emissions . . . 30
  - 2.6.1 Optically thin emission . . . 30
  - 2.6.2 Optically thick emission . . . 31

2.7 Useful expressions . . . 31

3 Markov chain Monte Carlo analysis on radio supernovae 35
3.1 Introduction . . . 35
3.2 Sample selection . . . 36
3.3 Modeling of radio SNe and analysis through the MCMC method . . . 37
3.3.1 Radio emission from SNe . . . 37
3.3.2 Bayesian framework and setup of MCMC simulations . . . 40
3.3.3 Surveyed parameters and prior functions . . . 41
3.3.4 Statistics . . . 43
3.4 Fitting results . . . 43
3.5 Implications on astrophysics . . . 45
3.5.1 n . . . 45
3.5.2 s . . . 49
3.5.3 $\log q$ . . . 49
3.6 Implications on plasma physics . . . 52
3.6.1 $\log \epsilon_e$ and $\log \epsilon_B$ . . . 52
3.6.2 p . . . 52
3.7 Outliers . . . 54
3.7.1 SN 2016X . . . 54
3.7.2 Type IIb SNe with extremely steep ejecta $n \sim 20$ . . . 55
3.7.3 Multiple solutions for radio LCs . . . 57
3.8 Discussion and summary . . . 57
3.8.1 Effect of free-free absorption . . . 57
3.8.2 Summary . . . 59

4 Radio Emission from Ultra-stripped Supernovae as Diagnostics for Properties of the Remnant Double Neutron Star Binaries 63
4.1 Introduction . . . 63
4.2 Properties of the ultra-stripped SN progenitors and mass-transfer rates . . . 64
4.3 Models and Method . . . 67
4.3.1 Models . . . 67
4.3.2 Shock evolution . . . 68
4.3.3 Particle Acceleration and Magnetic Field Amplification . . . 68
4.3.4 Synchrotron emission . . . 69
4.4 Results . . . 69
4.4.1 Light curves . . . 69
4.4.2 Maximum Luminosities . . . 70
4.5 Discussions . . . 73
4.5.1 Candidates for the ultra-stripped SNe and their radio observations . . . 73
4.5.2 Strategy in radio follow-up observations . . . 73
4.5.3 Contribution from an additional 'confined' CSM . . . 73
4.5.4 Event rate and Detectability . . . 75
4.5.5 Model uncertainties . . . 76
4.6 Summary . . . 76

5 Long-term evolution of a supernova remnant hosting a double neutron star binary 79
5.1 Introduction . . . 79
5.2 Progenitor model . . . 80
5.3 CSM formation . . . 82
5.3.1 Initial setup . . . 82

5.3.2 Wind hydrodynamics . . . 83
5.3.3 Composed CSM . . . 84
5.4 SNR evolution . . . 85
5.4.1 Method . . . 85
Ejecta dynamics . . . 85
Particle acceleration and magnetic field amplification . . . 86
Synchrotron emission . . . 87
Parameter sets . . . 88
5.4.2 Characteristics of a USSNR . . . 89
5.5 discussion . . . 95
5.5.1 The USSNR population . . . 95
5.5.2 General implications for stripped-envelope SNRs . . . 97
5.5.3 Radio emission from the hot plasma region . . . 97
5.5.4 Treatment of radiative cooling . . . 98
5.5.5 Effects of non-linear diffusive shock acceleration . . . 98
5.5.6 Parametrizations of ϵ_e and $E_{\rm min}$ . . . 98
5.5.7 Asphericity . . . 99
5.6 Summary . . . 99

6 Summary **103**

A Variations in definitions of quantities in radio SN modeling **105**

B Derivation of 1σ volumes in N dimensional Gaussian density **109**

C Physical parameters deduced from MCMC simulations **111**

D Derivation of $\rho_{\rm CE}$ **119**

E Tests for the numerical code **121**

Bibliography **125**

List of Figures

1.1 A diagram illustrating the evolutionary tracks of stars with $M_{\rm ZAMS} = 14\,M_\odot$, in addition to paths of low-mass and very massive stars. The critical catastrophic physical situations are also clarified (see the text). For the illustrative figure, see Janka, 2017. 2
1.2 The domains in which the pressure source denoted becomes most dominant over the other pressure sources. The numerical model of the evolutionary track of a star with $M_{\rm ZAMS} = 14\,M_\odot$ is also plotted by the orange line. 3
1.3 The dynamical evolution of the core-collapse SN around the iron core. (a) The iron core collapses to the center, leading the formation of the proto-neutron star. (b) The material falls onto the proto-neutron star and bounces outward, forming the shock wave. (c) The shock propagating outward stagnates in the way because of the endothermic reactions through iron photodissociations. (d) The neutrino emission from the central proto-neutron star heats the shock until the composition of the falling material changes into silicate. (e) As the density of the silicate layer is smaller than that of the iron, the shock could restart to propagate outward, resulting the revival of the shock. (f) Finally, the successful explosion would be reproduced, leading the SN and explosive nucleosynthesis. See also Figure 3 in Janka, 2017. . . . 6
1.4 Top : The flowchart of the SN classification, and their properties. Bottom : Montage of spectra of Type II (blue), IIb (orange), Ib (green), Ic (red), IcBL (violet), IIn(brown) and Ia (pink) SNe. The normalization of the flux are scaled. References are as follows: SN 2004et for Type II SN (Sahu et al., 2006), SN 2016gkg for Type IIb SN (Kilpatrick et al., 2017), SN 2008D for Type Ib (Tanaka et al., 2009), SN 2020oi for Type Ic SN (Rho et al., 2021), SN 1998bw for Type IcBL SN (Patat et al., 2001), SN 2010jl for Type IIn SN (Fransson et al., 2014), and SN 2011fe for Type Ia SN (Pereira et al., 2013). 8
1.5 Right : Montage of (pseudo) UVOIR bolometric LCs of Type II (blue), IIb (orange), Ib (green), Ic (red), IcBL (violet), IIn (brown), and Ia (pink) SNe. References are as follows: SN 2004et for Type II SN (Sahu et al., 2006), SN 1993J for Type IIb SN (Shigeyama et al., 1994), SN 2008D for Type Ib (Tanaka et al., 2009), SN 2020oi for Type Ic SN (but the template is displayed. See Lyman et al., 2016), SN 2016coi for Type IcBL SN (Terreran et al., 2019), SN 2010jl for Type IIn SN (Fransson et al., 2014), and SN 2014J for Type Ia SN (Srivastav et al., 2016). 10
1.6 Zoo of the various subclasses of Type Ia SNe with the Phillips relation (black line), displayed as functions of B-band maximum absolute magnitude and the decline rate. For the detailed discussion see Taubenberger, 2017. 17

2.1 The schematic picture that shows the hydrodynamical structure of the SN shock. The forward shock is propagating the CSM outward, while the reverse shock is heating up the ejecta. The shocked region consists of two component gas divided by the contact discontinuity. 20
2.2 CSM structures within the parameter space $0 < s < 3$. Gray lines overploteed in the background show the steady wind parametrized by its mass-loss rate. 21

2.3 The CSM structure with inhomogeneous density distribution, which we can speculate that the progenitor should experience the prominent mass-loss episode just prior to the explosion. . . . 21
2.4 Peak radio luminosities of SNe (L_p) are plotted as a function of the product of peak time (t_p) and the observed frequency (5 GHz) for Type II, IIb, Ib, Ic, and IcBL SNe. Gray dashed lines show the proportional dependences of L_p and t_p, given the annotated shock velocities. In this diagram $\alpha_e = 1, \gamma_{\rm min} = 1$, and $p = 3$ are assumed. . 30

3.1 Summary of the MCMC simulations. The figures compare the values of the medians with 1σ credible intervals between the presented survey frameworks. Top, middle, and bottom panels display the result of p, s, and n. The examined SNe are sorted as the order of Type II, IIb, Ib, Ic, and IcBL SNe from the left side. . . . 46
3.2 Same as Figure 3.1, but for log q (top), log ϵ_e (middle), and log ϵ_B (bottom). . . . 47
3.3 The PDFs of log q, s, and n, divided by the SN types (white for II, black for IIb, orange for Ib, green for Ic, and blue for IcBL). . . . 48
3.4 Collection of the proposed ejecta density profiles as a function of the four velocity. The edges of each line are determined by the maximum and minimum observation time of the radio emission. As a reference, the ejecta profiles of the gamma-ray bursts including sub-energetic events estimated in Margutti et al., 2014 are also plotted by the magenta dashdotted lines. . . . 49
3.5 Probability density function of log q for samples of SNe IIb. The line styles used in this figure indicate the degree of the fitting results (solid for $\chi^2_{\rm red} < 5$, dashed for $5 < \chi^2_{\rm red} < 10$, and dotted for $\chi^2_{\rm red} > 10$). . . . 50
3.6 Top: CSM density distribution for each SN samples. The best-fitted values are employed in the plot. The gray dashed lines denote the CSM structure molded by steady mass-loss activity As a reference, we also plot the CSM structures previously inferred for SN 2020oi (Maeda et al., 2021), SN 2018ivc (Maeda et al., 2022), and SN 2013fs (Yaron et al., 2017). Bottom: the converted mass-loss history. The typical velocity of the CSM needed to determine the normalization of the mass-loss rate depends on SN types; $v_w = 10\,{\rm km\,s^{-1}}$ for SNe II, $v_w = 100\,{\rm km\,s^{-1}}$ for SNe IIb, and $v_w = 1000\,{\rm km\,s^{-1}}$ for stripped-envelope SNe. In both panel the line styles are similarly used as Figure 3.5. . . . 51
3.7 Same as Figure 3.3, but for log ϵ_e, log ϵ_B, p. . . . 53
3.8 The correlation between the medians of log ϵ_B and those of log ϵ_e for each SN, plotted with 1σ credible intervals. The thicker points indicate good fitting results ($\chi^2_{\rm red} < 5$). . . . 54
3.9 The PDFs of the ejecta gradient n for samples of Type II SNe. The usage of the line style is same as Figure 3.5. . . . 55
3.10 The synthesized light curve and corner plot of SN 2016X. . . . 56
3.11 The PDFs of the ejecta gradient n for Type IIb SNe. The usage of the line style is same as Figure 3.5. . . . 56
3.12 the synthesized light curves and cornerplot of SN 2020oi. Red lines and points denote the best-fitted solutions, while blue ones correspond to the other solution described in Table 3.5. . . . 58
3.13 The synthesized light curves of SN 1993J (left) and SN 2013df (right). . . . 60

4.1 The histogram of the final mass-transfer rates in the models presented by Tauris, Langer, and Podsiadlowski, 2015. The difference in the color shows the type of SNe; FeCCSN (blue) or ECSN (red). The models in which either the binary is detached or no RLO initiates are separately shown in the left side of the histogram. . . . 65

4.2 Distribution of the mass-transfer rate as a function of the final separation. Only the models in which the secondary stars explode as SNe are plotted. Two different symbols are used depending on the difference in the ejected mass; $M_{\rm ej} < 0.2\ M_\odot$ (circles) or $M_{\rm ej} \geq 0.2\ M_\odot$ (triangles). The models plotted by the circles outlined in red are examined in details (see Section 4.4.1). For the models on the left side of the black dashed line, the remnant DNS binary is expected to merge within the cosmic age. 66
4.3 Examples of the synthesized radio light curves for the models shown in Table 1. The top and bottom panels are for the different models (sep_1Rsun and sep_10Rsun). The left and right panels are centimeter (8.46 GHz) and millimeter (100 GHz) ranges, respectively. The thickness of the lines shows the difference in $f_{\dot{M}}$; $f_{\dot{M}} = 0.10$ (thin blue) and $f_{\dot{M}} = 0.99$ (thick blue). The upper limit of the centimeter emission for SN 2005ek is shown by the black arrow. 70
4.4 Dependences of the radio maximum luminosity on the final separation, for different time windows since the explosion (within the first 30 days, 300 days, and 3000 days from the top to bottom). The frequency is set at 8.46 GHz in these figures. The left panels are for $f_{\dot{M}} = 0.10$, while the right ones are for $f_{\dot{M}} = 0.99$. 71
4.5 Same as Figure 4, but for 100 GHz. 72
4.6 The radio luminosity for the reference models shown by the different colors, as functions of the epoch and frequency. The x-axis is the frequency in a logarithmic scale, while the y-axis is the epoch in a logarithmic scale. Shown here are the models sep_1Rsun (Top) and sep_10Rsun (Bottom). In the left panels $f_{\dot{M}} = 0.1$ is used, while in the right panels $f_{\dot{M}} = 0.99$. The points show a combination of the epoch and frequency in the past observations (Table 4.2). 74
4.7 The modeled radio light curves of SN 2016coi, as compared with our ultra-stripped SN models. The left panels show the radio light curves in the centimeter range (8.46 GHz), while the right panels are models in the millimeter range (100 GHz). The thick red lines show the synthesized radio light curves for SN 2016coi with the mass-loss rate $\dot{M}_{\rm CSM} = 10^{-4} M_\odot {\rm yr}^{-1}$, for $t < 10$ days (dotted) or $t \geq 10$ days (solid). The thin red lines within 10 days indicate the radio light curves computed with the putative confined CSM around the SN 2016coi with the mass-loss rate $\dot{M}_{\rm CSM} = 10^{-3} M_\odot {\rm yr}^{-1}$. The black points in the left panels show the observational data of SN 2016coi in the centimeter range (Terreran et al., 2019). The ultra-stripped SN models sep_1Rsun (Top) and sep_10Rsun (Bottom), with $f_{\dot{M}} = 0.99$ as the fiducial value, are plotted with the solid blue lines. 75

5.1 Time evolution of the mass-loss history (top), total mass (bottom left), Roche lobe radius (bottom middle), and escape velocity (bottom right) of the USSN progenitor. Blue and orange lines correspond to the phases in which the binary system experiences RLO or not, respectively. Note that within the first 1.78 Myrs the progenitor is in a stable core He-burning stage, so that these values are kept constant. 81
5.2 Initial density profiles of the ISM with a component from CE ejection. Blue, orange, and black lines represent the model 'WARM', 'HOT' and 'UNIFORM', respectively. . 82
5.3 The density structure of the composed CSM. The dashed black line shows the distribution realized for the steady wind with its mass-loss rate $\dot{M} = 10^{-7}\ M_\odot\ {\rm yr}^{-1}$. The distributions of the gas pointed out by cursive alphabets represent that they are from the mass loss activity referred in Figure 5.1. 84
5.4 The temperature structure of the composed CSM. 85
5.5 Time evolution of the radial profiles of the density (left) and velocity (right) in 'WARM' (top) and 'HOT' (bottom). 89

5.6 Time evolution of the Mach number (dashed blue) and velocity (solid orange) of the blastwave in the model 'WARM' (top) and 'HOT' (bottom). After the steep drops of the blastwave velocity near the end of the curves, the shock Mach number drops to below 3 where we truncate the simulations. The black line shows the time dependence of the blastwave velocity expected in the Sedov phase, indicating a good agreement with the numerical solution. 91
5.7 Long-term radio light curves at 1 GHz compared to radio observations of SNRs. Also plotted are the luminosities of SN 1993J (orange stars), SN 1995N (green squares), SN 2006jd (red pentagons), and Galactic SNRs listed in Table 5.3 (black points with error bars), estimated by the distances to each objects. The right y-axis stands for the observed flux densities with which the source with the luminosity shown in the left y-axis is observed at a distance $d = 10\,\mathrm{kpc}$. The red dotted line indicates the detection limit of VLASS (Lacy et al., 2020). 92
5.8 Time evolution of the profile of the magnetic field in the model 'WARM_H_SN'. The development of the strength of the magnetic field at the forward shock can be observed at $t \gtrsim 500$ years (solid), rather than before (dotted). 93
5.9 Time evolution of surface brightness as a function of sky projection angle at 1 GHz. The colors of the curves depict the time evolution. 94
5.10 Time evolution of the surface brightness from our models are plotted as a function of the SNR diameter. The colored data points connected by solid lines show the time evolution for our model. The black points represent a selection of observed Galactic SNRs as summarized in Pavlović et al., 2013. 96

E.1 The shock tube test. Black lines and orange circles show the exact solution and numerical solution derived by our code, respectively. 122
E.2 The Sedov explosion test. The line and symbol have the same meaning as in Figure E.1. 123

List of Tables

2.1 Values of α and β . . . 31

3.1 Properties of samples of radio SNe treated in this chapter. . . . 38
3.2 Explosion parameters of stripped-envelope SNe derived in Lyman et al., 2016. . . . 39
3.3 Parameters and their ranges considered in this study. . . . 42
3.4 $\chi^2_{\rm red}$ in the best-fitted parameter set for each SN, followed by the number of the . . . 44
3.5 Best fitted parameters and medians of log q with 1σ credible intervals. . . . 57

4.1 Reference models . . . 69
4.2 Radio observations of the candidates for ultra-stripped SNe . . . 73

5.1 Parameters for initial profiles . . . 83
5.2 Grid of models . . . 88
5.3 Samples of the observed Galactic core-collapse SNRs . . . 101

C.1 Best fitted parameters and medians of log q with 1σ credible intervals. . . . 112
C.2 Best fitted parameters and medians of log ϵ_e with 1σ credible intervals. . . . 113
C.3 Best fitted parameters and medians of log ϵ_B with 1σ credible intervals. . . . 114
C.4 Best fitted parameters and medians of p with 1σ credible intervals. . . . 115
C.5 Best fitted parameters and medians of s with 1σ credible intervals. . . . 116
C.6 Best fitted parameters and medians of n with 1σ credible intervals. . . . 117

Chapter 1

General introduction

1.1 Roles of stars in the universe

A star is a minimum unitary object in the universe, and it can serve as a driver of various kinds of astrophysical phenomena occurring in the universe. One example is synthesizing heavy elements that cannot be produced in the Big Bang nucleosynthesis (e.g., carbon, oxygen, and calcium ...etc), enriching them in the universe (McWilliam, 1997). Another is the formation of compact objects such as white dwarfs (WDs), neutron stars (NSs), and black holes (BHs) (Camenzind, 2007). Needless to say, radiation in a galaxy we can observe comes from the collective of stars, and the evolution of the galaxy itself can be totally affected by the stellar behaviors (Madau and Dickinson, 2014). In addition, the role of stars is prominent even in the context of the cosmology; the reionization of the universe is considered to be completed around the redshift $z \sim 6$ thanks to ionizing photons radiated from low-metal stars formed in high-z universe (Barkana and Loeb, 2001). Understanding the formation, evolution, and fate of stars and their impacts on the universe is one of the ultimate goals in the stellar astrophysics.

This dissertation summarizes the author's recent accomplishments on the theoretical modeling of radio emission from supernovae. As is known, a supernova is an appearance of the final fate of massive stars. To grasp the standard understandings of stellar astrophysics, in this chapter we overview the important points in the evolution and fates of massive stars. (for the detailed explanation we refer readers to the popular textbook, Kippenhahn, Weigert, and Weiss, 2013)

1.2 Stellar evolution of massive stars

1.2.1 Thermodynamical evolution of stars

Let us consider the physical properties of the stellar core that will be derived from the fundamental laws. We assume that the stellar core balances its own gravity with the pressure gradient, and then the hydrostatic equilibrium must be realized. The equation of the hydrostatic equilibrium in the radial direction (r) is given as follows:

$$-\frac{1}{\rho}\frac{dP}{dr} - \frac{GM}{r^2} = 0 \tag{1.1}$$

where ρ, P, and M are the density, pressure, and mass of the stellar core, respectively, and G is the gravitational constant. We suppose that this relation is satisfied within orders of magnitude and rewrite as follows:

$$\frac{P_c}{\rho_c R_c} \sim \frac{GM_c}{R_c^2} \Longrightarrow P_c \sim \frac{GM_c^2}{R_c^4} \tag{1.2}$$

where the subscript c denotes that the quantity is associated with the stellar core, and $\rho_c \sim M_c R_c^{-3}$ is substituted. This description of the core pressure P_c is independent of the choice of the equation

of state (EoS). Choosing the EoS of ideal gas $P_c = \rho_c k_B T_c/(\mu m_p)$, where k_B, μ and m_p are the Boltzmann constant, the average molecular weight, and the atomic unit mass, respectively, then we can deduce the proportional relationship as follows:

$$\frac{T_c^3}{\rho_c} \sim \left(\frac{\mu m_p}{k_B}\right) G^3 M_c^2. \tag{1.3}$$

This equation indicates that given the stellar core mass M_c, the temperature of the core T_c is proportional to one thirds of the core density $\rho_c^{1/3}$. Figure 1.1 shows the stellar evolutionary tracks of stars with small mass, those with its zero-age main-sequence (ZAMS) mass $M_{\rm ZAMS} = 14\,M_\odot$, and very massive stars illustrated as functions of the temperature and the density of the stellar core. The numerical model of a star with $14\,M_\odot$ is constructed through the stellar evolution code `MESA` (Paxton et al., 2011; Paxton et al., 2013; Paxton et al., 2015; Paxton et al., 2018). We can see that the evolutionary track follows the proportional relation of $T_c \propto \rho_c^{1/3}$ in the beginning phase, verifying the validity that the physical state of the stellar core can be described by the hydrostatic equilibrium and that the other physical effects (e.g., the existence of the outer envelope) can be neglected. We also remark that as the stellar core mass is believed to follow the monotonically dependence on the ZAMS mass (see e.g., Sukhbold, Woosley, and Heger, 2018), it can be said that the overall picture of the stellar evolution would be primarily determined mostly only by the "initial" stellar mass[1], including the evolution of low-mass stars that would not explode as supernovae at their endpoints of their lives.

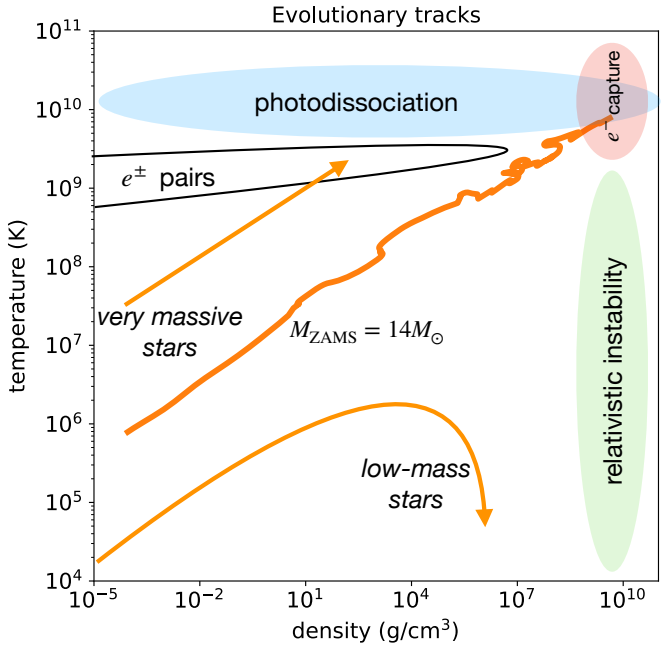

FIGURE 1.1: A diagram illustrating the evolutionary tracks of stars with $M_{\rm ZAMS} = 14\,M_\odot$, in addition to paths of low-mass and very massive stars. The critical catastrophic physical situations are also clarified (see the text). For the illustrative figure, see Janka, 2017.

[1]Certainly, other physical parameters such as metallicity, rotation, and binary interaction can become secondarily significant in characterizing the evolution of stars.

We note that the proportional relationship of $T_c \propto \rho_c^{1/3}$ would also appear in the discussion on what kind of the pressure sources would be mostly dominant. Since the radiation pressure is proportional to T^4 and the gas pressure is to ρT, the boundary at which the radiation pressure becomes comparable to that of the ideal gas would follow the relationship $T \propto \rho^{1/3}$. Figure 1.2 shows the domain of the parameter space in which the pressure sources shown below becomes dominant; radiation, ideal gas, non-relativistically (NR) degenerated gas, and extremely-relativistically (ER) degenerated gas. The boundary between the radiation pressure and the ideal gas pressure is parallel to the evolutionary track of the stellar core in their beginning phase. This implies that when the pressure of the ideal gas is dominant in the stellar core, the radiation pressure would not overcome the pressure of the ideal gas all along the evolutionary track, and the vice versa is also satisfied. Usually, stellar cores in stars with mass less than $\lesssim 70\,M_\odot$ are dominated by the pressure originated from the ideal gas, while those in massive stars more than $\gtrsim 140\,M_\odot$ are regulated by the radiation pressure. The special physical consequence attributed to the dominance by radiation pressure will be described in Section 1.6.3. On the other hand, it is often possible that during the stellar evolution the star happens to the situation where the pressure of degenerated gas becomes important. Then the evolutionary track will start deviating from the proportional relation of $T_c \propto \rho_c^{1/3}$. The fate of the stars depends on when the contribution from the degenerated gas becomes significant, or whether the star encounters to the catastrophic physical situations before the emergence of the contribution from the degenerated gas (e.g., electron captures or photodissociations).

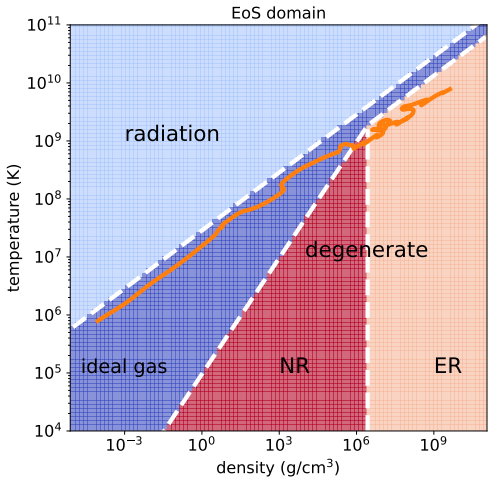

FIGURE 1.2: The domains in which the pressure source denoted becomes most dominant over the other pressure sources. The numerical model of the evolutionary track of a star with $M_{\rm ZAMS} = 14\,M_\odot$ is also plotted by the orange line.

We also mention to the entropy of the stellar core per unit mass s that can be formularized as follows:

$$s = c_V \ln\left(\frac{P_c}{\rho_c^\gamma}\right) + s_0 \tag{1.4}$$

where c_V and γ are the specific heat at constant volume and the adiabatic index, respectively, and s_0 is a constant value that determines the standard value of the entropy. Considering that c_V is given by the partial derivative of the internal energy per unit mass u by the temperature fixing the

volume as constant, then

$$c_V = \left(\frac{\partial u}{\partial T}\right)_V = \frac{1}{\gamma - 1}\frac{k_B}{\mu m_p} \tag{1.5}$$

is satisfied. Substituting this into equation 1.4 and assuming $s_0 = 0$ for simplicity and $\gamma = 5/3$, we can deduce the following result:

$$s \propto \frac{k_B}{\mu m_p} \ln\left(\frac{M_c}{\rho_c^{1/2}}\right) \propto \frac{k_B}{\mu m_p} \ln\left(\frac{M_c^2}{T_c^{3/2}}\right). \tag{1.6}$$

This equation shows that given the stellar core mass, if the entropy of the stellar core is drained by the energy transportation between the outer envelope or by neutrino cooling, the temperature and the density are forced to increase. This relationship follows in the inverse way compared with the usual material, and this consequence is a unique point in the thermodynamics of the self-gravitational system.

1.2.2 Nuclear evolution

The stellar evolution as an object in a main-sequence phases begins with the ignition of hydrogen burning in the stellar core. As for low-mass stars less than $M \lesssim 1\,M_\odot$, the hydrogen burning is mainly preceded through the nuclear reaction channel called *pp chain*, in which two protons collides each other resulting in the formation of the deuterium nucleus, and it further interacts with another proton forming ^{3}He. This ^{3}He actually takes three nuclear reaction paths to result in the formation of ^{4}He, and the difference of the rest mass energy between ^{4}He and four particles of ^{1}H would be extracted as an energy source in the stellar core. On the other hand the stellar core in massive stars more than $M \gtrsim 2\,M_\odot$ undergoes the hydrogen burning through the reaction chain called *CNO cycle*. In this channel a small amount of carbon, neon, and oxygen contained in the core are involved in the nuclear reaction network as catalyses, and carbons or the products are reacted with four protons one by one, resulting in the formation of ^{4}He. Note that the energy generation rate of CNO cycle depends very sensitively on the temperature than that of pp chain (Arnett, 1996).

Once the fuel for the hydrogen burning in the stellar core has been exhausted, the core starts gravitationally contracting until He burning would be ignited. On the other hand, the hydrogen shell burning continues at the boundary between the envelope and the core, and its high thermal pressure pushes the outer hydrogen envelope outward. As a result, the star evolves into the object consisting of the stellar core experiencing He burning engulfed by the extended hydrogen envelope, called a red giant or a red supergiant.

The subsequent evolution of the star would be affected by the pressure contribution from the degenerated gas which brings about the variety of the fates of stellar objects. In case of low-mass stars within $0.1 \lesssim M \lesssim 7\,M_\odot$, He burning in the core grows up the carbon-oxygen core through the nuclear reaction called triple-α process, and at the moment of the formation of the moderate carbon-oxygen core, the pressure from degenerate gas in the carbon-oxygen core overcomes the ideal gas pressure, and no more energy generation through nuclear burning would be required. On the other hand the outer envelope is considered to be ejected through thermal pulses induced in the helium layer. After the envelope has been completely gotten rid of, the object transforms itself into the object called a white dwarf.

Contrary to the evolution of low-mass stars, massive stars more than $M \gtrsim 10\,M_\odot$ continues the nuclear burning even after the formation of the moderate carbon-oxygen core through He burning at the center of the star. As the helium gas for the nuclear burning has been exhausted,

the core again begins to shrink itself until carbon burning will be ignited in the stellar core. Further nuclear burning phases such as oxygen, neon, and silicon burning phase, follows the carbon burning phase, and eventually the iron core will be formed. It is known that the binding energy per unit nucleon of iron is the largest among all of the elements, and it means that any kinds of nuclear burning reactions can no longer extract the energy from isotopes of iron. On the contrary, the stellar core drastically loses the pressure sources through endothermic reactions such as the iron photodissociation and electron capture reactions. Therefore, once the fuel of silicon burning has been completely spent, the system cannot sustain its own gravity itself, leading to the gravitational core collapse (see also the next section). This catastrophic phenomenon is an origin of the formation of neutron stars or black holes, and supernovae we can observe.

1.3 At the moment of the death: supernova explosion

1.3.1 Core collapse

A core collapse of the massive star is the beginning of the energetic astrophysical phenomenon, a supernova (SN) (see Figure 1.3, and e.g., Woosley, Heger, and Weaver, 2002; Janka, 2012). As the iron core at the center of an evolved massive star can no longer provide pressure against its own gravity, the gravitational collapse takes place. The iron core is compressed to the lengthscale ~ 10 km, which is a typical size of a neutron star, and then a proto-neutron star is formed. The material above the proto-neutron star continues to fall down to the proto-neutron star, and the core bounce occurs. The bounced material forms a shock propagating outward, but it stalls at only 100-200 km due to endothermic reactions through the iron photodissociation. Under this circumstance, it is proposed theoretically that the neutrino emissions from the proto-neutron star would revive the shock, resulting in ejecting all material and producing an SN explosion. However, numerical simulations of the SN explosion still suffer from some challenges and difficulties. So far, only a few experiments report the successful explosion (e.g., Suwa et al., 2010; Takiwaki, Kotake, and Suwa, 2014; Nakamura et al., 2014; Müller, 2016). As prescriptions, It is considered that the multi-dimensional effects such as convection, rotation, or standard-accreion-shock instability are important for the dynamics. There is also an implication that the stellar structure disordered by the turbulent motions just before the core collapse plays an important role in the explosion of the progenitor (Yadav et al., 2020; Bollig et al., 2021). Yet, there is a problem claiming that the diagnostic explosion energy computed by most of these simulations ($\sim 10^{50}$ ergs) does not reach the canonical value inferred by the observations ($\sim 10^{51}$ergs, Takiwaki, Kotake, and Suwa, 2016).[2] Furthermore, some studies indicate that the synthesized nickel mass or the energy growth rate computed by these numerical simulations do not agree with the observations (e.g., Sawada and Maeda, 2019; Suwa, Tominaga, and Maeda, 2019). In summary, there is a general consensus for the neutrino driven explosion scenario while the details have been still actively debated.

1.3.2 Shock breakout

The shock wave that have succeeded in sweeping up the iron core begins propagating the outside layer consisting of silicon, ONeMg, C+O, and helium and hydrogen layers if exist, one by one, and eventually reaches the surface of the star. At this moment when the optical depth of the shock wave (τ) becomes below c/v (here v is the shock velocity), the shock wave starts to transform the nature itself from radiation mediated shock to collisionless shock, and the intense ultraviolet and X-ray emission will be radiated (Waxman and Katz, 2017). The energy released in the shock breakout $E_{\rm sbo}$ is roughly estimated as

$$E_{\rm sbo} \sim aT^4R^3 \sim \delta M v^2, \tag{1.7}$$

[2]The exceptional simulation is suggested in Bollig et al., 2021, which has achieved the diagnostic energy of 10^{51} erg.

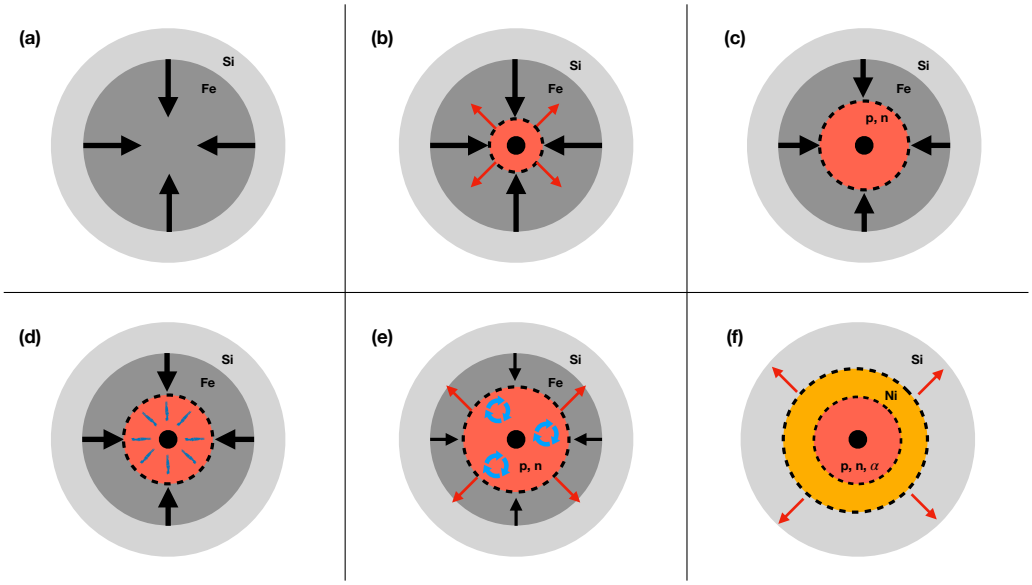

FIGURE 1.3: The dynamical evolution of the core-collapse SN around the iron core. (a) The iron core collapses to the center, leading the formation of the proto-neutron star. (b) The material falls onto the proto-neutron star and bounces outward, forming the shock wave. (c) The shock propagating outward stagnates in the way because of the endothermic reactions through iron photodissociations. (d) The neutrino emission from the central proto-neutron star heats the shock until the composition of the falling material changes into silicate. (e) As the density of the silicate layer is smaller than that of the iron, the shock could restart to propagate outward, resulting the revival of the shock. (f) Finally, the successful explosion would be reproduced, leading the SN and explosive nucleosynthesis. See also Figure 3 in Janka, 2017.

where a and R are the radiation constant and the progenitor radius, respectively. δM is the mass contained in the region where the optical depth is smaller than c/v, and thus

$$\delta M \sim \rho R^3 \sim \frac{cR^2}{\kappa v} \tag{1.8}$$

can be deduced. Here assumed is that the optical depth $\tau \sim \kappa\rho R$ is roughly equal to c/v. We consider the typical value of the electron scattering opacity $\kappa = 0.34\,\mathrm{cm^2 g^{-1}}$, and then the total energy of the shock breakout can be calculated as follows:

$$E_{\mathrm{sbo}} \sim 10^{46} R_{13}^2 v_9\,\mathrm{erg}, \tag{1.9}$$

where $R_{13} = R/(10^{13}\,\mathrm{cm})$ and $v_9 = v/(10^9\,\mathrm{cm\,s^{-1}})$. The temperature can be a indicator of the wavelength of the radiated photons, and can be estimated as follows:

$$T \sim \left(\frac{E_{\mathrm{sbo}}}{aR^3}\right)^{1/4} \sim 10^5 R_{13}^{-1/4} v_9^{1/4}\,\mathrm{K}. \tag{1.10}$$

As seen in the above discussion, the emission from the shock breakout contains information on the radius of the progenitor, ejecta velocity, and the explosion properties itself. If the progenitor is surrounded by the dense circumstellar medium (CSM) so that $\tau > c/v$ is satisfied even in the CSM, then the timing of the shock breakout may be delayed and the direct emission from the shock breakout itself cannot be observed. Instead, the radiation signal emitted through the interaction with the CSM can be used as a tracer of the CSM nature itself. (Forster et al., 2018; Haynie and Piro, 2021; Margalit, 2022)

We note that the after the shock breakout particle acceleration can be triggered. While radiation mediated shock is sustained by the radiation pressure and thus cannot flick charge particles here and there, collisionless shock is kept up by the pressure from the collision of the particles and has potential to drive the particle acceleration mechanism such as diffusive shock acceleration.

1.4 Exploding stars

The catastrophic core collapse of a massive star leaves a variety of the observational signatures. The total amount of the energy released during the core collapse comes up to $\sim GM_{\rm NS}^2/R_{\rm NS} \sim 10^{53}$ erg, where $M_{\rm NS} \sim 1.4\,M_\odot$ and $R_{\rm NS} \sim 10$ km are the mass and radius of the newborn neutron star, and most of them are released as neutrinos (Janka, 2012). The neutrino burst at the moment of the core collapse can be diagnostics for physical properties of the proto-neutron star (e.g., Suwa et al., 2022). In addition, the environment surrounding the proto-neutron star experiences the rapid variation of the gravitational field and thus has potential to emit gravitational waves (Abdikamalov, Pagliaroli, and Radice, 2020). Compared to these emitters, the kinetic energy of the ejected gas typically occupies 1% of the total released energy, $\sim 10^{51}$ erg, and the energy radiated as a form of photons accounts for only 1% of the "kinetic" energy of the ejecta, $\sim 10^{49}$ erg. Nevertheless, these energy budgets are enough for us to observe supernovae and extract the information on the nature of the explosion itself and the supernova progenitors.

The main electromagnetic observables we are usually utilizing are the spectra and light curves, and the polarization if detected. SN spectra provides us with information on the composition of the progenitor and the typical ejecta velocity, SN light curves can be used to infer the explosion properties such as ejected mass and the explosion energy, and SN polarizations leave an imprint of the asphericity of the ejecta (or CSM). In this section we expand an outline of the observational properties of the spectra and light curves of supernovae.

1.4.1 Spectra and SN types

Atomic lines in the observed spectra reflect the composition of the progenitor, and SNe are basically classified by these observationally inferred compositions. Figure 1.4 shows a flowchart of the SN classification scheme and the montage of typical SN spectra. Hereafter we describe the detailed characteristics core-collapse SNe in the following description, and Type Ia SNe in Section 1.7.

If the spectrum of the SN contains the hydrogen lines with the unique absorption feature called P-Cygni profile, then the SN is categorized as the Type II SN. The hydrogen features in the observed spectrum suggest a progenitor with a huge hydrogen envelope. In particular, some progenitors of Type II SNe events are identified as red supergiants (RSGs) by the pre-explosion images obtained by the Hubble Space Telescope (e.g., SN 2003gd was elaborately investigated by Hendry et al., 2005; Smartt et al., 2004). Type II SNe can be classified into some subclasses depending on the shape of the light curves denoted as Type II-P, Type II-L, and Type IIn SNe. Especially, hydrogen recombination is considered to play an important role as a radiation source in Type II-P SNe, the detail of which would be described later. Type IIn SNe serve as one of the subclass of Type II SNe, but have distinct observational properties from Type II-P or Type II-L SNe (Chugai and Danziger, 1994; Gal-Yam et al., 2007; Kiewe et al., 2012). The spectra is characterized not by P-Cygni profile but by the narrow Hα line emissions. Furthermore, SN 1987A, one of the most nearest SNe, is speculated as an explosion of a blue supergiant, and sometimes categorized as a Type II-pec SN through its peculiar light curve behavior. (e.g., Walborn et al., 1987; Podsiadlowski, 1992).

SNe without the hydrogen features are classified as Type I SNe (Wheeler and Levreault, 1985). Type I SNe are divided into some subclasses depending on the presence of the helium or silicate

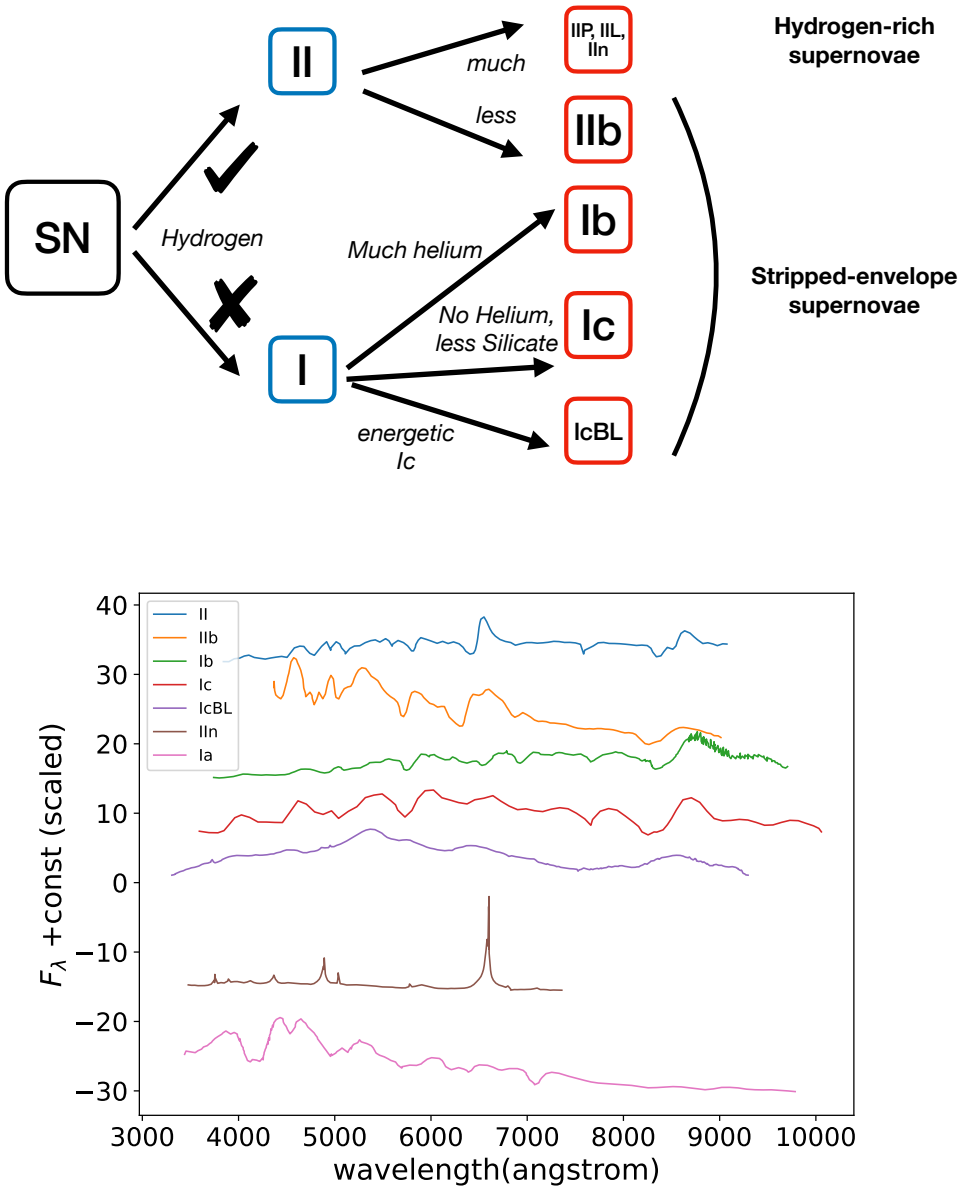

FIGURE 1.4: Top : The flowchart of the SN classification, and their properties. Bottom : Montage of spectra of Type II (blue), IIb (orange), Ib (green), Ic (red), IcBL (violet), IIn(brown) and Ia (pink) SNe. The normalization of the flux are scaled. References are as follows: SN 2004et for Type II SN (Sahu et al., 2006), SN 2016gkg for Type IIb SN (Kilpatrick et al., 2017), SN 2008D for Type Ib (Tanaka et al., 2009), SN 2020oi for Type Ic SN (Rho et al., 2021), SN 1998bw for Type IcBL SN (Patat et al., 2001), SN 2010jl for Type IIn SN (Fransson et al., 2014), and SN 2011fe for Type Ia SN (Pereira et al., 2013).

features; SNe with helium components are named Type Ib SNe, those with strong silicate features are Type Ia SNe, and those with neither of them are Type Ic SNe. Type Ib and Ic SNe are also the subclass of the core-collapse SNe, but their progenitors are considered to be different from red supergiants. The lack of the hydrogen features in the observed spectra implies the progenitor whose outer hydrogen envelope has been stripped away either by the binary interaction or by the stellar wind (e.g., Ensman and Woosley, 1988; Podsiadlowski, Joss, and Hsu, 1992; Smartt,

2009; Yoon, Woosley, and Langer, 2010; Groh, Georgy, and Ekström, 2013). For Type Ib SNe progenitors, helium Wolf-Rayet (WR) stars are suggested. For Type Ic, SNe carbon/oxygen WR stars are considered. What separates these two classes remains debated, but the effect of the binary interaction is believed to play an important role in characterizing the observed features of SNe (e.g., Eldridge et al., 2013; Ouchi and Maeda, 2017; Fang et al., 2019).

There is a special subclass in which a fraction of Type Ic SNe are categorized into. These objects exhibit broader line emissions in their spectra than those seen in other SN types, and are usually called broad-lined Type Ic SNe (Ic-BL SNe). The most famous representative would be SN 1998bw (Galama et al., 1998), in which the association between the gamma-ray emission possibly radiated from the long gamma-ray burst (GRB) and the electromagnetic emission from the SN has been confirmed. The broad line width in the spectra suggests the more energetic explosion than typical SNe (e.g., Taddia et al., 2019), and the association with the gamma-ray burst retrieves the fast-rotating progenitor (Woosley and Bloom, 2006; Woosley and Heger, 2006). It is also reported that recent observation has succeeded in capturing the high-velocity component in the ejecta of GRB 171205A/SN 2017iuk, possibly originating from the rapidly expanding hot cocoon generated by the relativistic GRB jet (Izzo et al., 2019). Constraining the physical nature of IcBL SNe allows us to approach even the origin of long GRBs, one of the most explosive phenomena in the universe.

1.4.2 Light curves

A light curve (LC) is a time evolution of the luminosity of transients. Figure 1.5 shows the collective (pseudo) bolometric LCs of various types of SNe. The characteristic variables of LCs are the typical timescale and the peak luminosity. As for SNe, the typical timescale is determined by the diffusion timescale of photons in the ejecta, which is defined as follows:

$$t_{\rm diff} \sim \tau \frac{R}{c} \sim \kappa \rho R \frac{R}{c} \sim \frac{\kappa M}{Rc}. \tag{1.11}$$

Comparing this diffusion timescale with dynamical timescale, we can obtain the typical timescale seen in SNe:

$$t_{\rm diff} \sim t \Longrightarrow t_{\rm SN} \sim 30 \kappa_{0.1}^{1/2} M_1^{3/4} E_{51}^{-1/4} \ [\rm day], \tag{1.12}$$

where $\kappa_{0.1}$, M_1, and E_{51} are the opacity, ejecta mass, and kinetic energy of the ejecta normalized by 0.1 g cm^{-2}, 1 $M_\odot$, and 10^{51} erg, respectively.

The luminosity provides us with the information on the energy source of the explosion. Actually the energy sources in SNe have a range of physical processes (Kasen and Woosley, 2009); the primary radiation sources are thermal radiation from the expanding ejecta and radioactive decay of ^{56}Ni, and secondarily energization by the interaction of SN ejecta with the circumstellar material or the relativistic wind from the pulsar wind nebula, if possible. The emission from the hydrogen recombination can be significant in case the massive hydrogen envelope resides in the ejecta (see below).

In the beginning phase during which the SN ejecta begins to expand outward, the system can become bright through the conversion from the kinetic energy of the shock wave into the internal energy of the radiation. On the assumption of the adiabatic variation with radiation-dominated gas (adiabatic index $\gamma = 4/3$), the typical temperature (T) and the radius (R) of the ejecta can be related with each other as follows:

$$T = T_0 \left(\frac{R}{R_0} \right)^{-1}, \tag{1.13}$$

where T_0 and R_0 are the initial temperature and radius, respectively. Since the internal energy of the ejecta just after the shock breakout ($E_{\rm int}$) is expected to be comparable with the kinetic energy

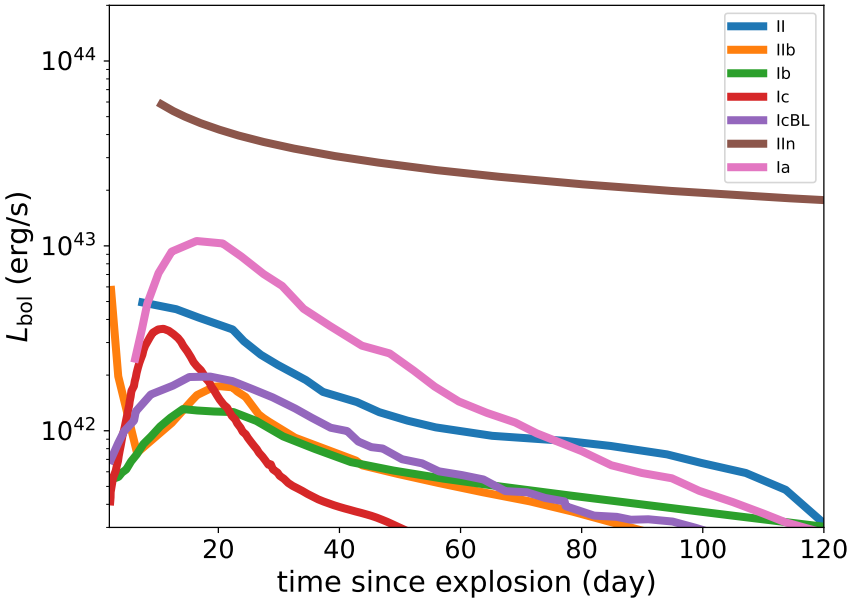

FIGURE 1.5: Right : Montage of (pseudo) UVOIR bolometric LCs of Type II (blue), IIb (orange), Ib (green), Ic (red), IcBL (violet), IIn (brown), and Ia (pink) SNe. References are as follows: SN 2004et for Type II SN (Sahu et al., 2006), SN 1993J for Type IIb SN (Shigeyama et al., 1994), SN 2008D for Type Ib (Tanaka et al., 2009), SN 2020oi for Type Ic SN (but the template is displayed. See Lyman et al., 2016), SN 2016coi for Type IcBL SN (Terreran et al., 2019), SN 2010jl for Type IIn SN (Fransson et al., 2014), and SN 2014J for Type Ia SN (Srivastav et al., 2016).

of the ejecta, and the photon diffusion dominates the radiative characteristics in the ejecta, the typical luminosity in the beginning phase can be written down as follows:

$$L_{\rm ad} \sim \frac{E_{\rm int}}{t_{\rm diff}} \sim 10^{42} E_{51} R_{13} \kappa_{0.1}^{-1} M_{10}^{-1}\,{\rm ergs}^{-1}, \tag{1.14}$$

where $R_{13} = R/(10^{13}\,{\rm cm})$ and $M_{10} = M/(10\,M_\odot)$ are substituted. We expect that adiabatic radiation can be bright enough to be observed if the progenitor is an extended star such as red supergiant. Indeed, it has been succeeded to capture the signature of the adiabatic radiation originating from the shock cooling in the beginning phase, particularly for Type IIb SNe (e.g., Bersten et al., 2018). On the other hand, it is hopeless for SNe coming from compact progenitors to give rise to luminous adiabatic radiation, because in such cases the internal energy of the ejecta would be used to expand the ejecta outward rather than converting itself into radiation.

The main radiative source in SNe is certainly believed to be the radioactive decay of ^{56}Ni (e.g., Arnett, 1982). ^{56}Ni is the radioactive isotope most synthesized in the explosion, decaying into ^{56}Co with the half time of 8.8 days. ^{56}Co is also one of the main radioactive isotopes in SNe, decaying into ^{56}Fe with the half time of 111.3 days. These two radioactive decays can power the radiative energies in the ejecta, and there is a simple formula describing the energy deposition rate of the radioactive decay of ^{56}Ni and ^{56}Co, so called "Arnett rule", as follows:

$$L_{\rm ra} = \frac{M_{\rm Ni}}{M_\odot}[(\epsilon_{\rm Ni} - \epsilon_{\rm Co})\exp(-t/t_{\rm Ni}) + \epsilon_{\rm Co}\exp(-t/t_{\rm Co})], \tag{1.15}$$

where $M_{\rm Ni}$ is the mass of ^{56}Ni synthesized in the SN explosion, and $\epsilon_{\rm Ni} = 3.9 \times 10^{10}\,{\rm erg\,s^{-1}\,g^{-1}}$,

$\epsilon_{\rm Co} = 6.789 \times 10^9\,{\rm erg\,s^{-1}\,g^{-1}}$, $t_{\rm Ni} = 8.8\,{\rm days}$, and $t_{\rm Co} = 111.3\,{\rm days}$ are the quantities related to radioactive decay processes. Measuring the peak luminosity of Type I SNe or the tail luminosity of Type II SNe with this formula allows us to observationally infer the synthesized nickel mass, providing us with the physical state of the internal region of the progenitor. However, there is a debate that this Arnett rule is likely to overestimate the nickel mass (Khatami and Kasen, 2019; Meza and Anderson, 2020), and the precise measurement of ^{56}Ni mass is an urgent issue so far, including the clarification of the degree of the gamma-ray trapping effect and the mixing of the nickel in the ejecta (Dessart et al., 2016). There is also a suggestion that stripped-envelope SNe (Type Ib and Ic SNe) may tend to have more massive Ni[5] mass than Type II SNe, possibly implying that stripped-envelope SNe might be originated from the more energetic explosion (Anderson, 2019). Yet Ouchi et al., 2021 discusses the possibility that the massive ^{56}Ni mass inferred for stripped-envelope SNe is just an observational bias. Furthermore, recently it has been proposed that the mass of ^{56}Ni is a sensitive indicator of the nature of the explosion; the suggestion is that the instantaneous explosion would be required for explaining the observationally inferred mass of the nucleosynthesis properties in SNe (Sawada and Maeda, 2019; Saito et al., 2022)[3]. In anyway, estimating the mass of radioactive isotopes from LCs is a unique tool to observationally constrain the explosive properties of SNe.

Hydrogen recombination is also an important radiation sources, particularly in Type II SNe. It plays a main role in characterizing the subclass of Type II SNe called Type II-P SNe with the long plateau phase during which the luminosity is maintained to be constant. This phenomenon is interpreted as follows. The progenitor of Type II SNe is considered to be a red supergiant, which has a large hydrogen envelope (see Section 1.4.1). The photosphere is roughly located on the hydrogen recombination surface. The adiabatic expansion of the ejecta increases the radius, while it also cools down the ejecta, resulting in the recession of the recombination surface. By balancing these two evolutions, the radius of the photosphere roughly remains constant. This picture continues until the photosphere reaches the center of the SN, $t \sim 100$ days. On the other hand, the LC in the subclass called Type II-L SN has a linearly decaying slope. Although this behavior has not been completely understood, one of the ideas is that Type II-L SN has the small amount of the hydrogen layer in its ejecta. Then the recession of the photosphere becomes faster for the smaller hydrogen envelope mass (Young and Branch, 1989; Blinnikov and Bartunov, 1993; Moriya et al., 2016).

Recently it has been observationally revealed that the behavior of LCs of Type II SNe has a diversity. Some studies reports the discoveries of the events where the behaviors of the LCs seem to be like the intermediate class of these two types (Anderson et al., 2014; Valenti et al., 2015). On the other hand, others discuss the possibility that there is a distinct gap between the LCs of Type II-P SNe and those of Type II-L SNe (e.g., Barbon, Ciatti, and Rosino, 1979; Arcavi et al., 2012; Faran et al., 2014). Another idea has been suggested that the light curves of Type II-L SNe can be also explained by a radiation emitted from the SN-CSM interaction (Maeda et al., 2022). Hence, The explanation for the origin of this diversity and the determination of the progenitor models are the theme enthusiastically investigated.

Thermalization through the circumstellar interaction is also a popular physical scenario explaining some LCs of SNe. The most striking example would be Type IIn SNe. The LC of Type IIn SNe tends to be characterized by the long timescale, and some of Type IIn SNe have extremely bright peak luminosities, sometimes classified as superluminous SNe (Ofek et al., 2007). The radiation source of Type IIn SNe is believed to be supplied from an interaction of the SN ejecta with a massive CSM (even orders of $1 - 10\,M_\odot$) (Moriya et al., 2014), but the origin of such a massive CSM is left as a mystery. Not limited to Type IIn SNe, circumstellar interaction is often taken up in order to explain the LC excess compared to the radioactive powering both in the late phase seen in other type of SNe (e.g., Kilpatrick et al., 2022). Furthermore, the circumstellar medium located

[3]For the counterargument see Imasheva, Janka, and Weiss, 2023.

in the vicinity of the SN progenitor is attracting attentions, in terms of explaining the (systematic) early excess of Type II SNe, suggesting the possible dynamical mass-loss activities just before the core collapses (e.g., Morozova et al., 2020; Moriya et al., 2017a; Forster et al., 2018).

1.5 Expanding into the interstellar space: supernova remnant

The ejected gas continues to expand into the interstellar space maintaining its rapid expansion velocity even after the thermal emission from the SN itself becomes too faint to be observed for us. Now the system is evolving into the spreaded and thin structure called a supernova remnant (SNR), and drives particle acceleration and magnetic field amplification reproducing the bright non-thermal emission from radio to gamma-ray band (for a basic guidace see Vink, 2020). A classical understanding on the whole evolution of a supernova remnant has been established by the works as Truelove and McKee, 1999; Cioffi, McKee, and Bertschinger, 1988.

1.5.1 Free expansion phase

Since the dynamics of the ejecta follows the homologous expansion (Chevalier, 1982a), the ejecta gas with the maximum velocity lies at the head of the ejecta. Until the density of the ejecta ahead is higher than the CSM density interacting with the ejecta, the velocity of the shock wave hardly suffers deceleration. In this circumstance the expansion of the system can be approximated by the free expansion; in short, $R_{\rm sh} \simeq V_{\rm ej} t$ would be satisfied, where $R_{\rm sh}$ is the shock radius and $V_{\rm ej}$ is the ejecta velocity at the head part.

1.5.2 Ejecta-dominated phase

The system soon come to reach a stage of deceleration as the mass of the CSM swept up by the shock wave is accumulating. Though, as long as the ejecta mass is sufficiently larger than the swept CSM mass, the evolution of the system is dominated by the properties of the dynamics of the ejecta. In this case, the shock wave follows the evolution slower than but akin to free expansion, depending on the power-law index of the ejecta density structure. If the ejecta is composed from the steep or shallow density structure, then the time evolution of the shock velocity becomes nearly constant or rapidly decaying, respectively. Radio emission from SNe we observe is basically originated from the signal radiated during this phase, and the detailed derivation of the time evolution of the shock velocity is presented in Section 2.2.

1.5.3 Sedov phase

Once the swept CSM mass exceeds the ejecta mass, then the dynamics of the system becomes dominated by the CSM and the natures of the ejecta would be disappearing. The evolution of the system can be described only by the explosion energy E and the density structure of the CSM. To be presented are the two cases of the uniform CSM and wind-like CSM. If the uniform CSM resides around the SN progenitor, then the shock radius in the Sedov phase can be given as follows (Sedov, 1959):

$$R_{\rm sh} = \zeta_0 \left(E/\rho_0\right)^{1/5} t^{2/5}, \text{ where } \rho_{\rm CSM} = \rho_0 = \text{const}, \zeta_0 \simeq 1.15 \tag{1.16}$$

whereas for the case of wind-like CSM, the shock radius would be revised as follows:

$$R_{\rm sh} = \zeta_2 \left(E/\mathcal{D}\right)^{1/3} t^{2/3}, \text{ where } \rho_{\rm CSM} = \mathcal{D} r^{-2}, \zeta_2 = \simeq 0.86. \tag{1.17}$$

The coefficient value (ζ_0 and ζ_2) depends on the dimensionality and adiabatic index of the gas, and is limited within orders of unity (Book, 1994). The above values are computed for the case

of the three-dimensional configuration with the adiabatic index $\gamma = 5/3$. We note that the Sedov velocity in case of wind-like CSM decelerates slower than the case of uniform CSM.

1.5.4 Radiative cooling and snow-plow phase

Since the evolutionary timescale of SNRs is as long as orders of 10^4 years, its later evolution would be influenced by the radiative cooling from the gas swept up by the shock wave. Specifically, if the cooling timescale of the gas $t_{\rm cool} \sim k_B T/(n\Lambda)$ becomes shorter than the SNR age, where n and Λ are the number density of the gas and the cooling function, respectively, then the internal energy of the SNR begins to be drained by the radiative cooling. Two important cooling processes can be presented; line emission from heavy element prominent at the temperature around $T \sim 10^6$ K, and bremsstrahlung emission from thermal electrons hotter than $T \gtrsim 10^7$ K (Chevalier and Fransson, 1994; Sutherland and Dopita, 1993; Chevalier and Fransson, 2017). As a rough criterion, it is believed that if the velocity of the shock wave decreases below $\sim 200\,{\rm kms}^{-1}$, then radiative cooling starts to play a primary role in the evolution of SNRs (Vink, 2020).

Once the radiative cooling becomes important in the evolution of the SNR, the dynamics of the system can be described no longer on the assumption of the adiabatic variation. The expansion of the system would be driven by the thermal pressure of the interior gas, and the standard analytic description of the evolution of the shock radius has been given as $R_{\rm sh} \propto t^{2/7}$ by McKee and Ostriker, 1977. Furthermore, if the pressure of the interior region has weakened down, then the system would be forced to expand by the momentum of the shell itself, and then the shock radius would be given roughly by $R_{\rm sh} \propto t^{1/4}$. Whichever the driver of the expansion of the system is the pressure in the interior region or the momentum of the shell itself, the evolution can be mimicked as the shell sweeping up the massive[4] interstellar medium, and termed as "snow-plow" phase. Finally, at the moment when the shock velocity decelerates down to the same order of the sonic velocity in the interstellar medium, $c_s \simeq 10\,{\rm kms}^{-1}$ for the temperature of 10^4 K, the expanding gas would be melted down into the interstellar medium, and completely ends up the journey of the gas consisting of the progenitor from the core collapse of massive stars.

1.6 Other fates of massive stars

While we have described the "standard" theoretical understandings of the physical process which massive stars with its ZAMS mass ranging $\sim 10 - 15\,M_\odot$ experience after the core collapse, the actual theoretical predictions are highly diverse, and certainly there are some exceptional evolutionary paths that deviate from the standard scenario depicted above. Many of them often have great importance in the context of astrophysics, and in this section we briefly introduce the properties of some theoretically predicted outliers.

1.6.1 Electron capture supernovae

The robust understandings on the evolutionary scenario of stars with $M_{\rm ZAMS} = 8 \sim 10\,M_\odot$, the smallest mass range that possibly explodes as an SN, have not been still established, but one of the popular scenarios can be said as an electron-capture supernova. Stars with this mass range can develop the carbon-oxygen core and ignite carbon burning. The satisfactory carbon burning can grow up the moderate ONeMg core at the center. However, when the pressure from the degenerated gas begins to be able to contribute to sustaining the gravity of the star, the ONeMg core mass has grown up so massive more than the Chandrasekhar critical mass. Then, due to the extremely dense environment ($\rho_c > 4 \times 10^9\,{\rm g\,cm}^{-3}$), nuclear isotopes such as ^{24}Na, ^{24}Mg, ...etc

[4] Due to the large radius of the shock in this phase, the enclosed mass of the interstellar medium can become enormous. See also the discussion in Chapter 5.

captures the electrons in the core, reducing the number of the electrons and even the degeneracy pressure. This leads to the rapid loss of the pressure maintaining the gravity of the star, and results in the core collapse of the star. As an electron capture reaction plays a crucial role in this core collapse, this kind of the explosion is termed as electron-capture supernova (ECSN).

Typically, the explosion energy of the ECSN is considered to be an order of magnitude smaller than normal iron core collapse SNe described in Section 1.3.1, $E \sim 10^{50}$ erg, and indeed the first-principle simulation have succeeded in realizing this kind of the explosion (e.g., Kitaura, Janka, and Hillebrandt, 2006). Theoretical modeling for photometric properties of ECSNe has been also investigated (Tominaga, Blinnikov, and Nomoto, 2013), suggesting the similar characteristics to Type II SNe except for the faint tail originated from low-mass amount of ^{56}Ni[5] . In addition, recently it has been reported that SN 2018zd should be a robust candidate for the ECSN, based on the plentiful observational evidences and implications from theoretical modelings (Hiramatsu et al., 2021).

Despite the ECSN has been successfully investigated for a long time, there is a weak consensus on the evolutionary path of stars with $M_{\rm ZAMS} = 8 \sim 10\,M_\odot$. The important issue is that the number of the events confirmed as an ECSN is still too small (the exceptional object would be SN 2018zd, Hiramatsu et al., 2021). If we consider the standard initial mass function (IMF) in which the number population of the star is proportional to the stellar mass to -2.35 given by the Salpeter IMF (Salpeter, 1955), the total number of stars with the ZAMS mass range $8\,M_\odot < M_{\rm ZAMS} < 10\,M_\odot$ should be large enough for us to observe a lot of ECSNe ever, but previous observations are likely to have failed to detect many of them. The possible explanation is that the progenitor experiences violent mass-loss activity in the phase of the super-asymptotic giant branch associated with the bulk muddling up motion in the convective layer called dredge-up (Jones et al., 2013). If this dredge-up activity has successfully ejected the convective envelope away completely, then the ONeMg core in the center just has to sustain the gravity from the "core" itself, not the whole of stellar mass. Then the electron-capture reactions would not be preceded, and instead the core evolves into a white dwarf consisting of mainly oxygen, neon, and magnesium (ONeMg WD). This type of a WD is considered to be massive ($\sim 1.3 M_\odot$) more than the median of the WDs observed ($\sim 0.6 M_\odot$) (Catalán et al., 2008), and believed to play a central role in the nova explosion. What makes complicated is that the quantification of the mass-loss rate during the phase of the super-asymptotic giant branch involves large uncertainties (Jones et al., 2013), and it is difficult to give a comprehensive explanation what kinds of the objects with $M_{\rm ZAMS} = 8 \sim 10\,M_\odot$ ends their lives as ECSN or ONeMg WDs, leaving the room to be discussed so far.

1.6.2 Failed SNe

If the shock wave after the core bounce shown in Section 1.3.1 has failed in penetrating the iron core, then all of the material in the system would fall into the proto-neutron star. Since the upper limit of the neutron star mass lies around $\sim 2\,M_\odot$ (Prakash, Ainsworth, and Lattimer, 1988; Kalogera and Baym, 1996; Margalit and Metzger, 2017), the proto-neutron star is impossible to sustain the gravity from all of the falling gas, resulting in the collapse and the formation of the black hole. This kind of the physical process is regarded as that the system has failed in exploding all of the gas, and thus called failed supernovae (failed SNe).

Though a failed SN is an important astrophysical phenomena in the viewpoint of the formation theory of black holes, it would be difficult to attempt an observational examinations, because we cannot expect strong optical electromagnetic emission from such a kind of transients. The popular observational implication on the black hole forming transient is related to the issue called red supergiant problem (Smartt et al., 2009; Davies and Beasor, 2020a; Davies and Beasor, 2020b),

[5]Though the explosion energy is roughly 10 times smaller than typical Type II SNe, the luminosity in the plateau phase is similar each other, because the main radiation source is coming from the recombination in the massive hydrogen envelope.

claiming that a large fraction of the progenitor mass inferred for samples of Type II-P SNe are below the threshold, $M_{\rm ZAMS} \lesssim 18\,M_\odot$. It is speculated that stars with the mass above this threshold fails in exploding the progenitor itself and collapses into stellar mass black holes. Surprisingly, the monitoring program of nearby galaxies for several years has succeeded in discovering the candidate for the failed SN event (Gerke, Kochanek, and Stanek, 2015); they have found that the red supergiant in NGC 6946 has actually disappeared during the long-term monitoring. This observational evidence supports the idea that the formation of the stellar mass black hole originates from red supergiants with $M_{\rm ZAMS} \gtrsim 18 M_\odot$. Recently there are increasing theoretical attempts to examine the observational diagnostics for the formation of the black holes. The model has been proposed that the super-Eddington accretion onto the newborn black hole can power the emission of strong X-rays and the subsequent radio-loud transient (Kashiyama, Hotokezaka, and Murase, 2018; Tsuna, Kashiyama, and Shigeyama, 2021). Furthermore, to give a comprehensive explanation of recently discovered fast blue optical transients, represented by AT2018cow (Perley et al., 2019; Margutti et al., 2019), wild-driven transient at the formation of a black hole has been also suggested (Piro and Lu, 2020; Uno and Maeda, 2020).

1.6.3 (Pulsational) Pair instability SN

Very massive stars more than $M_{\rm ZAMS} \gtrsim 140\,M_\odot$ evolves with its gravity maintained by not the pressure of ideal gas, but by the radiation pressure. The evolutionary track of such a star in the oxygen burning phase encounters to the parameter space in which photons can be annihilated to a pair of an electron and a positron (see Figure 1.1). The annihilation reaction of photons leads to the decrease of the pressure sustaining the gravity of the star, and the star experiences the collapse. The situation distinct from the other evolutionary scenario is that the explosive oxygen burning in the core would be forced at the core collapse, and the energy released at the moment due to the nuclear reaction can repulse outward all of the material infalling to the center. This type of the explosion is termed as a pair-instability supernova (PISN) (Heger and Woosley, 2002). In addition, stars with mass range of $70\,M_\odot \lesssim M_{\rm ZAMS} \lesssim 140\,M_\odot$ are considered to lie in the critical parameter space at which the pressure of radiation and ideal gas competes each other in the stellar core (Woosley, 2017). In this case the implosion at the oxygen burning phase induces less explosive nucleosynthesis, and in total the star ejects a fraction of the envelope up to several solar mass. Since such ejections of the envelope is supposed to be repeated for several times, this kind of the phenomenon is called pulsational pair instability supernovae (PPISNe). There is a theoretical model arguing that PISNe can be observed as an extremely luminous supernovae (Woosley, Blinnikov, and Heger, 2007) and PPISNe can account for some fraction of the Type Ibn SNe (Renzo et al., 2020) though their robust observational candidates have not been confirmed yet. Another intriguing topic related to PISNe and PPISNe is that they would make a mass gap of the black hole mass function at around $M_{\rm BH} \sim 60 - 90\,M_\odot$. It has become recently possible to be examined through the detection of gravitational waves from binary black holes consisting of such a mass range of black holes (Abbott et al., 2020).

1.7 Type Ia SNe

Besides the core-collapse SNe mentioned above, a Type Ia SN is one of the major population of the observed SNe, from which we can detect strong absorption lines of silicon (Filippenko, 1997). Unlike the core collapse supernova, a Type Ia SN is categorized as a thermonuclear explosion, where a massive white dwarf near the Chandrasekhar limit mass is considered to trigger the runaway of the nuclear burning (for a detail see Hillebrandt and Niemeyer, 2000; Maoz, Mannucci, and Nelemans, 2014).

Despite there is a consensus that Type Ia SNe are originated from the thermonuclear explosion of a white dwarf, it is also true that there are some crucial problems about the origin of the thermonuclear explosion, which have not yet been solved yet. One is what the progenitor of a Type Ia SN is (Maeda and Terada, 2016). To increase the mass of the WD up to the Chandrasekhar limit, two models for the progenitors have been suggested; the single degenerate model (the mass accretion onto a WD from a non-degenerate star), or the double degenerate model (double WDs merger. For a detail discussion, see e.g., Whelan and Iben, 1973; Iben and Tutukov, 1984; Wang and Han, 2012). Recent observations for some nearby Type Ia SNe (such as SN 2011fe, one of the nearest Type Ia SN events) are consistent with the double degenerate model based on the non-detection of the radiative component possibly originated from the companion star (see e.g., Chomiuk, 2013; Kasen and Nugent, 2013). Moreover, Type Ia SNe typically observed scarcely has features related on the circumstellar medium. This indicates that the mass loss activity possibly originated from the companion star (say, non-degenerate star) or the wind from the accretion disk around the progenitor WD would be absent, supporting the double-degenerated scenario. On the other hand when we turn our eyes on Type Ia SNRs in our galaxy, there are an increasing evidences arguing that they are interacting with dense circumstellar medium, implying the past mass-loss activity consistent with the single-degenerate scenario (Tanaka et al., 2021; Sano et al., 2022). Therefore, it can be said that the discrepancy between observations of extragalactic supernovae and Galactic SNRs has been deepened lately, and enthusiastically debated.

Another problem is related to the explosion mechanism of Type Ia SNe. It has been claimed that if a WD near the Chandrasekhar limit would be exploded with a full detonation (combustion wave faster than sonic velocity), the supplement of iron-group elements is too much to be consistent with the observational properties of Type Ia SNe and galactic chemical enrichment (Arnett, 1969; Woosley, Taam, and Weaver, 1986), while the deflagration (flame slower than the sonic velocity) all along the expansion is not enough to produce the typical amount of mass of ^{56}Ni (e.g., Timmes and Woosley, 1992). Taking these constraints into consideration, now two main explosion models have been highlighted. First is the delayed-detonation model (e.g., Iwamoto et al., 1999; Röpke and Niemeyer, 2007), where the flame triggered around the center of the white dwarf transit from subsonic to supersonic, combusting all of the material consisting of the WD near the Chandrasekhar mass. Second is the double-detonation model (e.g., Fink et al., 2010), in which the burning in the possible He layer on the sub-Chandrasekhar mass WD is ignited and the flame would be transmitted to the center of the WD leading to the explosion. So far the robust conclusion has not been reached yet, but there are continuing investigations including the capability of explaining the typical observational features of Type Ia SNe.

Though there are fundamental problems related to the progenitor and the explosion mechanism, the homogeneity of observational features of Type Ia SNe has been highlighted. It should be noted that there is a strong correlation between the absolute magnitude and the decline rate of Type Ia SNe called Phillips relation (Phillips, 1993; Phillips et al., 1999). With a variety of the corrections of light curves of Type Ia SNe, it becomes possible to utilize Type Ia SNe as the standard candles, contributing to the discovery of the accelerating expansion of the universe (e.g., Riess et al., 1998).

Contrary to the homogeneous nature of Type Ia SNe accepted by researchers, recent efforts on the detailed observations of transients have discovered the diversity of Type Ia SNe, deviating from the Phillips relations. Figure 1.6 displays the Phillips relation that standard Type Ia SNe are believed to follow, and the subclasses of SNe Ia as functions of B-band maximum absolute magnitude $M_{\rm B}$ and the decline rate Δm_{15} (see also Figure 1 in Taubenberger, 2017). The examples of subclasses are as follows; 91T-like SNe with high luminosity and the spectra in which lines of Fe III is prominent (Filippenko et al., 1992a), 91bg-like SNe with cool and subluminous photometric properties (Filippenko et al., 1992b), 02es-like SNe with subluminous but slowly-decaying light curves (Ganeshalingam et al., 2012), Ia-CSM with strong features possibly originated from

CSM (Silverman et al., 2013), and super-Chandrasekhar group (Howell et al., 2006) whose over-luminous photometric properties cannot be explained without the overmassive amount of mass of ^{56}Ni. In addition, the existences of outlier called 'SNe Iax', which show faint optical properties (e.g., Foley et al., 2013), Ca-rich transients that exhibits strong calcium features (Jacobson-Galán et al., 2020), and the possibility of the peculiar thermonuclear explosion of a WD as origins of such subclasses has been suggested. Clarifying the origin of the diversities of Type Ia SNe and identifying the main branch would also be the present goal for the study of Type Ia SNe.

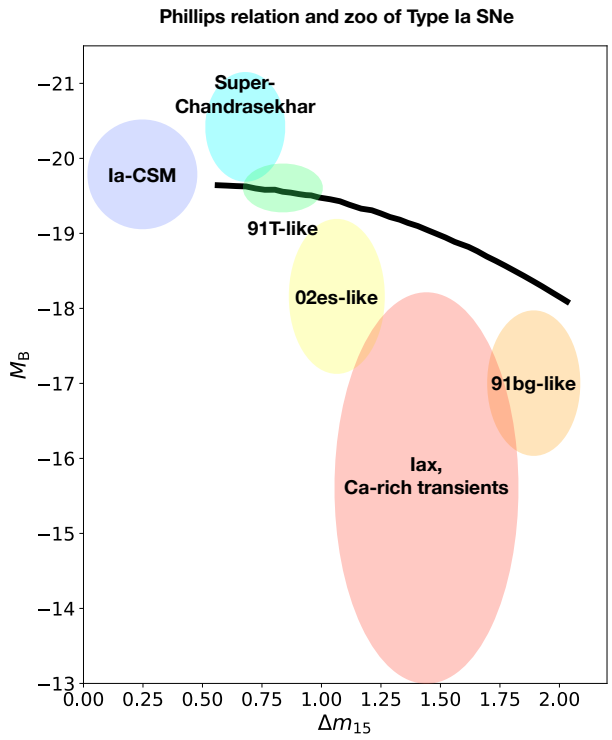

FIGURE 1.6: Zoo of the various subclasses of Type Ia SNe with the Phillips relation (black line), displayed as functions of B-band maximum absolute magnitude and the decline rate. For the detailed discussion see Taubenberger, 2017.

1.8 What is the "modern" approach? The objectives in this dissertation

As guided in the previous sections, there is a diverse range of stellar evolutionary paths of massive stars that have a possibility to result in the SN explosion. Disentangling the question "what kinds of SN progenitors end their lives as what kinds of explosions, through what kinds of stellar evolutionary path?" would be requisite for the completion of the construction of the stellar evolution theory. One of the methods achieving the goal is to extract the information on the evolutionary characteristics of SN progenitors from the observed radiative properties itself. The way treated in this dissertation is radio emission from SNe (radio SNe), emitted from the interacting region between the SN ejecta and the CSM through synchrotron emission of accelerated electrons (the detailed descriptions are given in Chapter 2). Since the physical structure of the CSM contains the hint to the mass-loss activity of the SN progenitor, radio SNe can be used as a tracer of the mass-loss activity of massive stars prior to their core collapse. It is believed that mass loss from the star is believed to be one of the critical physical processes to determine the evolution and even the fate of the stars (Yoon, 2015), and recently there is a report that the mass-loss history may be associated

with the internal nuclear burning activity (Maeda et al., 2021). Therefore, it can be said that studying radio SNe would be a direct method to tackle with the unknown evolutionary appearance of SN progenitors. Despite modeling of radio SNe itself has been attempted since 20th century (e.g., Chevalier, 1982b), it has been regarded as a powerful tool to interpret the stellar evolution of SN progenitor, even at present. In this dissertation we introduce the "modern" approaches to the modeling of radio emission from SNe, paying attention to the topics described in the following subsections.

1.8.1 Statistical properties

It has become possible to give great importance to “systematic” investigations through the employment of “statistical approaches” to reveal universal features of SN progenitors producing bright radio emissions. Now that there is a catalog of observed data on radio emission from core-collapse SNe accumulating so far (Bietenholz et al., 2021), it allows us to examine the general properties of radio SNe with statistical tools recently developed so that many people feel free to undertake (Foreman-Mackey et al., 2013; Foreman-Mackey, 2016). These properties would allow us to investigate the comprehensive nature of the mass-loss activity of massive stars and the physics of the particle acceleration. The results about this systematic study will be discussed in Chapter 3.

1.8.2 New frontier of the research on transients

We are living in the era when transients beyond our understandings have been found every day. Constructing a theoretical model to be consistent with observational features of such peculiar transients is a pressing issue so far, as well as can contribute to updating the current stellar evolution theory. Particularly, it would be expected that radio emission from such peculiar objects reflects the unique evolutionary path of the progenitor and even provide us with the innovative constraints, which may not be reproduced from the standard objects, methods, or assumptions. In Chapter 4 and 5 we pick up an ultra-stripped supernova, a precedent SN event of the formation of a binary neutron star, and treat its evolution of the dynamics and radio emission.

1.8.3 Structure of the dissertation

This dissertation is structured as follows. In Chapter 2 we introduce the basic framework of the interaction between the SN shock and the CSM, and show the procedure and the characteristics of radio emission from SNe. In Chapter 3 we investigate the systematic properties of radio SNe by making use of Markov chain Monte Carlo analysis method. In Chapter 4 we go through the radio emission from an ultra-stripped SN, a precursor event to the formation of a binary neutron star. In Chapter 5 we consider the theoretical modeling of the subsequent long-term evolution of the ultra-stripped SN as an appearance of an SNR, termed as "ultra-stripped supernova remnant". Finally, the conclusions proposed in this dissertation are summarized In Chapter 6.

The content of Chapter 3 is in preparation for the submission for the academic journal. The discussion in Chapter 4 and 5 are published in Matsuoka and Maeda, 2020 and Matsuoka et al., 2022, respectively.

Chapter 2

Radio emission from supernovae: interaction with circumstellar medium

2.1 A concept of the interaction with circumstellar medium

Figure 2.1 shows the schematic picture that draws the hydrodynamical structure of the SN shock expanding into the circumstellar environment. At the moment of the explosion, the huge energy up to $\sim 10^{51}$ erg would be deposited into the central region of the SN progenitor, leaving the newborn neutron star. The gas which had consisted of the progenitor would be ejected into the surroundings at high speed, and begins to sweep up the circumstellar medium (CSM). There are two kinds of the shock wave formed; one is the forward shock propagating the CSM outward, and the other one is the reverse shock sweeping up the ejecta. We note that the reverse shock is shrinking inward if seen in the rest frame of the contact discontinuity. The shocked region is divided by the contact discontinuity and its geometrical thickness is assumed to be thin so that the evolution of the shocked region can be regarded as a motion of the shell.

The region of the shocked CSM can be a potential site to trigger high-energy phenomena such as particle acceleation and magnetic field amplification (e.g., Drury, 1983), and to produce the radio and X-ray emission (Chevalier and Fransson, 1994; Fransson and Björnsson, 1998; Chevalier, Fransson, and Nymark, 2006). As for radio emission from SNe, modeling of the shocked CSM region and the evolution of the accompanied forward shock is a primary issue [1] . This chapter reviews the analytical treatment of time evolution of the hydrodynamics shaped by the SN shock interacting with the CSM, and the characteristics of the resulting radio emission.

2.2 Hydrodynamics

Let us consider the SN ejecta colliding with the CSM and aim at deducing the time evolution of the SN shock. As the SN ejecta acquires an enormous amount of energy at the explosion up to orders of $\sim 10^{51}$ erg, it follows the dynamics of the homologous expansion in which the velocity and the density of the ejecta are described as

$$v_{\rm ej} = \frac{r}{t} \tag{2.1}$$

$$\rho_{\rm ej} = t^{-3}\left(\frac{v}{U_c}\right)^{-n} \tag{2.2}$$

where U_c is time-independent scale factor of the ejecta density, and is determined by the mass and the total kinetic energy of the ejecta. n specifies the concentration of the energy distribution of the ejecta, Originally the value of n has been numerically investigated by (Matzner and McKee,

[1] The contribution from the reverse shock can be neglected because the relative velocity between the unshocked and the shocked gas can be regarded small. As the velocity of the forward shock is sufficiently higher than the wind velocity, the effective particle acceleration is supposed to be triggered only in the front of the forward shock.

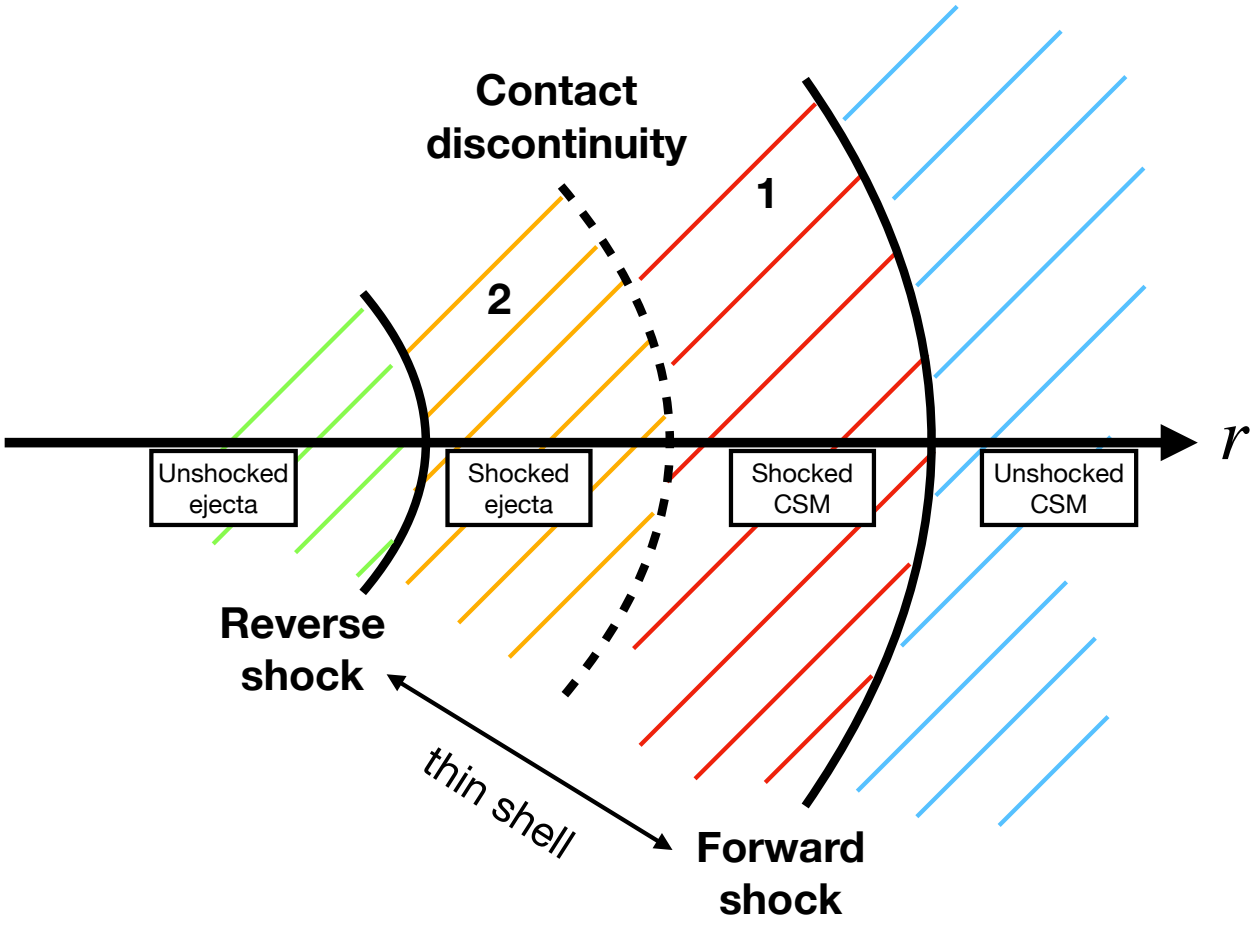

FIGURE 2.1: The schematic picture that shows the hydrodynamical structure of the SN shock. The forward shock is propagating the CSM outward, while the reverse shock is heating up the ejecta. The shocked region consists of two component gas divided by the contact discontinuity.

1999), and suggested that the SN progenitors with the convective hydrogen envelope is shaped by $n \sim 12$, while for the progenitors characterized by the radiative core $n \lesssim 10$ is preferred. It is also proposed from the collective data of the observed energetic SNe that the difference in n can be interpreted as the difference of the nature of the explosion itself (Margutti et al., 2014). To avoid the divergence of the kinetic energy of the ejecta for $r \to 0$, n is regulated within the range more than 5 (Chevalier, 1982a).

In addition to the ejecta configuration, we consider the CSM density distribution as follows:

$$\rho_{\rm CSM} = \mathcal{D} r^{-s} = 5 \times 10^{19} q \left(\frac{r}{10^{15}\,{\rm cm}} \right)^{-s} \ {\rm g\ cm^{-3}}, \tag{2.3}$$

where q quantifies the magnitude of the CSM density and for the power-law index $0 < s < 3$ is required for the mass convergence for $r \to 0$. The value $s = 2$ describes the situation where the CSM is characterized by the steady wind, and serves as a benchmark of the mass-loss activity of the star. For $0 < s < 2$ and $2 < s < 3$, the mass-loss rate follows decreasing and increasing evolutions as the time passes, respectively (Figure 2.2).

The point to be noted is that we can convert the physical properties of the CSM into the nature of the mass loss history; since the released gas propagates the circumstellar environment with some speed for the time scale until the core collapse, it retains the dynamical feature of the mass

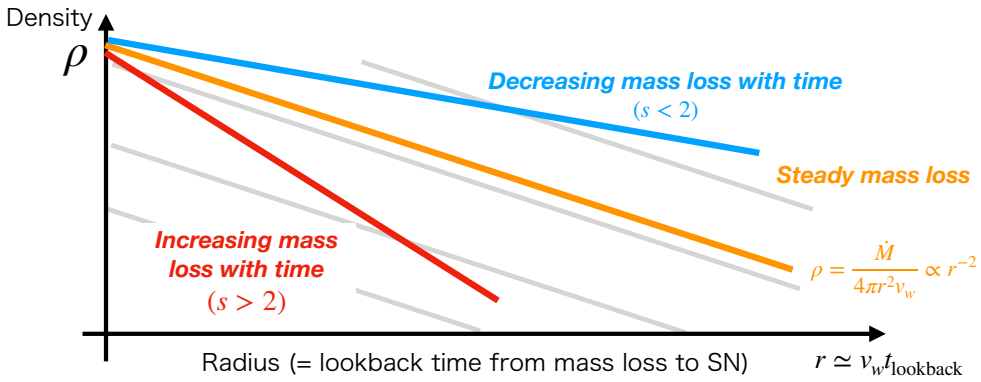

FIGURE 2.2: CSM structures within the parameter space $0 < s < 3$. Gray lines overploteed in the background show the steady wind parametrized by its mass-loss rate.

loss all the time. Thus, given the velocity of the released gas, the density and length scale of the CSM have information on the magnitude and timescale of pre-SN mass loss, respectively. Typically, the velocity of the gas is speculated as orders of the escape velocity of the star. This description is valid unless the gas induces the collisions with each other, and such a situation is realized in the case when we consider the longer length scale realized in an SNR (Chapter 5).

We can even consider the inhomogeneous density distribution as shown in Figure 2.3. To realize such a structure we need an additional mass-loss episode other than the steady wind, and such a specification can be a key to approach the nature of the mass-loss from SN progenitors. Numerical experiments of such a CSM configuration and the practical observations have been investigated in Matsuoka et al., 2019; Maeda et al., 2021.

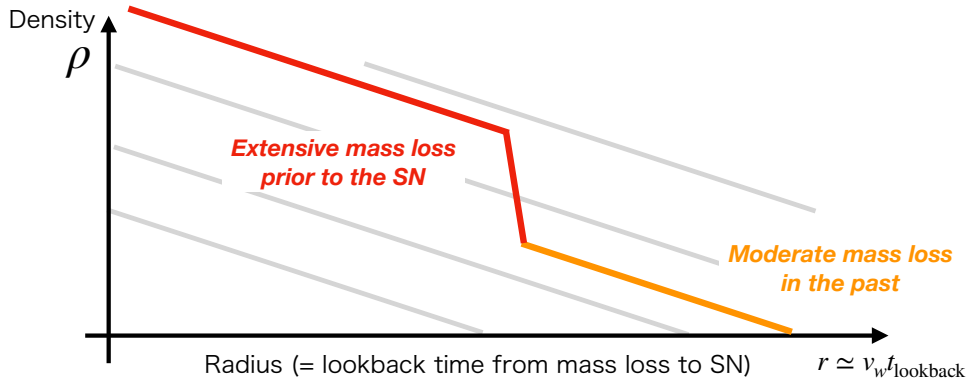

FIGURE 2.3: The CSM structure with inhomogeneous density distribution, which we can speculate that the progenitor should experience the prominent mass-loss episode just prior to the explosion.

The motion of the shocked shell is determined by the balance between the pressure of the ejecta expanding outward and the surrounding CSM, and the equation of the motion of the shell can be described as follows:

$$(M_1 + M_2)\frac{d^2 R_{\rm sh}}{dt^2} = 4\pi R_{\rm sh}^2 (P_2 - P_1) \tag{2.4}$$

where M_1 and M_2 are the mass of the shocked CSM and ejecta, and P_1 and P_2 are the total pressure at the blastwave and reverse shock, respectively. They are estimated as follows:

$$M_1 = \int_{R_p}^{R_{\rm sh}} 4\pi r^2 \rho_{\rm CSM} dr \simeq \frac{4\pi\mathcal{D}}{3-s} R_{\rm sh}^{3-s}, \tag{2.5}$$

$$M_2 = \int_{R_{\rm sh}}^{\infty} 4\pi r^2 \rho_{\rm SN} dr \simeq \frac{4\pi}{n-3}\left(\frac{t}{R_{\rm sh}}\right)^{n-3} U_c^n, \tag{2.6}$$

$$P_1 = \rho_{\rm CSM}(R_{\rm sh})\left(\frac{dR_{\rm sh}}{dt}\right)^2 = \mathcal{D}R_{\rm sh}^{-s}\left(\frac{dR_{\rm sh}}{dt}\right)^2, \tag{2.7}$$

$$P_2 = \rho_{\rm ej}\left(\frac{R_{\rm sh}}{t} - \frac{dR_{\rm sh}}{dt}\right)^2 = t^{n-3}R_{\rm sh}^{-n}U_c^n\left(\frac{R_{\rm sh}}{t} - \frac{dR_{\rm sh}}{dt}\right)^2, \tag{2.8}$$

where R_p is the radius of the progenitor, which can be ignored due to $R_p \ll R_{\rm sh}$. As the pressure of the ejecta is dominated by its bulk motion, we only take the ram pressure into account in the calculations of P_1 and P_2. We note that P_2 is estimated by the relative velocity between the shell itself and the head of the ejecta. Substituting these quantities to equation 2.4, we obtain

$$\begin{aligned}&\left\{\frac{4\pi\mathcal{D}}{3-s}R_{\rm sh}^{3-s} + \frac{4\pi}{n-3}\left(\frac{t}{R_{\rm sh}}\right)^{n-3}U_c^n\right\}\frac{d^2R_{\rm sh}}{dt^2}\\ &= 4\pi R_{\rm sh}^2\left\{t^{n-3}R_{\rm sh}^{-n}U_c^n\left(\frac{R_{\rm sh}}{t} - \frac{dR_{\rm sh}}{dt}\right)^2 - \mathcal{D}R_{\rm sh}^{-s}\left(\frac{dR_{\rm sh}}{dt}\right)^2\right\}.\end{aligned} \tag{2.9}$$

The density distributions of the CSM and the ejecta are scale free, so the shock radius should also be scale free. Hence we impose the power-law solution as follows:

$$R_{\rm sh} = Kt^m, \tag{2.10}$$

where K is a constant value. Substituting this to equation 2.9 results in

$$\begin{aligned}&\frac{\mathcal{D}K^{4-s}}{3-s}m(m-1)t^{2(m-1)-m(s-2)} + \frac{K^{4-n}U_c^n}{n-3}m(m-1)t^{(1-m)(n-3)+m-2}\\ &\quad = -\mathcal{D}K^{4-s}m^2t^{2(m-1)-m(s-2)} + K^{4-n}U_c^n(1-m)^2t^{(1-m)(n-3)+m-2}.\end{aligned} \tag{2.11}$$

Here we require that the power-law index of the time of all these four terms must be equal. Then we obtain the index as

$$m = \frac{n-3}{n-s}, \tag{2.12}$$

sometimes termed as an expansion parameter or a deceleration parameter (Vink, 2020). Furthermore, comparing the coefficients in equation 2.9 provides the solution for K as follows:

$$K = \left[\frac{(3-s)(4-s)}{(n-3)(n-4)}\frac{U_c^n}{\mathcal{D}}\right]^{1/(n-s)}. \tag{2.13}$$

Finally, we find the solution of the time evolution of the shock radius,

$$R_{\rm sh} = \left[\frac{(3-s)(4-s)}{(n-3)(n-4)}\frac{U_c^n}{\mathcal{D}}\right]^{1/(n-s)} t^{(n-3)/(n-s)}, \tag{2.14}$$

and the shock velocity

$$V_{\rm sh} = \frac{n-3}{n-s}\frac{dR_{\rm sh}}{dt} = \frac{n-3}{n-s}\left[\frac{(3-s)(4-s)}{(n-3)(n-4)}\frac{U_c^n}{\mathcal{D}}\right]^{1/(n-s)} t^{(s-3)/(n-s)}. \tag{2.15}$$

To determine the normalization of K, the dependence of U_c should be described. U_c is calculated by the integral for the ejecta mass $M_{\rm ej}$ and the explosion energy $E_{\rm ej}$. To avoid the divergence of the integrations, we consider the inner part of the ejecta ($v \leq V_{\rm in}$) where the density distribution is constant. Through this prescription the integrals can be computed as follows;

$$M_{\rm ej} = \int_0^{R_{\rm sh}} 4\pi r^2 \rho_{\rm ej} dr = 4\pi U_c^n V_{\rm in}^{3-n}\left[\frac{1}{3} + \frac{1}{n-3}\right], \tag{2.16}$$

$$E_{\rm ej} = \int_0^{R_{\rm sh}} \left(\frac{1}{2}\rho_{\rm ej} v^2\right) 4\pi r^2 dr = 2\pi U_c^n V_{\rm in}^{5-n}\left[\frac{1}{5} + \frac{1}{n-5}\right], \tag{2.17}$$

and finally these equations can lead the following relation,

$$U_c^n = \left[\frac{2\pi}{E}\left(\frac{1}{5} + \frac{1}{n-5}\right)\right]^{-(n-3)/2}\left[\frac{4\pi}{M}\left(\frac{1}{3} + \frac{1}{n-3}\right)\right]^{(n-5)/2}. \tag{2.18}$$

For $n = 7$, this description coincides with the equation (24) in Chevalier, 1982a, but U_c is notated as g therein.

2.3 Particle acceleration and magnetic field amplification

2.3.1 Parametrizations

At the collisionless shock front, charged particles such as electrons or protons become energetic by diffusive shock acceleration (DSA, Fermi, 1949; Bell, 1978; Drury, 1983). The motion of the charged particles is relativistic and random, followed by magnetic field amplification. We parametrize the energy density of the electrons (u_e) and magnetic field (u_B) as a fraction of the post-shocked energy density as follows:

$$u_e = \epsilon_e \rho_{\rm sh} V_{\rm sh}^2, \tag{2.19}$$

$$u_B = \frac{B^2}{8\pi} = \epsilon_B \rho_{\rm sh} V_{\rm sh}^2, \tag{2.20}$$

where $\rho_{\rm sh}$ is the CSM density at the forward shock [2] . ϵ_e and ϵ_B are the parameters which determine the efficiency of the shock acceleration and the magnetic field amplification. There remains a debate on the realistic values of these parameters (e.g., Spitkovsky, 2008; Maeda, 2012; Caprioli, Pop, and Spitkovsky, 2015; Caprioli and Spitkovsky, 2014b).

[2] Indeed the definition of this parametrization is not unified; in Matsuoka and Maeda, 2020 the "shocked" CSM density is adopted and the energy density is multiplied by 4, while in Murase et al., 2019 the energy density is divided by 2 in order to mimic that the energy carried to relativistic particles and amplified magnetic field are originally from the "kinetic" energy of the shock. Besides the choice of the coefficient of the shock velocity also depends on the paper. See also Appendix A and the discussion in DeMarchi et al., 2022.

2.3.2 Energy density distribution of accelerated electrons

We consider the power-law distribution of the number density of the accelerated electrons N as a function of the Lorentz factor (γ) as follows:

$$N(\gamma) = C\gamma^{-p}. \tag{2.21}$$

The index p characterizes the hardness of the spectrum of the electron distribution. The theoretical value predicted by DSA is $p = 2$, and the values smaller (harder) than 2.5 is also supported in the observations of Galactic SNRs (Vink, 2020). Contrary to this argument, modeling of optically thin radio emissions from Type Ib/Ic SNe suggests the larger (softer) value, $p \sim 3$ (Chevalier and Fransson, 2006). The reason for this discrepancy has not been revealed yet, but one idea suggested is that the characteristic Lorentz factor of electrons that emit centimeter ($\sim$GHz) emission in SNe would be small so that the condition for the realization of DSA is not satisfied (Maeda, 2013a). In any way, understanding the origin of the soft spectrum of the accelerated electrons in SNe would be a key to approaching the physics of particle acceleration.

The coefficient C is determined by equating the integrated energy density of the electrons with u_e,

$$\int_{\gamma_{\rm min}}^{\gamma_{\rm max}} d\gamma N(\gamma)\gamma m_e c^2 = u_e \Rightarrow C = \frac{(p-2)u_e}{\gamma_{\rm min}^{2-p} m_e c^2}, \tag{2.22}$$

where m_e, c, and $\gamma_{\rm min}$ are the electron mass, the speed of light, and the minimum Lorentz factor of the accelerated electrons, respectively. $\gamma_{\rm max}$ can be determined by the balance between the acceleration timescale and mainly cooling timescale of electrons, generally greater than $\gamma_{\rm min}$ by orders of magnitude so as to be regarded as infinity. We can associate ϵ_e and $\gamma_{\rm min}$ with the fraction of the "number" (not the energy) density of the accelerated electrons, f_e, through the derivation of the equation about the number density of accelerated electrons as follows:

$$\int_{\gamma_{\rm min}}^{\infty} d\gamma N(\gamma) = f_e \frac{\rho_{\rm sh}}{\mu_e m_p} \Rightarrow C = \frac{f_e(p-1)\rho_{\rm sh}}{\gamma_{\rm min}^{1-p}\mu_e m_p}, \tag{2.23}$$

where μ_e and m_p are the average molecular weight of (thermal) electrons and the atomic unit mass. Eliminating the coefficient C from equation 2.22 and 2.23 results in the following relation:

$$f_e = \epsilon_e \frac{p-2}{p-1}\frac{\mu_e m_p V_{\rm sh}^2}{\gamma_{\rm min} m_e c^2}. \tag{2.24}$$

By definition, $f_e < 1$ and $\gamma_{\rm min} > 1$ are imposed, but there is no consensus about the realistic values for these quantities. One of the parametrizations frequently employed is fixing $\gamma_{\rm min}$ as a constant value. Another method is to set f_e to the constant value (e.g., 1 or 0.1), and leave $\gamma_{\rm min}$ dependent on ϵ_e.

Though the energy distribution of electrons injected at the shock front follows the equation 2.21, the electrons spans within some physical lengthscale ΔR. Since the advected electrons can lose a fraction of their energies through some cooling effects, the spectrum integrated in the radial direction in the shocked CSM region can be deviated from the pure power-law distribution. The physical lengthscale ΔR in which electrons with potential of radiating synchrotron emission is determined by the following considerations. First is that the accelerated electrons would be advected inward with the velocity of $\sim V_{\rm sh}/4$ in the rest frame of the forward shock. Second is that electrons would be advected for a cooling timescale with the energy itself retained. Summing up these points, the effective thickness ΔR in which the relativistic electrons reside can be estimated

as follows:

$$\Delta R \simeq \frac{V_{\rm sh} t_{\rm cool}}{4}, \tag{2.25}$$

where $t_{\rm cool}$ is the cooling timescale of electrons. This geometrical thickness is also used to determine the optical depth to SSA. As for the cooling timescale, usually we consider 4 kinds of cooling processes that may become important; synchrotron, inverse Compton, adiabatic, and Coulomb cooling. These timescales are described as

$$t_{\rm syn} = \frac{6\pi m_e c}{\sigma_T}\gamma^{-1}B^{-2} = \frac{6\pi}{\sigma_T}(em_e c)^{1/2}\nu^{-1/2}B^{-3/2} \tag{2.26}$$

$$t_{\rm IC} = \frac{3m_e c}{4\sigma_T}\gamma^{-1}U_{\rm ph}^{-1} = \frac{3}{4\sigma_T}(em_e c)^{1/2}\nu^{-1/2}B^{1/2}U_{\rm ph}^{-1} \tag{2.27}$$

$$t_{\rm ad} \simeq \frac{R_{\rm sh}}{V_{\rm sh}} \tag{2.28}$$

$$t_{\rm coulomb} = \frac{\gamma m_p m_e^2 c^3}{4\pi e^4 X\mathcal{D}R^{-s}\ln\Lambda} = \frac{m_p m_e^{5/2}c^{7/2}}{4\pi e^{9/2}X\mathcal{D}R^{-s}\ln\Lambda}B^{-1/2}\nu^{1/2} \tag{2.29}$$

where $e, \sigma_T, U_{\rm ph}, X$, and $\ln\Lambda \simeq 30$ are the elementary charge, Thomson cross section, the seed photon density, mass fraction of the hydrogen gas, and the Coulomb logarithm, respectively. The right expressions in $t_{\rm syn}, t_{\rm IC}$, and $t_{\rm coulomb}$ are derived by replacing the Lorentz factor with the synchrotron frequency given as follows:

$$\nu_{\rm syn} = \frac{qB}{m_e c}\gamma^2. \tag{2.30}$$

The total cooling timescale of electrons $t_{\rm cool}(\nu)$ emitting a synchrotron photon at frequency ν is then given as

$$t_{\rm cool}(\nu) = \left(\frac{1}{t_{\rm syn}} + \frac{1}{t_{\rm IC}} + \frac{1}{t_{\rm ad}} + \frac{1}{t_{\rm coulomb}}\right)^{-1}. \tag{2.31}$$

Before going to the discussion about the radiative processes we mention to the difference of the treatment on the electron cooling between the analytic and numerical framework. The analytic treatment presented in this chapter is limited in the description of the electron spectrum with the one-zone approximation, represented by the single-component power-law distribution. Instead, defining the thickness of the region where the accelerated electrons reside with the electron cooling timescale allows us to effectively take into accout for the cooling effect and to express the modification of the spectrum. Through the suggestion of the equation 2.30 as a relation between the Lorentz factor of the electron and the corresponding frequency for the synchrotron emission, we can associate the cooling timescale with the frequency we are now focusing on. This idea enable us to directly estimate the radiative quantities such as the luminosity described later, and the discussion in Chapter 3 and Chapter 4 is based on this idea. On the other hand in the numerical treatment, it is possible to follow the time evolution of the electron spectrum directly because we can consider the time evolutions of electron spectrums on the assumption of the multi-zone model. Two conditions are required. One is the number conservation of electrons; the number of electrons whose Lorentz factor settles within γ and $\gamma + d\gamma$ is written as $N(\gamma)d\gamma$, and this must be conserved with time. Second is that the cooling evolution of the Lorentz factor of electrons should be given as

$$\frac{d\gamma}{dt} = -\frac{\gamma}{t_{\rm cool}}. \tag{2.32}$$

Combining these two requests can straightforwardly evaluate the time evolution of the electron spectrum itself. Then, substituting the obtained spectrum into the definitions of the emissivity and absorption coefficient described below allows us to directly estimate the radiative properties such as luminosity, taking the effect of the cooling into account. Indeed, the discussions in Chapter 5 and Matsuoka et al., 2019 are based on this idea. In addition, if we consider only two process of the cooling, synchrotron and adiabatic cooling, then the analytical formula describing the time evolution of the electron spectrum can be derived (see Chapter 5). Whichever treatments we will employ, the essential point is to identify the bending of the spectrum, so called "cooling break" (e.g., Granot and Sari, 2002). The frequency corresponding to the cooling break can be derived by equaling the adiabatic timescale with others. If we consider the synchrotron or inverse Compton cooling as a main cooling process, then the frequency can be written down as follows:

$$\nu_{\rm syn,break} \simeq \frac{36\pi^2 e m_e c}{\sigma_T^2 B^3 t^2}, \tag{2.33}$$

$$\nu_{\rm IC,break} \simeq \frac{9\pi^2 e m_e c^3 R_{\rm sh}^4 B}{\sigma_T^2 L_{\rm bol}^2 t^2}. \tag{2.34}$$

$$\tag{2.35}$$

These expressions are useful to evaluate the cooling regime of the frequency in the modeling of radio SNe.

2.4 Radiative process

To interpret the observational results we need the model that treats the radiative process in the object emitting the radiation. Going back to the basics, the equation of the radiative transfer is written as

$$\frac{dI_\nu}{dz} = -\alpha_\nu I_\nu + j_\nu \tag{2.36}$$

$$\Leftrightarrow \frac{dI_\nu}{d\tau_\nu} = -I_\nu + S_\nu \tag{2.37}$$

where $z, I_\nu, j_\nu, \alpha_\nu, S_\nu, \tau_\nu$ is the coordinate along the light path, the intensity of the radiation, the emissivity, the absorption coefficient, the source function, and the optical depth, respectively. The last two quantities are defined as

$$S_\nu = \frac{j_\nu}{\alpha_\nu}, \tag{2.38}$$

$$\tau_\nu = \int \alpha_\nu dz. \tag{2.39}$$

We can derive the formal solution of the inhomogeneous linear differential equation 2.36. First we consider deriving the general solution of the homogeneous linear differential equation as follows:

$$\frac{dI_\nu}{d\tau_\nu} = -I_\nu \Rightarrow I_{\nu,\rm general} = I_{\nu,0} e^{-\tau_\nu}, \tag{2.40}$$

where $I_{\nu,0}$ is the arbitrary constant. Next, we can deduce the special solution of the equation 2.36 by regarding $I_{\nu,0}$ as a variable and taking the differential of $I_{\nu,0}$ by τ_ν as follows:

$$\frac{dI_\nu}{d\tau_\nu} = -I_\nu + S_\nu \Rightarrow I_{\nu,\rm special} = \int_0^{\tau_\nu} S(\tau'_\nu) e^{\tau'_\nu - \tau_\nu} d\tau'_\nu. \tag{2.41}$$

If the source function S_ν is constant with respect to the integration, the general solution of the equation 2.36 can be written down as follows:

$$I_\nu = I_{\nu,\mathrm{general}} + I_{\nu,\mathrm{special}} = I_{\nu,0}e^{-\tau_\nu} + S_\nu(1-e^{-\tau_\nu}). \tag{2.42}$$

We note that the first term of the last expression in denotes the decay of the initial intensity along the light path, while the second term corresponds to the enhancement of the radiative intensity. In the studies in this theses the initial intensity $I_{\nu,0} = 0$ is assumed.

Approximating the coordinate of the light path as radial coordinate and the spherical symmetry in the system, we can write down the observed flux density F_ν through the integration of the intensity I_ν over the solid angle of the radiative region as

$$F_\nu = \int I_\nu \cos\theta d\Omega \quad = \quad \int I_\nu \cos\theta \frac{R^2}{D^2}\sin\theta d\theta d\phi = \frac{\pi R^2}{D^2} I_\nu, \tag{2.43}$$

and the luminosity of the object L_ν as

$$L_\nu = 4\pi D^2 F_\nu = 4\pi^2 R^2 S_\nu (1-e^{-\tau_\nu}), \tag{2.44}$$

where R and D is the radius of the region emitting the radiation and the distance to the object, respectively. Comparing the computed F_ν with the observed flux and quantifying the luminosity L_ν allows us to explore the feasible physical parameters and to argue the intrinsic properties of the objects emitting the radiation.

Next we give a descriptions on the physical quantities relevant to synchrotron radiation. Radio emission from SNe can be raised as one of the direct tracer of the CSM, and is attributed to the synchrotron emission. Once the energy distribution of the electrons and the strength of the magnetic field are given, the physical quantities for the synchrotron emission can be calculated (Rybicki and Lightman, 1979). The emissivity $j_{\nu,\mathrm{syn}}$, the synchrotron self-absorption (SSA) coefficient $\alpha_{\nu,\mathrm{SSA}}$, and the source function $S_{\nu,\mathrm{syn}}$ are described as follows:

$$\begin{aligned}
j_{\nu,\mathrm{syn}} &= \frac{1}{4\pi}\int d\gamma P_{\nu,\mathrm{syn}}(\gamma)N(\gamma), \\
&= \frac{\sqrt{3}e^3 CB\sin\theta}{4\pi m_e c^2}\frac{2^{(p-1)/2}}{p+1}\Gamma\left(\frac{3p+19}{12}\right)\Gamma\left(\frac{3p-1}{12}\right)\left(\frac{\nu}{\nu_c(\gamma=1)}\right)^{-(p-1)/2}, \qquad (2.45)\\
\alpha_{\nu,\mathrm{syn}} &= -\frac{1}{8\pi\nu^2 m_e}\int d\gamma P_{\nu,\mathrm{syn}}(\gamma)\gamma^2\frac{\partial}{\partial\gamma}\left[\frac{N(\gamma)}{\gamma^2}\right] \\
&= \frac{2\sqrt{3}\pi}{9}2^{p/2}\frac{eC}{B\sin\theta}\Gamma\left(\frac{3p+2}{12}\right)\Gamma\left(\frac{3p+22}{12}\right)\left(\frac{\nu}{\nu_c(\gamma=1)}\right)^{-(p+4)/2}, \qquad (2.46)\\
S_{\nu,\mathrm{syn}} &= \frac{8\pi m_e}{p+1}\left(\frac{2\pi m_e c}{3eB\sin\theta}\right)^{1/2}\nu^{5/2}\frac{\Gamma(p/4+19/12)\Gamma(p/4-1/12)}{\Gamma(p/4+1/6)\Gamma(p/4+11/6)} \qquad (2.47)
\end{aligned}$$

Here, the power-law energy distribution of electrons is assumed in the process of the integrations. $P_{\nu,\mathrm{syn}}(\gamma)$ is the power per unit frequency emitted by one electron defined as follows:

$$\begin{aligned}
P_{\nu,\mathrm{syn}}(\gamma) &= \frac{\sqrt{3}e^3 B\sin\theta}{m_e c^2}F\left(\frac{\nu}{\nu_c}\right), \qquad (2.48)\\
\nu_c &= \frac{3\gamma^2 eB\sin\theta}{4\pi m_e c}, \qquad (2.49)\\
F(x) &= x\int_x^\infty K_{5/3}(y)dy, \qquad (2.50)
\end{aligned}$$

where θ is the pitch angle of the electron [3] , respectively. $K_{5/3}(y)$ is the modified Bessel function. The optical depth to SSA, the critical value for the modelling for radio emission is written down as

$$\tau_{\nu,\mathrm{syn}} \simeq \alpha_{\nu,\mathrm{syn}} \Delta R. \tag{2.51}$$

As noted before, we remark that the spectrum of the accelerated electrons can be modified due to the cooling process.

If the CSM is very dense, free-free absorption (FFA) in the pre-shocked CSM region plays an important role as an external absorber. The FFA absorption coefficient and its optical depth are estimated as follows:

$$\alpha_{\nu,\mathrm{ff}} = \frac{4e^6}{3m_e k_B c}\left(\frac{2\pi}{3k_B m_e}\right)^{1/2} T_e^{-3/2} Z^2 \frac{\rho_{\mathrm{CSM}}^2}{\mu_i \mu_e m_p} \nu^{-2} g_{\mathrm{ff}}, \tag{2.52}$$

$$\tau_{\nu,\mathrm{ff}} = \int_R^\infty \alpha_{\nu,\mathrm{ff}} dr = \frac{4e^6}{3m_e k_B c}\left(\frac{2\pi}{3k_B m_e}\right)^{1/2} T_e^{-3/2} Z^2 \frac{1}{\mu_i \mu_e m_p} \nu^{-2} g_{\mathrm{ff}} \mathcal{D}^2 \frac{R^{1-2s}}{2s-1} \tag{2.53}$$

where T_e, Z, μ_i, and g_{ff} are the thermal electron temperature, the charge of the thermal ions, the molecular weights of ions, and the free-free gaunt factor, respectively. The conventionally used electron temperature in the unshocked CSM is $T_e = 10^5$ K in order to explain the absorption feature of radio emission from Type II-L SNe (see e.g., Lundqvist and Fransson, 1988; Chevalier, Fransson, and Nymark, 2006). We note, however, that T_e involves large uncertainties and this could have effect on the radio emission in the early phase of SNe.

The observed radio luminosity per unit frequency (L_ν), characterized by the synchrotron source function ($S_{\nu,\mathrm{syn}}$) and the optical depths to SSA ($\tau_{\nu,\mathrm{syn}}$), taking FFA ($\tau_{\nu,\mathrm{ff}}$) into consideration, can be estimated as follows (Fransson and Björnsson, 1998; Chevalier and Fransson, 2017):

$$L_\nu = 4\pi^2 R_{\mathrm{sh}}^2 S_{\nu,\mathrm{syn}} (1 - e^{-\tau_{\nu,\mathrm{syn}}}) e^{-\tau_{\nu,\mathrm{ff}}}, . \tag{2.54}$$

The calculation of the radio light curves is summarized as follows. At given time t, the hydrodynamical properties ($V_{\mathrm{sh}}, R_{\mathrm{sh}}, \rho_{\mathrm{sh}}$) are first specified (equations 2.14, 2.15). Then, the energy densities of the accelerated electrons and the magnetic field are calculated through the parametrizations in equations 2.19 and 2.20. The distribution of the number density of the accelerated electrons is then given by equation 2.22. The natures of the electrons and the magnetic field thus specified are used in the computation of the quantities relevant to synchrotron emission ($j_{\nu,\mathrm{syn}}, \alpha_{\nu,\mathrm{syn}}$, and $S_{\nu,\mathrm{syn}}$). As the cooling timescale of electrons ($t_{\mathrm{cool}}(\nu)$) as well as optical depths to SSA and FFA are also determined, the radio luminosity per unit frequency can be calculated by equation 2.54.

2.5 $L_p - t_p$ relation

In this section we derive the fundamental relation between the peak luminosity L_p and the peak time t_p for radio SNe. Originally this relationship is suggested and visualized by Chevalier, 1998, Figure 4 of which has been referred to discuss the relative properties between the radio SNe. The peak of radio SNe is defined as the moment when optical depth to SSA becomes to be unity. Hence the goal is to give the radio luminosity as a function of the peak time with the condition of the optical depth of unity.

[3] Usually assumed is orders of 1. An alternative is to employ the formalizm that takes the average the synchrotron power in equation 2.48 over the solid angle (Granot and Sari, 2002; Aharonian, Kelner, and Prosekin, 2010).

First, we can arrange the dependence of $\tau_{\nu,\mathrm{syn}}$ on the variables as follows:

$$\tau_{\nu,\mathrm{syn}} \simeq K_\tau C B^{(p+2)/2} \nu^{-(p+4)/2} V_{\mathrm{sh}} t_{\mathrm{cool}}, \tag{2.55}$$

$$K_\tau = \frac{2\sqrt{3}\pi}{9} 2^{p/2} e \Gamma((3p+2)/12)\Gamma((3p+22)/12) \left(\frac{3e}{4\pi m_e c}\right)^{(p+4)/2}. \tag{2.56}$$

In addition, we can show that the normalization of the electron spectrum C and the magnetic field B can be related as follows:

$$C = 8\pi K_C \epsilon_e \rho_{\mathrm{sh}} V_{\mathrm{sh}}^2 = K_C \frac{\epsilon_e}{\epsilon_B} B^2 \propto \alpha_\epsilon B^2, \tag{2.57}$$

$$K_C = \frac{p-2}{8\pi \gamma_{\mathrm{min}}^{2-p} m_e c^2} \tag{2.58}$$

where $\alpha_\epsilon = \epsilon_e/\epsilon_B$ is the ratio between the acceleration efficiencies. Here assumed is that $\gamma_{\mathrm{min}} \sim 1$ is constant with time. This condition would not be broken unless the velocity of the shock is not high so much. Substituting the equation 2.57 into 2.55 leads to the following result:

$$\tau_{\nu,\mathrm{syn}} \simeq K_\tau K_C \alpha_\epsilon B^{(p+6)/2} V_{\mathrm{sh}} t_{\mathrm{cool}} \nu^{-(p+4)/2}. \tag{2.59}$$

If we require $\tau_{\nu,\mathrm{syn}} \simeq 1$ and postulate that adiabatic cooling is dominant, $t_{\mathrm{cool}} \simeq t$, this formula can be used to derive the peak time t_p as follows:

$$t_p \simeq (K_\tau K_C \alpha_\epsilon)^{-1} B^{-(p+6)/4} V_{\mathrm{sh}}^{-1} \nu^{(p+4)/2}, \tag{2.60}$$

or the peak frequency as a function of α_ϵ, B, and R_{sh} as

$$\nu_p \simeq (K_\tau K_C \alpha_\epsilon)^{2/(p+4)} B^{(p+6)/(p+4)} R_{\mathrm{sh}}^{2/(p+4)}. \tag{2.61}$$

We can also eliminate B from the expression of the radio luminosity as follows:

$$\begin{aligned} L_p &\simeq 4\pi^2 R^2 S_{\nu,\mathrm{syn}\,|\mathrm{peak}} \\ &\simeq 4\pi^2 K_S (K_\tau K_C)^{1/(p+6)} \alpha_\epsilon^{1/(p+6)} V_{\mathrm{sh}}^{(2p+13)/(p+6)} (t_p \nu)^{(2p+13)/(p+6)}, \end{aligned} \tag{2.62}$$

$$K_S = \frac{8\pi m_e}{p+1} \left(\frac{2\pi m_e c}{3e \sin\theta}\right)^{1/2} \frac{\Gamma(p/4+19/12)\Gamma(p/4-1/12)}{\Gamma(p/4+1/6)\Gamma(p/4+11/6)}. \tag{2.63}$$

The point worth mentioning is that the peak luminosity and the peak frequency (equation 2.62 and 2.61), both of which are able to be measured by observations, can be written as functions of the shock radius and the magnetic field at the peak time. If we give the acceleration efficiency ratio α_ϵ we can observationally determine the shock radius and the magnetic field at the peak time. Furthermore, it should be noted that the peak luminosity is proportional to the product of the peak time and the observation frequency with the index of $(2p+13)/(p+6)$.

Figure 2.4 shows the relationship between the peak luminosity L_p and the product of peak time (t_p) and the observed frequency, here fixed as 5 GHz. Given the values of α_ϵ and V_{sh}, these two characteristics can be connected through the unique solution, drawn by the dashed gray lines. Comparing this relations with observational plots allows us to infer the shock velocity of the SN and to investigate the relative properties between radio SNe.

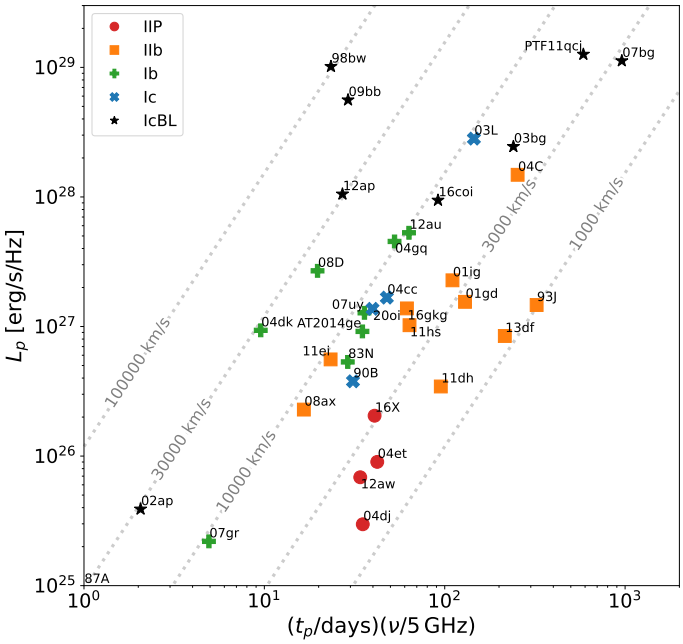

FIGURE 2.4: Peak radio luminosities of SNe (L_p) are plotted as a function of the product of peak time (t_p) and the observed frequency (5 GHz) for Type II, IIb, Ib, Ic, and IcBL SNe. Gray dashed lines show the proportional dependences of L_p and t_p, given the annotated shock velocities. In this diagram $\alpha_\epsilon = 1, \gamma_{\rm min} = 1$, and $p = 3$ are assumed.

2.6 Time and frequency dependences of optically thin and thick emissions

In this section we deduce the time and frequency dependences of the luminosity of radio SNe. These dependences can be a useful tool to interpret the observational radio light curves and spectra in SNe. Unlike the previous section, we do not discuss the normalization but focus on only the proportional relations. This is enough because the absolute values of the observed radio luminosity would be highly controlled by parameters such as $\mathcal{D}, \epsilon_e$, and ϵ_B involving large uncertainties, while the time and frequency dependences of the radio luminosity are represented by the values of the power-law index, which can be relatively determined rather robustly through observations.

2.6.1 Optically thin emission

Let us start from the equation of the optically thin emission, which can be written down as follows:

$$L_{\nu,\rm thin} \simeq 4\pi^2 R_{\rm sh}^2 j_{\nu,\rm syn} \Delta R \propto R_{\rm sh}^3 j_{\nu,\rm syn} \frac{t_{\rm cool}}{t}. \tag{2.64}$$

Substituting the equation 2.57 and equation 2.45, this can be arranged as

$$L_{\nu,\rm thin} \propto \alpha_\epsilon R_{\rm sh}^3 B^{(p+5)/2} \nu^{-(p-1)/2} \frac{t_{\rm cool}}{t}, \tag{2.65}$$

TABLE 2.1: Values of α and β

optical depth	**cooling regime**	α	β
Thin	adiabatic	$3m + \frac{(p+5)((2-s)m-2)}{4}$	$\frac{1-p}{2}$
Thin	synchrotron	$3m - 1 + \frac{(p+2)((2-s)m-2)}{4}$	$\frac{-p}{2}$
Thin	inverse Compton	$5m - 1 - \delta + \frac{(p+6)((2-s)m-2)}{4}$	$\frac{-p}{2}$
Thick	-	$2m - \frac{(2-s)m-2}{4}$	$\frac{5}{2}$

in which the cooling effect is taken into account. This indicates that depending on the cooling regime, the time and frequency dependences of the radio luminosity differs. Hereafter we expand the discussion dividing the cooling regime.

1. Adiabatic regime. $t_{\rm cool} \simeq t_{\rm ad} \propto t$ leads to

$$L_{\nu,\rm thin} \propto \alpha_\epsilon R_{\rm sh}^3 B^{(p+5)/2} \nu^{-(p-1)/2} \propto t^{3m+(p+5)((2-s)m-2)/4} \nu^{-(p-1)/2}. \tag{2.66}$$

2. Synchrotron regime. $t_{\rm cool} \simeq t_{\rm syn} \propto B^{-3/2}\nu^{-1/2}$ leads to

$$L_{\nu,\rm thin} \propto \alpha_\epsilon \frac{R_{\rm sh}^3}{t} B^{(p+2)/2} \nu^{-p/2} \propto t^{3m-1+(p+2)((2-s)m-2)/4} \nu^{-p/2}. \tag{2.67}$$

3. Inverse Compton regime. $t_{\rm cool} \simeq t_{\rm IC} \propto L_{\rm bol}^{-1} R_{\rm sh}^2 B^{1/2} \nu^{-1/2}$ leads to

$$L_{\nu,\rm thin} \propto \alpha_\epsilon \frac{R_{\rm sh}^5}{t} B^{(p+6)/2} \nu^{-p/2} L_{\rm bol}^{-1} \propto t^{5m-1-\delta+(p+6)((2-s)m-2)/4} \nu^{-p/2}, \tag{2.68}$$

   where $L_{\rm bol} \propto t^\delta$ is assumed.

It might be possible that Coulomb cooling can be a dominant cooling process. However, it is realized if we are paying attention to the lower frequency (small Lorentz factor for electrons) in the extremely dense CSM. In such a case free-free absorption will damp the radio signals with the low frequency, and expected not to be observed for us. Hence we do not consider such a situation.

2.6.2 Optically thick emission

Although the combination of the peak characteristics (L_p and t_p) and the properties of the optically thin emission is enough in interpreting the observation of radio SNe, the derivation of the dependence of optically thick emission can be useful. It is depicted as follows:

$$L_{\nu,\rm thick} \propto R_{\rm sh}^2 B^{-1/2} \nu^{5/2} \propto t^{2m-((2-s)m-2)/4} \nu^{5/2}. \tag{2.69}$$

We note that this is independent of the spectral index p.

Defining the dependencies as $L_{\nu,\rm thin} \propto t^\alpha \nu^\beta$, the power-law indexes can be summarized as shown in Table 2.1.

2.7 Useful expressions

So far we have guided the general formalizations of time evolutions of the SN shock behavior and quantities related to particle acceleration and magnetic field amplification. It is useful to

summarize the typical values of these quantities on the usual assumption. For simplicity, in the whole of this section we assume steady mass-loss activity ($s = 2$) and the soft spectral index ($p = 3$). We adopt the notation of the quantities $Q = 10^x Q_{,x}$ normalized by cgs unit unless definitely declared.

First we give an estimation of CSM density, which can be used to directly infer the mass-loss history of SN progenitors as noted in Section 2.2. The common description is given as follows (e.g., Chevalier, Fransson, and Nymark, 2006; Chevalier and Fransson, 2006; Maeda, 2012; Maeda et al., 2021):

$$\rho_{\rm CSM} = 5 \times 10^{11} A_* r^{-2}, \tag{2.70}$$

$$A_* \simeq \left(\frac{\dot{M}}{10^{-5}\,M_\odot\,{\rm yr}^{-1}}\right)\left(\frac{v_w}{10^8\,{\rm cm\,s}^{-1}}\right)^{-1}. \tag{2.71}$$

We note that A_* is equivalent with q defined in equation 2.3 on the assumption of $s = 2$. For a red supergiant, the typical progenitor of Type II SNe with $\dot{M} \sim 10^{-6}\ M_\odot\ {\rm yr}^{-1}$ and $v_w \sim 10\,{\rm km\,s}^{-1}$, A_* is orders of ~ 10, while for a Wolf-Rayet star, the typical progenitor of Type Ibc SNe with $\dot{M} \sim 10^{-5}\ M_\odot\ {\rm yr}^{-1}$ and $v_w \sim 10^3\,{\rm km\,s}^{-1}$, A_* becomes the orders of ~ 1.

Next we estimate the typical radius and velocity of the forward shock for Type II and Ibc SNe on the assumption of the steady mass-loss activity ($s = 2$). Here we use the notations of mass-loss rate, ejecta mass, and time since the explosion denoted as $\dot{M}_l = \dot{M}/(10^l\ M_\odot\ {\rm yr}^{-1})$, $M_{{\rm ej},l} = M/(l \times 1 M_\odot)$, and $t_{\rm 10d} = t/(10\,{\rm days})$, respectively. For Type II SNe $n \simeq 12$ is often assumed, and then

$$V_{\rm sh} = 9.8 \times 10^8 \dot{M}_{-6}^{-0.1} v_{w,6}^{0.1} E_{\rm ej,51}^{0.45} M_{\rm ej,10}^{-0.35} t_{\rm 10d}^{-0.1}\,{\rm cm\,s}^{-1}, \tag{2.72}$$

$$R_{\rm sh} = 9.4 \times 10^{14} \dot{M}_{-6}^{-0.1} v_{w,6}^{0.1} E_{\rm ej,51}^{0.45} M_{\rm ej,10}^{-0.35} t_{\rm 10d}^{0.9}\,{\rm cm}, \tag{2.73}$$

$$\tag{2.74}$$

can be deduced. On the other hand for Type Ibc SNe $n \sim 10$ is satisfied, and

$$V_{\rm sh} = 2.5 \times 10^9 \dot{M}_{-5}^{-0.13} v_{w,8}^{0.13} E_{\rm ej,51}^{0.44} M_{\rm ej,1}^{-0.313} t_{\rm 10d}^{-0.13}\,{\rm cm\,s}^{-1}, \tag{2.75}$$

$$R_{\rm sh} = 2.5 \times 10^{15} \dot{M}_{-5}^{-0.13} v_{w,8}^{0.13} E_{\rm ej,51}^{0.44} M_{\rm ej,1}^{-0.313} t_{\rm 10d}^{0.88}\,{\rm cm}, \tag{2.76}$$

$$\tag{2.77}$$

can be derived. We mention that even if we focus on the same timescale (10 days since the shock breakout for the above examples), the traced lengthscale of the CSM differs between SN types.

Next we go into the quantities relevant to particle acceleration and magnetic field amplification. The energy density of the shock and the accordingly determined magnetic field B and the normalization of the electron spectrum C are respectively given by

$$\rho_{\rm CSM} V_{\rm sh}^2 = 0.67 A_* t_{\rm 10d}^{-2}\,{\rm erg\,cm}^{-3}, \tag{2.78}$$

$$B = \sqrt{8\pi\epsilon_B \rho_{\rm CSM} V_{\rm sh}^2} = 4.6 \epsilon_{\rm B,-1}^{1/2} A_*^{1/2} t_{\rm 10d}^{-1}\,{\rm G}, \tag{2.79}$$

$$C = 8.3 \times 10^6 \epsilon_{\rm e,-1} A_* t_{\rm 10d}^{-2} \gamma_{\rm min,0}\,{\rm erg\,cm}^{-3}. \tag{2.80}$$

Here $n = 10$ is assumed in the computation of the magnetic field, though the dependence of n on B is weak.

As for the cooling timescale, the adiabatic timescale can be approximated by the SN age itself, whereas the estimate of the other timescales depends on which we choose the γ-dependent (Lorentz factor dependent) or frequency-dependent formulae. When we consider γ-dependent

formalizations the estimates are as follows:

$$t_{\rm syn} = 90\,\gamma_2^{-1}B_0^{-2}\,{\rm days}, \tag{2.81}$$
$$t_{\rm IC} = 1.3\,\gamma_2^{-1}L_{\rm bol,42}^{-1}r_{15}^2\,{\rm days}, \tag{2.82}$$
$$t_{\rm coulomb} = 7.9\times10^2\,\gamma_2 X_{0.75}^{-1}\rho_{\rm CSM,-20}^{-1}(\ln\Lambda)_{30}^{-1}\,{\rm years}, \tag{2.83}$$

where $X_{0.75} = X/0.75$ and $(\ln\Lambda)_{30} = \ln\Lambda/30$ are newly introduced, and $\mathcal{D}R^{-s}$ in equation 2.29 is replaced with $\rho_{\rm CSM}$. These formalizations can be used in the multi-zone modeling of non-thermal emission from SNe and SNRs. On the other hand if we consider frequency-dependent formalizations employed in one-zone modeling, the above estimates should be arranged as follows:

$$t_{\rm syn} = 3.7\times10^2\,B_0^{-3/2}\nu_{10}^{-1/2}\,{\rm days} \tag{2.84}$$
$$t_{\rm IC} = 2.8\,R_{\rm sh,15}^2L_{\rm bol,42}^{-1},\nu_{10}^{-1/2}B_0^{1/2}\,{\rm days} \tag{2.85}$$
$$t_{\rm coulomb} = 1.9\times10^2\,B_0^{-1/2}\nu_{10}^{0.5}X_{0.75}^{-1}\rho_{\rm CSM,-20}^{-1}(\ln\Lambda)_{30}^{-1}\,{\rm years}. \tag{2.86}$$

Equating cooling timescales with the SN age enables us to deduce the cooling break frequency defined in equation 2.33. For the cases of synchrotron and inverse Compton cooling, the corresponding cooling frequencies are given as follows:

$$\nu_{\rm syn,break} \simeq 6.6\epsilon_{B,-1}^{-3/2}A_*^{-3/2}t_{\rm 10d}\,{\rm THz}, \tag{2.87}$$
$$\nu_{\rm IC,break} = 0.74\epsilon_{B,-1}^{1/2}A_*^{1/2}V_9^4L_{\rm bol,42}^{-2}t_{\rm 10d}\,{\rm GHz}. \tag{2.88}$$

Finally we show the estimates of quantities relevant to synchrotron emission. The emissivity, self absorption coefficient, and the source function of synchrotron emission are computed as follows:

$$j_{\nu,\rm syn} \simeq 1.50\times10^{-23}CB\left(\frac{\nu}{\nu_c(\gamma=1)}\right)^{-1}\,{\rm erg\,s^{-1}\,cm^{-3}\,Hz^{-1}\,str^{-1}}, \tag{2.89}$$
$$\alpha_{\nu,\rm syn} \simeq 2.45\times10^{-9}CB^{-1}\left(\frac{\nu}{\nu_c(\gamma=1)}\right)^{-7/2}\,{\rm cm^{-1}}, \tag{2.90}$$
$$S_{\nu,\rm syn} = \frac{j_{\nu,\rm syn}}{\alpha_{\nu,\rm syn}} \simeq 6.12\times10^{-15}B^2\left(\frac{\nu}{\nu_c(\gamma=1)}\right)^{5/2}\,{\rm erg\,s^{-1}\,cm^{-2}\,Hz^{-1}\,str^{-1}}, \tag{2.91}$$

where the pitch angle is set to $\sin\theta = 1$ for simplicity. The most important quantity for synchrotron emission is the optical depth, which can be evaluated as follows:

$$\tau_{\nu,\rm syn} \simeq 2.45CB^{-1}V_{\rm sh,9}t_{\rm cool,0}\left(\frac{\nu}{\nu_c(\gamma=1)}\right)^{-7/2}. \tag{2.92}$$

When the CSM density is very high, free-free absorption becomes significant, and its absorption coefficient and optical depth can be deduced as follows:

$$\alpha_{\nu,\rm ff} = 2.0\times10^{-18}T_{e,5}^{-3/2}Z^2A_*^2r_{15}^{-4}\mu_i^{-1}\mu_e^{-1}\nu_{10}^{-2}g_{\rm ff}\,{\rm cm^{-1}}, \tag{2.93}$$
$$\tau_{\nu,\rm ff} = 6.8\times10^{-4}T_{e,5}^{-3/2}Z^2A_*^2R_{\rm sh,15}^{-3}\mu_i^{-1}\mu_e^{-1}\nu_{10}^{-2}g_{\rm ff}. \tag{2.94}$$

Chapter 3

Markov chain Monte Carlo analysis on radio supernovae

3.1 Introduction

Radio emission from core-collapse supernovae (termed as radio SNe in this chapter) is one of the electromagnetic signals we can observe from a kinds of SNe (for a review see Chevalier and Fransson, 2017). It is understood to be radiated when the SN shock emerging after the shock breakout propagates in the circumstellar medium (CSM) surrounding the SN progenitors. The collision of the SN shock with CSM drives acceleration of charged particles such as protons and electrons following amplification of turbulent magnetic field, through the mechanism such as diffusive shock acceleration (Fermi, 1949; Drury, 1983). Modeling of the hydrodynamics of the SN ejecta interacting with CSM and assuming the efficiency of particle acceleration and magnetic field amplification allows us to estimate the luminosity of the radio SNe per unit frequency (L_ν). One of the important physical information we are able to extract by comparing our light curve model with observations is the physical properties of the CSM. Since the physical structure of the CSM density can be interpreted as the mass-loss history of the SN progenitor prior to the core collapse through the conversion of the radius into the lookback time given the CSM velocity, radio SNe have been focused on as a tracer of the final mass-loss activity of massive stars (Margutti et al., 2017; Maeda et al., 2021).

In addition to the usefulness of radio SNe in the context of astrophysics, microphysics parameters assumed in the model have potential to constrain the physics relevant to particle acceleration and magnetic field amplification driven by non-relativistic SN shock. Theoretically, a variety of particle-in-cell simulations have raised a possible parameter range of the efficiency of the electron acceleration and of the amplification of magnetic field (e.g., Sironi and Spitkovsky, 2011; Park, Caprioli, and Spitkovsky, 2015; Caprioli, Pop, and Spitkovsky, 2015; Caprioli and Spitkovsky, 2014b). Construction of an evolutionary model for supernova remnants has also contributed to constraining the nature of particle acceleration (Lee, Ellison, and Nagataki, 2012). A series of these studies implies that the fraction of the energy density which is carried into the accelerated electrons or amplified magnetic field in the shock-heated gas from the upstream gas ranges roughly orders of magnitude of $10^{-5} - 0.1$. Gamma-ray burst afterglows also provide us with the opportunities to give constraints on the efficiency parameters, though the shock wave in gamma-ray bursts are considered to be in a relativistic regime (Eichler and Waxman, 2005; Barniol Duran, 2014; Beniamini and van der Horst, 2017; Duncan, van der Horst, and Beniamini, 2023; Sato et al., 2021).

Interpreting the observed data of radio SNe based on the standard model involves a tricky problem, however. We need several input parameters for the computation of the radio SN model; relevant to the structure of the CSM, the shape of the accelerated electron spectrum, and microphysics related to particle acceleration and magnetic field amplification. The larger number of the input parameters compared to the observational characteristics (e.g., peak luminosity, peak time, and cooling break if observed) leaves place of the generation the parameter degeneracy. This

leads to the complicated discussion on what kinds of the feasible physical parameters should be. Another problem is that the methodology of the modeling of radio SNe is not unified between the published papers (see also Section 3.3.3). For instance, as a case study of SN 2011dh, Maeda, 2012 has explored the plausible parameters of the CSM density and the efficiencies of the electron acceleration and the magnetic field amplification with the power-law indices of the CSM density, ejecta density, and the electron spectrum fixed. Another example is that Terreran et al., 2019 has deduced the best-fitted parameters of the physical structure of the CSM and the ejecta gradient with sets of microphysics parameters given. Yadlapalli, Ravi, and Ho, 2022 examined the parameter estimation of the ejecta properties of Type IIn and Ibn SNe such as mass, energy, and density gradient of the ejecta, in addition to the properties of the CSM. It can be said that the combination of the parameters to be surveyed, represented by the CSM properties and microphysics related to particle acceleration and magnetic field amplification, has not been unified among the previously published papers. Furthermore, it has been pointed out by DeMarchi et al., 2022 that the definition of the efficiencies of the electron acceleration and magnetic field amplification an the shock velocity involves variations by factors (for the details see Appendices therein). These situations prevent us from comparing the results of each case study and make the systematic investigations of radio SNe complicated. The aim of this chapter is to conquer the concerns described above through the performance of the Markov chain Monte Carlo (MCMC) analysis to tens of radio SN samples based on a consistently unified method to fit the observational data. This thorough systematic investigation can be expected to find out the statistical tendencies of the parameters related to astrophysics of SN progenitors and plasma physics associated with particle acceleration and magnetic field amplification.

This chapter is organized as follows. In Section 3.2 we show the selection procedure of the radio SN samples treated in our simulations. In Section 3.3 we describe the method to analytically compute the luminosity of radio SNe and to apply the model to MCMC analysis. In Section 3.4 we present the overall fitting results reproduced by our MCMC simulations. The implications for astrophysics and plasma physics related to particle acceleration and magnetic field amplification are discussed in Section 3.5 and Section 3.6, respectively. Section 3.7 describes the properties of the outlier objects of radio SNe that possibly deviate from the standard sequence of the behavior theoretically predicted. Finally, the contents of this chapter are summarized with a sort of discussion and caveats in Section 3.8.

3.2 Sample selection

Bietenholz et al., 2021 presented a comprehensive data set of radio SNe observed ever, and investigated the overall observational properties of radio SNe (e.g., peak luminosity and peak time). Indeed, observations of 294 radio SNe have been conducted ever mainly in the centimeter range, and the significant detections have been confirmed for 90 objects, corresponding to just $\sim$ 30% of all of the samples. We checked the 90 objects with the detected radio data one by one, and chose the samples obeying the following conditions; (i) the radio data set has been published, and (ii) there is plenty of radio data points illustrating the obvious peak luminosity, so that the surveyed parameters are expected to be constrained well. As a result we succeeded in collecting 33 golden samples of radio SNe from the assembly in Bietenholz et al., 2021. In addition, we include the radio data set of SN 2016X whose observations have been recently reported (Ruiz-Carmona, Sfaradi, and Horesh, 2022). In total, we treat 34 core-collapse SNe with golden data set for radio observations, including Type II, IIb, Ib, Ic, and broad-lined Ic (IcBL) SNe.

We note that samples of Type IIn SNe are excluded from our study, because the long-term evolution of Type IIn SNe requires us to continue the observations for a long period, making it difficult to obtain full data set of radio observations (for an example of radio data of SNe IIn, see e.g., Chandra et al., 2015). Another reason is that some Type IIn SNe may experience the

metamorphosis from Type Ibc to Type IIn SNe (Chandra et al., 2020; Margutti et al., 2017). Such SNe have been proposed to be interacting with shell-like CSM, which requests us to construct the detailed model apart from the smooth CSM.

Although the characteristics of radio SNe would depend largely on the structure of the CSM and the state of particle acceleration and magnetic field amplification, the explosive properties of the SN progenitors themselves such as the mass and kinetic energy of the ejecta ($M_{\rm ej}$ and $E_{\rm ej}$), as well as the distances to the objects (D), are also important to compare the computed models with observational data. Particularly $M_{\rm ej}$ and $E_{\rm ej}$ affects the velocity of the SN shock itself, while the distances to the SNe determines the normalization of the observed flux of the radio emission. We adopt the values inferred from the previous studies for every object. Table 3.1 summarizes the explosive properties of 34 radio SNe. For some stripped-envelope SNe (Type IIb, Ib, Ic, and IcBL SNe), the plausible ejecta properties of each object have not been published, and in such cases we employ the representative parameters proposed in Lyman et al., 2016, which are also summarized in Table 3.2.

3.3 Modeling of radio SNe and analysis through the MCMC method

3.3.1 Radio emission from SNe

We consider the SN ejecta experiencing homologous expansion in which the velocity and the density of the ejecta are described as follows:

$$v_{\rm ej} = \frac{r}{t} \tag{3.1}$$

$$\rho_{\rm ej} = t^{-3}\left(\frac{v}{U_c}\right)^{-n}, \tag{3.2}$$

where U_c is time-independent scale factor of the ejecta density, and is determined by the mass and the total kinetic energy of the ejecta. n specifies the density gradient of the SN ejecta and is limited within $n > 5$ (Chevalier, 1982a). In addition to the ejecta configuration, we consider the CSM density distribution as follows:

$$\rho_{\rm CSM} = \mathcal{D}_{\rm CSM} r^{-s} = 5\times10^{19} q \left(\frac{r}{10^{15}\,{\rm cm}}\right)^{-s}, \tag{3.3}$$

where q quantifies the magnitude of the CSM density at the radius $r = 10^{15}$ cm. For the power-law index, $0 < s < 3$ is required for the mass convergence. The value $s = 2$ describes the situation where the CSM is characterized by the steady wind, and then

$$q(s=2) = \frac{\dot{M}}{4\pi v_w} \times \frac{1}{5\times10^{11}\,{\rm g\,cm^{-1}}} = A_* \tag{3.4}$$

is realized, where $\dot{M}$ and v_w are the mass-loss rate of the progenitor and the CSM velocity, respectively. We mention that if we focus on $s = 2$ then q is equivalent with A_* used in the literature e.g., Maeda, 2012; Suzuki and Maeda, 2018; for typical Wolf-Rayet stars with the steady wind ($v_w = 1000\,{\rm km\,s^{-1}}$), $q(s=2) = A_* \sim 1$ can be expected (Chevalier and Fransson, 2006).

We describe the time evolution of the SN shock following the formalism based on the thin-shell approximation shown in (Chevalier, 1982a; Chevalier, 1982b). Specifically, we use the equations of the radius $R_{\rm sh}$ and the velocity $V_{\rm sh}$ of the SN shock as follows:

TABLE 3.1: Properties of samples of radio SNe treated in this chapter.

SN name	SN type	$M_{\rm ej}$ ($M_\odot$)	$E_{\rm ej}$ (10^{51} erg)	D (Mpc)	References of $M_{\rm ej}$, $E_{\rm ej}$ [1]	References of $L_{\rm bol}$ [1]	References of radio data[1]
SN 1983N	Ib	3.0	1.0	4.9	1	2	2
SN 1987A	IIP	14.0	1.1	0.051	3	4	5
SN 1990B	Ic	3.0	1.9	17.4	Lyman+16	Lyman+16	6
SN 1993J	IIb	2.7	1.0	3.7	7	7	8
SN 1998bw	IcBL	2.0	2.0	41.4	9	10	11
SN 2001gd	IIb	2.2	1.0	17.5	Lyman+16	Lyman+16	12
SN 2001ig	IIb	2.2	1.0	9.3	Lyman+16	Lyman+16	13
SN 2002ap	IcBL	3.8	7.0	8.9	14[2]	14	15
SN 2003L	Ic	3.0	1.9	92.0	Lyman+16	Lyman+16	16
SN 2003bg	IcBL	4.8	5.0	19.3	17	17	18
SN 2004C	IIb	2.2	1.0	35.9	Lyman+16	Lyman+16	19
SN 2004cc	Ic	3.0	1.9	17.4	Lyman+16	Lyman+16	20
SN 2004dj	IIP	10.0	0.75	3.4	21	21	22
SN 2004dk	Ib	3.7	1.8	20.8	23[3]	23[3]	20
SN 2004et	IIP	15.0	1.2	5.6	24, 25	24	26
SN 2004gq	Ib	1.8	1.9	24.3	23[3]	23[3]	20
SN 2007bg	IcBL	1.5	4.0	155.0	27	27	28
SN 2007gr	Ib	2.7	2.5	5.2	29	29	30
SN 2007uy	Ib	4.4	15.0	28.6	31	31	32
SN 2008D	Ib	4.0	3.0	28.6	33	33	34
SN 2008ax	IIb	2.9	0.5	6.2	35	36	35
SN 2009bb	IcBL	4.1	18.0	43.5	37	37	38
PTF11qcj	IcBL	2.9	6.0	135.0	Lyman+16	Lyman+16	39
SN 2011dh	IIb	3.0	1.0	7.9	40	40	41, 42
SN 2011ei	IIb	1.6	2.5	28.7	43	43	43
SN 2011hs	IIb	1.8	0.8	21.3	44	44	44
SN 2012ap	IcBL	2.7	9.0	40.0	45	45	46
SN 2012au	Ib	4.0	10.0	22.9	47	47	48
SN 2012aw	IIP	20.0	1.5	10.0	49	49	50
SN 2013df	IIb	1.1	0.8	18.1	51	51	52
AT2014ge	Ib	2.6	1.6	15.5	Lyman+16	Lyman+16	53
SN 2016X	IIP	28.0	1.7	15.2	54	55	56
SN 2016coi	IcBL	5.5	7.0	18.1	57	58	57
SN 2016gkg	IIb	3.4	1.2	26.4	59	60	61
SN 2020oi	Ic	1.0	1.0	15.0	62	63	63, 64

[1] References. (1) Weiler et al., 1986, (2) Shigeyama et al., 1990, (3) Blinnikov et al., 2000, (4) Suntzeff and Bouchet, 1990, (5) Turtle et al., 1987, (6) van Dyk et al., 1993, (7) Shigeyama et al., 1994, (8) Weiler et al., 2007, (9) Höflich, Wheeler, and Wang, 1999, (10) Patat et al., 2001, (11) Kulkarni et al., 1998, (12) Stockdale et al., 2007, (13) Ryder et al., 2004, (14) Mazzali et al., 2002, (15) Berger, Kulkarni, and Chevalier, 2002, (16) Soderberg et al., 2005, (17) Mazzali et al., 2009, (18) Soderberg et al., 2006, (19) DeMarchi et al., 2022, (20) Wellons, Soderberg, and Chevalier, 2012, (21) Zhang et al., 2006, (22) Nayana, Chandra, and Ray, 2018, (23) Lyman et al., 2016, (24) Sahu et al., 2006, (25) Li et al., 2005, (26) Chevalier, Fransson, and Nymark, 2006, (27) Young et al., 2010, (28) Salas et al., 2013, (29)Hunter et al., 2009, (30) Soderberg et al., 2010b, (31) Roy et al., 2013, (32) van der Horst et al., 2011, (33) Tanaka et al., 2009 (34) Soderberg et al., 2008, (35) Roming et al., 2009, (36) Pastorello et al., 2008, (37) Pignata et al., 2011, (38) Soderberg et al., 2010a, (39) Corsi et al., 2014, (40) Bersten et al., 2012, (41) Krauss et al., 2012, (42) Soderberg et al., 2012, (43) Milisavljevic et al., 2013a, (44) Bufano et al., 2014, (45) Milisavljevic et al., 2015, (46) Chakraborti et al., 2015, (47) Milisavljevic et al., 2013b, (48) Kamble et al., 2014, (49) Dall'Ora et al., 2014, (50) Yadav et al., 2014, (51) Morales-Garoffolo et al., 2014, (52) Kamble et al., 2016, (53) Chandra et al., 2019, (54) Utrobin and Chugai, 2019, (55) Huang et al., 2018, (56) Ruiz-Carmona, Sfaradi, and Horesh, 2022, (57) Terreran et al., 2019, (58) Prentice et al., 2018, (59) Bersten et al., 2018, (60) Prentice et al., 2019, (61) Nayana et al., 2022, (62) Rho et al., 2021, (63) Horesh et al., 2020, (64) Maeda et al., 2021

[2] The average value of the parameter ranges indicated therein.

[3] Parameters presented in Table 5 of Lyman et al., 2016 are employed.

TABLE 3.2: Explosion parameters of stripped-envelope SNe derived in Lyman et al., 2016.

SN type	$M_{\rm ej}$ $(M_\odot)$	$E_{\rm ej}$ $(10^{51}$ erg)
IIb	$2.2(\pm0.8)$	$1.0(\pm0.6)$
Ib	$2.6(\pm1.1)$	$1.6(\pm0.9)$
Ic	$3.0(\pm2.8)$	$1.9(\pm1.3)$
IcBL	$2.9(\pm2.2)$	$6.0(\pm5.0)$

$$R_{\rm sh} = \left[\frac{(3-s)(4-s)}{(n-3)(n-4)}\frac{U_c^n}{\mathcal{D}}\right]^{1/(n-s)} t^{(n-3)/(n-s)}, \tag{3.5}$$

$$V_{\rm sh} = \frac{dR_{\rm sh}}{dt} = \frac{n-3}{n-s}\frac{R_{\rm sh}}{t}, \tag{3.6}$$

where U_c^n is given as follows:

$$U_c^n = \left[\frac{2\pi}{E_{\rm ej}}\left(\frac{1}{5}+\frac{1}{n-5}\right)\right]^{-(n-3)/2}\left[\frac{4\pi}{M_{\rm ej}}\left(\frac{1}{3}+\frac{1}{n-3}\right)\right]^{(n-5)/2}. \tag{3.7}$$

We can see that the formalisms of the time evolution of the SN shock described in equations 3.5 and 3.6 depend on explosion properties $M_{\rm ej}$ and $E_{\rm ej}$ as well as the configuration of the CSM. It is speculated that fitting observational data of radio SNe based on this equations allows us to constrain even the ejecta properties. However, they can also be constrained through modeling of optical observables (e.g., Lyman et al., 2016), while the CSM configuration as well as the ejecta gradient n can be sensitively determined by non-thermal emission, not by optical emission. Thus we make the explosion parameters fixed as those shown in Table 3.1.

Next we move to the parametrization of particle acceleration and magnetic field amplification. Once the SN shock sweeps up the material consisting of the CSM, particle acceleration mechanism such as diffusive shock acceleration would be induced (Fermi, 1949; Drury, 1983). Then a fraction of the energies injected into the SN shock are carried into electrons in the shocked CSM and they are forced to be relativistically accelerated, followed by the magnetic field amplification. We parametrize these physical processes with the parameters ϵ_e and ϵ_B introduced as follows:

$$u_e = \epsilon_e \rho_{\rm sh} V_{\rm sh}^2, \tag{3.8}$$

$$u_B = \frac{B^2}{8\pi} = \epsilon_B \rho_{\rm sh} V_{\rm sh}^2, \tag{3.9}$$

where $\rho_{\rm sh}$ is the (unshocked) CSM density at the radius of the SN shock. [1] Equation 3.9 allows us to estimate the amplified magnetic field. In addition to ϵ_e and ϵ_B, we introduce the parameter f_e, the fraction of the "number" of the electrons that becomes relativistic transiting from thermal state as follows:

$$N_e = f_e \frac{\rho_{\rm sh}}{\mu_e m_p} \tag{3.10}$$

where N_e, μ_e and m_p are the number density of relativistic electrons, mean molecular weight of

[1] In other words, we just suppose $\rho_{\rm sh} = \mathcal{D} R_{\rm sh}^{-s}$. However, we need to mention that the

thermal electrons in the CSM and proton mass, respectively. We consider the power-law distribution for the assembly of the accelerated electrons $N(\gamma)$ described as follows:

$$N(\gamma) = C\gamma^{-p}, \tag{3.11}$$

where p is the spectral index. Equating the number and energy density of the relativistic electrons with equation 3.8 and 3.8 with those derived from the integration of equation 3.11 leads to the relationship between ϵ_e, f_e, and the minimum Lorentz factor of the electrons $\gamma_{\rm min}$ as follows:

$$\gamma_{\rm min} = \frac{p-2}{p-1}\frac{\epsilon_e \mu_e m_p V_{\rm sh}^2}{f_e m_e c^2}. \tag{3.12}$$

Thus if we give two values out of (ϵ_e, f_e, and $\gamma_{\rm min}$), the rest parameter would be automatically calculated. ϵ_e is one of the surveyed parameters in the MCMC simulations, which are introduced in Section 3.3.3, while we fix $f_e = 1$ as constant. If the value of $\gamma_{\rm min}$ through equation 3.12 falls below 1, then $\gamma_{\rm min} = 1$ is instead adopted. Then the normalization of the electron spectrum C would be calculated as a function of (ϵ_e and $\gamma_{\rm min}$) through the description of the energy density of the electrons.

Once the shape of the electron spectrum has been described, then the expected radio luminosity can be estimated without newly introducing parameters. By using the computed electron spectrum $N(\gamma)$ and the magnetic field B we can estimate the synchrotron emissivity $j_{\nu,\rm syn}$ and the corresponding absorption coefficient of synchrotron self-absorption $\alpha_{\nu,\rm syn}$, and we follow the formalisms described in Matsuoka and Maeda, 2020, except that synchrotron pitch angle θ_p is set to $\sin\theta_p = 1$ for simplicity. Optical depth to synchrotron self-absorption $\tau_{\nu,\rm syn}$ would be given in the form depending on the cooling timescale as follows (Chevalier and Fransson, 2017):

$$\tau_{\nu,\rm syn} \approx \int_{\rm shock} \alpha_{\nu,\rm syn} dr \approx \alpha_{\nu,\rm syn}\frac{V_{\rm sh} t_{\rm cool}}{4}, \tag{3.13}$$

where $t_{\rm cool}$ is the cooling timescale of the accelerated electrons. We consider four kinds of cooling processes; synchrotron, inverse Compton, adiabatic, and Coulomb cooling, though the last one can hardly affect the results (Fransson and Björnsson, 1998; Matsuoka et al., 2019; Maeda et al., 2021). Since the timescales of synchrotron cooling and inverse Compton process depend on the frequency ν that is emitted from electrons with Lorentz factor γ related by $\nu = \gamma^2 eB/(m_e c^2)$, where e is the elementary charge, the short cooling timescale has potential to make the observed radio spectrum bent in the higher frequency range (Björnsson, 2022). Our model is capable of taking this effect into account by associating the cooling timescale with the optical depth to synchrotron self-absorption through equation 3.13. Finally the observed flux of radio emission from SNe can be estimated as follows:

$$F_{\nu,\rm model} = \pi\frac{R_{\rm sh}^2}{D^2}\frac{j_{\nu,\rm syn}}{\alpha_{\nu,\rm syn}}(1 - e^{-\tau_{\nu,\rm syn}}). \tag{3.14}$$

We refer to Chevalier and Fransson, 2017; Matsuoka and Maeda, 2020 for the specific formalisms of $j_{\nu,\rm syn}$, $\alpha_{\nu,\rm syn}$, $\tau_{\nu,\rm syn}$, and $t_{\rm cool}$.

3.3.2 Bayesian framework and setup of MCMC simulations

To find out the parameter set which is possible to explain the observed data of the radio SN investigated, we employ the python package `emcee` (Foreman-Mackey et al., 2013). `emcee` is capable of performing MCMC sampler with walkers for a large number of iterations and suggesting the probability density function (PDF) in the parameter space. For a simulation of one radio SN, we prepare 100 walkers iterating enough times for the solution to be converged, and discard the first

several thousand steps to exclude the samples before the burn-in phase from the subsequent analysis. In order to realize the random sampling from the iterated data set, we extracted the samples from the iterated data with the distance of auto-correlation time for each walker. If the number of the samples per a walker did not exceed more than around 50, then we restart the MCMC simulation with the greater number of the iterations (for details see Foreman-Mackey et al., 2013) [2] . We quit the restarting simulations once the iteration number becomes larger than $\sim 10^6$ due to the limitation of the computational cost.

The plausible parameter sets are searched in order for the posterior distribution $P(\{\theta\}|F_{\nu,\mathrm{obs}})$ (in other words, the conditional probability that the parameter set $\{\theta\}$ should be realized given the observational data $F_{\nu,\mathrm{obs}}$) to be maximized, which is defined as follows:

$$P(\{\theta\}|\{F_{\nu,\mathrm{obs}}\}) = \frac{P(\{F_{\nu,\mathrm{obs}}\}|\{\theta\})P(\{\theta\})}{Z(\{F_{\nu,\mathrm{obs}}\})}, \tag{3.15}$$

where $\{\theta\}$ is the parameter set, $\{F_{\nu,\mathrm{obs}}\}$ is the data set of the observed radio flux, $P(\{F_{\nu,\mathrm{obs}}\}|\{\theta\})$ is the likelihood function, $P(\{\theta\})$ is the prior distribution of the parameters, and $Z(\{F_{\nu,\mathrm{obs}}\})$ denotes the normalization factor dependent on only the data set of the radio SN. The logarithm of the likelihood function is defined by the summation of the residual between the observed and computed radio flux ($F_{\nu,\mathrm{model}}$) as follows:

$$\ln\, P(\{F_{\nu,\mathrm{obs}}\}|\{\theta\}) = -\frac{1}{2}\sum_{\mathrm{obs}}\left[\frac{(F_{\nu,\mathrm{obs}} - F_{\nu,\mathrm{model}})^2}{\sigma_{\mathrm{obs}}^2} + \ln\,\sigma_{\mathrm{obs}}^2\right], \tag{3.16}$$

where σ_{obs} is the observed error associated with the detected radio flux. Observed errors in the radio SNe mainly consist of intrinsic and systematic errors, and the latter may depend on the method to analyse the raw data as well as the weather at the observation and the way of calibrations, etc. For example, Kamble et al., 2014 has reported only the flux error associated with the image rms for SN 2012au, though the systematic error are noted to be taken into account in the process of the analysis. Hence it can be said that σ_{obs} may have uncertainties. In this study, we basically adopt the values of the error published in the each paper shown in Table 3.1, but if those are too small then we put an additional condition as $\sigma_{\mathrm{obs}} = 0.1F_{\nu,\mathrm{obs}}$.

3.3.3 Surveyed parameters and prior functions

As described in the previous section, we can see that there are many kinds of input parameters to calculate the radio luminosity from SNe. Especially the following parameters are considered to be crucial to characterize the spectrum and the light curve of radio SNe (Chevalier and Fransson, 2006; Chevalier, Fransson, and Nymark, 2006; Chevalier and Fransson, 2017).

1. Magnitude of the CSM density q,
2. Acceleration efficiency of electrons ϵ_e,
3. Amplification efficiency of magnetic field ϵ_B,
4. A spectral index of the accelerated electrons p,
5. A power-law index of the CSM density distribution s, and
6. A power-law index of the ejecta density distribution n.

[2] The description in `https://emcee.readthedocs.io/en/sTables/tutorials/autocorr/` is also useful and specialized.

TABLE 3.3: Parameters and their ranges considered in this study.

Parameter	range	`Usual`	`Astro`	`Plasma`	`ALL`
$\log q$	(-2, 3)	✓	✓	variable[1]	✓
$\log \epsilon_e$	(-5, 0)	✓	-1.30[2]	✓	✓
$\log \epsilon_B$	(-5, 0)	✓	-1.30[2]	✓	✓
p	(2, 3.1)	3.0	3.0	✓	✓
s	(0, 3)	2	✓	2	✓
n	(5, 30)	variable[3]	✓	variable[3]	✓

[1] $\log q = 1$ for SNe II, 2 for SNe IIb, and 0 for SNe Ib, Ic, and IcBL.
[2] This is equivalent to $\epsilon_e = \epsilon_B = 0.05$.
[3] $n = 12$ for SNe II, 10 for SNe IIb, and 7 for SNe Ib, Ic, and IcBL.

We consider uniform distributions as prior functions of these parameters within the range shown in Table 3.3, enabling us to conduct unbiased investigations. We note that q, ϵ_e, and ϵ_B are complied into the logarithmic scale because they can take the values in the wide range of orders of magnitude. The initial distributions of walkers in the MCMC simulations are uniformly and randomly arranged within the range of the surveyed parameters to seek out the parameter solution which can locally maximize the posterior distribution. This allows us to explore the localized solutions deviating from the main solution that maximizes the posterior distribution among the all area of the parameter space, and to visualize the degeneracy relationships between the surveyed parameters (see Section 3.7.3).

We mention to two points about the parameter range assumed in Table 3.3. First is that the upper limit of p is set to 3.1 to include the value $p = 3.0$, which is commonly adopted in the modeling of radio SNe. This is justified because previous radio observations of Type Ibc SNe support the electron spectrum shaped by $p \sim 3.0$, softer than the index theoretically predicted $p \sim 2.0$ (Chevalier and Fransson, 2006; Terreran et al., 2019; Horesh et al., 2020; Maeda et al., 2021). Second is that the power-law index of the ejecta density is ranging up to 30, to explore the possibility that the outer structure of the SN ejecta is extremely steepened. Actually there are some implications for Type IIb SN 1993J that favours the very steep index of the ejecta density as $n \sim 20$, based on the modeling of the hydrodynamics, X-ray emission, and very-long-baseline interferometry observations (Suzuki et al., 1993; Bartel et al., 1994; Fransson, Lundqvist, and Chevalier, 1996). To search another example of the radio SNe that may be consistent with such a steep density gradient of the ejecta, we build up the setting of the upper limit as $n < 30$ (see also Section 3.7.2).

In this study we examine four combinations of the choice of the surveyed parameters. We call each survey as `Usual`, `Astro`, `Plasma`, and `All`, and the simulated parameter sets in each survey are displayed in Table 3.3. As for the survey scheme `Usual`, `Astro`, and `Plasma`, the parameters for which we would not explore are fixed to values which are believed to be typical to each SN types. Here we need to remark that there has been a variety of the combinations of the explored parameters in a range of previous studies, and the discussion about the model for the argued radio SN has been often limited to the case study for each object. For instance, Maeda, 2012 investigated the properties of radio and X-ray emission from SN 2011dh on the assumption of $p = 3, s = 2$, and $n = 10.2$, and surveyed the most possible parameter set of q, ϵ_e, and ϵ_B (q is denoted as A_* therein because of $s = 2$). This combination of the surveyed parameters corresponds to the framework `Usual`. Another example is that Terreran et al., 2019 has investigated the features of radio emission from Type Ic SN 2016coi based on $p = 3$, and showed that given $\epsilon_e = \epsilon_B = 0.33$, the derived mass-loss rate of the progenitor is $\sim 1 - 2 \times 10^{-4}\, M_\odot\, \mathrm{yr}^{-1}, s \simeq 1.8$, and $n \simeq 8.2$. They also remarked

that the realistic values of ϵ_e and ϵ_B should be smaller than assumed, taking implications of recent particle-in-cell simulations into account, but the smaller ϵ_e and ϵ_B suggest the improbably high mass-loss rate. The framework therein is, giving values of p, ϵ_e, and ϵ_B and determining the rest of the parameters $q(= A_*), s$, and n, all of which are related to the physics of the SN progenitor. This attempt is named as `Astro`. In addition, we prepare the survey scheme `Plasma` to explore the possibility whether the parameter combination consisting of only microphysics parameters relevant to plasma physics (ϵ_e, ϵ_B, and p) have potential to play important role in explaining the characteristics of radio SNe. Finally, in the framework `All` we examine all of the parameters as much as we can suppose important.

3.3.4 Statistics

We propose the parameter set that maximize the posterior distribution defined in equation 3.15 extracted from the unbiased samples from our MCMC simulations as the best-fitted parameters for each SN. Furthermore, in order to inspect the statistical distributions of each surveyed parameter, we consider marginalizing our N-dimensional structured samples into one-dimensional distributions of the parameter we are focusing on (where N is the number of the surveyed samples, i.e., $N = 3$ or 6). We process the marginalized distributions into the kernel density estimation by making use of the python package `scikit-learn` with Scott rule (Pedregosa et al., 2011), and then we are capable of examining the statistical properties of each parameters in radio SNe, as well as giving the medians of the surveyed parameters with the relevant 1σ errors for each SN. We leave a caveat that the medians derived from the marginalized PDFs do not necessarily coincide with the best-fitted parameters.

To quantitatively evaluate the degree of the fitting results, we estimate the reduced chi-square $\chi^2_{\rm red}$ for the best-fitted parameter set and categorise the simulated objects into three classes depending on the value of $\chi^2_{\rm red}$; if $\chi^2_{\rm red} < 5$, then the object would be labelled as "well fitted". If $5 < \chi^2_{\rm red} < 10$, the SN would be regarded as "neither good nor bad", and if $\chi^2_{\rm red} > 10$ the object would be judged as "incapable of being fitted with the current model".

3.4 Fitting results

Table 3.4 shows the $\chi^2_{\rm red}$ of the best-fitted models for each SN. It is natural that `All` can reproduce the most best-fitted models $N(\chi^2_{\rm red} < 5) = 20$ because it surveys all of the physical parameters. One of the important remark is that `Plasma` reproduces the least model that can be fitted well with observations compared with the other survey frameworks. The difference of `Plasma` and the others is that `Plasma` fix the value of the normalization of the CSM density log q, depending on the SN type of the objects, while the other frameworks explore the feasible values of log q. We suggest that the normalization of the CSM density log q is an important key parameter to construct the model fitted to the radio SNe. It is also found that `Usual` produces the worse results than `Astro` or `All`. What fixed in `Usual` is the power-law index of the density structure of the CSM and the ejecta s and n. Thus we ascertain that the responsible parameters for making the fitting result unfavorable in `Usual` should be the gradient of the CSM and the ejecta s and n. Furthermore, we can see that the score of $\chi^2_{\rm red}$ smaller than 5 for the scheme `Astro` is comparable to that for `All`, indicating the possibility that the assumption $\epsilon_e = \epsilon_B = 0.05$ would be reasonable. However, as shown later, the survey framework in `All` suggests that the efficiencies do neither necessarily take the value orders of 0.05, nor satisfies the energy equipartition (see Section 3.6). Therefore, it should be concluded that we can extract poor information on the plasma physics related to microphysics parameters such as ϵ_e and ϵ_B.

Before the arguments on the statistical properties of the radio SNe, we need to insure the dependence of the MCMC scheme on the inferred parameters. Figure 3.1 shows the summing-up

TABLE 3.4: $\chi^2_{\rm red}$ in the best-fitted parameter set for each SN, followed by the number of the

SN name	Usual	Astro	Plasma	ALL
SN 1983N	0.78	0.82	1.82	0.66
SN 1987A	9.89	8.43	16.69	7.7
SN 1990B	6.57	1.52	7.36	1.0
SN 1993J	9.68	8.4	9.84	5.81
SN 1998bw	46.2	36.18	57.89	24.43
SN 2001gd	4.25	3.89	3.86	2.56
SN 2001ig	10.18	7.87	10.85	6.83
SN 2002ap	4.66	4.65	2.32	2.01
SN 2003L	12.7	2.29	47.2	1.6
SN 2003bg	14.34	8.12	77.79	7.12
SN 2004C	22.39	23.82	22.26	10.12
SN 2004cc	44.67	28.98	52.36	30.4
SN 2004dj	1.59	1.6	1.79	1.16
SN 2004dk	12.94	9.61	15.61	7.84
SN 2004gq	6.08	4.69	6.8	4.1
SN 2007bg	20.9	17.92	28.31	16.83
SN 2007gr	3.99	1.77	13.52	1.63
SN 2007uy	3.21	3.21	16.99	2.31
SN 2008D	4.79	5.7	10.78	4.02
SN 2008ax	13.94	7.45	30.04	7.46
SN 2009bb	12.27	7.9	11.86	7.59
PTF11qcj	23.55	18.04	49.18	13.85
SN 2011dh	8.71	2.87	7.4	2.4
SN 2011ei	11.39	4.71	6.69	4.36
SN 2011hs	10.3	11.03	10.69	9.82
SN 2012ap	1.63	0.6	4.14	0.58
SN 2012au	1.72	1.6	12.69	0.91
SN 2012aw	4.01	4.16	3.61	3.64
SN 2013df	15.44	13.16	24.55	13.38
AT2014ge	8.11	4.48	14.38	3.98
SN 2016X	5.23	0.91	6.74	0.85
SN 2016coi	4.99	3.05	100.08	2.15
SN 2016gkg	11.01	4.59	5.94	3.94
SN 2020oi	3.87	3.5	15.94	2.73
$N(\chi^2_{\rm red} < 5)$	12	19	6	20
$N(5 < \chi^2_{\rm red} < 10)$	7	8	7	8
$N(\chi^2_{\rm red} > 10)$	15	7	21	6

results of the MCMC simulations showing the medians and the relevant 1σ credible intervals of the parameters for each SNe dividing the surveying scheme (`Usual` : orange, `Astro` : blue, `Plasma` : green, and `All` : red). First we go through the results of parameters indicating power-law indices; p, s, and n. The power-law indices we are surveying have their own benchmark values that make the physical situation qualitatively distinct; $p \sim 2.5$ is the intermediate value between the soft and hard spectrum of the relativistic electrons, $s = 2$ indicates the steady mass-loss history of the progenitor, and $n \simeq 10$ denotes the existence of the extended convective envelope of the progenitor (Matzner and McKee, 1999). Comparing these reference values is required to check the consistency between the survey scheme. We can see that many of the objects with $\chi^2_{\rm red} < 5$ support the soft spectral index of the relativistic electrons ($p \gtrsim 2.5$). This result is consistent with a range of previous studies on radio SNe (e.g., Chevalier, Fransson, and Nymark, 2006; Chevalier and Fransson, 2006) and the assumption in `Usual` and `Astro`. It is also seen that whether the deduced value of s is larger or smaller than 2 and n than 10 can also be estimated without discrepancies between the survey scheme in the most of the objects examined. Thus we conclude that as for the power-law index parameters, the inferred medians are correctly estimated in the viewpoint of qualitative perspectives.

Next we look into Figure 3.2 showing medians and the relevant 1σ credible intervals of $\log q$, $\log \epsilon_e$, and $\log \epsilon_B$, the parameters determining the absolute magnitudes of the radio luminosity. It is shown that the parameters deduced from each survey scheme are consistent each other within 1 or 2 orders of magnitudes. This is a bit ambiguous because when we interpret these parameters in the physical contexts, the difference of orders of magnitude may become significant. Hence, it would not be recommended to interpret the deduced values of $\log q$, $\log \epsilon_e$, and $\log \epsilon_B$ literally. Nevertheless, they can be used to qualitatively examine the systematic tendencies of each parameter toward the SN type, which will be discussed in Section 3.5 and 3.6.

3.5 Implications on astrophysics

In this section we discuss the statistical tendencies of the parameters related to astrophysics (i.e., $\log q, s$, and n) to aim at giving constraints on stellar evolution theories and explosion properties of SN progenitors. Figure 3.3 shows the marginalized PDFs of astrophysical parameters convoluted by each SN type. The PDFs are constructed from the result of the MCMC simulation in the framework `All`, and hereafter we rely on this survey scheme as a reference.

3.5.1 n

The PDF of n shows a diversity between SNe II, IIb, and the others (stripped-envelope SNe). For stripped-envelope SNe, the feasible value of n is concentrated on the range of $5 < n < 10$, and this is consistent with the theoretical prediction that SN ejecta with radiation-dominated outer structure tends to have power-law index smaller that 10 (Matzner and McKee, 1999). Meanwhile, the PDF of SNe II and SNe IIb shapes bimodality with the peaks at $n \sim 12$, as well as $n \sim 7$, whereas the index predicted by Matzner and McKee, 1999 is $n \sim 12$. Since the progenitors of Type IIb SNe are considered to suffer the stripping of most (but not all of) their own hydrogen envelope through binary interaction (Ouchi and Maeda, 2017), it may not be inconsistent with that some of the samples of Type IIb SNe have the shallower power-law index that $n \sim 10$. As for Type II SNe, it is surprising that SN 2016X exhibits the power-law index of $n \sim 7$ independent of the survey scheme (see Figure 3.1), contradicting the theoretical prediction. SN 2016X may be a kind of an outlier for SNe II due to its large ejecta mass originated from the massive zero-age main sequence mass (see Section 3.7.1). We note that for SN 2004dj $n \sim 8$ is inferred from the scheme in `All`, but $n \sim 12$ from the scheme of `Astro`, making the argument ambiguous.

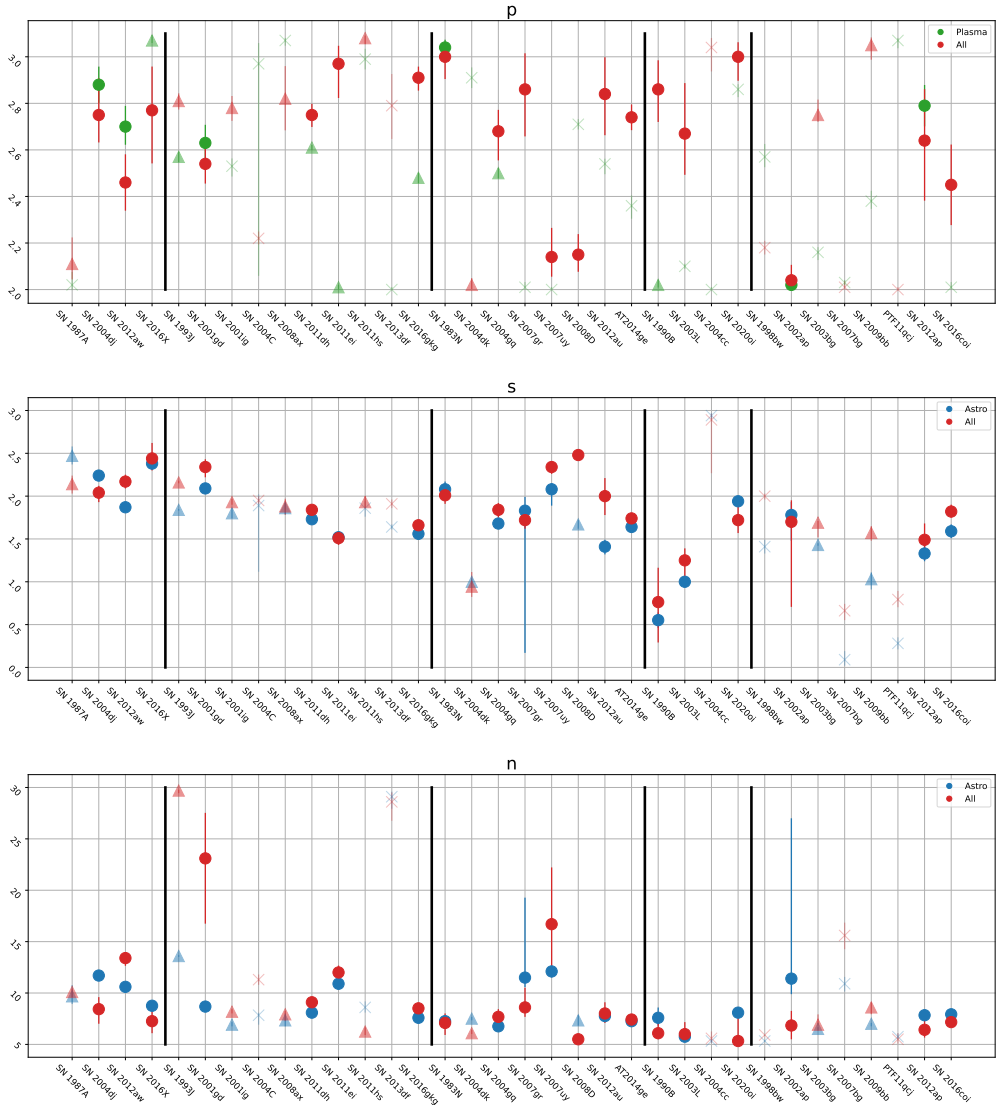

FIGURE 3.1: Summary of the MCMC simulations. The figures compare the values of the medians with 1σ credible intervals between the presented survey frameworks. Top, middle, and bottom panels display the result of p, s, and n. The examined SNe are sorted as the order of Type II, IIb, Ib, Ic, and IcBL SNe from the left side.

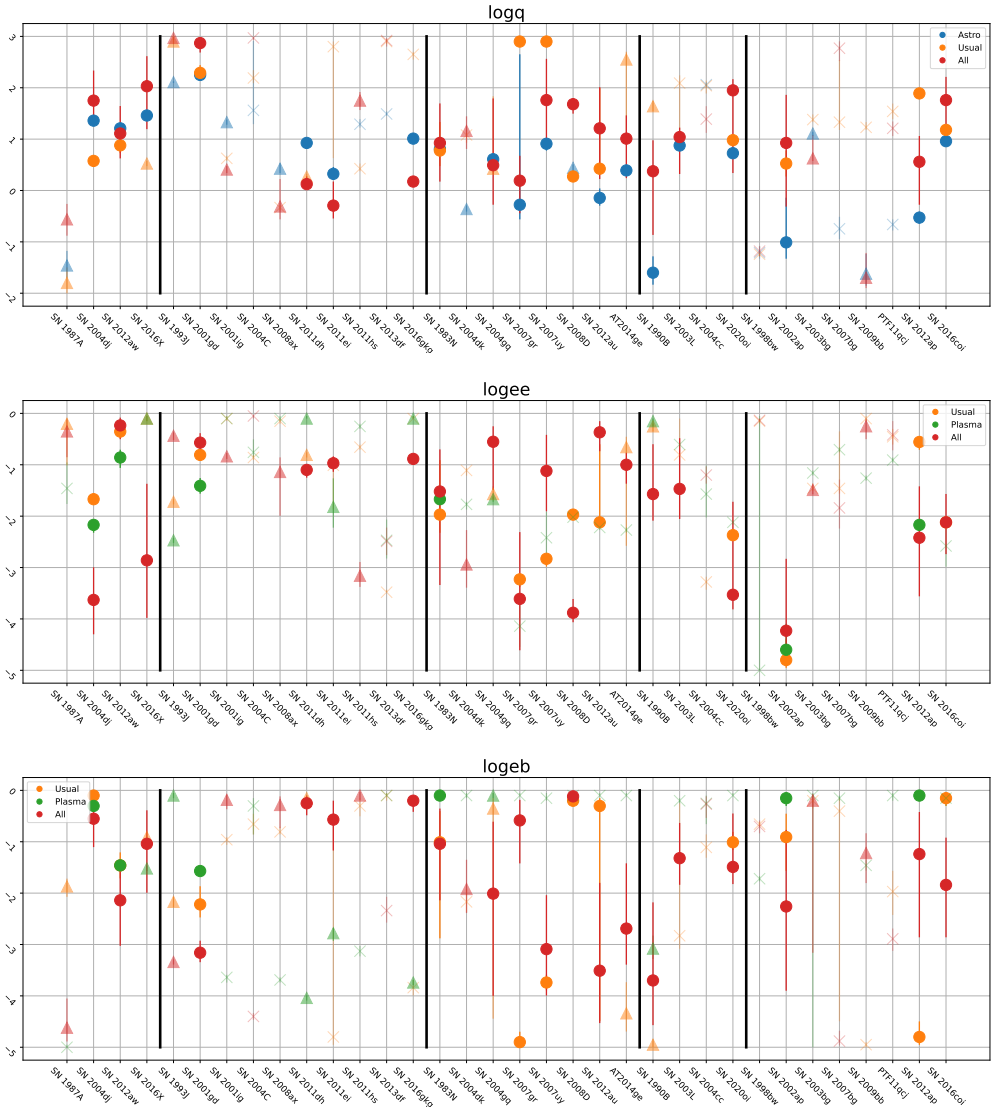

FIGURE 3.2: Same as Figure 3.1, but for log q (top), log ϵ_e (middle), and log ϵ_B (bottom).

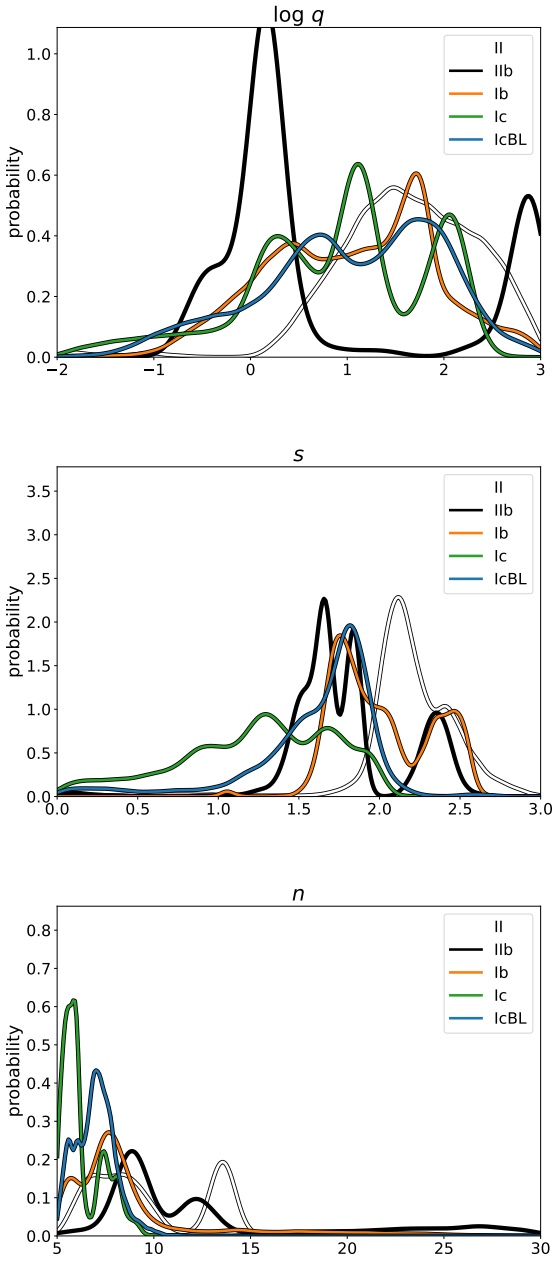

FIGURE 3.3: The PDFs of log q, s, and n, divided by the SN types (white for II, black for IIb, orange for Ib, green for Ic, and blue for IcBL).

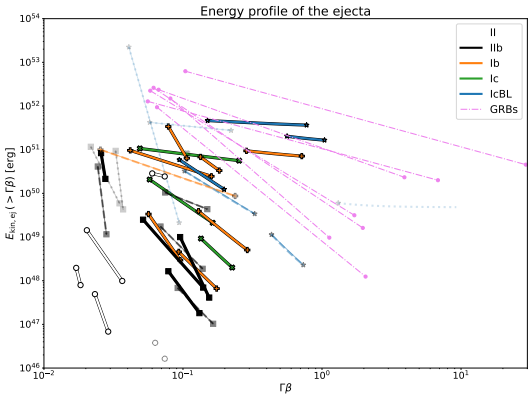

FIGURE 3.4: Collection of the proposed ejecta density profiles as a function of the four velocity. The edges of each line are determined by the maximum and minimum observation time of the radio emission. As a reference, the ejecta profiles of the gamma-ray bursts including sub-energetic events estimated in Margutti et al., 2014 are also plotted by the magenta dashdotted lines.

The characteristics of the ejecta properties can be clearly observed in the collective of the ejecta profiles shown in Figure 3.4. Within the velocity space traced only by the radio emission, the ejecta structure in Type II SNe can be characterized by the slow and steeply shaped ejecta. On the other hand those of stripped-envelope SNe tend to have rather faster and flatter ejecta profiles, and even their gradient is similar to those seen in gamma-ray bursts (Margutti et al., 2014). From this figure we can speculate the association between the degree of the stripping of the outer hydrogen envelope and the way of partition of the explosion energy into the ejecta.

3.5.2 s

We can also find out the characteristics of the probability density function of the power-law index of the CSM s. For SNe II the typical value lies in the range of $s \gtrsim 2$, whereas stripped-envelope SNe, especially Type Ic and IcBL SNe, have more flatter gradient given by $s \lesssim 2$. Both of the probability density distributions are distinct each other. Intriguingly, the criterion of the mass-loss activity $s = 2$, giving a picture of the steady wind, is likely to separate the progenitors of SN samples into two groups; it means that a red supergiant as a progenitor of Type II SNe would undergo increasing mass-loss activity towards the core collapse, while the progenitors with its hydrogen envelope stripped away would experience decreasing mass-loss activity in contrast. This would not be trivial because the existence of the hydrogen envelope should be originally determined independently of the time evolution of the mass-loss activity.

We have proposed the possibility that the degree of the stripping of the outer layer in the SN progenitors may be related to the time variation of the mass-loss activity. However, if the damping effect due to strong free-free absorption would be taken into account in the presented radio SN model, this relationship may be modified especially for Type II SNe. We refer readers to look to Section 3.8.1.

3.5.3 $\log q$

Although it is pointed out in Section 3.4 that the values of $\log q$ inferred in our simulations would involve uncertainties of orders of magnitude of 1 or 2, showing results relevant to $\log q$ would be useful for inferring the qualitative tendencies of the CSM density around the progenitors of radio SNe. The CSM density is speculated to be directly characterized by the SN type, because the

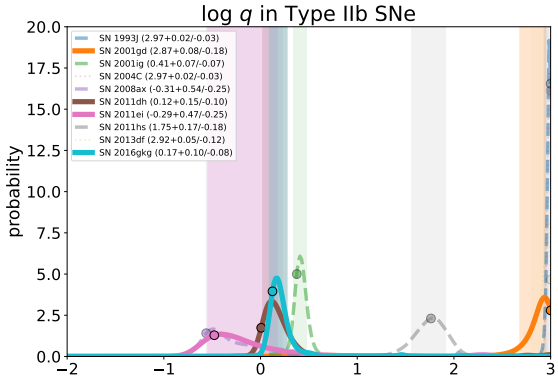

FIGURE 3.5: Probability density function of log q for samples of SNe IIb. The line styles used in this figure indicate the degree of the fitting results (solid for $\chi^2_{\rm red} < 5$, dashed for $5 < \chi^2_{\rm red} < 10$, and dotted for $\chi^2_{\rm red} > 10$).

magnitude of the mass-loss activity of the progenitor is reflected. Actually, our simulations have shown some tendencies depending on SN types. First, the probability density function of SNe IIb has bimodality consisting of the peaks with log $q \sim 3$ and log $q \sim 0$. This may be related with the diverse nature of the progenitor of SN IIb. It is pointed out that a red supergiant with an extended hydrogen envelope seen in SN 1993J, SN 2011hs and SN 2013df (Maund et al., 2004; Bufano et al., 2014; Van Dyk et al., 2014), a yellow supergiant with an attenuated hydrogen envelope supporting SN 2011dh and SN 2016gkg (Maund et al., 2011; Bersten et al., 2012; Bersten et al., 2018), and even a blue supergiant composed with a compact radiative core in SN 2008ax and SN 2011ei (Pastorello et al., 2008; Milisavljevic et al., 2013a) could be candidates for the progenitor of SNe IIb (see also the discussion in Maeda et al., 2022). Indeed, we can see from Figure 3.5 that the samples of SNe IIb are separated into three groups characterized by log $q \sim -1, 0$, and 3, and that each value of log q can be associated with the radii of the progenitors; red, yellow, and blue supergiants as progenitors of Type IIb SNe would be related with the CSM with its density quantified by log $q \sim 3, 0$, and 1, respectively. Surprisingly, this suggestions is consistent with results of stellar evolution computations and analysis on optical observational implications (Maeda et al., 2015; Ouchi and Maeda, 2017). We propose that the magnitude of the CSM density can be used to infer the nature of the progenitors of SNe IIb and even the physical process of the binary interaction.

Figure 3.6 shows the CSM density model composed from the best-fitted parameter sets proposed by the survey `All` and the converted mass-loss history of each SN progenitor given the velocity of the CSM typical for the progenitor. The traced physical lengthscale of the CSM is $\sim 10^{15-16}$ cm irrespective of SN types. However, considering that the typical wind velocity should depend on SN types, the converted mass-loss history would take a range of parameter space. We can see from Figure 3.6 that the typical mass-loss rate of Type II SN progenitors are $10^{-6}\,M_\odot{\rm yr}^{-1} \lesssim \dot{M} \lesssim 10^{-5}\,M_\odot{\rm yr}^{-1}$ ($v_w = 10\,{\rm km\,s}^{-1}$), which is consistent with estimates in previous studies (Chevalier, Fransson, and Nymark, 2006). On the other hand, those of stripped-envelope SN progenitors range around $10^{-5}\,M_\odot{\rm yr}^{-1} \lesssim \dot{M} \lesssim 10^{-3}\,M_\odot{\rm yr}^{-1}$ ($1 \lesssim A_* \lesssim 100$. Here assumed is $v_w = 1000\,{\rm km\,s}^{-1}$). The value previously considered to be feasible is $\dot{M} \sim 10^{-5}\,M_\odot{\rm yr}^{-1}$ (Chevalier and Fransson, 2006; Alexander, Soderberg, and Chomiuk, 2015; Terreran et al., 2019), and the upper limit is orders of magnitudes higher than this mass-loss rate. We note that the mass-loss rate described here represents the magnitude at the CSM radius of 10^{15} cm. Given the wind velocity v_w the CSM lengthscale of 10^{15} cm can be interpreted as the lookback time of the progenitors, corresponding to 30 years for Type II SNe and 0.3 years for stripped-envelope SNe, respectively. Particularly, many of the stripped-envelope SNe is likely to undergo the decreasing mass-loss episode 10 years before the explosion, tracing the late carbon burning phase or oxygen burning

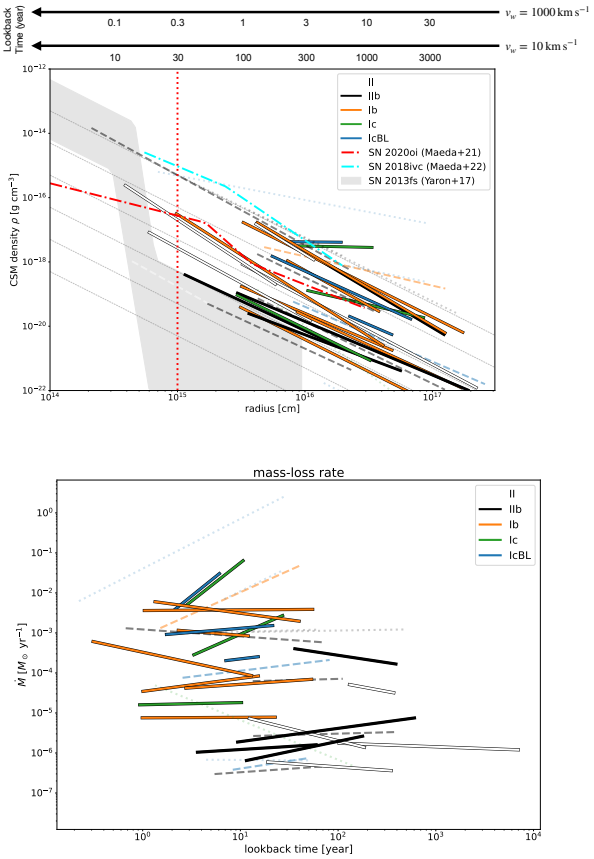

FIGURE 3.6: Top: CSM density distribution for each SN samples. The best-fitted values are employed in the plot. The gray dashed lines denote the CSM structure molded by steady mass-loss activity As a reference, we also plot the CSM structures previously inferred for SN 2020oi (Maeda et al., 2021), SN 2018ivc (Maeda et al., 2022), and SN 2013fs (Yaron et al., 2017). Bottom: the converted mass-loss history. The typical velocity of the CSM needed to determine the normalization of the mass-loss rate depends on SN types; $v_w = 10\,\mathrm{km\,s^{-1}}$ for SNe II, $v_w = 100\,\mathrm{km\,s^{-1}}$ for SNe IIb, and $v_w = 1000\,\mathrm{km\,s^{-1}}$ for stripped-envelope SNe. In both panel the line styles are similarly used as Figure 3.5.

phase (Woosley and Janka, 2005).

One of the matters concerning the deduced CSM density is that such a dense CSM in stripped-envelope SNe would affect the observational properties other than radio wavelength; if the very dense CSM resides around the SN progenitor then the interaction between SN ejecta and the dense CSM can power the radiation from the SN itself overwhelming the other radiative sources, classified as Type IIn SNe (e.g., Moriya et al., 2014). Indeed, Terreran et al., 2019 argues for SN 2016coi that the solution of high mass-loss rate should be excluded to avoid the enormous contribution to radiative properties powered by CSM interaction. However, recently Maeda et al., 2022 proposed that the CSM with $A_* \gtrsim 300$ ($\log q \gtrsim 2.5$) has potential to fully power the radiation from the SN itself through the demonstration of SN 2018ivc, and showed that the CSM thinner than that reference value is possible even in the normal stripped envelope SNe (e.g., SN 1993J). Thus we suggest that the mass-loss rate $\dot{M} \sim 10^{-3}\,M_\odot \mathrm{yr}^{-1}$ would not be inconsistent with properties of Type Ib/c SNe.

3.6 Implications on plasma physics

In this section we examine the statistical properties of the parameters related to plasma physics determining the nature of particle acceleration and magnetic field amplification ($\log \epsilon_e$, $\log \epsilon_B$, and p). Figure 3.7 shows the marginalized PDFs of microphysics parameters based on the result of the framework `All`, similarly convoluted by each SN type.

3.6.1 $\log \epsilon_e$ and $\log \epsilon_B$

As noted in Section 3.4, it should be remarked that both equipartition with $\epsilon_e = \epsilon_B = 0.05$ and non-equipartition can reproduce the good fitting results, implying the poorly informative results on ϵ_e and ϵ_B. Nevertheless, illustrating the PDFs of $\log \epsilon_e$ and $\log \epsilon_B$ may be useful to inspect the tendencies towards the SN types. We show in the top panels of Figure 3.7 the probability density distribution of $\log \epsilon_e$ and $\log \epsilon_B$ for each SN type. Actually it is hard to extract how the typical values of these parameters depend on SN types; these parameters can take diverse values in the range of orders of magnitude, indicating less correlation with SN types.

Figure 3.8 shows the best-fitted parameter or the median of $\log \epsilon_B$ plotted as a function of those of $\log \epsilon_e$. The realistic values of ϵ_e and ϵ_B have been still debated and not well constrained yet. Caprioli, Pop, and Spitkovsky, 2015 have suggested through particle-in-cell simulations that tens of percents of ions in the unshocked region will be energized relativistically by the non-relativistic shock, and if the acceleration efficiency of electrons is $\sim 1\,\%$ of ions, then $\epsilon_e \sim 10^{-3}$ can be expected. Magnetic field amplification through the propagation of non-relativistic shock has been also investigated theoretically, proved that the efficient amplification would be possible so that the observed strengths of the magnetic field in supernova remnants in our galaxy can be consistent with implications from the simulations (Caprioli and Spitkovsky, 2014b). On the other hand our MCMC simulation is showing that there is a diversity of the value of ϵ_e independent of the SN type of the object. It is also examined by particle-in-cell simulations that for a fast shock parallel to the background magnetic field, higher Mach number of the non-relativistic shock can stimulate higher acceleration efficiencies of electrons (Caprioli and Spitkovsky, 2014a). We have calculated the time evolution of the Mach number of the SN shock by assuming typical progenitor radius and the surface temperature and modeling the distribution of the sonic velocity in the unshocked CSM, and found less correlations between the Mach number and the efficiencies. These implications may propose the possibility that the important physical elements determining the acceleration and amplification efficiencies are different from SN types or the relevant astrophysical components. For instance, the inhomogeneity of the CSM density, an important physical parameter for Richtmyer-Meshkov instability but not taken into consideration in our model, may be crucial for determining the efficiency of the acceleration and amplification efficiencies (Brouillette, 2002).

3.6.2 p

We can see that the spectral index of electrons accelerated in the SN shock tends to be soft ($p \gtrsim 2.5$), contrary to the theoretical predicted value $p \sim 2$. This has been pointed out by a range of previous studies (e.g., Chevalier and Fransson, 2006; Chevalier, Fransson, and Nymark, 2006). Especially Maeda, 2013b suggests that the soft spectral may be originated from the fact that the Lorentz factor related to the synchrotron frequency we are observing is too small to satisfy the condition to be accelerated by diffusive shock acceleration ($\gamma \gtrsim 200$). Yet it should be noted that some objects have hard spectral index, $p \sim 2$, especially for the energetic SN (SN 2002ap, SN 2007uy, and SN 2008D). Indeed, Björnsson and Fransson, 2004 has pointed out the possibility that based on the time dependence of the optically thin emission from SN 2002ap, SNe with energetic explosions

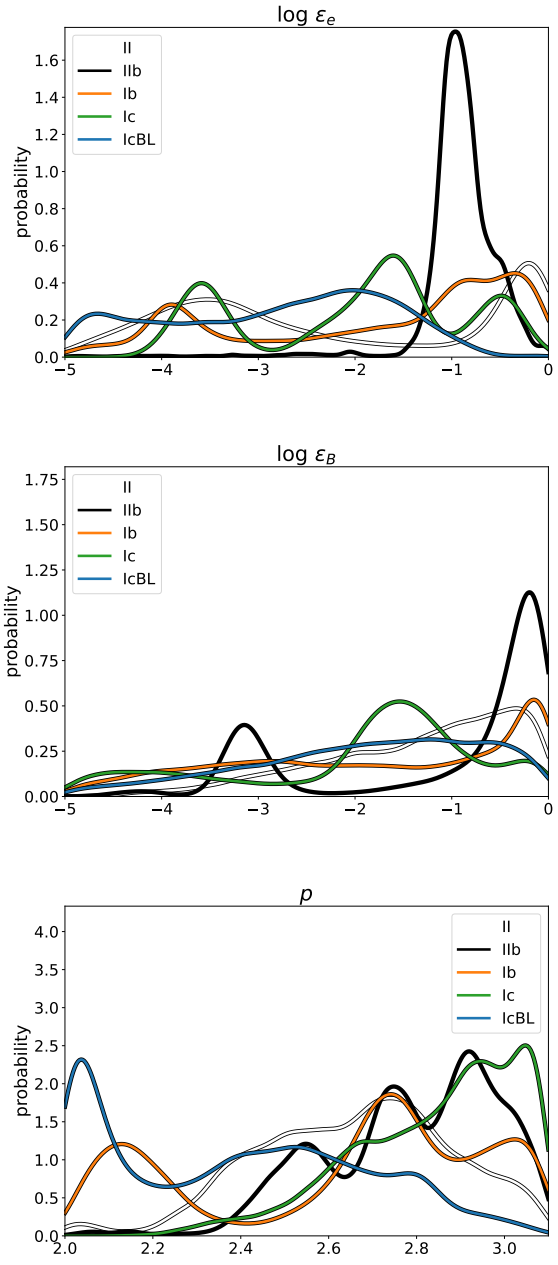

FIGURE 3.7: Same as Figure 3.3, but for log ϵ_e, log ϵ_B, p.

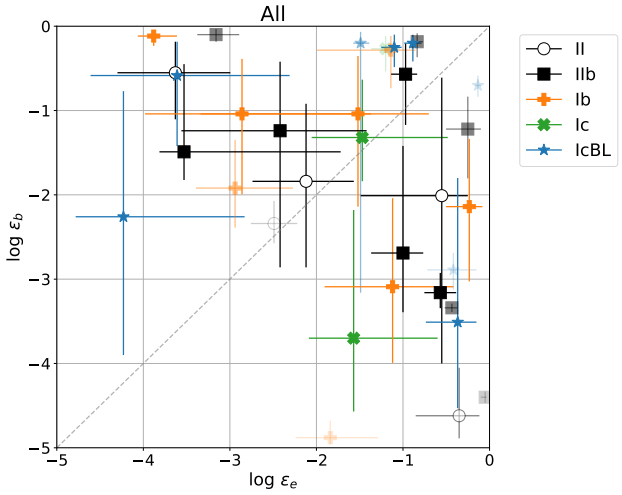

FIGURE 3.8: The correlation between the medians of log ϵ_B and those of log ϵ_e for each SN, plotted with 1σ credible intervals. The thicker points indicate good fitting results ($\chi^2_{\rm red} < 5$).

may have potential to promote the formation of the hard electron spectrum with $p \sim 2$, following the theoretical prediction.

3.7 Outliers

The systematic investigation presented in this study has potential to explore the universality of the deduced physical parameters as discussed in Section 3.5 and 3.6. At the same time it is possible to highlight on the properties of the object that lies out of the main sequence of the solution. Examinations on such "outlier" objects enable us to reveal the peculiar characteristics of the explosion or the stellar evolutionary path. In this section we mention to some objects showing a striking peculiar features.

3.7.1 SN 2016X

SN 2016X is a nearby Type II SN discovered in the galaxy UGC8041 (Bock et al., 2016). Ultraviolet and optical photometry and spectroscopy have been examined by Huang et al., 2018, revealing that SN 2016X is likely to be a fast-declining Type II-P SN similar to SN 2013ej, except the long rise time and the bright luminosity in the tail phase. They also argue that the high photospheric temperature inferred from the data obtained by *Swift* implies larger progenitor radius for a red supergiant ($\sim 900\,R_\odot$) and the zero-age main sequence (ZAMS) mass may be greater than $M_{\rm ZAMS} \gtrsim 19\,M_\odot$. Utrobin and Chugai, 2019 has proposed $M_{\rm ej} \simeq 28\,M_\odot$ and $M_{\rm ZAMS} \simeq 28 - 38\,M_\odot$ by making use of hydrodynamical simulation of the SN ejecta and of the resulting bolometric light curve. In addition to the examination on the optical observational properties, Ruiz-Carmona, Sfaradi, and Horesh, 2022 has reported the series of the observational data of radio emission from SN 2016X.

Figure 3.9 shows the PDFs of the ejecta gradient n deduced for each sample of type II SNe. We can see that the power-law index of the ejecta density in SN 2016X is shallower than other samples of SN II. As suggested in Figure 3.2, our MCMC simulation indicates the ejecta gradient of SN 2016X $n \sim 8$ both in the survey scheme `Astro` and `All`, suggesting the robustness of the deduced value smaller that 10, while other objects of SN II have a steeper power-law index of the ejecta, $n \sim 12$. This manifests the peculiar density structure of the ejecta outside of the envelope. The existence of the convective hydrogen envelope is considered to lead to the steep density structure

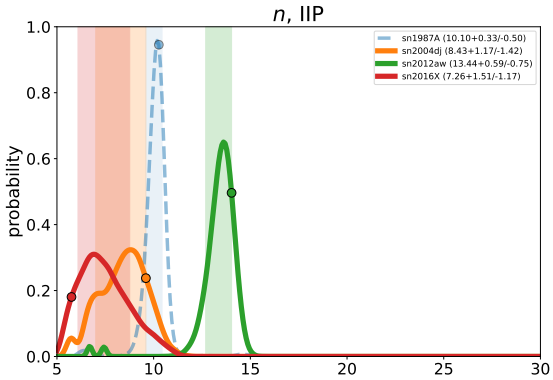

FIGURE 3.9: The PDFs of the ejecta gradient n for samples of Type II SNe. The usage of the line style is same as Figure 3.5.

shaped by $n \gtrsim 10$, while the SN progenitors originating from radiative stars are expected to be shallower than the convective envelope with $n \lesssim 10$ (Chevalier, 1982a; Matzner and McKee, 1999). Many of the SN II samples treated in this study fall into the theoretically expected region, except for SN 2016X. Figure 3.10 shows the radio light curves and the corner plot of SN 2016X, and the collection of the probability density function of n for samples of SN II in the framework of `All`.

As noted above, there are arguments that the progenitor of SN 2016X comes from massive ZAMS mass range more than 20 $M_\odot$ (Huang et al., 2018; Utrobin and Chugai, 2019). Indeed, this ZAMS mass range is intriguing in the context of the faint luminosity of the observed progenitors of Type II-P SNe, so called 'red supergiant problem' (Smartt et al., 2009; Davies and Beasor, 2020a; Davies and Beasor, 2020b). The collective progenitor mass of Type II-P SNe inferred by a series of previous observational studies ranges below $M_\odot \lesssim 19$[3], indicating the possible scenario in which red supergiants in the massive end may directly collapse into black holes without producing observable radiations. Actually it has been proposed theoretically that the ZAMS mass range more than $M_{\rm ZAMS} \gtrsim 18\,M_\odot$ tends to fail in exploding the star itself due to its large compactness parameter (Sukhbold, Woosley, and Heger, 2018). Our result suggest the possibility that the peculiarly flat ejecta gradient of SN 2016X for Type II SNe would be relevant with implosion of the massive red supergiants forming stellar mass black holes.

3.7.2 Type IIb SNe with extremely steep ejecta $n \sim 20$

It has been pointed out that SN 1993J, an prototype of Type IIb SNe, would have been shaped by the steep gradient give by $n \sim 20$ (Suzuki et al., 1993; Bartel et al., 1994; Fransson, Lundqvist, and Chevalier, 1996). This value is higher than theoretical predictions for SN ejecta originating from both the progenitor engulfed by the convective envelope and that consisting of radiative core (Matzner and McKee, 1999). The generality of such a steep density gradient would be an interesting problem in the context of the stellar evolution, because it can be associated with the physical processes that the outer envelope of the progenitor experiences. Figure 3.11 shows the PDFs of the ejecta gradient n for each Type IIb SN, suggesting another candidate for the SN shaped by the steep ejecta, SN 2001gd. Our simulation is showing that many of the Type IIb SN progenitors would not be necessarily shaped by the steep ejecta distribution, but highlighting the special evolutionary path of a small fraction of Type IIb SN progenitors.

[3]However the precise threshold of the masscut has been still debated. For instance, see Kochanek, 2020.

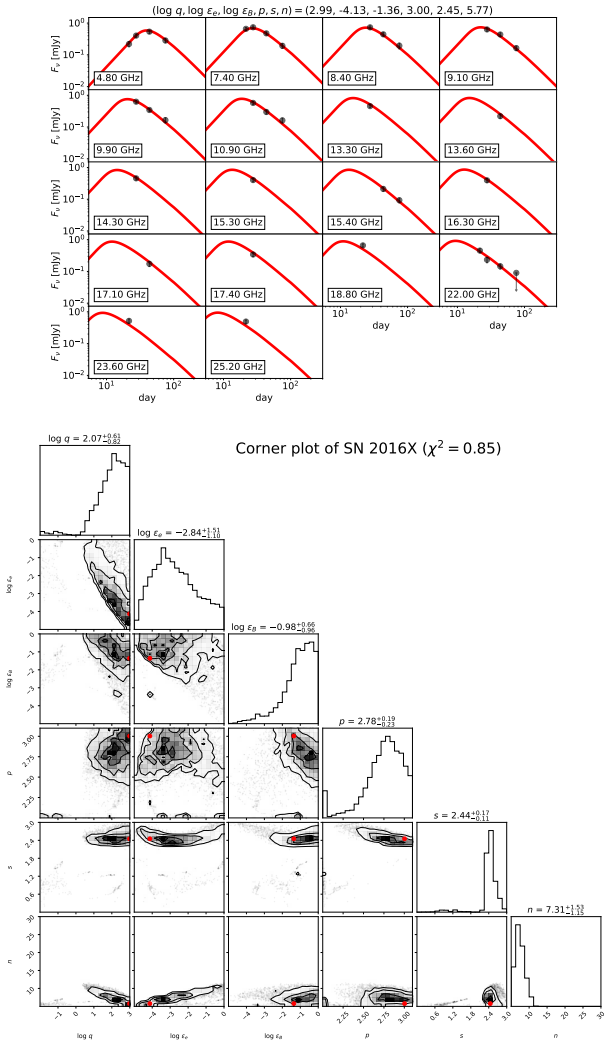

FIGURE 3.10: The synthesized light curve and corner plot of SN 2016X.

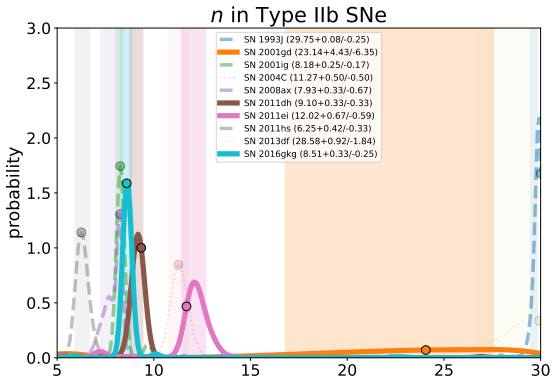

FIGURE 3.11: The PDFs of the ejecta gradient n for Type IIb SNe. The usage of the line style is same as Figure 3.5.

TABLE 3.5: Best fitted parameters and medians of log q with 1σ credible intervals.

SN name	log q	log ϵ_e	log ϵ_B	p	s	n	$\chi^2_{\rm red}$
SN1983N	0.98	-1.0	-2.0	3.06	2.02	7.0	1.34
SN1990B	-0.5	-0.65	-2.6	2.87	1.0	8.4	2.49
SN2002ap	0.0	-3.5	-0.9	2.02	1.9	8.0	2.65
SN2003L	1.1	-1.5	-1.5	2.63	1.3	6.0	4.94
SN2004gq	0.13	-1.7	-0.1	2.7	1.84	7.1	5.15
SN2004gq	0.25	-0.4	-2.1	2.7	1.84	8.0	9.74
SN2007uy	1.07	-0.5	-2.44	2.09	2.35	20.0	3.42
AT2014ge	1.25	-0.9	-3.3	2.75	1.7	6.8	6.09
SN2020oi	2.1	-3.6	-1.6	3.02	1.72	5.5	4.59

3.7.3 Multiple solutions for radio LCs

If the multiplicity of the solutions has been found in the posterior distributions, the possibility can be raised that there are a few kinds of the sequences of the solution that can explain the observed radio emission features. The possible multiple solutions can be displayed in the marginalized one-dimensional probability density functions or two-dimensional corner plots, and our simulations have found several objects with multiple solutions for the parameters surveyed, all of which are shown in Table 3.5. We note that these another sequences for the solution can reproduce the fitting results with $\chi^2_{\rm red} \lesssim 5$ guaranteeing the possible robustness of the solution.

As an example, we discuss the deduced properties of SN 2020oi, a Type Ic SN discovered in a spiral galaxy M100 (Rho et al., 2021; Gagliano et al., 2022). Figure 3.12 shows the radio light curves and the corner plot of SN 2020oi. We can see from the corner plot that there are two solutions that have potential to be fitted with the observational data, and we found that both solutions can be actually consistent with the observational data with the fitting precision $\chi^2_{\rm red} < 5$. There is an idea that the progenitor of SN 2020oi may have undergone the time-variable mass-loss activity based on the fine-tuned modeling of radio emission with the inhomogeneous density distribution of the CSM (Maeda et al., 2021). The method employed in our MCMC simulation is not capable of probing the CSM distribution deviating from the smooth profile, and the occurrence of the multiple solutions might be caused by the peculiar time evolution of the radio light curve originating from the multiple components of the CSM density distribution. The result showing that there are several (not one) samples of SNe showing multiple solutions may indicate the universality of such an inhomogeneous CSM density distribution and the possible time-dependent mass-loss histories of SN progenitors. We advocate that to disentangle the multiple solutions, observational constraints in another wavelength such as optical or X-ray would be helpful.

3.8 Discussion and summary

3.8.1 Effect of free-free absorption

We have to mention that there is a risk that it may be possible to be deceived by the apparent result for $s \gtrsim 2$ and $p \lesssim 2.5$. Our model does not treat free-free absorption that can be important when the CSM density is high and the observation frequency is low (Fransson and Björnsson, 1998; Chandra et al., 2020). We have conducted the survey of the normalization of the CSM density log q within the parameter range $-2 <$ log $q < 3$. At the upper end of this parameter range free-free absorption should be important, and in such a case the optically thick emission in the early phase becomes steeper and steeper (Matsuoka et al., 2019). The radio luminosity in the optically

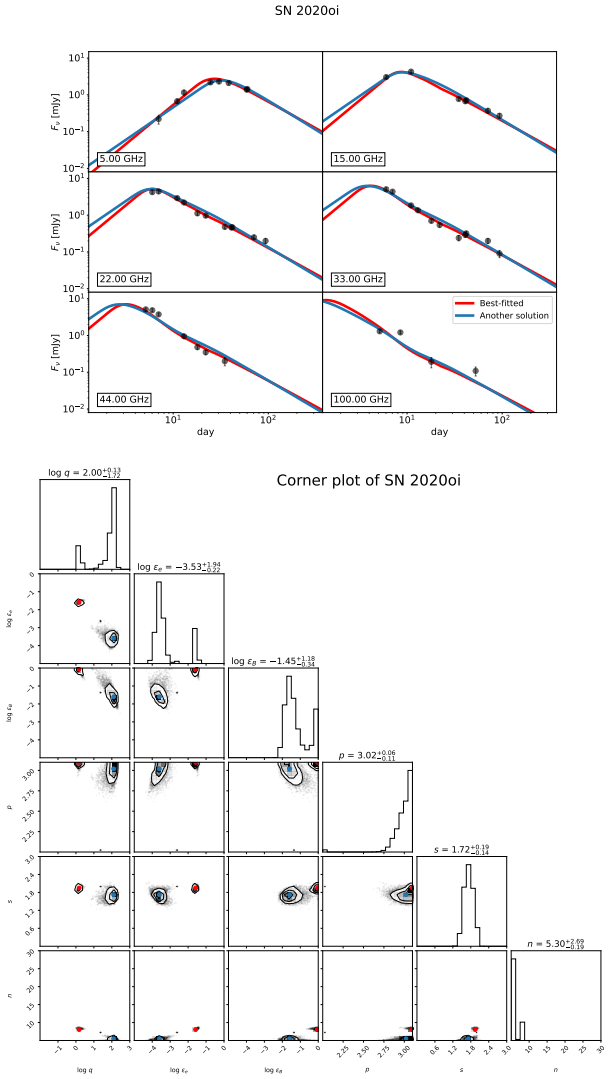

FIGURE 3.12: the synthesized light curves and cornerplot of SN 2020oi. Red lines and points denote the best-fitted solutions, while blue ones correspond to the other solution described in Table 3.5.

thick phase ($L_{\nu,\mathrm{thick}}$) characterized by only synchrotron self-absorption is proportional to

$$L_{\nu,\mathrm{thick}} \propto t^{\alpha}, \alpha = \left(\frac{s+6}{4}\right) m + \frac{1}{2}, \tag{3.17}$$

where $m = (n-3)/(n-s)$ is the deceleration parameter of the SN shock. This indicates that the rapid rising of the radio luminosity in the early phase can also be explained by increasing s (steepening the CSM density gradient), without introducing free-free absorption. Hence, the possibility would be arisen that our results may be biased towards the model with stepper CSM density structure. Furthermore, if free-free absorption is important in the early phase of radio SNe, the the expected spectrum of the radio emission would be hardened, apt to deduce the small spectral index of the relativistic electrons.

It is hard to quantify the degree of the free-free absorption in detail because it depends on the electron temperature and the distribution itself in the unshocked CSM, which has merely constrained ever. Lundqvist and Fransson, 1988 suggests the electron temperature $\sim 10^5$ K for SNe IIL, but it is not well understood how about the temperature would be in the other types of SNe[4] . However, visual inspection of the radio light curve models fitted with observational data allows us to verify our model without free-free absorption. Figure 3.13 shows the synthesized light curve of SN 1993J and SN 2013df, both of which has been suggested to have dense CSM ($\log q \sim 3$). We can see that for SN 1993J the peak time and peak luminosity in each band are consistent between observational data and the theoretical model each other, whereas for SN 2013df the model treated in this study fails to be fitted with observational data. We have checked the overall properties of the synthesized radio SN models for each SN whether the reproduced peak time and the peak luminosity are consistent with observational results. We have confirmed that the radio data of the most of the objects treated in this study has been fitted by the model without considering free-free absorption, except for SN 2013df. Indeed, the reduced chisquare of SN 2013df is too large to be regarded as fitted with observational data. Therefore, we believe that the statistical implications described in Section 3.5 and 3.6 would not be biased by the exclusion of free-free absorption.

3.8.2 Summary

In this study we have conducted the systematic investigation of 34 samples of radio SNe by making use of MCMC analysis based on the Bayesian statistics framework. This allows us to investigate the statistical properties of radio SNe including the progenitor's mass-loss history, information on the physics related to particle acceleration and magnetic field amplification, and even the explosion properties. Our findings are summarized as follows:

1. The key parameter having a significant influence on the modeling of radio SNe is the normalization of the CSM density ($\log q$). The secondarily important parameters are the density gradient of the ejecta (n) and the CSM (s). With the spectral index of the relativistic electrons p fixed to 3 and the assumption of the energy equipartition between electrons and magnetic field with of $\epsilon_e = \epsilon_B = 0.05$, it is possible to reproduce a number of SN samples to be fitted with observational data. The comprehensive survey of all parameters also supports the soft spectral index $p \gtrsim 2.5$ in a large sample of radio SNe except for a few Type IcBL SNe. On the other hand, the values of ϵ_e and ϵ_B involve degree of freedom, indicating that we cannot access the observational constrains on efficiencies of acceleration of electrons and amplification of magnetic field.

[4]We have excluded SN 2004et from our samples, because the observational data of SN 2004et published lacks the overall data of optically thin phase and the degeneracy effect discussed here would be expected to become important, making the discussion on statistical properties of Type II SNe complicated. See also Chevalier, Fransson, and Nymark, 2006.

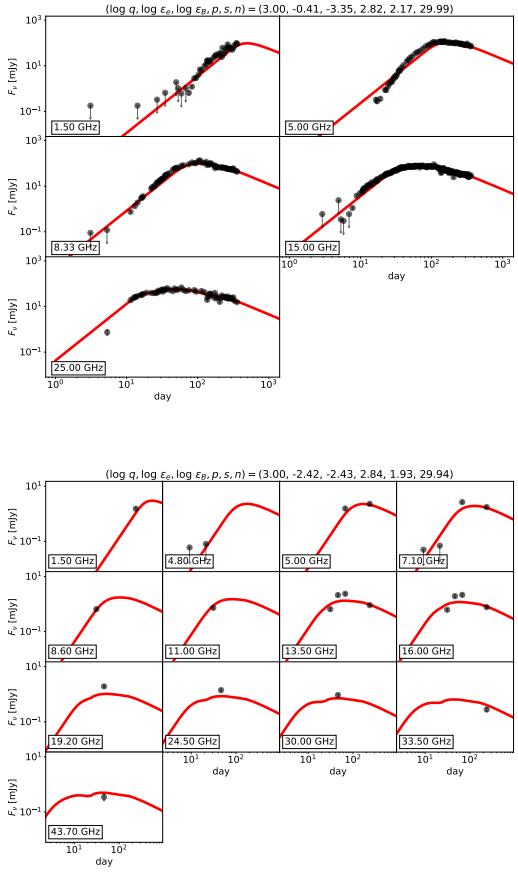

FIGURE 3.13: The synthesized light curves of SN 1993J (left) and SN 2013df (right).

2. The density gradient of the ejecta n has typical values of $n \sim 7$ and $n \sim 12$. A large samples of stripped-envelope SNe (Type Ib, Ic, and IcBL SNe) support the flatter ejecta gradient, which is consistent with the previous theoretical prediction (Matzner and McKee, 1999), while SNe encompassed by hydrogen envelope more or less can take both values; giving a statistical evaluation on the ejecta gradient of Tye II(b) SNe would be a delicate issue.

3. The samples of radio SNe treated in this study can be classified into two classes depending on the feasible density gradient of the CSM s. Many of the stripped-envelope SNe favor the flat CSM gradient characterized by $s \lesssim 2$, while Type II SNe prefers the steeper gradient given by $s \gtrsim 2$.

4. The parameter estimation of the magnitude of the CSM density $\log q$ normalized at the radius of 10^{15} cm can be done with the precision of the one or two orders of magnitude. Taking this uncertainty into consideration, Type II SNe can have typical CSM density characterized by $1 \lesssim \log q \lesssim 2$, while the parameter range inferred for stripped-envelope SNe lies in $1 \lesssim \log q \lesssim 3$. Assuming the velocity of the gas in the CSM as orders of the escape velocity of the typical SN progenitor (a red supergiant for Type II SNe and a WR star for stripped-envelope SNe), the corresponding mass-loss rate of Type II SNe ranges over $10^{-6}\,M_\odot\,\mathrm{yr}^{-1} \lesssim \dot{M} \lesssim 10^{-5}\,M_\odot\,\mathrm{yr}^{-1}$ about 30 years before the core collapse, whereas that of stripped-envelope SNe can be interpreted as $10^{-5}\,M_\odot\,\mathrm{yr}^{-1} \lesssim \dot{M} \lesssim 10^{-3}\,M_\odot\,\mathrm{yr}^{-1}$ with the lookback timescale of 0.3 years prior to the explosion. The upper end of the mass-loss rate of stripped-envelope SNe would be higher than previously expected (Chevalier and Fransson, 2006; Alexander, Soderberg, and Chomiuk, 2015; Maeda et al., 2021), but certain that the additional radiative features originated from the interaction of SN shock with such a dense CSM would not contribute to the overall observational properties of stripped-envelope SNe (Maeda et al., 2022). As for Type IIb SNe the typical magnitude of the CSM density can take three possible values, $\log q \sim 3, 0$, or -1. It would be possible to associate these subclasses with the nature of the SN progenitors previously constrained; Type IIb SN samples with $\log q \sim 3$ tend to originate from a progenitor with large radius, whose possible candidate would be a red supergiant, while those with $-1 \lesssim \log q \lesssim 0$ is likely to rather prefer the compact progenitor such as yellow or blue supergiants. This possible association has potential to uncover the nature of the binary interaction related with the properties of the progenitor.

5. The relativistic electron spectrum formed through the acceleration by the non-relativistic SN shock prefers the soft spectral index characterized by $p \gtrsim 2.5$. Despite this general tendency, there are some exceptional objects that favor the hard spectral index with $p \lesssim 2.5$. Many of the exceptional objects are categorised as Type IcBL SNe or considered to stem from an energetic explosion. This could imply that the SN shock that can be regarded as in the relativistic regime drives the formation of the hard electron spectrum, while non-relativistic shocks typical for SNe tend to produce the soft electron spectrum.

In addition to these overall tendencies of radio SNe, we have shown that the samples of radio SNe treated in this study involve some kinds of outlier objects. SN 2016X is a Type II SN characterized by its massive ejecta mass and the flat ejecta profile for the explosion of a red supergiant. This indicates the possible association about massive red supergiants more than $M_{\mathrm{ZAMS}} \gtrsim 18\,M_\odot$ between the ejecta profile and the explodability itself or the scenario of the formation of stellar mass black holes. As for the ejecta gradient we also observed that a small samples of Type IIb SNe exhibit the extremely steep density gradient characterized by $n \sim 20$, suggesting a possible peculiar evolutionary path of Type IIb SN progenitors. Furthermore, we have found the samples of radio SNe that can have multiple parameter sets to be consistent with observational data. We have shown the result for SN 2020oi displaying a clear multiplicity in the multi-dimensional

posterior distribution and demonstrated that both of the solutions can be well fitted with observational data. One of the probable reasons why the multiplicity has been arisen in the posterior distribution would be an inhomogeneous density distribution of the CSM suggested in Maeda et al., 2021. Hence we advocate that not all, but a fraction of radio SNe may be characterized by the CSM density with not single component, but with multiple components, indicating that some of the SN progenitors may be experiencing a time-variable mass-loss activities towards their core collapses.

Chapter 4

Radio Emission from Ultra-stripped Supernovae as Diagnostics for Properties of the Remnant Double Neutron Star Binaries

4.1 Introduction

The existence of double neutron star (DNS) binaries has been confirmed by the detection of the gravitational wave and the electromagnetic counterpart from a DNS merger (e.g., Abbott, Abbott, Abbott, et al., 2017a; Abbott, Abbott, Abbott, et al., 2017b; Abbott, Abbott, Abbott, et al., 2017c; Cowperthwaite et al., 2017; Tanaka et al., 2017), as well as by the direct observations of radio pulsars (e.g., Burgay et al., 2003). In the formation process of the DNS binary, the system must experience the core-collapse supernova (SN) twice, which is an explosion of a massive star at the endpoint of the stellar evolution. Hence, studies on DNS binaries provide us with the information on the stellar evolution of massive stars involved in a binary system (for a review, see Bhattacharya and van den Heuvel, 1991).

One of the leading models for the formation of DNS binaries is the ultra-stripped SN scenario (Tauris et al., 2017). In a close binary consisting of two massive stars, the secondary star loses its hydrogen envelope through the common envelope interaction with the companion NS after the first SN explosion. Subsequently, even the helium layer of the secondary star is fully or partly stripped away by the Roche lobe overflow (RLO). The secondary star then explodes as an ultra-stripped SN. This evolution scenario leads to small ejecta mass in the second SN, which is crucial for the binary to survive as a DNS binary system. The characteristics of the progenitor, nucleosynthesis, and expected observational properties of the ultra-stripped SNe in the optical wavelength have been theoretically investigated (Tauris et al., 2013; Tauris, Langer, and Podsiadlowski, 2015; Moriya et al., 2017b).

Thanks to the development of high-cadence transient surveys and fast-turnaround follow-up observations, a few candidates for ultra-stripped SNe have been discovered (e.g., iPTF 14gqr, De et al., 2018). The timescale of the optical light curve of iPTF 14gqr is $\sim$ 5 days, whereas those of typical Type Ib/Ic SNe are 10 $\sim$ 20 days (Lyman et al., 2016). This implies that the ejecta mass of iPTF 14gqr is small ($\sim 0.1 M_{\odot}$). The maximum-light spectrum is reminiscent of those of Type Ic SNe, indicating that the progenitor is a C+O star. These observational features agree with the prediction for the ultra-stripped SN (Moriya et al., 2017b). Furthermore, a few other candidates have been suggested from the viewpoints of their spectra and rapidly decaying evolutions, including SN 2005ek (Drout et al., 2013; Tauris et al., 2013) and SN 2010X (Kasliwal et al., 2010)[1]. We note that for SN 2010X a progenitor model originated from a white dwarf has also been suggested.

[1]See Moriya et al. (2017b) and Nakaoka et al. (2021) for the other candidates.

However, the remnant DNS binaries do not necessarily have sufficiently small separations to merge within the cosmic age (Tauris, Langer, and Podsiadlowski, 2015, see also Section 4.2). In fact, a DNS binary with a long orbital period ($\sim$ 45 days, corresponding to the separation of $\sim$ 0.4 AU) has been discovered by the radio pulsar observation (Swiggum et al., 2015). Optical properties of ultra-stripped SNe are sensitive to the ejecta mass (Moriya et al., 2017b), but not to the separation of the remnant DNS binary. Ultra-stripped SNe with the small ejecta mass ($\lesssim 0.2 M_\odot$) can indeed originate in a wide range of the binary separation (see Section 4.2 for details). Therefore, independent diagnostics for the remnant DNS binary separation after an ultra-stripped SN event will be important.

A key ingredient in the ultra-stripped SN scenario is the RLO mass transfer from the progenitor to the companion NS. A large fraction of the material is expected to be ejected from the system and form circumstellar material (CSM), which will lead to intense radio emission following an SN explosion (e.g., Chevalier, 1982b). In this paper, we investigate properties of radio emission from the ultra-stripped SN-CSM interaction. We suggest that the strong radio emission can be a tracer of an ultra-stripped SN which leaves a remnant DNS binary with sufficiently small separation to merge within the cosmic age.

This paper is organized as follows. In Section 4.2, we review the characteristics of the ultra-stripped SN progenitors in the stellar evolution models proposed by Tauris, Langer, and Podsiadlowski, 2015. We thereby find a trend that the mass-transfer rate is larger for the small binary separation, especially for the models with small ejecta mass ($< 0.2 M_\odot$). In Section 4.3, we describe the method for calculating the radio emission. The results are shown in Section 4.4. We discuss the observational prospects, together with some limitations in the present models, in Section 4.5. The paper is closed in Section 4.6 with a summary of our findings.

4.2 Properties of the ultra-stripped SN progenitors and mass-transfer rates

(Tauris, Langer, and Podsiadlowski, 2015) presented a series of the evolution models for a helium star with the helium envelope stripped away by a companion NS, providing a table for the final RLO mass-transfer rates and the fates of the helium stars. Figure 4.1 shows a histogram of the final mass-transfer rates ($\dot{M}_{\rm RLO}$) reproduced from Table 1 of Tauris, Langer, and Podsiadlowski, 2015. For the models in which the final fate is either the iron core-collapse SN (FeCCSN) or the electron capture SN (ECSN), we observe that the average mass-transfer rate ($\dot{M}_{\rm RLO} \sim 10^{-4}\ M_\odot {\rm yr}^{-1}$) is higher than the canonical mass-loss rate expected for helium stars ($\dot{M}_{\rm wind} \sim 10^{-5}\ M_\odot {\rm yr}^{-1}$, Chevalier and Fransson, 2006; Alexander, Soderberg, and Chomiuk, 2015). There are some models in which either the binary is detached or no RLO initiates. In these models the CSM around the progenitor will be dominated by the stellar wind. Note that the models, in which either a white dwarf is left or the common envelope interaction is realized, are not included in Figure 4.1, because the secondary stars in these models would not explode as SNe.

Figure 4.2 shows the distribution of the final mass-transfer rate ($\dot{M}_{\rm RLO}$) as a function of the final separation calculated by the Keplerian law ($a_{\rm fin}$), reproduced from Table 1 of Tauris, Langer, and Podsiadlowski, 2015. The ejecta mass in each model is estimated as follows:

$$M_{\rm ej} = M_{*,\rm f} - M_{\rm NS}, \tag{4.1}$$

where $M_{*,\rm f}$ and $M_{\rm NS} (= 1.4\ M_\odot)$ are the final mass of the helium star computed by Tauris, Langer, and Podsiadlowski, 2015 and the mass of the newly born NS, respectively.

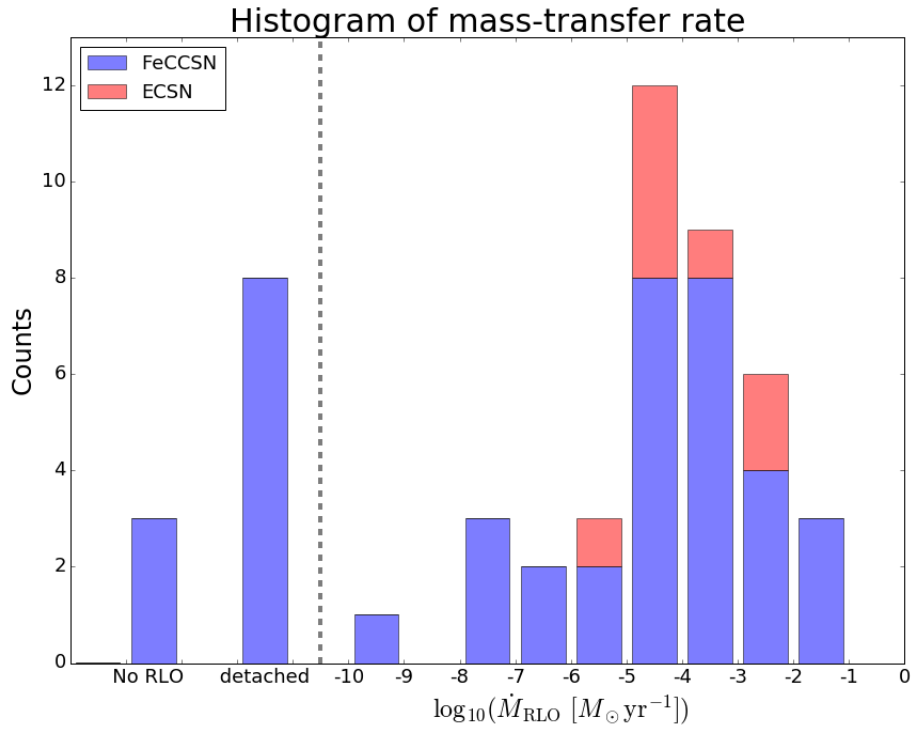

FIGURE 4.1: The histogram of the final mass-transfer rates in the models presented by Tauris, Langer, and Podsiadlowski, 2015. The difference in the color shows the type of SNe; FeCCSN (blue) or ECSN (red). The models in which either the binary is detached or no RLO initiates are separately shown in the left side of the histogram.

In Figure 4.2 we find two characteristics on the mass-transfer rate and the final binary separation. First, there are some models located at $(a_{\rm fin}, \dot{M}_{\rm RLO}) \sim (1R_\odot, 10^{-2}M_\odot {\rm yr}^{-1})$. This separation satisfies the condition that the remnant DNS binary will merge within the cosmic age ($a_{\rm fin} \lesssim 3.3\ R_\odot$). The mass-transfer rate is at least by an order of magnitude larger than those of the models with the larger separations. In fact, one of the models with the parameter set $(a_{\rm fin}, \dot{M}_{\rm RLO}) \sim (1R_\odot, 10^{-2}M_\odot {\rm yr}^{-1})$, shown by the circle outlined in red in the top left of Figure 4.2, has been adopted to explain the optical properties of an ultra-stripped SN candidate SN 2005ek (Tauris et al., 2013). Hence, we conclude that if the very high mass-transfer rate ($\gtrsim 10^{-2}M_\odot {\rm yr}^{-1}$) is derived for a progenitor of an ultra-stripped SN candidate through the property of the CSM, this will infer that the binary is sufficiently close for the remnant DNS binary to make a coalescence within the cosmic age.

Second, for the models with $M_{\rm RLO} \sim 10^{-4}M_\odot {\rm yr}^{-1}$, a range of final separations ($a_{\rm fin}$) could be associated. However, if we focus only on the models with the small ejecta mass ($M_{\rm ej} < 0.2M_\odot$), there is a tendency for $\dot{M}_{\rm RLO}$ to decrease as $a_{\rm fin}$ increases. Therefore, in case the small ejecta mass is derived through the optical properties, the mass-loss rate could be used as a rough tracer of the DNS binary separation.

In summary, we see the following trend on the mass-transfer rate. The ultra-stripped SN progenitor tends to have a higher mass-transfer rate than the typical mass-loss rate of a helium star. Especially, for the model with which an extraordinarily high mass-transfer rate ($\dot{M}_{\rm RLO} \gtrsim 10^{-3}M_\odot {\rm yr}^{-1}$) is associated, the binary separation is so small that the remnant DNS binary will make a coalescence within the cosmic age.

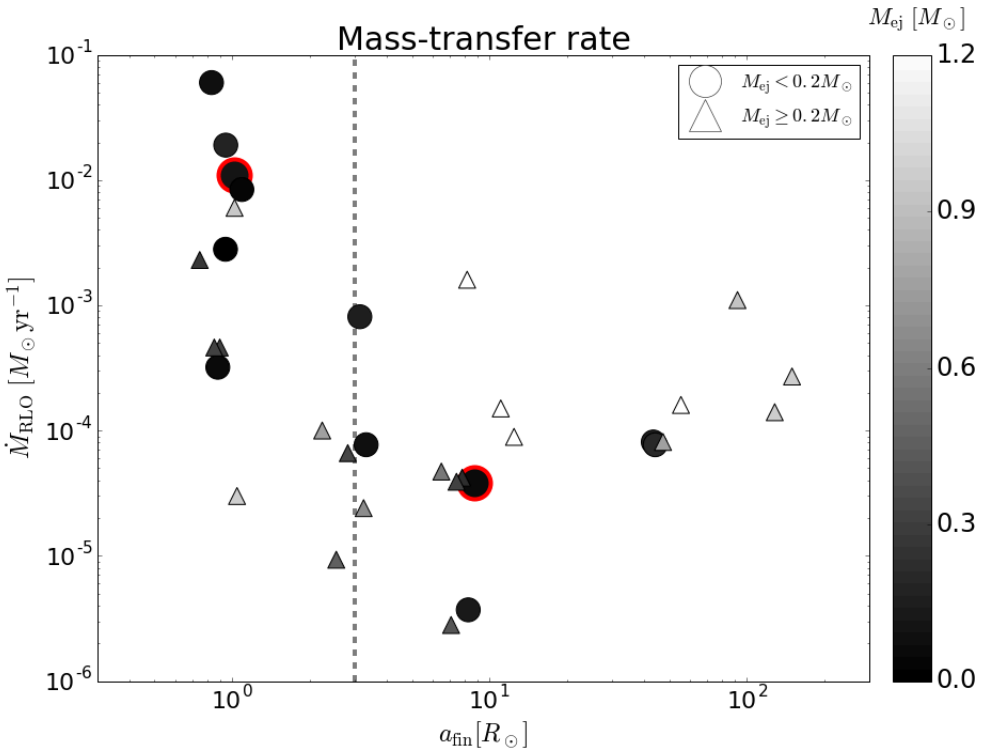

FIGURE 4.2: Distribution of the mass-transfer rate as a function of the final separation. Only the models in which the secondary stars explode as SNe are plotted. Two different symbols are used depending on the difference in the ejected mass; $M_{\rm ej} < 0.2\ M_\odot$ (circles) or $M_{\rm ej} \geq 0.2\ M_\odot$ (triangles). The models plotted by the circles outlined in red are examined in details (see Section 4.4.1). For the models on the left side of the black dashed line, the remnant DNS binary is expected to merge within the cosmic age.

4.3 Models and Method

After the shock breakout, the collisionless shock is formed. It is a site for non-thermal particle acceleration and magnetic field amplification, followed by multi-wavelength emissions including synchrotron radio emission. In this section we describe the method to model the synchrotron emission, which basically follows the previous studies (e.g., Chevalier, 1982b; Chevalier, 1998; Fransson and Björnsson, 1998; Chevalier and Fransson, 2006; Chevalier and Fransson, 2017; Maeda, 2012; Maeda, 2013a).

4.3.1 Models

The evolution of the shock velocity is determined by the natures of the SN ejecta and the CSM. The outer ejecta structure can be described by a power-law, $\rho \propto t^{-3} v^{-n}$, where $v = r/t$ is the velocity coordinate. In case that the outer envelope of the progenitor is radiative, the power-law index $n = 11.73$ matches to the density structure of the outermost layer of the SN ejecta (Matzner and McKee, 1999). The ultra-stripped SN progenitors likely have a radiation-dominant envelope (e.g., Suwa et al., 2015), and we employ the same index.

For the ejecta mass exceeding $\sim 0.2 M_\odot$, the evolution of the optical light curve becomes too slow to be consistent with the rapid evolutions seen in the previously observed candidates for the ultra-stripped SNe (Moriya et al., 2017b; De et al., 2018). Thus, in this study, we impose a threshold on the ejecta mass, and focus on the models in which the ejecta mass is smaller than $0.2 M_\odot$ (the circles in Figure 4.2).

With the ejecta properties given, the synchrotron emission can be computed once the properties of the CSM are specified. A fraction of the gas transferred from the helium star to the NS is expected to escape from the binary system. This material will be distributed around the binary as the CSM. In this study, we parametrize the CSM density distribution $\rho_{\rm CSM}(r)$ as follows:

$$\rho_{\rm CSM}(r) = \frac{\dot{M}_{\rm CSM}}{4\pi u_{\rm w}} \frac{1}{r^2}, \text{ and } \dot{M}_{\rm CSM} = f_{\dot{M}} \dot{M}_{\rm RLO}, \tag{4.2}$$

where $u_{\rm w}$ and $f_{\dot{M}}$ are the mass-loss velocity and the fraction of the gas escaping from the system, respectively.

The value of $u_{\rm w}$ involves a large uncertainty. We adopt the typical escape velocity from a helium star, $u_{\rm w} = 10^8$ cm s^{-1} (Nugis and Lamers, 2000), because this value is larger than the binary orbital velocity ($\sim 2\pi a_{\rm fin} P_{\rm fin}^{-1} \sim 10^7$ cm s^{-1}, where $P_{\rm fin}$ is the final orbital period). However, we note that the velocity of the outflow from the NS might be even larger than the typical escape velocity from a helium star (Miller et al., 2016).

$f_{\dot{M}}$ is also an important parameter which determines the efficiency of the formation of the CSM around the progenitor. It is expected that $f_{\dot{M}}$ is large ($f_{\dot{M}} \sim 1$) for the following reasons. First, the mass-transfer rate here is a few orders of magnitude higher than the Eddington accretion rate onto a NS ($\dot{M}_{\rm Edd,NS} \sim 10^{-8}\ M_\odot {\rm yr}^{-1}$). Therefore, most of the materials cannot accrete onto the NS, and will escape from the binary system. This is also required in order for the NS to avoid a collapse to a black hole. Second, the NS should be spinning up rapidly under the ultra-stripped SN scenario, and it can no longer receive the angular momentum from the accreting gas. We thus consider $f_{\dot{M}} = 0.99$ as our fiducial model. We also examine $f_{\dot{M}} = 0.10$ to investigate the dependence of the radio emission on this parameter. Finally, we remark that any asphericity of the CSM is not considered in this work, although the gas escaping from the system will not necessarily be distributed spherically.

4.3.2 Shock evolution

Assuming that the shocked region is geometrically thin, the velocity ($V_{\rm sh}$) and the radius ($R_{\rm sh}$) of the shocked shell can be derived analytically as follows (Chevalier, 1982a; Chevalier, 1982b):

$$\begin{aligned} V_{\rm sh} &= 1.1\times10^{9}\left(\frac{\dot{M}_{\rm CSM}}{10^{-2}\ M_{\odot}{\rm yr}^{-1}}\right)^{-0.10}\left(\frac{u_{\rm w}}{10^{8}\ {\rm cm\ s}^{-1}}\right)^{0.10} \\ &\times \left(\frac{E_{\rm kin}}{10^{50}\ {\rm erg}}\right)^{0.45}\left(\frac{M_{\rm ej}}{0.1\ M_{\odot}}\right)^{-0.35}\left(\frac{t}{10\ {\rm days}}\right)^{-0.10}\ {\rm cm\ s}^{-1}, \qquad (4.3) \\ R_{\rm sh} &= 8.5\times10^{14}\left(\frac{\dot{M}_{\rm CSM}}{10^{-2}\ M_{\odot}{\rm yr}^{-1}}\right)^{-0.10}\left(\frac{u_{\rm w}}{10^{8}\ {\rm cm\ s}^{-1}}\right)^{0.10} \\ &\times \left(\frac{E_{\rm kin}}{10^{50}\ {\rm erg}}\right)^{0.45}\left(\frac{M_{\rm ej}}{0.1\ M_{\odot}}\right)^{-0.35}\left(\frac{t}{10\ {\rm days}}\right)^{0.90}\ {\rm cm\ s}^{-1}, \qquad (4.4) \end{aligned}$$

where $\dot{M}_{\rm CSM}$ and $E_{\rm kin}$ are the mass-loss rate converted from the CSM density (see above) and the kinetic energy of the ejecta, respectively. We do not take radiative cooling into account, which could decelerate the shock velocity by roughly a ten percent if the CSM density is high. The radio light curves are hardly affected by this assumption (Matsuoka et al., 2019).

4.3.3 Particle Acceleration and Magnetic Field Amplification

At the collisionless shock front, charged particles such as electrons or protons become energetic by diffusive shock acceleration (DSA, Fermi, 1949; Bell, 1978; Drury, 1983). The motion of the charged particles is relativistic and random, followed by magnetic field amplification. We parametrize the energy density of the electrons (u_e) and magnetic field (u_B) as a fraction of the post-shocked energy density as a function of time as follows:

$$u_e = \epsilon_e \rho_{\rm sh} V_{\rm sh}^2, \qquad (4.5)$$

$$u_B = \frac{B^2}{8\pi} = \epsilon_B \rho_{\rm sh} V_{\rm sh}^2, \qquad (4.6)$$

where $\rho_{\rm sh}$ is the post-shocked density of the CSM, which is 4 times larger than that of the pre-shocked CSM. ϵ_e and ϵ_B are the parameters which determine the efficiency of the shock acceleration and the magnetic field amplification. In this study we use the values $\epsilon_e = 0.01$ and $\epsilon_B = 0.1$, but we note that there remains a debate on the realistic values of these parameters (e.g., Spitkovsky, 2008; Maeda, 2012; Caprioli, Pop, and Spitkovsky, 2015).

We consider the power-law distribution of the number density of the accelerated electrons N as a function of the Lorentz factor (γ) as follows:

$$N(\gamma) = C\gamma^{-p}. \qquad (4.7)$$

The index p characterizes the hardness of the spectrum of the electron distribution. We employ $p = 3$, which can explain observations of optically thin radio emissions from Type Ib/Ic SNe (Chevalier and Fransson, 2006; Maeda, 2013a). The coefficient C is determined by equating the integrated energy density of the electrons with u_e,

$$\int_{\gamma_{\rm min}}^{\infty} d\gamma N(\gamma)\gamma m_e c^2 = u_e \Rightarrow C = \frac{(p-2)u_e}{\gamma_{\rm min}^{2-p} m_e c^2}, \qquad (4.8)$$

where m_e, c, and $\gamma_{\rm min} = 2$ are the electron mass, the speed of light, and the minimum Lorentz factor of the accelerated electrons, respectively.

TABLE 4.1: Reference models

model	$E_{\rm kin}$ **[erg]**	$M_{\rm ej}$ $[M_\odot]$	$\dot{M}_{\rm RLO}$ $[M_\odot$ **yr**$^{-1}]$	**comments**
sep_1Rsun	10^{50}	0.10	1.1×10^{-2}	Model for SN 2005ek (Tauris et al., 2013)
sep_10Rsun	10^{50}	0.06	3.8×10^{-5}	-

Our treatment does not include the contribution from hadronic interactions. It is possible that the relativistic protons collide with target protons in the dense CSM, producing electrons and positrons via pion decay (e.g., Petropoulou, Kamble, and Sironi, 2016; Murase, Thompson, and Ofek, 2014; Murase et al., 2019). However, the previous simulation of the radio emission from infant Type II-P SNe has shown that the synchrotron emission from these secondary particles would receive strong self-absorption when the luminosity is at its maximum (Matsuoka et al., 2019). Therefore, in this study we neglect the contribution from the hadronic interactions.

4.3.4 Synchrotron emission

Once the energy distribution of the electrons and the strength of the magnetic field are given, the physical quantities for the synchrotron emission can be calculated (Rybicki and Lightman, 1979). The method for estimating the luminosity of synchrotron emission is basically following the way described in Chapter 2, so here we just briefly review the outline of estimating the radio luminosity originating from synchrotron emission.

The synchrotron emissivity $j_{\nu,\rm syn}$, the synchrotron self-absorption (SSA) coefficient $\alpha_{\nu,\rm SSA}$, and the source function of synchrotron emission $S_{\nu,\rm syn}$ can be estimated by equation 2.45, 2.46, and 2.47. Then the radio luminosity would be given through the equation 2.54. In this calculation the pitch angle is set to $\sin\theta = 2/3$, and free-free absorption (FFA) is taken into consideration by making use of equation 2.52. Here we use electron temperature in the unshocked CSM $T_e = 10^5$ K, which is conventionally used for explaining the absorption of radio emission from Type II SNe (see e.g., Lundqvist and Fransson, 1988; Chevalier, Fransson, and Nymark, 2006). We note, however, that T_e involves large uncertainties and this could have effect on the radio emission in the early phase of SNe. The composition of the CSM is dominated by fully ionized helium, and thus $Z = 2$ is used. For the free-free gaunt factor, we use the formalization described by Rybicki and Lightman, 1979. As for cooling timescales, inverse Compton cooling is not taken into account, because the bolometric luminosity of ultra-stripped SNe is much fainter than those of typical SNe (e.g., Moriya et al., 2017b). We note that in this section the normalization of the shocked CSM density is 4 times larger than the unshocked CSM density (see equation 4.5 and 4.6), which affects the order estimates shown in Chapter 2 by factors.

4.4 Results

4.4.1 Light curves

Figure 4.3 shows the light curves at the frequency 8.46 and 100 GHz with $f_{\dot{M}} = 0.10$ and 0.99. The models shown here are described in Table 1. These models are selected as representative cases having $M_{\rm ej} \sim 0.1 M_\odot$ to be consistent with the ejecta mass estimated for the ultra-stripped SN candidates SN 2005ek and iPTF 14gqr, through their rapid evolutions in the optical light curves (Sections 4.2 and 4.3.1). The explosion energy $E_{\rm kin} = 10^{50}$ erg is predicted by the theoretical simulation (Suwa et al., 2015), which is also consistent with those estimated for SN 2005ek and iPTF 14gqr (Tauris et al., 2013; De et al., 2018).

Qualitatively, the radio emission from SNe at higher frequency becomes transparent to the CSM in the earlier epoch. This trend can be seen in all of the models. For example, in the model sep_1Rsun, where the dense CSM is distributed ($\dot{M}_{\rm CSM} \gtrsim 10^{-3}\ M_\odot {\rm yr}^{-1}$), the synchrotron emission at 8.46 GHz is damped by the strong SSA and FFA in the first 10 days, while in the late epochs (100 - 1000 days), it shows a high luminosity. This behavior is commonly seen in the observed radio emission from Type IIn SNe (e.g., Chevalier, 1998). On the other hand, the emission at 100 GHz is peaked within 1 month, followed by the optically thin, decaying emission in 100 - 1000 days.

In the model sep_10Rsun, the peak date of the radio luminosity at 8.46 GHz is at 10 - 100 days, which is similar to the observed radio peak dates for typical Type Ib/Ic SNe (see e.g., Margutti et al., 2014; Terreran et al., 2019). However, the maximum luminosity is smaller than those of the typical Type Ib/Ic SNe, because of the low explosion energy of the ultra-stripped SNe (see also Section 4.5.3). The 100 GHz emission is similarly weak ($L_\nu \sim 10^{26}$ erg s^{-1} Hz^{-1}) which is peaked at $t \lesssim 10$ days.

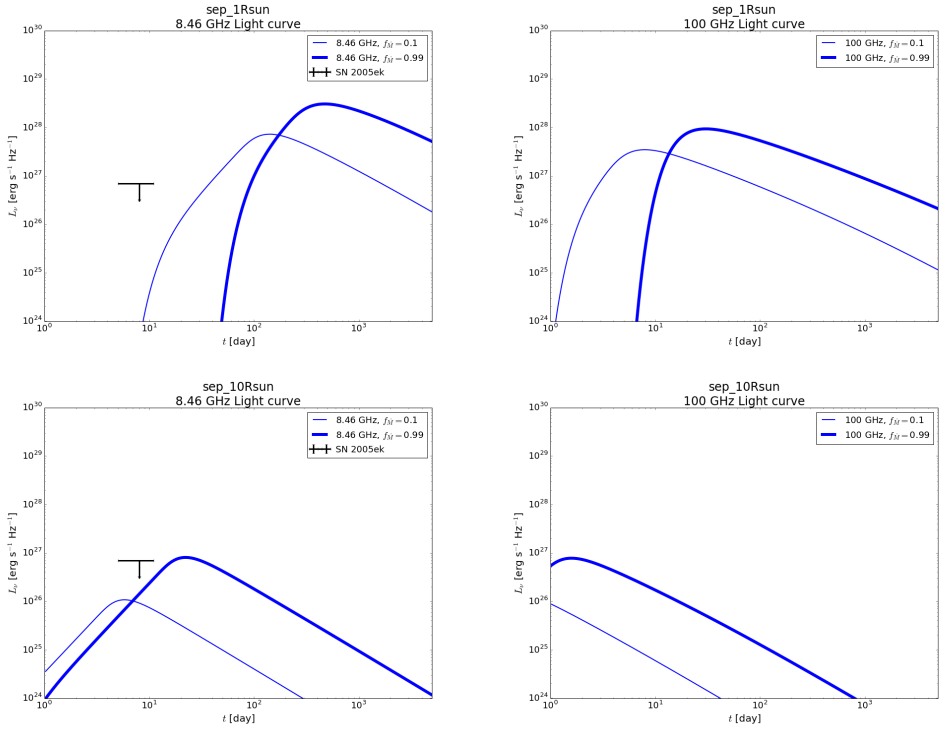

FIGURE 4.3: Examples of the synthesized radio light curves for the models shown in Table 1. The top and bottom panels are for the different models (sep_1Rsun and sep_10Rsun). The left and right panels are centimeter (8.46 GHz) and millimeter (100 GHz) ranges, respectively. The thickness of the lines shows the difference in $f_{\dot{M}}$; $f_{\dot{M}} = 0.10$ (thin blue) and $f_{\dot{M}} = 0.99$ (thick blue). The upper limit of the centimeter emission for SN 2005ek is shown by the black arrow.

4.4.2 Maximum Luminosities

Figure 4.4 shows the distribution of the maximum luminosities of the centimeter emission (8.46 GHz) for various models, measured within fixed time interval of the first 30, 300, and 3000 days, as a function of the final binary separation. The maximum luminosities in the centimeter range within the first 30 days do not show a characteristic difference among all of the binary evolution models. However, if we extend the time-window to 300 or 3000 days, we can observe strong centimeter emissions ($\gtrsim 10^{28}$ erg s^{-1} Hz^{-1}) from some models with $a_{\rm fin} \sim 1 R_\odot$. This strong

radio signal can be robust diagnostics for the dense CSM around the progenitor; a large amount of the helium layer of the progenitor has been stripped away, and the small binary separation is responsible for this strong envelope stripping.

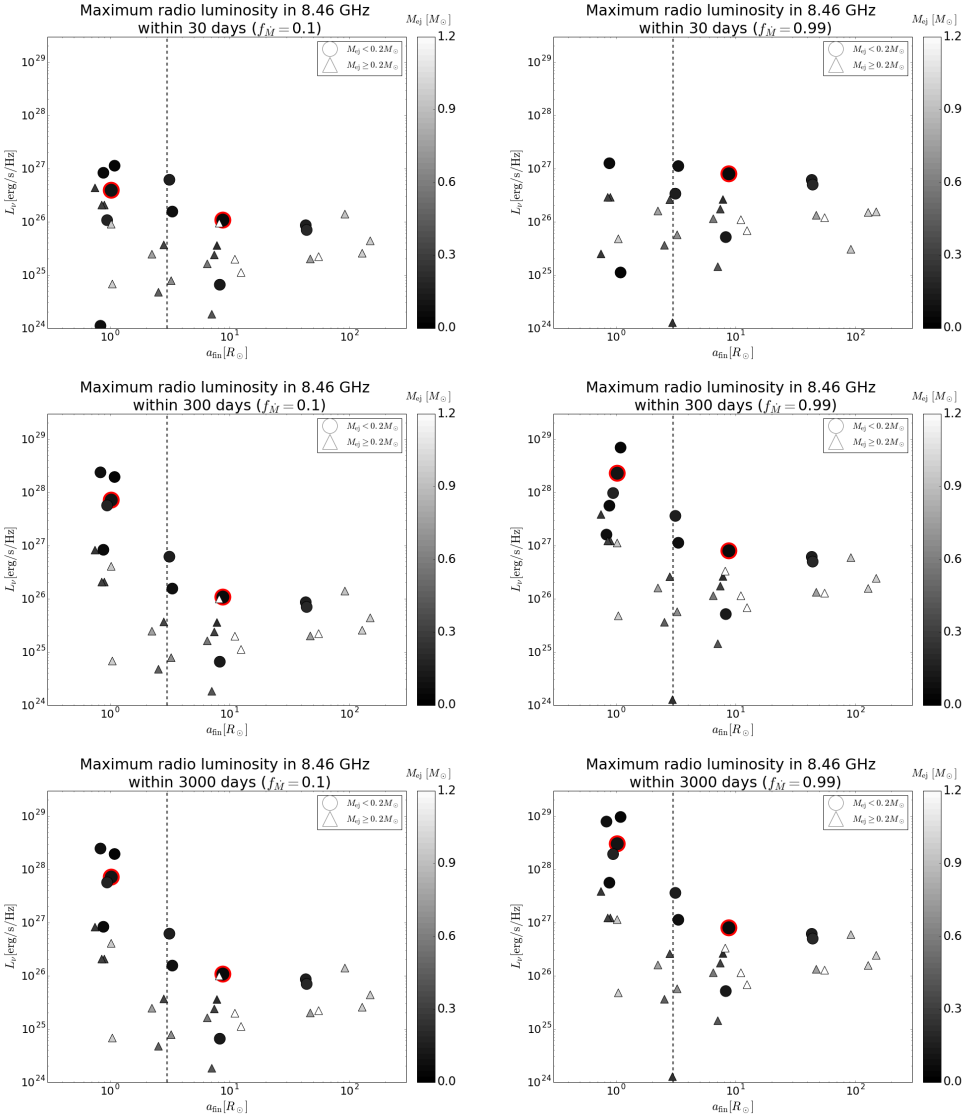

FIGURE 4.4: Dependences of the radio maximum luminosity on the final separation, for different time windows since the explosion (within the first 30 days, 300 days, and 3000 days from the top to bottom). The frequency is set at 8.46 GHz in these figures. The left panels are for $f_{\dot{M}} = 0.10$, while the right ones are for $f_{\dot{M}} = 0.99$.

Figure 4.5 shows the same result as Figure 4.4, but for the millimeter emission (100 GHz). The millimeter emissions are enhanced in some models with $a_{\rm fin} \sim 1R_\odot$ already within 30 days. The bright early-phase millimeter signals, as well as the bright late-phase centimeter signals, are useful as indicators of the small binary separation. We note that the maximum luminosity in the millimeter range is reached within 30 days for all of the models, followed by an optically thin, decaying emission in the late epoch (see Figure 4.3). These features lead to the optimized strategy to detect the radio signals from ultra-stripped SNe; either a long-term monitoring in the centimeter range or a quick follow-up in the millimeter range, or a combination of both.

If the observed maximum luminosity (or upper limit) is $L_\nu \lesssim 10^{26}$ erg s^{-1} Hz^{-1} (both in centimeter range and in millimeter range), the interpretation will not be straightforward. Many models with a range of the final binary separation can lead to $L_\nu \sim 10^{26}$ erg s^{-1} Hz^{-1}. However, this

behavior is largely driven by the models with the large ejecta mass; if we focus on the models with the small ejecta mass ($M_{\rm ej} < 0.2 M_\odot$), there is a tendency for L_ν to decrease as $a_{\rm fin}$ increases (see e.g., (f) in Figure 4.4 or (b) in Figure 4.5). This trend results from the correlation between $\dot{M}_{\rm RLO}$ and $a_{\rm fin}$ discussed in Section 4.2. The ejecta mass can be estimated by the optical data. Therefore, the combination of the observational data in the radio and optical ranges might be a useful indicator of an ultra-stripped SN forming a DNS binary which will not merge within the cosmic time, in case the radio signal is weak.

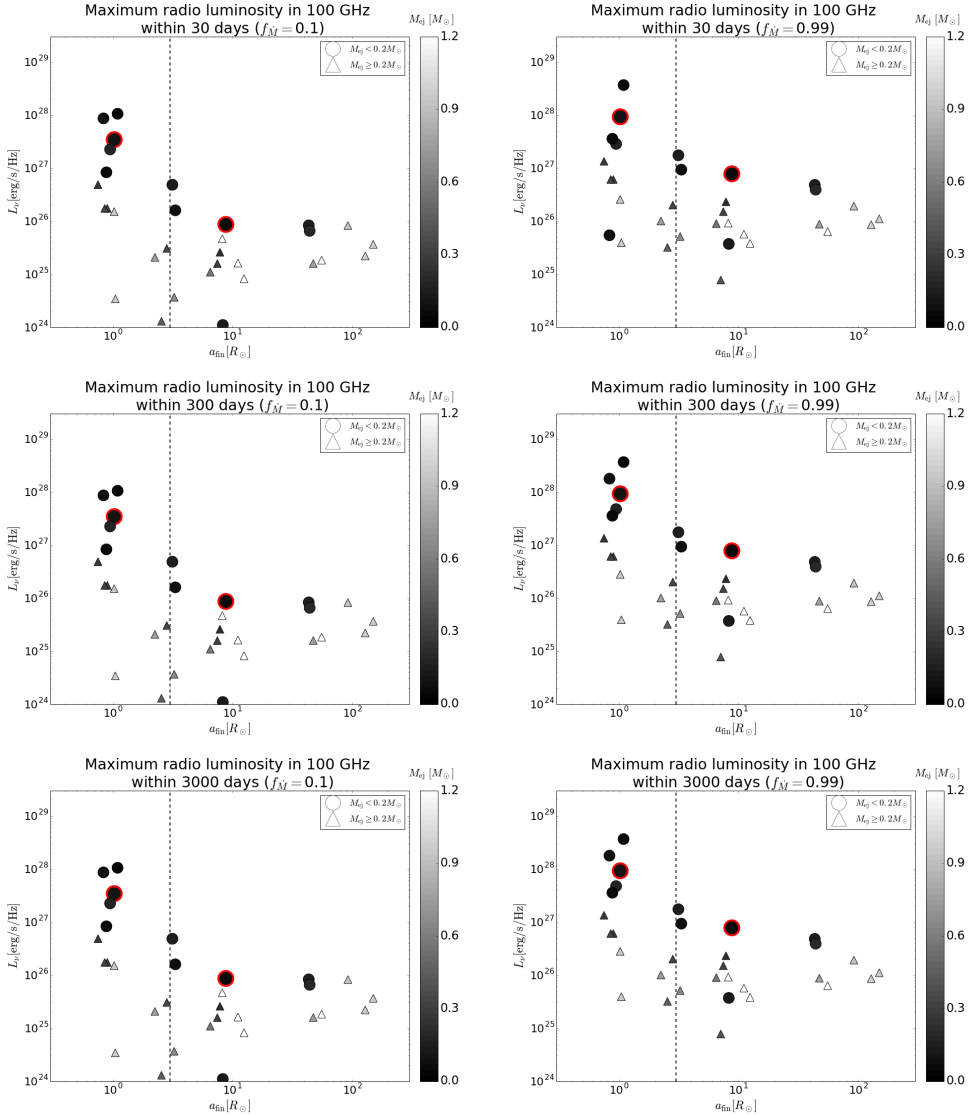

FIGURE 4.5: Same as Figure 4, but for 100 GHz.

Our findings on the relation between the observed radio luminosity and the binary evolution scenario are summarized as follows. Strong signals around 300 - 3000 days in the centimeter range or within 300 days in the millimeter range indicate large $\dot{M}_{\rm RLO}$ due to small separation. For such a system, the DNS binary left after the ultra-stripped SN event will make a coalescence within the cosmic age. On the other hand, a low radio luminosity implies small $\dot{M}_{\rm RLO}$, which can be realized for a wide range of the binary separation. However, once small ejecta mass is inferred by the optical data, it is suggested that the binary system has large separation and the remnant DNS binary will not merge within the cosmic age.

TABLE 4.2: Radio observations of the candidates for ultra-stripped SNe

Object	**Distance [Mpc]**	$t_{\rm obs}$ **[day]**[1]	$\nu_{\rm obs}$ **[GHz]**[2]	**upper limit of** L_ν **[erg s**$^{-1}$ **Hz**$^{-1}$**]**
SN 2005ek	67	$5-11$	8.46	7×10^{26}
iPTF 14gqr	284.5	~1	15	5.6×10^{27}
iPTF 14gqr	-	~1.7	6.1	1.12×10^{27}
iPTF 14gqr	-	~1.7	22	1.13×10^{27}
iPTF 14gqr	-	~11	6.1	1.26×10^{27}
iPTF 14gqr	-	~11	22	1.50×10^{27}

References: SN 2005ek : Drout et al., 2013, iPTF 14gqr : De et al., 2018

[1] Observed epoch since the explosion.
[2] Observational frequency.

4.5 Discussions

4.5.1 Candidates for the ultra-stripped SNe and their radio observations

Table 4.2 summarizes the constraints on radio luminosities of the ultra-stripped SN candidates (SN 2005ek and iPTF 2014gqr). All of the observations were conducted in the centimeter range within 10 days since the explosion, although the observed epoch ($t_{\rm obs}$) of SN 2005ek has an uncertainty due to the unknown explosion date (see Drout et al., 2013). Non-detections are reported in all of the cases. The upper limits for the radio luminosity per unit frequency are given as $L_\nu \lesssim 10^{27}$ erg s^{-1} Hz^{-1}. While these observations in principle allow us to investigate the nature of the CSM, these available upper limits are not deep enough to be a strong constraint (see Figure 4.3 for SN 2005ek).

4.5.2 Strategy in radio follow-up observations

Figure 4.6 summarizes the radio luminosity as functions of the observational epoch and frequency for the ultra-stripped SN models shown in Table 1. For the model sep_1Rsun, the centimeter emission after 100 days or the millimeter emission around 10-100 days provides the optimized windows. For the model sep_10Rsun, the centimeter emission at 10-100 days or millimeter emission within 10 days would become the best tracer of the CSM, although even for these windows the peak luminosity is less than 10^{27} erg s^{-1} Hz^{-1}.

The previous radio observations for the ultra-stripped SN candidates were conducted in the centimeter range within 10 days, during which the absorption effect is still strong (see Table 4.2). In such an early phase, the signal will be damped by the SSA and the FFA. The rapid observation in the centimeter range is not suitable as the diagnostics of the binary separation. Hence, it is necessary to continue the centimeter observation until $t \sim 100-1000$ days. On the other hand, the millimeter emission is enhanced around 10 days. We suggest that a rapid millimeter follow-up observation can be a potential tracer of the nature of the progenitor binary.

4.5.3 Contribution from an additional 'confined' CSM

While our model is constructed based on the RLO mass-transfer history in the ultra-stripped SN models, massive stars may experience an additional mass-loss process for which the origin has not yet been clarified. Recently, the possibility of a pre-SN enhanced mass loss, especially for Type II SN progenitors, has been proposed (e.g., Yaron et al., 2017; Forster et al., 2018). It has also been reported that the progenitor of iPTF 14gqr was surrounded by the dense CSM existing up to $\sim 10^{15}$

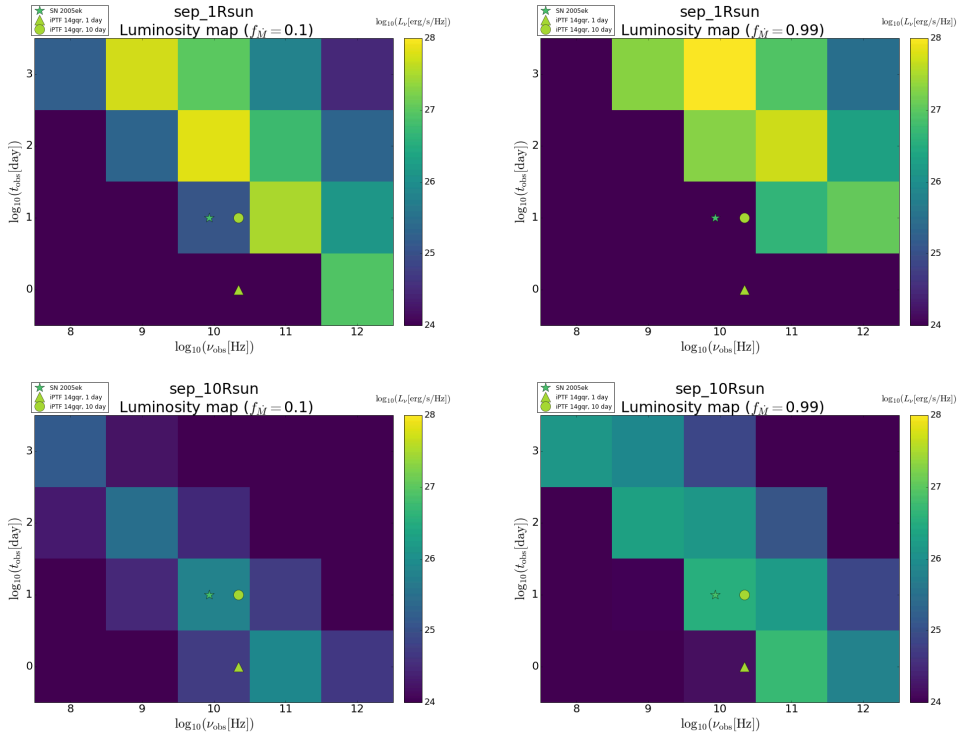

FIGURE 4.6: The radio luminosity for the reference models shown by the different colors, as functions of the epoch and frequency. The x-axis is the frequency in a logarithmic scale, while the y-axis is the epoch in a logarithmic scale. Shown here are the models sep_1Rsun (Top) and sep_10Rsun (Bottom). In the left panels $f_{\dot{M}} = 0.1$ is used, while in the right panels $f_{\dot{M}} = 0.99$. The points show a combination of the epoch and frequency in the past observations (Table 4.2).

cm (De et al., 2018). In this section, we show that it is possible to distinguish the potential radio signal contributed by the confined CSM from that created by the RLO mass transfer associated with the evolution of the ultra-stripped SN progenitor binary.

Figure 4.7 shows the modeled radio light curves of SN 2016coi, as compared with our fiducial ultra-stripped SN models ($f_{\dot{M}} = 0.99$). For the physical parameters of SN 2016coi, we adopt the following values: $M_{\rm ej} = 4.0 M_\odot$, $E_{\rm kin} = 7 \times 10^{51}$erg, and $\dot{M}_{\rm CSM} = 1.0 \times 10^{-4} M_\odot {\rm yr}^{-1}$, as derived by Terreran et al., 2019. Assuming that the progenitor of SN 2016coi would have the confined CSM with the mass-loss rate $\dot{M}_{\rm CSM} = 1.0 \times 10^{-3} M_\odot {\rm yr}^{-1}$ up to $\sim 10^{15}$ cm, we also examine the radio emission produced by the collision between the SN ejecta and the confined CSM. This setup corresponds to the situation that the confined CSM will be swept up by the shock within ~ 10 days. The observational data for the radio signals from SN 2016coi at 8.46 GHz are also plotted in Figure 4.7, which are roughly consistent with our model light curve for SN 2016coi.

The characteristic radio signal produced by the confined CSM appears only within ~ 10 days (thin red lines in Figure 4.7, see also Matsuoka et al., 2019). It is damped due to the FFA in the centimeter range, while it is strongly enhanced in the millimeter range. On the other hand, the final RLO mass transfer in the ultra-stripped SN progenitor binary models continues for $\gtrsim 10$ years, forming a dense CSM up to $\sim 10^{17}$ cm. This extended CSM produces a slowly-decaying radio emission up to ~ 1000 days, unlike the signal from the confined CSM. Therefore, a long-term radio monitoring can solve the degeneracy between the RLO expected in the ultra-stripped SN progenitor binary evolution and the pre-SN enhanced mass loss seen in some core-collapse SNe.

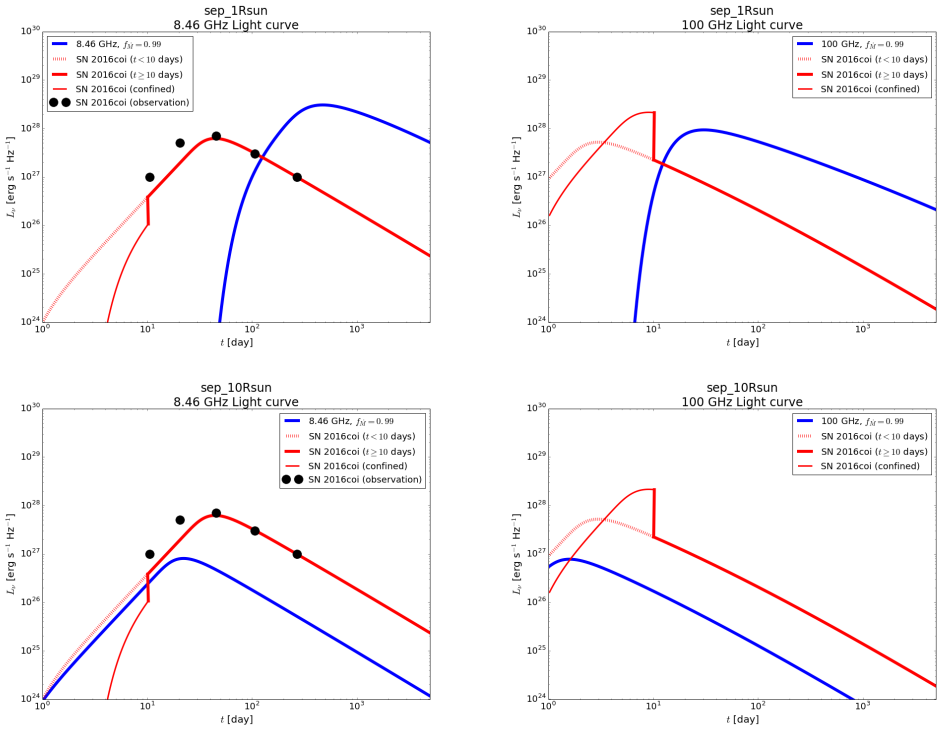

FIGURE 4.7: The modeled radio light curves of SN 2016coi, as compared with our ultra-stripped SN models. The left panels show the radio light curves in the centimeter range (8.46 GHz), while the right panels are models in the millimeter range (100 GHz). The thick red lines show the synthesized radio light curves for SN 2016coi with the mass-loss rate $\dot{M}_{\rm CSM} = 10^{-4} M_\odot {\rm yr}^{-1}$, for $t < 10$ days (dotted) or $t \geq 10$ days (solid). The thin red lines within 10 days indicate the radio light curves computed with the putative confined CSM around the SN 2016coi with the mass-loss rate $\dot{M}_{\rm CSM} = 10^{-3} M_\odot {\rm yr}^{-1}$. The black points in the left panels show the observational data of SN 2016coi in the centimeter range (Terreran et al., 2019). The ultra-stripped SN models sep_1Rsun (Top) and sep_10Rsun (Bottom), with $f_{\dot{M}} = 0.99$ as the fiducial value, are plotted with the solid blue lines.

In addition, we note that the radio emissions from SN 2016coi after 10 days are also distinguishable from those from the ultra-stripped SNe. The gap in the mass-loss rate between SN 2016coi and the model sep_1Rsun results in the difference in the radio peak dates. For the model sep_10Rsun, the mass-loss rate is similar to that of SN 2016coi, but the radio luminosity is weaker due to the small explosion energy of the ultra-stripped SN. However, we note that there are some uncertainties on the parameters describing the shock acceleration such as ϵ_e and ϵ_B.

4.5.4 Event rate and Detectability

The fraction of ultra-stripped SNe is suggested to be 0.1 - 1 percent of the total number of SNe (Tauris et al., 2013). If transient observational facilities are able to completely detect all of the SNe within the distance $D_{\rm max}$, the detection rate of ultra-stripped SNe is estimated as $\sim 10 (D_{\rm max}/300$ Mpc$)^3$ yr^{-1} (Hijikawa et al., 2019), corresponding to once per one month. At the typical distance of 300 Mpc for the ultra-stripped SNe (corresponding to iPTF 14gqr), the expected flux density of the radio signal is $\sim 0.1 (L_{\rm max}/10^{28}$erg s^{-1} Hz$^{-1})$ mJy. An integration time of $\sim$ 5 minutes is required for Very Large Array (VLA) or Atacama Large Millimeter/submillimeter Array (ALMA) to detect such a signal with 5σ sensitivity. We suggest a long-term monitoring of ultra-stripped SN

candidates in the centimeter range with VLA, or a quick millimeter follow-up observation with ALMA as interesting proposals.

4.5.5 Model uncertainties

Before closing this chapter, we comment on a few uncertainties involved in our modeling. First is the velocity of the CSM, which is important for determining the normalization of the CSM density. In this study we have assumed the typical escape velocity of a helium star ($u = 10^8$ cm s^{-1}). However, if the origin of the CSM is dominated by the outflow from the neutron star, the expected signals will become weaker than those in the present models.

Second, we employ the free parameter $f_{\dot{M}}$ to describe how much fraction of the gas transferred from the helium star will be distributed as the CSM. This parameter could be attributed to two physical processes; one is the direct leakage from the Roche Lobe, and the other is the outflow caused by the super-Eddington accretion onto the neutron star (see e.g., Chashkina et al., 2019, and references therein). As discussed in Section 4.3.1, the large value is plausible for $f_{\dot{M}}$ from various viewpoints. If the small $f_{\dot{M}}$ is realized, then the companion NS would experience the gravitational collapse to a black hole, or the accreting gas would stagnate around the NS and the binary would evolve into the common envelope again. The small $f_{\dot{M}}$ thus neither produce the ultra-stripped SN, nor form the DNS binary.

Finally, we adopt the standard parameters to describe the shock acceleration, ϵ_e and ϵ_B, to calculate the radio light curves. As noted in Section 4.3.3, the uncertainty in these parameters will affect the peak date and the optically thin, decaying luminosity of the radio emission. However, we emphasize that the optimized combinations of the observational epoch and frequency for detecting the radio signals from the ultra-stripped SN suggested in this paper would hardly be affected by the uncertainty in these shock acceleration parameters.

4.6 Summary

A DNS binary imprints the stellar evolution history of massive stars in its formation process. Detections of radio pulsars, gravitational waves from a DNS merger and the associated kilonova, have uncovered the universal existence of close DNS binaries. The system must experience two SN explosions, and strong binary interaction, in the evolution process. The ultra-stripped SN scenario has been proposed as a promising system to form a DNS binary, thanks to its small ejecta mass. Recent transient observations have discovered some candidates for the ultra-stripped SNe, and the nature of the candidates has been investigated in detail. However, an ultra-stripped SN progenitor system may have large separation, and then a remnant DNS binary would not merge within the cosmic age. Observational properties of ultra-stripped SNe in the optical range are not sensitive to the separation of the remnant DNS binary. An alternative method for investigating the binary separation and the possibility of the remnant DNS merger within the cosmic age is thus required.

We have focused on the mass-transfer rate of the ultra-stripped SN progenitor binary, which is highly sensitive to the orbital separation. The high mass-transfer rate in the ultra-stripped SN progenitor binary results from the strong binary stripping associated with the small binary separation, and will be directly linked to the high CSM density around the progenitor. In such a circumstance, radio emission induced by the SN-CSM interaction should be strong, and this will become a potential tracer of the mass-transfer rate and the separation of the progenitor binary.

Guided by the stellar evolution models developed by Tauris, Langer, and Podsiadlowski, 2015, we have analytically calculated the radio emission from the ultra-stripped SNe. We have shown that the peak luminosities both in the centimeter and millimeter ranges are high in some of the models with small separations. A strong radio signal can thus indicate that the remnant DNS

binary can merge within the cosmic age. Furthermore, we have also suggested an optimized combination of the time and frequency windows to study the radio signals from the ultra-stripped SNe. The centimeter emission in the late epoch ($\gtrsim$ 100 days) and the millimeter emission in the early epoch ($\lesssim$ 30 days) serve as potential probes for investigating the nature of the remnant DNS binary.

Chapter 5

Long-term evolution of a supernova remnant hosting a double neutron star binary

5.1 Introduction

A double neutron star (DNS) binary is believed to be the fossil object from a binary system of two massive stars which have both exploded as core-collapse supernovae (SNe) in the past (e.g., Podsiadlowski et al., 2005). Observations of Galactic radio pulsars have revealed that some DNS binaries are in an orbit tight enough to merge within the cosmic age (Burgay et al., 2003). Indeed, previous observations for the short gamma-ray burst GRB 130603B have implied the association between the gamma-ray emission and kilonova in the DNS merger (Tanvir et al., 2013; Tanaka and Hotokezaka, 2013; Hotokezaka et al., 2013). Furthermore, recent gravitational wave detectors and rapid follow-up electromagnetic observations have succeeded in probing the coalescence of a DNS, confirming the link of these objects to the origin of short gamma-ray bursts and the nucleosynthesis of r-process elements (e.g., Abbott, Abbott, Abbott, et al., 2017b; Abbott, Abbott, Abbott, et al., 2017a; Tanaka et al., 2017).

The formation of a DNS requires that the binary system is not disrupted by the evolution history of the massive stars all the way through their core-collapses. One of the plausible scenarios of DNS formation invokes an ultra-stripped supernova (USSN, Tauris et al., 2017; Yoshida et al., 2017). In a close binary consisting of two massive stars, the primary star first explodes as a SN. After a phase as a high-mass X-ray binary, the outer layer of the secondary star is stripped away in two steps: (1) the ejection of its hydrogen-rich envelope through a phase of common envelope (CE) interaction, and (2) the stripping of the helium layer through Roche lobe overflow (RLO). These binary interactions lead to the formation of an helium star ($\lesssim 2M_{\odot}$), which eventually explodes as a USSN. Indeed, some of the rapidly evolving transients such as SN 2005ek (Drout et al., 2013), iPTF14gqr (De et al., 2018), and SN 2019dge (Yao et al., 2020) are suggested to be possible candidates for USSNe (Moriya et al., 2017b). In addition, it has been proposed that during the operation period of the Zwicky Transient Facility (ZTF, Graham et al., 2019; Bellm et al., 2019), roughly 10 USSNe within 300 Mpc will be detected per a year (Hijikawa et al., 2019). Hence, it is expected that future surveys and follow-up observations of transients will enable us to examine in detail the validity of the USSN scenario as the formation mechanism of DNS binaries.

Another way to experimentally test the USSN scenario is to search for supernova remnants (SNRs) hosting a DNS binary. After the explosion, the ejecta of the USSN sweeps up the surrounding CSM while expanding into the interstellar space. Intriguingly, this kind of system can be potentially detected as a SNR hosting a DNS binary, which we will refer to as an ultra-stripped supernova remnant (USSNR) hereafter. While the current SNR surveys have not identified any of these remnants so far, we note that the observable characteristics of a USSNR have not been discussed and quantified in the literature. It is hence essential to investigate the dynamical evolution

and emission properties of USSNRs using a dedicated simulation model to shed light on how they can be identified.

Tauris et al., 2013 developed a progenitor evolution model for the USSN, and showed that the mass-transfer rate through RLO can be enhanced up to $\dot{M} \sim 10^{-5}\ M_\odot\ \mathrm{yr}^{-1}$ in the last 0.1 Myr prior to the core collapse. Because the mass-transfer rate is orders of magnitude larger than the Eddington accretion rate onto the neutron star, a large fraction of the stripped gas escapes the binary system and distributes around the progenitor as CSM. Assuming a wind velocity $v_w \sim 1000\,\mathrm{km\,s}^{-1}$, the gas which has been expelled from the binary system in the RLO phase can reach a distance of $\sim 100\,\mathrm{pc}$ from the progenitor, implying that the evolution of the USSNR is heavily influenced by the CSM created by the RLO mass loading process. However, detailed models for the mass-loss history driven by binary interaction are in most cases not incorporated in the simulations of SNR dynamics, which is particularly critical for understanding the properties of USSNRs.

In this study, we investigate the characteristics of a USSNR using a grid of one-dimensional hydrodynamic simulations. By employing the binary evolution model presented in Tauris et al., 2013, we first construct the large-scale structure of the CSM surrounding the USSN progenitor. We next calculate the hydrodynamics of the USSN ejecta interacting with the composed CSM and the resulted synchrotron radiation. Our simulations reveal that the blastwave of USSNRs has a difficulty in penetrating the hot plasma, which had been shaped by the preceding mass loss from the progenitor binary. Radio emission from a young USSNR is predicted to be bright enough to be detected if it inhabits our Galaxy, while its luminosity starts to decrease at $t \gtrsim 10^3$ years, making the USSNR observable for a relatively short time period. Besides, the low surface brightness of a USSNR predicted by our models at its typical diameters ($D \sim \mathcal{O}(10\,\mathrm{pc})$) can serve as a key to the identification of these remnants in the future.

This chapter is organized as follows. In Section 5.2, we review the USSN scenario as a formation theory of DNS, and describe the progenitor models used in our simulations. In Section 5.3, we discuss the formation sequence of the CSM, followed by a description of the procedures for constructing our CSM models. In Section 5.4, we examine the hydrodynamic evolution of a USSNR and show the properties of the expected radio signals, including the light curve and surface brightness. Their implications are discussed in Section 5.5, and our results are summarized in Section 5.6.

5.2 Progenitor model

Tauris et al., 2013 investigated the binary stellar evolution of a $2.9M_\odot$ He star with a neutron star companion, having an initial orbital period of 0.1 day. They found that the He star reduces its own mass down to $1.5M_\odot$ through RLO, and suggested that the He star explodes as a USSN which can be a candidate for some rapidly evolving transients. Here we overview the stellar evolution of the progenitor of a USSN, which is crucial for understanding the formation of the CSM adopted in this study.

Figure 5.1 shows the time evolution of the mass (M), radius of the Roche lobe (R), escape velocity $(V_{\rm esc})$, and mass-transfer rate $(\dot{M})$ of the USSN progenitor presented in Tauris et al., 2013. Here, the escape velocity is defined as $V_{\rm esc} = \sqrt{2GM/R}$, where G is the gravitational constant. When the progenitor is in the state illustrated by the blue line, its outer layer is stripped away by the companion neutron star through RLO. Until the core collapse, the He star experiences RLO three times; the first phase is at 1.78 Myr $\lesssim t \lesssim$ 1.84 Myr during which the core has exhausted its He-burning fuel ($\mathcal{A}$). The second is at $t \sim 1.851$ Myr when the core C-burning has ended ($\mathcal{B}$), and the third is at $t \gtrsim 1.854$ Myr in which the off-center O-burning is about to onset ($\mathcal{C}$ and $\mathcal{D}$). The CSM around the USSN progenitor is hence expected to be shaped by these three phases of mass loss activities. We note that the progenitor spends most of its lifetime in the state shown by the

orange line prior to $\mathcal{A}$, and that the increase of the mass-loss rate is realized in the last 0.1 Myr before core collapse.

The progenitor does not experience RLO in the detached phases, during which we conservatively assume a mass loss rate of $10^{-7}\ M_\odot\ \mathrm{yr}^{-1}$. This mimics the stellar wind from the progenitor, but the mass and kinetic energy released by this wind are smaller than those carried by the gas stripped away through the RLO. Thus, we can assume that the stellar wind from the progenitor has an insignificant influence on the overall wind hydrodynamics, and that the consistency with the stellar evolution model is maintained. The model developed by Tauris et al., 2013 covers the lifetime of the He star only until 10 years prior to its core collapse. To trace the evolution up to the moment of the explosion, we use the final values of M, R, V_{esc}, and $\dot{M}$ from the model for the last 10 years.

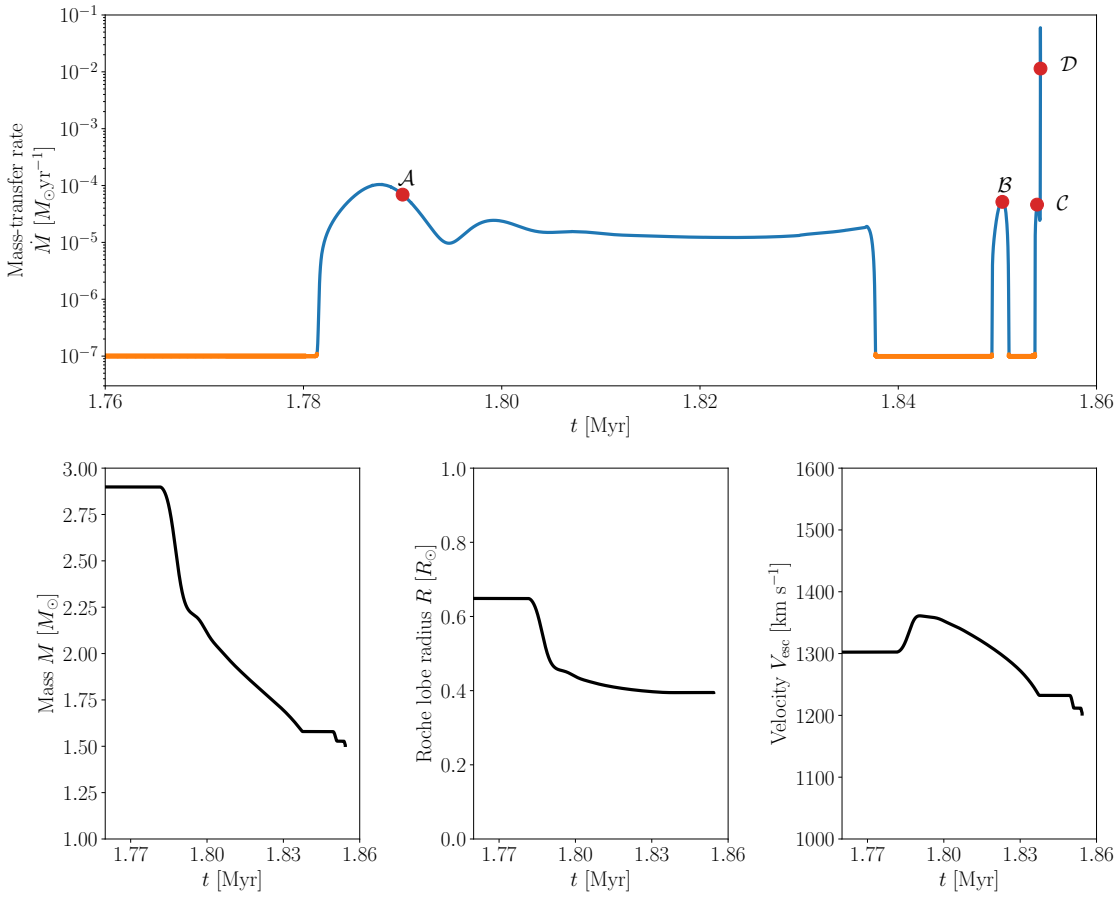

FIGURE 5.1: Time evolution of the mass-loss history (top), total mass (bottom left), Roche lobe radius (bottom middle), and escape velocity (bottom right) of the USSN progenitor. Blue and orange lines correspond to the phases in which the binary system experiences RLO or not, respectively. Note that within the first 1.78 Myrs the progenitor is in a stable core He-burning stage, so that these values are kept constant.

The gas transferred from the progenitor first flows toward the neutron star with an accretion rate orders of magnitude larger than the Eddington accretion rate (Tauris et al., 2013). The neutron star cannot feed up anymore and thus drives the accreted gas outward by mechanisms such as propeller effect (Tauris et al., 2017). However, resolving the detail of this outflow dynamics is beyond the scope of this work. For simplicity, we assume that the material which has been stripped away from the He star launches outward spherically at the radius of the Roche lobe R with a velocity V_{esc} and mass-loss rate $\dot{M}$. Then, the mass density at the Roche lobe radius $(\dot{M}/4\pi R^2 V_{\mathrm{esc}})$ can be estimated. Given the density and velocity of the gas at the Roche lobe radius as an inner

boundary condition, we can solve the hydrodynamics of the gas launched from the progenitor binary to model the CSM formation around the progenitor. Combined with a parametric survey described in the following sections, this strategy allows us to demonstrate the long-term evolution properties of a USSNR with the mass loss history of the progenitor taken into account.

5.3 CSM formation

In this section, we describe our procedure for modeling the formation of the CSM surrounding the USSN progenitor. First, we construct the initial profile of the interstellar medium (ISM) in Section 5.3.1. We then explain our methodology for simulating the hydrodynamics of the mass-loss material in Section 5.3.2, and the properties of the composed CSM in Section 5.3.3.

5.3.1 Initial setup

The progenitor experiences a hydrogen-rich envelope ejection driven by the CE interaction before the stripping of the helium gas through RLO. The distribution of this expelled hydrogen-rich gas is important because it interacts with the helium gas released through RLO later on. Although some recent multi-dimensional simulations have succeeded in completely ejecting the hydrogen-rich envelope of a red supergiant through the CE interaction under some assumptions and realizations (Law-Smith et al., 2020; Lau et al., 2022, but see also Vigna-Gómez et al., 2022), the distribution of the material ejected by the CE interaction is still not completely understood.

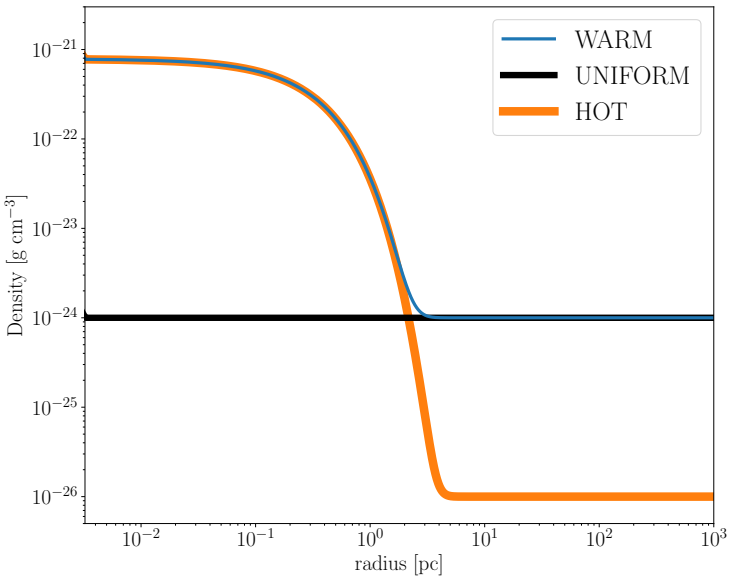

FIGURE 5.2: Initial density profiles of the ISM with a component from CE ejection. Blue, orange, and black lines represent the model 'WARM', 'HOT' and 'UNIFORM', respectively.

Figure 5.2 shows three models we adopt for the initial density profile of the CE material. We consider a situation where the ejected gas with a mass $M_{\rm CE} = 10 M_\odot$ is distributed within a radius $R_{\rm CE}$ which smoothly connects with the ISM. Given that the characteristic timescale of the CE interaction is around thousands of years (Ivanova et al., 2013), the gas ejected with a speed ~ 100 km s^{-1} can reach a radius $R_{\rm CE} \sim 10^{18}$ cm. Since there is a variety in the ISM properties such as density and temperature (e.g., Berkhuijsen and Fletcher, 2008; Draine, 2010), we consider two ISM phases; a warm phase ($\rho_{\rm ism} = 10^{-24}\,{\rm g\,cm^{-3}}$, $T_{\rm ism} = 10^4\,{\rm K}$) and a hot phase ($\rho_{\rm ism} = 10^{-26}\,{\rm g\,cm^{-3}}$,

TABLE 5.1: Parameters for initial profiles

name	$\rho_{\rm ism}$ **[g cm^{-3}]**	$\rho(r)$	$T_{\rm ism}$ **[K]**
WARM	10^{-24}	$\rho_{\rm CE}\exp(-r/R_{\rm CE})+\rho_{\rm ism}$	10^4
HOT	10^{-26}	$\rho_{\rm CE}\exp(-r/R_{\rm CE})+\rho_{\rm ism}$	10^6
UNIFORM	10^{-24}	$\rho_{\rm ism}$	10^4

$T_{\rm ism} = 10^6$ K). We remark that the thermal pressure in these two initial profiles are equal to each other. In addition, we prepare a reference model 'UNIFORM', in which a static and uniform ISM resides throughout the simulation domain with a density $\rho_{\rm ism} = 10^{-24}\,{\rm g\,cm^{-3}}$, to evaluate the effect of the CE ejection activity. The specific profiles of the initial density for each model are described in Table 5.1. The derivation of the exact value of $\rho_{\rm CE}$ is explicated in Appendix D. We consider a static ISM profile ($v = 0$). The initial velocity profile of the CE component does not have an important role in the hydrodynamics of the CSM formation because the expected $V_{\rm CE}$ is negligibly lower than the velocity of the wind from the progenitor binary. To verify this we conducted simulations in which the initial velocity of the CE component is assumed to be $100\,{\rm km\,s^{-1}}$ and confirmed that the outcome is not changed. We assume the temperature $T = T_{\rm ism}$ and a solar metallicity throughout the entire profiles at this stage. A comparison of the results among these models enables us to evaluate how much the properties of the CE ejection affect the CSM formation and the subsequent SNR evolution.

5.3.2 Wind hydrodynamics

We solve the one-dimensional equations of ideal gas hydrodynamics where the internal energy is taken away by radiative cooling in spherical coordinates. The governing equations are described as follows:

$$\frac{\partial\rho}{\partial t}+\frac{1}{r^2}\frac{\partial(r^2\rho v)}{\partial r}=0, \tag{5.1}$$

$$\frac{\partial v}{\partial t}+v\frac{\partial v}{\partial r}=-\frac{1}{\rho}\frac{\partial p}{\partial r}, \tag{5.2}$$

$$\frac{\partial}{\partial t}\left[\rho\left(\frac{1}{2}v^2+e\right)\right]+\frac{1}{r^2}\frac{\partial}{\partial r}\left[r^2\rho v\left(\frac{1}{2}v^2+h\right)\right] = -n_i n_e\Lambda(T), \tag{5.3}$$

where ρ is the mass density, v is the velocity, p is the pressure, e is the specific internal energy, $h = e + p/\rho$ is the specific enthalpy, n_i and n_e are the number density of ions and electrons. $\Lambda(T)$ represents the radiative cooling function, for which we employ the power-law formalism introduced by Chevalier and Fransson, 1994. The energy loss by radiative cooling is calculated only in the optically thin region where $\tau \leq 1$ which is sufficient for tracing the evolution of the blastwave (see also Section 5.5.4). These governing equations are closed with the equation of state, $p = (\gamma-1)\rho e$, where $\gamma = 5/3$ is the adiabatic index. The equations are solved by a Roe Riemann solver with the second entropy fix by Harten and Hyman to treat the contact discontinuity and the shock wave (Harten and Hyman, 1983). The numerical accuracy of the code used in this study is verified in Appendix E.

We divide the simulation domain from 10^{16} cm to 3×10^{21} cm into 2047 zones in a logarithmic scale. Inside 10^{16} cm as an inner boundary condition, we inject the blowing He-rich gas whose time evolution is described in Section 5.2.

We trace the distribution of the chemical abundances by advection, assuming that no mixing of the chemical composition occurs. The abundance distribution is required in order to accurately estimate the number density of ions and electrons in the radiative cooling term.

5.3.3 Composed CSM

Figure 5.3 shows the snapshot of the density structure of the CSM at the moment of core collapse of the progenitor. The model 'WARM' and 'UNIFORM' share an identical CSM structure in the entire simulation domain. It is also the case for the model 'HOT' within $\sim 3\,\mathrm{pc}$, but its outer configuration deviates from the other two models. The distribution of the density within $\sim 3\,\mathrm{pc}$ reflects the mass loss history. Namely, the dense CSM being distributed around $r \sim 0.01\,\mathrm{pc}$ and $0.1\,\mathrm{pc}$ are originated from the mass loss at points $\mathcal{D}$ and $\mathcal{C}$ in Figure 5.1. Yet, a segment resides around $10\,\mathrm{pc}$ in which the density is roughly constant with some fluctuations. This non-smooth segment is created by the collision between the wind launched at point $\mathcal{B}$ and the reverse shock generated by the gas ejected at point $\mathcal{A}$ before. The ISM wall is located at a radius of $20\,\mathrm{pc}$ in the model 'WARM' and 'UNIFORM' and $30\,\mathrm{pc}$ in the model 'HOT', respectively.

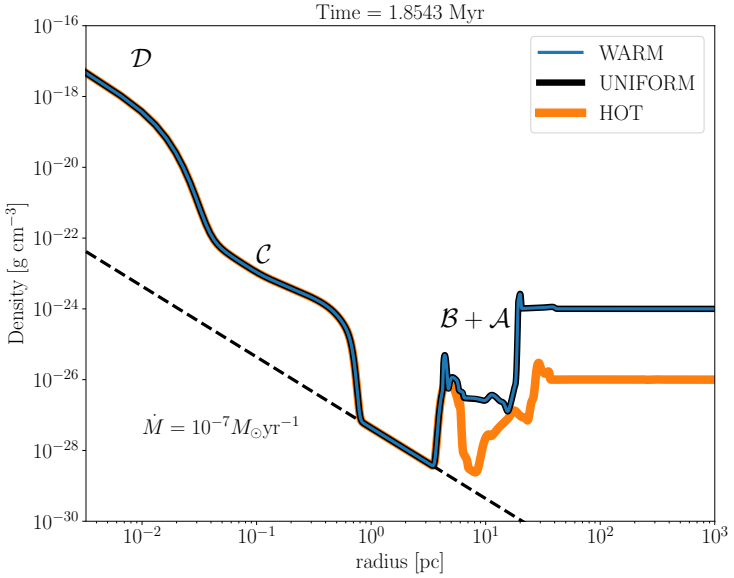

FIGURE 5.3: The density structure of the composed CSM. The dashed black line shows the distribution realized for the steady wind with its mass-loss rate $\dot{M} = 10^{-7}\ M_\odot\ \mathrm{yr}^{-1}$. The distributions of the gas pointed out by cursive alphabets represent that they are from the mass loss activity referred in Figure 5.1.

We will briefly elaborate on the importance of the CE component on the ISM profile. The reference model 'UNIFORM' without the CE component allows us to investigate the contribution of the CE component on the hydrodynamics of the wind. The results obtained from this reference model are found to be almost identical to the outcome from 'WARM', being nearly indistinguishable just in Figure 5.3. This can be interpreted as follows. The radius of the ISM wall is roughly determined by the balance between the ram pressure of the wind and the thermal pressure of the swept-up material (Weaver et al., 1977), which is computed as $\sim 20\,\mathrm{pc}$ in our simulations. The enclosed mass of the initial ISM profile at $r \sim 20\,\mathrm{pc}$ is $\sim 400 M_\odot$, indicating that the mass of the CE component can be regarded to be negligibly small. Hence, the composed CSM has similar characteristics between 'WARM' and 'UNIFORM'. We confirmed that even when considering a uniformly distributed hot ISM ($\rho_{\mathrm{ism}} = 10^{-26}\,\mathrm{g\,cm^{-3}}$, $T\mathrm{ism} = 10^6\,\mathrm{K}$), the consequent CSM

structure does not differ from the model 'HOT' significantly other than slight quantitative modifications. This implies that as long as the CE ejection before the USSN is considered within a range of typical time and energy scales, it does not play an important role in the formation of the CSM around the USSN progenitor.

Figure 5.4 shows the temperature structure of the CSM at the moment of core collapse. Similar to the density structure, the models 'WARM' and 'UNIFORM' have the same temperature structure over the entire region. The model 'HOT' also possesses the identical distribution with the other models within 3 pc, but the quantitatively different structure is formed outside 3 pc. A hot plasma with $\sim 10^8$ K is located in the vicinity of the ISM wall in all models. The location of the inner edge of this hot plasma coincides with the radius of the termination shock of the wind driven by RLO. The geometrical thickness of the plasma is $\sim$ 10 pc. The existence of this hot plasma region plays a critical role in weakening the SNR blastwave as it propagates through the region as discussed later.

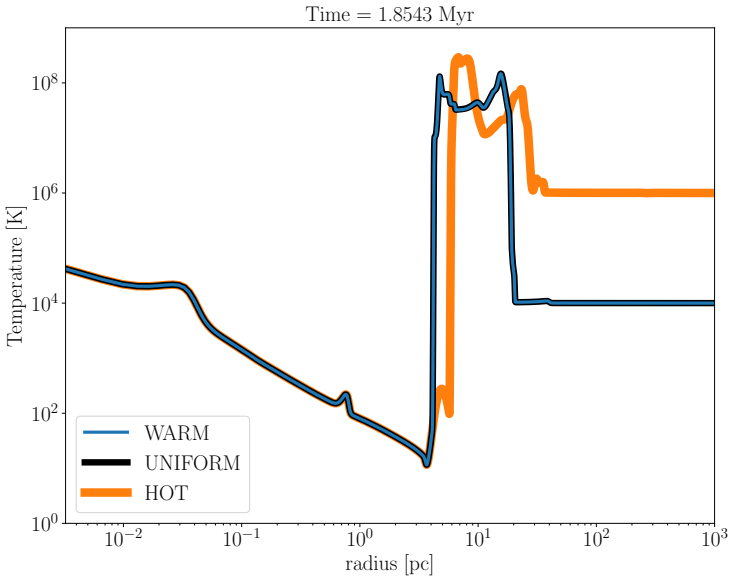

FIGURE 5.4: The temperature structure of the composed CSM.

5.4 SNR evolution

In this section, we investigate the evolution of a USSNR interacting with the CSM constructed in the previous section. In Section 5.4.1, we show the method to simulate the dynamics of the ejecta and the expected synchrotron emission, and the results are presented in Section 5.4.2. As was confirmed in the previous section, the solution derived from the model without a CE component ('UNIFORM') converges to that of 'WARM'. We will therefore examine results from the models 'WARM' and 'HOT' hereafter.

5.4.1 Method

Ejecta dynamics

The initial profile of the USSN progenitor is taken from Moriya et al., 2017b, who evolved the model of the He star previously presented by Tauris et al., 2013 further until core collapse. Then we attach the CSM composed in Section 5.3 to the progenitor while retaining the distribution of the density, velocity, temperature, and chemical abundance.

We next examine the hydrodynamics of the SN explosion to obtain the SN ejecta structure. We excise the remnant mass $M_{\rm rem} = 1.35 M_\odot$ from the inner region of the progenitor, and inject an explosion energy $E_{\rm exp} = 10^{50}$ erg to the rest of the material in the progenitor ($M_{\rm ej} \sim 0.15 M_\odot$) as a thermal energy following the method developed by Morozova et al., 2015. The explosion energy is chosen based on light curve models (Moriya et al., 2017b), which is also consistent with that proposed by state-of-the-art simulations (Suwa et al., 2015; Müller et al., 2018). The profile is resolved into more than 4000 meshes with a logarithmic spacing, and the hydrodynamics of the ejecta is calculated by the same method as described in Section 5.3.2, except that a reflective condition is employed at the inner boundary. As a result, we obtain the time evolution of the blastwave velocity and the trajectory of Lagrangian particles, which are used to compute the energy distribution of relativistic electrons and the amplified magnetic field (see the next section).

As the SNR evolves into the Sedov phase, its reverse shock begins to propagate towards the inner region and heats up the ejecta (e.g., Truelove and McKee, 1999). Since the simulation domain is resolved under a logarithmic mesh, the high temperature in the inner region can cause small timesteps, making it difficult for the simulation to progress. To solve this numerical difficulty, we excise the Eulerian meshes in the innermost region within 10^{18} cm when the blastwave radius has reached 10^{19} cm. This does not affect the consistency of the simulations since the total gas mass within 10^{18} cm at the moment of the excision is negligibly small and hence dynamically unimportant. This allows us to trace the long-term evolution of the USSNR within a reasonable simulation time. The computations are terminated at 10^5 years since the explosion.

Particle acceleration and magnetic field amplification

Once the gas is heated by the forward shock, the diffusive shock acceleration (DSA) imparts relativistic energies to the injected charge particles and induces amplification of the turbulent magnetic field (e.g., Fermi, 1949; Drury, 1983). The region shocked by the blastwave serves as a site of synchrotron emission from SNRs (Reynolds, 2008; Dubner and Giacani, 2015). In this study, we define the blastwave as the discontinuity which satisfies the following two conditions: (1) the pressure jump is the largest in the simulation domain, and (2) the Mach number is greater than 3. The latter is justified because strong shocks have a potential to drive DSA, whilst weak shocks are less capable of efficient particle acceleration, confirmed by the observations for radio relics in galaxy clusters (e.g., Botteon et al., 2020, and references therein).

We first consider a Lagrangian mesh a_s through which the blastwave passes at time t_s. As the shock sweeps through the mesh, the charged particles are accelerated to relativistic energies, coupled with an amplification of the turbulent magnetic field. We model the energy densities of the accelerated relativistic electrons (u_e) and the magnetic field (u_B) in the Lagrangian mesh a_s as follows:

$$u_e = \epsilon_e \rho_{\rm sh} (V_b - v_u)^2, \tag{5.4}$$

$$u_B = \frac{B^2}{8\pi} = \epsilon_B \rho_{\rm sh} (V_b - v_u)^2, \tag{5.5}$$

where ϵ_e and ϵ_B are the acceleration and amplification efficiencies, $\rho_{\rm sh}$ is the mass density in the Lagrangian mesh a_s, V_b is the velocity of the blastwave, and v_u is the velocity of the unshocked gas upstream of the shock, respectively. These parametrizations are conventionally used in the modeling of radio SNe (e.g., Chevalier, Fransson, and Nymark, 2006; Chevalier and Fransson, 2006; Matsuoka et al., 2019). These equations apply to the mesh only when $V_b - v_u > 0$.

The energy distribution of the accelerated electrons, $N(a_s, E)$, is described by a power-law distribution as follows:

$$N(a_s, E) = C E^{-p}, \tag{5.6}$$

where E and p are the energy and the spectral index of the electrons, respectively. The coefficient C is determined by performing a normalization of the energy density:

$$\int_{E_{\rm min}}^{\infty} EN(a_s, E)dE = u_e, \tag{5.7}$$

where $E_{\rm min} = 2m_e c^2$ is used (see Section 5.5.6 for a discussion on the uncertainty related to $E_{\rm min}$).

As the system evolves, the ejecta expands and the blastwave propagates to the next Lagrangian mesh. Meanwhile, the relativistic electrons lose their energies by both synchrotron and adiabatic cooling, and the magnetic field also decays with the adiabatic expansion. We consider a Lagrangian mesh (a) which had been heated by the shock at mass coordinate a_s and time t_s, and assume that the relativistic particles are confined within the mesh and the magnetic field is frozen in the plasma. We calculate the cooling processes of the accelerated particles and the time evolution of the energy distribution following previous studies (e.g., Reynolds, 1998; Orlando et al., 2011; Ferrand, Decourchelle, and Safi-Harb, 2014). An electron's energy E declines to E' through synchrotron and adiabatic cooling, which can be written as follows:

$$E'(a,t) = E\frac{\alpha(a,t)^{\frac{1}{3}}}{1+\Theta(a,t)\frac{E}{m_e c^2}}, \tag{5.8}$$

$$\alpha(a,t) = \frac{\rho(a,t)}{\rho(a_s,t_s)}, \tag{5.9}$$

$$\Theta(a,t) = \int_{t_s}^{t} \frac{\lambda}{m_e c^2} B(a,t')^2 \alpha(a,t')^{1/3} dt', \tag{5.10}$$

$$\lambda = \frac{4q^4}{9m_e^2 c^3} \tag{5.11}$$

where c is the speed of light, q is the elementary charge, and m_e is the mass of electron, respectively. The energy distribution of the electrons evolves following number conservation, i.e.

$$N(a,E') = N(a_s,E)\frac{dE}{dE'}. \tag{5.12}$$

As for the strength of the magnetic field, we consider a magnetic flux conservation in each Lagrangian mesh.

Synchrotron emission

Given the energy distribution of electrons and the strength of the magnetic field, the intensity of the synchrotron emission I_ν can be calculated by integrating the radiative transfer equation written as follows:

$$\frac{dI_\nu}{da} = \begin{cases} -\alpha_{\nu,\rm syn} I_\nu + j_{\nu,\rm syn} & (a \le R_b) \\ -\alpha_{\nu,\rm ff} I_\nu & (a > R_b) \end{cases} \tag{5.13}$$

where $j_{\nu,\rm syn}, \alpha_{\nu,\rm syn}$, and $\alpha_{\nu,\rm ff}$ are the synchrotron emissivity, synchrotron self-absorption and free-free absorption coefficient, respectively (Rybicki and Lightman, 1979), and R_b is the blastwave radius.

We also calculate the surface brightness $\Sigma(\theta)$ which is often used as a diagnostic observable for SNRs. Σ-D diagrams which show the relation between the surface brightness and the diameter of SNRs are commonly used for determining the distance to the objects (see e.g., Poveda and Woltjer, 1968; Pavlović et al., 2013, and references therein). Since the surface brightness $\Sigma(\theta)$ is independent of the distance to the SNR, it can be a useful quantity for investigating the intrinsic

TABLE 5.2: Grid of models

ID	name	p	(ϵ_e, ϵ_B)
1	WARM_H_SN	2.1	$(10^{-2}, 10^{-1})$
2	WARM_H_SNR	2.1	$(10^{-3}, 10^{-2})$
3	WARM_I_SN	2.5	$(10^{-2}, 10^{-1})$
4	WARM_I_SNR	2.5	$(10^{-3}, 10^{-2})$
5	WARM_S_SN	3.0	$(10^{-2}, 10^{-1})$
6	WARM_S_SNR	3.0	$(10^{-3}, 10^{-2})$
7	HOT_H_SN	2.1	$(10^{-2}, 10^{-1})$
8	HOT_H_SNR	2.1	$(10^{-3}, 10^{-2})$
9	HOT_I_SN	2.5	$(10^{-2}, 10^{-1})$
10	HOT_I_SNR	2.5	$(10^{-3}, 10^{-2})$
11	HOT_S_SN	3.0	$(10^{-2}, 10^{-1})$
12	HOT_S_SNR	3.0	$(10^{-3}, 10^{-2})$

nature of the USSNR compared to the rest of the SNR population. $\Sigma(\theta)\delta\theta$, the power per unit surface area and unit frequency emitted from a ring with sky projection angles θ to $\theta + \delta\theta$, can be evaluated by integrating the total power of the synchrotron emission per unit volume along the line of sight as follows:

$$\Sigma(\theta)\delta\theta = \frac{\int_{\rm LOS} dl \epsilon_\nu \delta A(\theta)}{4\pi d^2 \Delta\Omega(\theta)} \simeq \int_{\rm LOS} dl \frac{\epsilon_\nu}{4} \frac{\delta\theta^2}{\theta^2} \tag{5.14}$$

where $d, \epsilon_\nu = 4\pi j_{\nu,\rm syn}, \delta A(\theta) = \delta(\pi d^2 \theta^2)$, and $\Delta\Omega(\theta)$ are the distance to the SNR, the total power of the synchrotron emission per unit volume, the area of the ring with projection angle θ, and the total solid angle of the SNR. The angle-averaged surface brightness can then be estimated, which allows us to examine the position of USSNRs on the Σ-D diagram.

Parameter sets

Our treatment of DSA involves uncertainties from the DSA parameters p, ϵ_e, and ϵ_B. Although these parameters should in principle be constrained by particle-in-cell simulations (e.g., Park, Caprioli, and Spitkovsky, 2015; Caprioli, Pop, and Spitkovsky, 2015), the appropriate values are still debated. To investigate the dependence of the shock acceleration parameters on the radio light curves, we prepare 6 combinations of parameters chosen as follows. For the spectral index of electrons $p = 2.1$ (hard), $p = 2.5$ (intermediate), and $p = 3.0$ (soft) are employed, while for the efficiency of particle acceleration and magnetic field amplification, the combinations $(\epsilon_e, \epsilon_B) = (10^{-2}, 10^{-1})$ (typical for radio SNe, Chevalier and Fransson, 2006; Maeda, 2012) and $(\epsilon_e, \epsilon_B) = (10^{-3}, 10^{-2})$ (typical for SNRs, Lee, Ellison, and Nagataki, 2012) are adopted. Our grid of 6 models for the shock acceleration parameters is then applied to the two kinds of CSM model 'WARM' and 'HOT'. The models are named by a sequence of labels from the CSM model ('WARM' and 'HOT'), the first character of the word representing the spectral state (Hard, Intermediate, and Soft), and the object type (SN and SNR) for which the chosen value of the shock acceleration efficiency is typical. The different combinations of the CSM models and shock acceleration parameters are summarized in Table 5.2. While our study employs time-independent values for the microphysics parameters ϵ_e, ϵ_B, and p, it is possible that they vary with time depending on the hydrodynamic evolution of the shock front (see Section 5.5.6 for a more detailed discussion).

5.4.2 Characteristics of a USSNR

Firstly, we discuss the hydrodynamics of the interaction between the USSN ejecta and the CSM. In Figure 5.5, the time evolutions of the density and velocity profile are shown. Here we mention on the dependence of the density profile on the ISM state. We can see that the model 'HOT' has a larger radius of the ISM wall than the model 'WARM', even though these two models have initially the same pressure. This suggests that the ISM density is important for dictating the location of the ISM wall; the lower ISM density (hot ISM) allows the exploding SNR gas to further expand. This feature is critical for quantifying the surface brightness of the USSNRs (see Figure 5.9 and Figure 5.10).

From the density distributions, we can see that the ejecta keeps expanding until $t \sim 10000$ years but starts decelerating around the ISM wall. The system can expand further for another ~ 3 and 10 pc at most from the location of the ISM wall in the model 'WARM' and 'HOT', respectively. This can be observed in the panel of the velocity profile; the system experiences fast expansion at $t \lesssim 3000$ years, while after the collision with the ISM wall it only possesses several hundreds km s^{-1} of the outward velocity. This implies that the diameter of the USSNR is highly constrained by the location of the ISM cavity wall, which in turn depends on the pre-SN mass loss activity of the progenitor. This picture can be applied to all core-collapse SNRs in general, for which the diameters of SNRs are associated with the pre-SN mass loss activity of their progenitors (e.g., Yasuda, Lee, and Maeda, 2021; Yasuda, Lee, and Maeda, 2022).

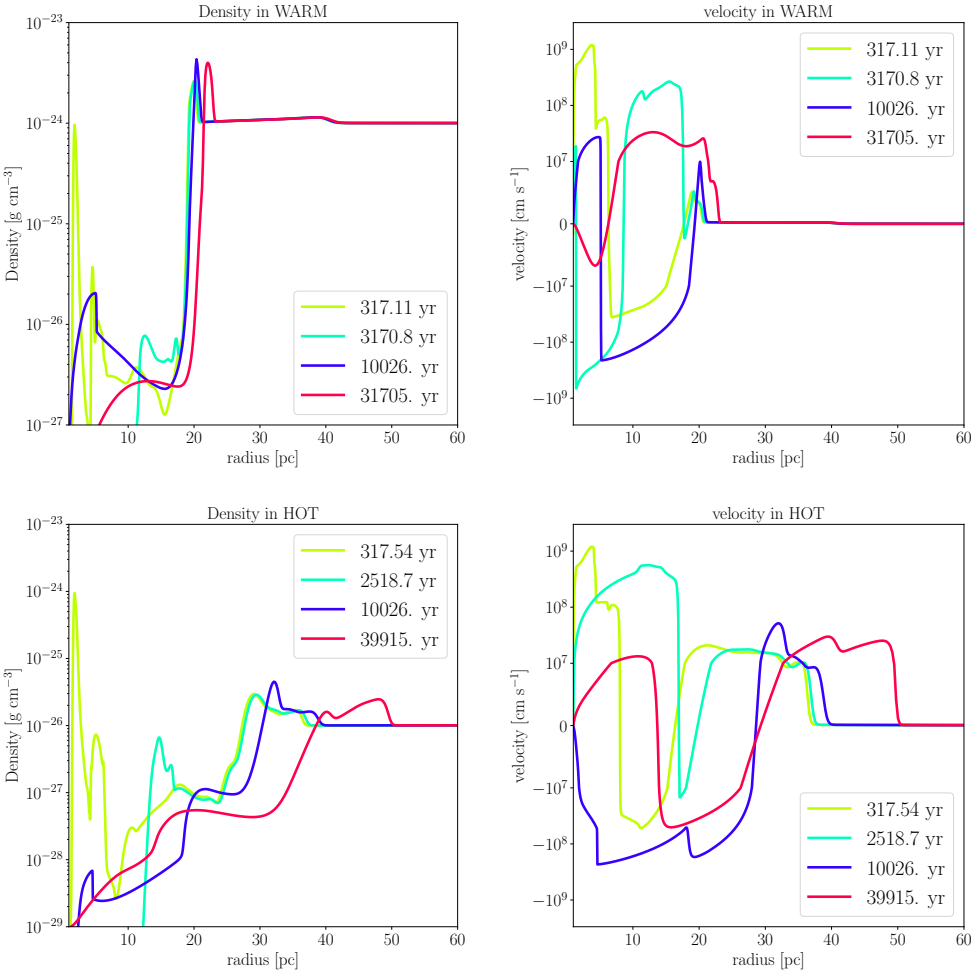

FIGURE 5.5: Time evolution of the radial profiles of the density (left) and velocity (right) in 'WARM' (top) and 'HOT' (bottom).

Figure 5.6 shows the time evolution of the Mach number and the blastwave velocity. Within the first 300 years, these two quantities both in the model 'WARM' and 'HOT' behave similarly each other since in this phase the identical CSM structure is traced. We can see two epochs at which the blastwave accelerates at $r \sim 0.01$ pc and $r \sim 0.1$ pc respectively, where the CSM density drops by orders of magnitude. Correspondingly, the Mach number also increases by more than an order of magnitudes at the same time. Overall, the velocity stays at about $10^9\,\mathrm{cm\,s^{-1}}$, leaving the USSNR active for the first 300 years. Furthermore, at 5 years $\lesssim t \lesssim$ 50 years when the swept CSM mass begins to exceed the ejecta mass, the velocity of the blastwave decays proportional roughly to $t^{-1/3}$. This agrees with the expected time dependence of the velocity in the Sedov phase for a CSM density profile proportional to r^{-2} (Book, 1994). The gradual increase of the Mach number during that phase can be also observed, due to the decrease of the upstream temperature (see Figure 5.4).

After $t \sim 300$ years, the blastwave decelerates down to $\sim 10^8\,\mathrm{cm\,s^{-1}}$, and then simply disappears out, as well as the Mach number decreases rapidly down to $\mathcal{O}(1)$. This phenomenon can be observed both in 'WARM' and in 'HOT' though there are some quantitative differences between these two models. This is caused by the hot plasma at $r \sim 5$ pc shown in Figure 5.4; as the blastwave plunges into the plasma where the sound speed is high, the Mach number of the blastwave quickly decreases down to unity. It is implied that such a weak shock cannot support an efficient DSA. Additionally, the density jump at $r \sim 3$ pc can also give rise to the deceleration of the blastwave. In conclusion, this result indicates that the blastwave in a USSNR dies out by propagating into a region of hot plasma at $\lesssim 10^3$ years.

Figure 5.7 shows the long-term 1 GHz radio light curves from the models shown in Table 5.2. The observed flux density F_ν shown in the right y-axis is normalized by a distance $d = 10$ kpc. The peak luminosity of the light curve is determined by synchrotron self-absorption with their shapes slightly modified by free-free absorption (see also Matsuoka et al., 2019). Note that for a USSN candidate iPTF14gqr non-detections of radio signals at the frequency 6 GHz and 22 GHz within 10 days have been reported, placing upper limits (De et al., 2018). In such a very early phase, free-free absorption completely damps the centimeter radio emissions, much more for 1 GHz (Matsuoka and Maeda, 2020). Since more electrons are accelerated and magnetic field is more intensively amplified in the models which assume larger efficiencies for DSA, brighter radio emission from USSNRs can be expected in the model with $(\epsilon_e, \epsilon_B) = (10^{-2}, 10^{-1})$ than those with $(\epsilon_e, \epsilon_B) = (10^{-3}, 10^{-2})$. Besides, a harder spectral index increases the number of more energetic electrons in the shocked region, which also results in the luminous radio signals. This behavior can be confirmed by comparing the luminosity between the models with $p = 2.1$ and those with $p = 2.5, 3.0$. We note that there are no qualitative difference in the light curve behaviors between the two CSM models over the entire timespan up to 10^5 years. Actually as 'HOT' has a more extended structure than 'WARM' as seen in Figure 5.5, a difference between these two models is expected in their surface brightness as we will discuss later.

We first look at the behaviors of the young USSNR at ages less than 1000 years, and compare them with SNe well-observed at the frequency $\sim$ 1 GHz even 1 year after their explosions such as SN 1993J (Martí-Vidal et al., 2011), SN 1995N (Chandra et al., 2009), and SN 2006jd (Chandra et al., 2012), and one of the youngest Galactic SNR Cas A (DeLaney and Rudnick, 2003, the point plotted at $t \sim 300$ years). As seen in Figure 5.7, our models show that young USSNRs at an age $t \sim 10$ years and $t \sim 300$ years produce fainter radio signal than those from the bright SNe and Cas A, respectively. The relatively weak emissions can be partially attributed to the shock velocity which is by a factor of a few lower than what is inferred for these objects (see, e.g., Fransson and Björnsson, 1998). Another possible reason is that at $t \sim 100$ years the blastwave is propagating at $r \sim 1$ pc where the dense CSM formed by the mass loss driven by the RLO is absent. Then the density of the CSM swept by the blastwave is considerably small there, making the DSA less efficient. However, we note that the expected flux density of the radio emission from the USSNR at $d = 10$ pc keeps greater than 0.1 mJy within an age $t \lesssim 1000$ years, which is bright enough to be

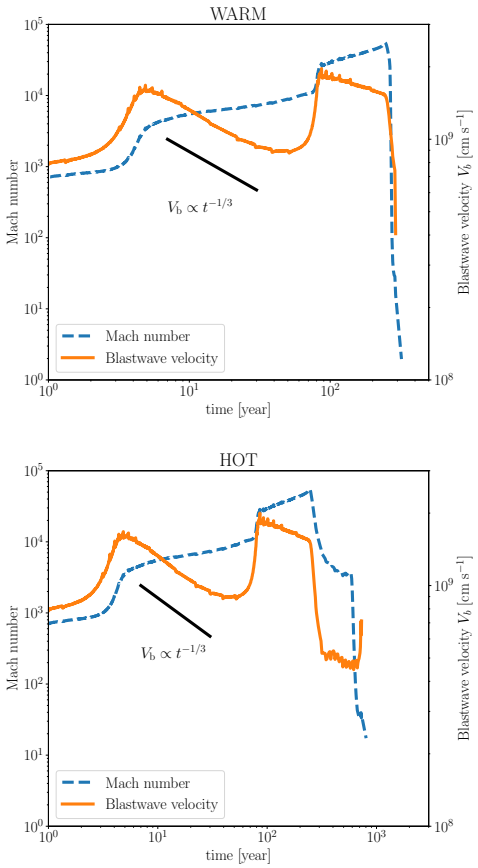

FIGURE 5.6: Time evolution of the Mach number (dashed blue) and velocity (solid orange) of the blastwave in the model 'WARM' (top) and 'HOT' (bottom). After the steep drops of the blastwave velocity near the end of the curves, the shock Mach number drops to below 3 where we truncate the simulations. The black line shows the time dependence of the blastwave velocity expected in the Sedov phase, indicating a good agreement with the numerical solution.

detected by the present radio surveys such as Very Large Array Sky Survey (VLASS, Lacy et al., 2020), if it inhabits inside our galaxy.

Next we discuss the properties of the light curves of USSNR at larger ages (1000 years $\lesssim t \lesssim 10^5$ years). At $t \sim 1000$ years, the radio emission brightens by a factor to an order of magnitude compared to $t \sim 300$ years, even though the synchrotron emission in this phase is optically thin to self-absorption. This enhancement stems from the interaction between the SN ejecta and the relatively dense CSM located at $\sim$ 3–10 pc; a larger amount of the gas injection into the shocked region leads to a larger number of the synchrotron emitting electrons, resulting in a higher radio luminosity. In addition, the compression of the gas around the blastwave by the collision with the dense CSM brings about the further amplification of the magnetic field through the conservation of the magnetic flux (see Figure 5.8). This can also be a cause of the brightening of the radio luminosity. We note that this brightening is one of the characteristics of a USSNR associated with the time dependent mass loss driven by RLO, since a CSM with a simple power-law distribution cannot reproduce such a rise in radio luminosity in the optically-thin regime. Yet, the subsequent radio signals are fainter than those observed from the Galactic SNRs enumerated in Table 5.3. The stalled blastwave at $t \sim 300$ years can no longer execute efficient DSA any further. Even so, it is worth mentioning that SNRs discovered so far are biased towards bright objects. Deep surveys such as VLASS will have potential to uncover the population of the SNRs as faint as the aged USSNRs.

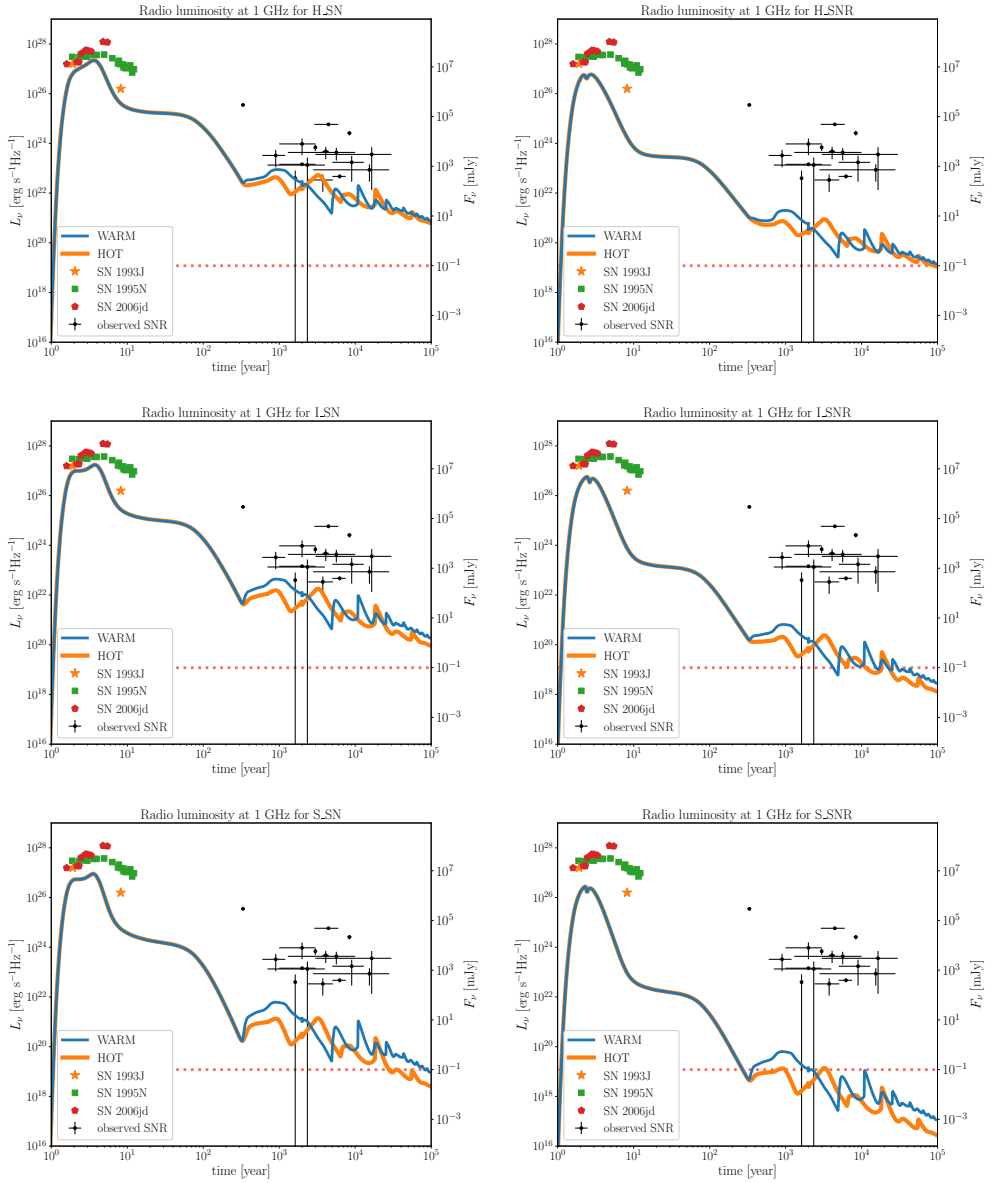

FIGURE 5.7: Long-term radio light curves at 1 GHz compared to radio observations of SNRs. Also plotted are the luminosities of SN 1993J (orange stars), SN 1995N (green squares), SN 2006jd (red pentagons), and Galactic SNRs listed in Table 5.3 (black points with error bars), estimated by the distances to each objects. The right y-axis stands for the observed flux densities with which the source with the luminosity shown in the left y-axis is observed at a distance $d = 10\,\mathrm{kpc}$. The red dotted line indicates the detection limit of VLASS (Lacy et al., 2020).

After the death of the blastwave, DSA will no longer be triggered, and the non-thermal emissions are forced to decline through adiabatic cooling. The timing of dominance by adiabatic cooling is roughly 1000 years, and is more-or-less determined by the location of the hot plasma (Figure 5.4). The hot plasma is formed by the interaction between the He-rich wind blown from the progenitor binary and the H-rich gas originated from the CE ejection or the uniform ISM. Our result implies that the location of the hot plasma in the CSM is key to determining the lifetime of the blastwave and hence the observable lifespan of the USSNR.

We also observe oscillations of the light curves at $t \gtrsim 10^4$ years. This is an one-dimensional artifact due to the reflective condition at the inner boundary of the simulation domain. As the reverse

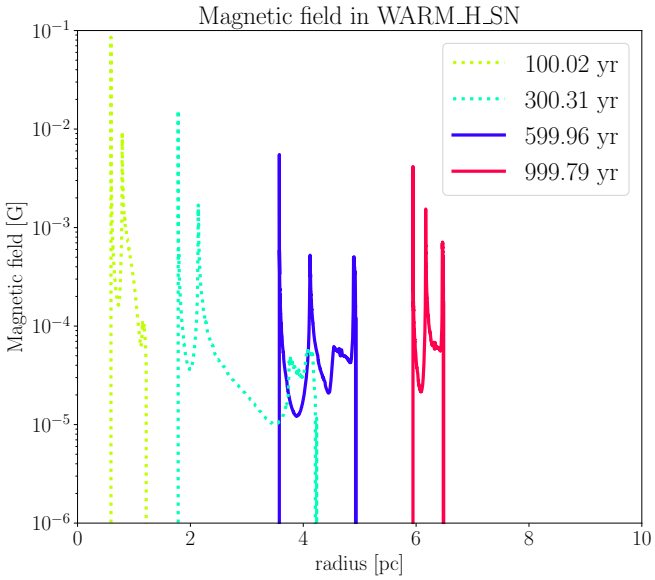

FIGURE 5.8: Time evolution of the profile of the magnetic field in the model 'WARM_H_SN'. The development of the strength of the magnetic field at the forward shock can be observed at $t \gtrsim 500$ years (solid), rather than before (dotted).

shock of the USSNR brings along an inward gas flow back to the explosion center, it rebounds back to the outer interacting region. Then the material around the shocked region is compressed, inducing an amplification of the magnetic field through flux conservation. A repeating occurrence of this inward and outward motion results in the oscillation of the radio luminosity in our models for the aged USSNR. In practice, multi-dimensional dynamics should suppress the motion of the gas described above due to a broken spherical symmetry. Even so, it can be noted that the global evolution of the radio luminosity of the aged USSNR roughly follows an adiabatic evolution when averaged over a longer timescale.

Figure 5.9 shows the time evolution of the surface brightness as a function of the sky projection angle. The model 'HOT' has fainter surface brightness and larger projection angles at which the surface brightness becomes maximum ($\theta_{\rm max}$) than those in the model 'WARM', because the model 'HOT' has a more extended CSM density structure than the model 'WARM' (see Figure 5.3). Yet the qualitative behavior of the surface brightness as a function of the sky projection angle is similar between these two models. $\theta_{\rm max}$ is mainly dictated by the location of the ISM wall, which prevents the gas in the shocked region from expanding any further outward (see Figure 5.5). As mentioned before, the hot plasma and the ISM cavity wall are shaped by the wind colliding with the CE and/or the ISM, which ultimately determines the detectability of the USSNR.

The evolution of the relation between the surface brightness and diameter of the USSNR can be assessed by the Σ-D diagram shown in Figure 5.10. For the same reason as the relation between Σ and $\theta_{\rm max}$ (Figure 5.9), the model 'HOT' has a fainter surface brightness and larger diameter than the model 'WARM'. This results in the lower right position of the evolutionary path of the model 'HOT' in the $\Sigma - D$ diagram. The magnitude of the surface brightness strongly depends on the parameters relevant to the DSA (i.e., p, ϵ_e, and ϵ_B). The surface brightness of the model appears to be relatively faint compared to those of the Galactic SNRs in the models such as 'H_SNR', 'I_SNR', 'S_SN', and 'S_SNR', in which the expected flux density of the radio emission from the aged USSNRs are approximately 0.1 mJy. This poses a challenge to detection and is consistent with the current non-detection of the SNR hosting a DNS binary in our Galaxy. On the other hand, in all of our models the USSNR diameter is in the order of 10 pc, which is also typical of the observed Galactic SNRs (Pavlović et al., 2013). We suggest that a faint surface brightness combined with

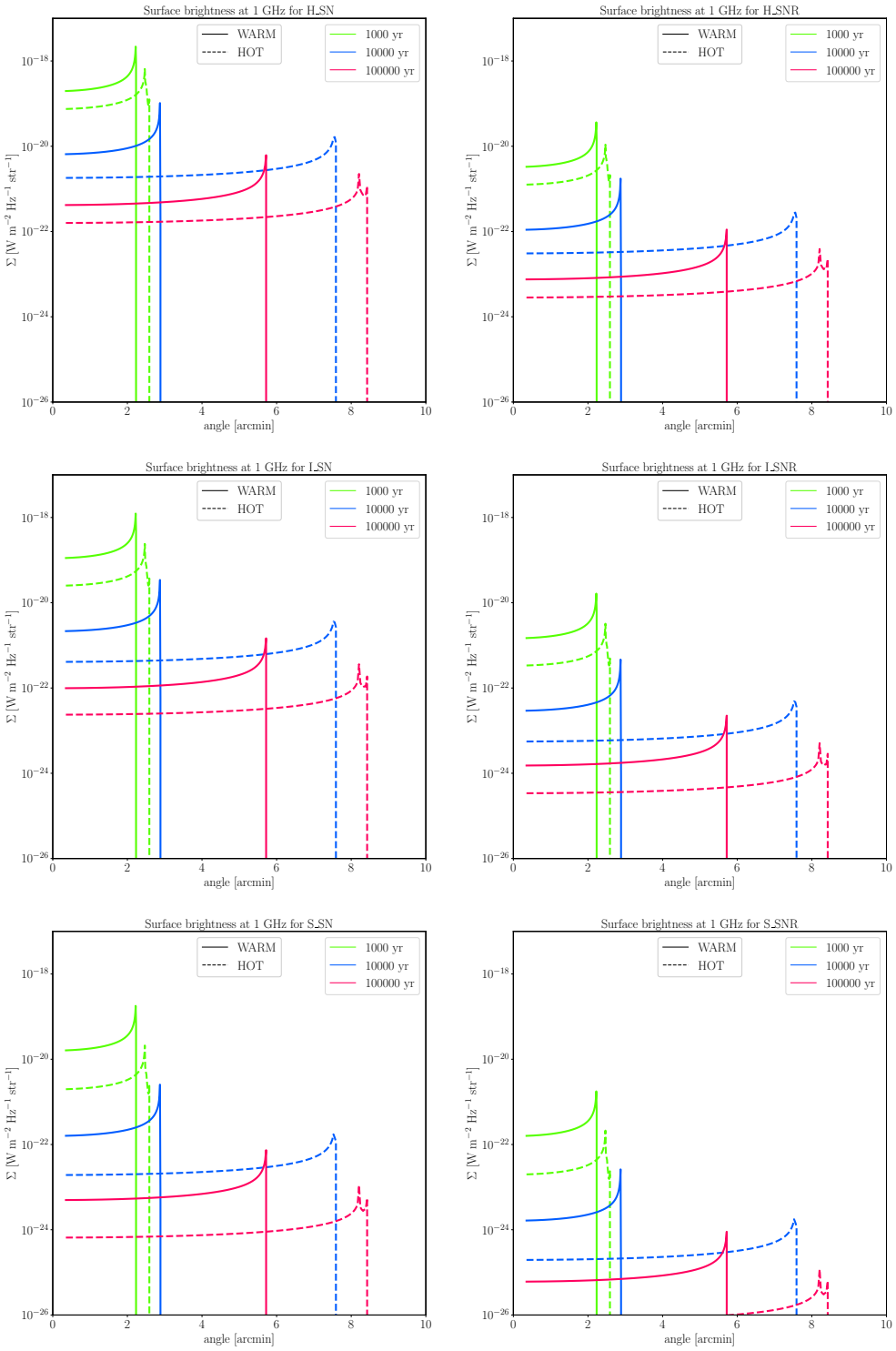

FIGURE 5.9: Time evolution of surface brightness as a function of sky projection angle at 1 GHz. The colors of the curves depict the time evolution.

a diameter $D \sim 10\,\mathrm{pc}$ can be a characteristics of a USSNR, and might be useful diagnostics for searching SNRs hosting a DNS binary.

At last we comment on the role of the ISM state on the radiative characteristics of the USSNRs. Comparisons of the solid and dashed lines in Figure 5.9 and Figure 5.10 demonstrate that the surface brightness of 'HOT' is fainter than that of 'WARM' at the same age. This is attributed to the fact that 'HOT' has a larger diameter and sky-projected angular size than 'WARM' and that the luminosities of these two models are similar to each other. Our simulations of CSM formation (Section 5.3) assume that the models 'WARM' and 'HOT' have the same thermal pressure but different densities in the initial profiles; we have shown that the model with a lower initial density leads to a larger diameter of the USSNR. Thus we conclude that the ISM density plays a role in determining the physical scale of the USSNR, which also affects the surface brightness.

5.5 discussion

5.5.1 The USSNR population

Equipped with our models, it is possible for us to make predictions for general properties of the USSNR population. Two timescales are important for characterizing the SNR population. One is the observable lifespan of the SNR, t_{snr}, defined here as the timescale in which the radio emission from the SNR can be detected. The other one is t_{sn}, the time interval between subsequent SNe or the inverse of the SN rate in a galaxy. The number of active SNRs can then be estimated as $t_{\mathrm{snr}}/t_{\mathrm{sn}}$. As for USSNRs, Hijikawa et al., 2019 predicted the event rate of USSNe as $510.88\,\mathrm{gal}^{-1}\,\mathrm{Myr}^{-1}$ in their feasible population synthesis model, leading to $t_{\mathrm{sn}} \sim 2 \times 10^3$ years[1] . For the SNR lifetime, $t_{\mathrm{snr}} \sim 100$–$10^5$ years can be implied from our models depending on the DSA efficiencies and the spectral index of accelerated electrons. Hence, the expected number of active USSNRs can be derived as $0.002 - 20$.

These estimations involve uncertainties from observational conditions (e.g., sensitivity) as well as the DSA parameters. Models with high DSA efficiencies or hard power-law index for the accelerated electrons (e.g., 'H_SN' and 'H_SNR') probably over-estimate the observable lifespan; typical shock acceleration efficiency constrained by SNR observations are usually found to be lower than those inferred from the observations of radio SNe (Lee, Ellison, and Nagataki, 2012). Moreover, it has been suggested that the spectral index of the accelerated particles in young SNRs can be modified and steepened by non-linear effects associated with magnetic field amplification in an efficient DSA and Alfvénic drift effect (Vink et al., 2006; Zirakashvili and Ptuskin, 2008; Yasuda and Lee, 2019), whereas in mature SNRs it tends to follow the prediction by the standard DSA (Reynoso and Walsh, 2015). The former is more appropriate for the situation considered in the present work, since our simulations indicate that the blastwave dies out at a young age in our CSM model. From these arguments, we can refer 'I_SNR' as our fiducial models for the evolution of a USSNR, which predicts an observable lifespan $t_{\mathrm{snr}} \sim 10^4$ years. Then we can further constrain the expected number of the observable USSNRs to be ~ 2. Since the detected number of the Galactic SNRs reaches ~ 400 (Green, 2019), the most probable fraction of USSNRs is then at most ~ 0.5 % of all active SNRs. We note however that the quantification of the observable lifespan of the USSNRs involves uncertainties and depends on the sensitivity of the detectors as well.

The expected number of active USSNRs in a galaxy, ~ 2, poses a severe challenge on the search of USSNRs. Radio observation facilities capable of deep surveys such as the Square Kilometre Arrays (SKA) are requisite to solving this difficulty. A Galactic SNR survey with a sensitivity ~ 0.1 mJy is one of the solutions to search for USSNRs, as well as for eliminating the possible bias

[1] Hijikawa et al., 2019 defined a USSN as an explosion of the star with its helium envelop mass less than $0.2\,M_\odot$, and an iPTF 14gqr-like USSN as a USSN with its ejecta mass $0.15 - 0.30\,M_\odot$ containing the helium component $0.003 - 0.01, M_\odot$. The event rate of USSNe is estimated to be ~ 10 times larger than that of iPTF 14gqr like USSNe, and we adopt the former value.

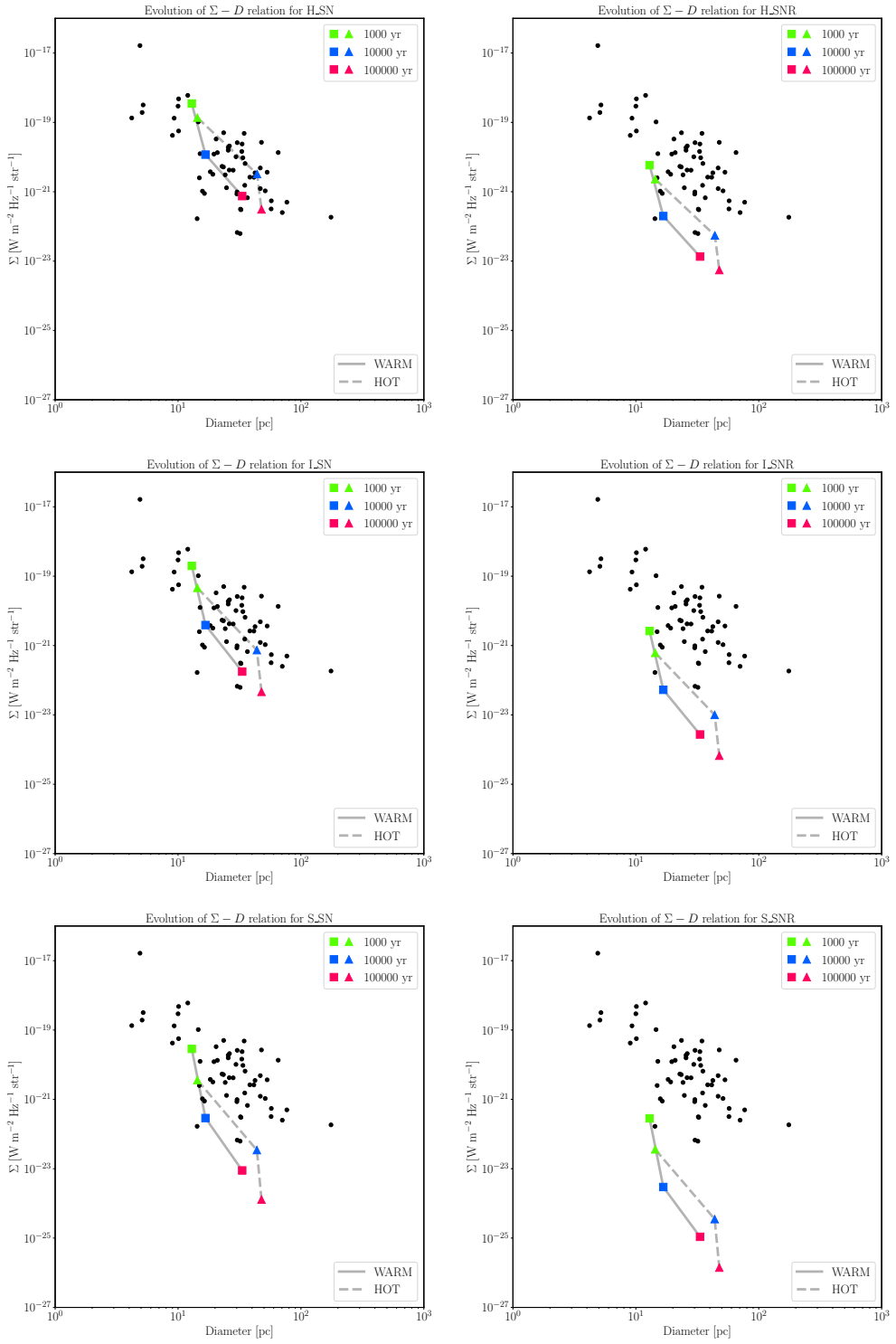

FIGURE 5.10: Time evolution of the surface brightness from our models are plotted as a function of the SNR diameter. The colored data points connected by solid lines show the time evolution for our model. The black points represent a selection of observed Galactic SNRs as summarized in Pavlović et al., 2013.

against faint SNRs. Another possible solution is to extend the search to other galaxies in the local group. SNRs producing radio emission brighter than $\sim 10^{21}(d/\mathrm{Mpc})^2(F_{\mathrm{lim}}/\mu\mathrm{Jy})$ erg s^{-1} Hz^{-1} in the local group can be detected by making use of the deepest observation projects, where F_{lim} is the maximum sensitivity of SKA (Braun et al., 2019). This sensitivity enables us to detect the radio emission from USSNRs (proved by the model 'H_SN' and 'H_SNR' in Figure 5.7). Assuming that the galaxies in the local group have the same proportion of USSNRs to all kinds of SNRs ($\sim 0.5\%$), this attempt might offer an opportunity to discover USSNRs.

5.5.2 General implications for stripped-envelope SNRs

We have shown that the blastwave of a USSNR suddenly loses its punch by being blunted by the hot plasma. The lifetime of the blastwave is limited to $\lesssim 10^3$ years, and the diameter is roughly a few 10 pc. The evolution of USSNRs is different from that elucidated classically. Generally, after the Sedov phase at $\sim 10^4$ years, radiative cooling from the swept ISM drains the internal energy away from the system, leading to a fast deceleration of the blastwave. Through the pressure-driven snowplow phase and momentum-driven snowplow phase, the SNR merge with the surrounding ISM at $t \sim 5 \times 10^5$ years (Cioffi, McKee, and Bertschinger, 1988). On the other hand, the evolution of USSNRs is heavily influenced by the non-uniform CSM density distribution and the presence of a hot plasma in the vicinity of the ISM wall, both of which are attributed to the wind driven by the binary interaction. The binary interaction is a key physical process in the evolutionary behaviors of USSNRs that deviate from the classical picture of SNR evolution.

Besides USSNe, it is widely believed that stripped-envelope SNe (Type IIb, Ib, and Ic SNe) are explosions of a massive star involved in binary interaction (e.g., Yoon, Woosley, and Langer, 2010; Ouchi and Maeda, 2017; Fang et al., 2019). It can be speculated that the evolution of SNRs originated from stripped-envelope SNe also deviates from the classical theory. Considering that some fraction of the observed SNe are classified as stripped-envelope SNe (Type IIb, Ib, and Ic SNe, Eldridge et al., 2013), it is natural that some of the confirmed SNRs in our Galaxy also come from a stripped-envelope SN origin. Previously, in terms of hydrodynamics, the effect of the wind bubble and its multi-dimensional behaviors on the subsequent SNR evolutions have been investigated by making use of simple models for stellar mass loading (Tenorio-Tagle et al., 1990; Tenorio-Tagle et al., 1991; Dwarkadas, 2005; Dwarkadas, 2007), but models for mass loss history based on detailed binary evolution calculations have not been incorporated. We thus suggest that such stripped-envelope SNRs should be modeled with the mass loss history of the progenitor binary taken into account for their surrounding CSM environments (e.g., Yasuda, Lee, and Maeda, 2021; Yasuda, Lee, and Maeda, 2022).

5.5.3 Radio emission from the hot plasma region

The velocity of the RLO wind is high, reaching $\sim 1000\,\mathrm{km\ s^{-1}}$. It is therefore possible that in the formation process of the hot plasma driven by the RLO wind, electron acceleration and magnetic field amplification can happen through the DSA mechanism. Such effects can contribute to the radio luminosity and surface brightness of the subsequent USSNRs, and thus an evaluation of this process is required. Our simulations show that the velocity of the RLO wind shock is $V_{\mathrm{sh,RLO}} \sim 200\,\mathrm{km\ s^{-1}}$. If we consider a hot ISM state ($T_{\mathrm{ism}} \sim 10^6$ K), the Mach number of the shock-wave launched by the RLO wind is in the order of unity. This indicates that the contribution from the hot plasma to the total flux of the radio emission from USSNRs is negligible in a hot ISM. On the other hand, in a warm ISM ($T_{\mathrm{ism}} \sim 10^4$ K), the Mach number is large enough to sustain DSA. The hot plasma can then be a potential emitter of synchrotron radiation. Assuming that the region is optically thin for synchrotron radiation, the radio luminosity is written as $L_\nu \sim 4\pi^2 R^3 j_{\nu,\mathrm{syn}}$, where R is the position of the RLO wind shock. Based on the formulae introduced in this study, the luminosity can be roughly estimated as $L_\nu \sim 10^{21} R_{20\mathrm{pc}}^3 \epsilon_{e,-3} \epsilon_{B,-2}^{3/4} \rho_{\mathrm{ism},-24}^{11/8} V_{\mathrm{sh,RLO},200}^{11/4}\,\mathrm{erg\,s^{-1}\,Hz^{-1}}$,

where $R_{20\mathrm{pc}} = R/(20\mathrm{pc}), \epsilon_{e,-3} = \epsilon_e/10^{-3}, \epsilon_{B,-2} = \epsilon_B/10^{-2}, \rho_{\mathrm{ism},-24} = \rho_{\mathrm{ism}}/(10^{-24}\,\mathrm{g\,cm^{-3}})$, and $V_{\mathrm{sh,RLO},200} = V_{\mathrm{sh,RLO}}/(200\mathrm{km\,s^{-1}})$. Comparing this magnitude to the models, we can see that this contribution from the hot plasma in a warm ISM is negligibly small with respect to the predicted luminosities of young USSNRs ($t \lesssim 1000$ years), but can be comparable to or even brighter than those of older USSNRs ($t \gtrsim 1000$ years), especially for the 'I_SNR', 'S_SN', and 'S_SNR' models. In addition, we note that at later ages, the hot plasma can experience a compression from the expanding remnant, and the radio emission contribution from the plasma can be boosted further by this compression. Although the primary purpose of our study is on the modeling of USSNRs, the above discussion further advocates the importance of taking into account the CSM environment formed by the pre-SN mass loss activity of the progenitor in the USSNR emission model.

5.5.4 Treatment of radiative cooling

Apart from the models presented so far, we have also performed extra simulations in which radiative cooling occurs in regions with a broader range of optical depths with $\tau < c/v$ to approximate the contribution of photon diffusion to the energy loss. While this approach overestimates the energy loss from radiative cooling, it is helpful nonetheless for assessing the robustness of our results. In these models with an enhanced energy loss, we found that the blastwave velocity is decreased by a few percent. This confirms that the impact of radiative cooling on the overall dynamics is small enough that it plays an insignificant role in the modeling of USSNRs.

5.5.5 Effects of non-linear diffusive shock acceleration

We have employed the simplified treatment of particle acceleration and magnetic field amplification. In our study, non-linear effects in DSA are not considered, and the contribution of the pressure from cosmic-rays and its feedback to the hydrodynamics are not included. These effects can soften the energy distribution of accelerated electrons and could decrease the luminosity of non-thermal emission, including X-rays and gamma-rays (e.g., Vink et al., 2006; Yasuda and Lee, 2019). Our estimate of the USSNR population can thus be altered by including such effects (see Section 5.5.1). On the other hand, however, the dynamics of the USSNR blastwave is mainly determined by the distribution of the CSM. The lifetime of the blastwave is mainly limited by its interaction with the hot plasma in the vicinity of the ISM wall formed by the pre-SN mass loss. Thus, improving the treatment of the microphysics in shock acceleration plays a secondary role in the observable lifespan of a USSNR.

5.5.6 Parametrizations of ϵ_e and E_{min}

There are two major simplifications in the parametrization for particle acceleration adopted in our study. First, some particle-in-cell simulations imply that the decrease of the Mach number (or the blastwave velocity) leads to a drop of the acceleration efficiency of protons (Caprioli and Spitkovsky, 2014a; Ha et al., 2018). This suggests the possibility that the acceleration efficiency of electrons also declines with a decreasing Mach number, while our study fixes ϵ_e at a constant value with time. Second, it is believed that electrons with momentum greater than $\sim \sqrt{m_e m_p} V_b$ follow a power-law distribution even below the relativistic regime. However, we have fixed the minimum energy of the power-law distribution at E_{min} in Equation (5.7) (see also Sironi and Giannios, 2013). Hence, a decrease of the blastwave velocity leads to an increase of the number of electrons with a momentum p_{mom} within $\sqrt{m_e m_p} V_b \lesssim p_{\mathrm{mom}} \lesssim E_{\mathrm{min}}/c$. This effect is not included in our models. In summary, our study is over-estimating the radio luminosities and the actual brightness of the USSNRs could be fainter if the above two factors are accounted for. However, the blastwave velocity in our calculations is in the order of $\sim 10^9 \mathrm{cm\,s^{-1}}$ and the Mach number is sufficiently high in the young phase before the collision with the hot plasma. In the late phase ($t \gtrsim 1000$ years), the

blastwave dies away rapidly. Therefore, the system considered in our study is not prone to the situation described above. Moreover, even if we include the two effects mentioned above in our modeling, the resulted radio luminosities should be fainter than those reported in Section 5.4.2, so that our conclusions on the characteristics and populations of USSNRs would not be affected qualitatively. Furthermore, we have examined two values for ϵ_e shown in Table 5.2, and believe that the effect of the microphysics noted here can be investigated within this parameter space.

5.5.7 Asphericity

An aspherical configuration of the CE component and its effect on the wind hydrodynamics can be important as well. For instance it has been suggested that the material released by the CE ejection tends to distribute along the equatorial plane (Iaconi et al., 2019). Thus if the CE component resides in the vicinity of the SN progenitor it could affect the subsequent wind hydrodynamics. The gas ejected through the CE interaction should concentrate on the equatorial plane of the binary, while in the polar direction a static ISM should dominate. Then, the propagation of the wind driven by the RLO in the direction of the equatorial plane and the polar axis are regulated by the interaction between the ISM with and without the CE component, respectively. Our simulations in Section 5.3 show that the effect of the presence of the CE component is not significant regardless of the state of the ISM. From this point of view, by assuming a spherically blown wind from the progenitor binary, we can qualitatively speculate that the effect of possible non-spherical CE distributions would not be important.

Besides, an anisotropy of the conformation of the wind can be expected to shape the non-spherical geometry of the CSM as proposed in the literature of Type IIn SNe (Patat et al., 2011; Katsuda et al., 2016; Kumar et al., 2019). It is worth investigating the multi-dimensional structures of the composed CSM taking into account the anisotropy of the circumstellar environment and the wind outflows. These aspherical configurations of the CSM can alter the properties of the radiation from the SNe or SNRs, which will be examined in detail in a future work (see also e.g., Kurfürst and Krtička, 2019; Suzuki, Moriya, and Takiwaki, 2019).

5.6 Summary

In this chapter, we have investigated the characteristics of a SNR hosting a DNS binary, which we have termed a USSNR, using a grid of numerical models. A USSN has been proposed to be a transient event preceding the formation of a DNS binary. Before the USSN, the He star envelope is stripped away by the companion neutron star and escapes the binary system. By employing the mass-transfer history presented by Tauris et al., 2013, we simulated the hydrodynamics of the wind expelled from the progenitor binary, and constructed the large-scale CSM structure around the USSN progenitor up to $\sim 100\,\mathrm{pc}$. A hot plasma is formed in the vicinity of the ISM wall, which is found to play a critical role in governing the lifetime of the blastwave of the USSNR.

We also examined the dynamical and radiative evolution of a USSNR by considering a progenitor surrounded by the CSM composed by our simulation. We found that within the first ~ 1000 years the blastwave traces the inner part of the CSM, producing a radio emission bright enough to be detected if the USSNR inhabits inside our Galaxy, though it is still fainter than those from typical SNRs. Once the blastwave collides with the hot plasma, it stalls rapidly and the radio luminosity also starts to decrease steadily. This dynamical behavior does not depend much on the strength of the CE ejection before the release of the helium gas from the progenitor binary. The surface brightness of the USSNR tends to be fainter than those of typical SNRs, while the diameter settles at $D \sim \mathcal{O}(10\,\mathrm{pc})$ similarly to the Galactic SNRs. Therefore, the USSNRs populate in the lower portion on the Σ-D diagram compared to the observed Galactic SNRs, and this can serve as a useful diagnostics for the search of a USSNR. We also confirmed that the initial ISM profile with

a lower density allows the USSNR to expand further, leading to a lower surface brightness and a larger diameter. Furthermore, we evaluated the observable lifespan of a USSNR to be $\sim 10^4$ years, defined as the time interval from the explosion to the point when the radio luminosity has declined beyond the detection limit of the present radio surveys. Combining the short observable lifespan of the USSNRs with the small event rate of USSNe, we conclude that the expected number of active USSNRs is less than one out of the observed 10^{2-3} SNRs, which is consistent with the current non-detection of a SNR hosting a DNS.

TABLE 5.3: Samples of the observed Galactic core-collapse SNRs

SNR name	Common name	Age [yr]	Distance [kpc]	Flux density [Jy]	References
G15.9+0.2		1000 - 3000	8.5 - 16.7	5.0	1
G34.7-0.4	W44	7900 - 8900	2.7 - 3.3	240	2, 3
G43.3-0.2	W49B	2900 - 6000	10.9 - 11.7	38	4, 5
G67.7+1.8		5000 - 13000	7.0 - 17.0	1	6
G111.7-2.1	CasA	316 - 352	3.3 - 3.7	2400	7
G189.1+3.0	IC 433	3000 - 30000	0.7 - 2.0	165	2, 8
G260.4-3.4	Puppis A	3700 - 4500	1.3 - 2.2	130	9
G266.2-1.2	Vela Jr	2400 - 5100	0.5 - 1.0	50	10
G291.0-0.1		1300 - 10000	3.5 - 6.0	16	11
G292.0+1.8		2930 - 3050	5.3 - 7.1	15	12
G296.1-0.5		2800 - 28000	2.0 - 4.0	8	13, 14
G308.4-1.4		5000 - 7500	9.1 - 10.7	0.4	15
G309.2-0.6		700 - 4000	2.0 - 6.0	7	16, 17
G330.2+1.0		1000 - 3000	4.6 - 5.2	5	18
G347.3-0.5		1624 - 1626	0.5 - 1.6	30	19, 20
G350.1-0.3		600 - 1200	4.5 - 9.0	6	21

The values of the radio flux are cited from Green, 2017. Notice that the explosion types of some of these samples have not been clarified. For details, see also Table 3 in Yasuda and Lee, 2019.

The references are as follows: (1) Sasaki et al., 2018, (2) Ackermann et al., 2013, (3) Uchida et al., 2012, (4) Moffett and Reynolds, 1994, (5) Zhu, Tian, and Zuo, 2014, (6) Hui and Becker, 2009, (7) DeLaney and Rudnick, 2003, (8) Ambrocio-Cruz et al., 2017, (9) Reynoso, Cichowolski, and Walsh, 2017, (10) Allen et al., 2015, (11) Roger et al., 1986, (12) Gaensler and Wallace, 2003, (13) Whiteoak and Green, 1996, (14) Gök and Sezer, 2012, (15) Prinz and Becker, 2012, (16) Gaensler, Green, and Manchester, 1998, (17) Rakowski, Hughes, and Slane, 2001, (18) Whiteoak and Green, 1996, (19) Ellison, Slane, and Gaensler, 2001, (20) Fukui et al., 2003, (21) Lovchinsky et al., 2011

Chapter 6

Summary

We have overviewed the modern approaches of the modeling of radio emission from SNe, based on the author's accomplishments. An SN is a terminal explosive phenomenon of massive stars in which the explosion properties as well as the way of the stellar evolution are imprinted. Giving a comprehensive answer to the question "what kinds of SN progenitors end their lives as what kinds of explosions, through what kinds of stellar evolutionary path" would be an ultimate goal for the research on SNe and the relevant transients. Among the various methods to investigate the characteristics of SNe, radio SNe traces the CSM around the progenitor. Given the velocity of the CSM, the length scale and the density scale of the CSM can be converted to the timescale of until the SN and the magnitude of the mass-loss episode, respectively. Therefore, theoretical modeling for radio SNe and SNRs can become a hint to reveal the mass-loss activity of the SN progenitor. As the mass-loss activity is believed to be one of the crucial process for the lives of stars, and there is even an implication of the association between the mass-loss activity and the internal nuclear reaction process or the dynamical motions (Maeda et al., 2021) (reference), studying radio SNe can contribute to the completion of updating the stellar evolution of massive stars in their final stage.

Radio emission from SNe can be basically modeled as synchrotron emission from electrons in the CSM accelerated by the SN shock. Once the SN shock propagates in the CSM, particle acceleration and magnetic field amplification would be driven through the mechanism such as diffusive shock acceleration (e.g., Drury, 1983), and the non-thermal component of electrons following the power-law distribution would be appearing in the energy density distribution of electrons attached from the thermal component. With the possible cooling break included, the power-law component of the electrons can power the radio emission in SNe. One of the points noted is that the emission mechanism of radio signals in SNe is considered to be unique to this SN-CSM interaction, and thus we can employ radio emission as robust diagnostics for the CSM properties.

We have conducted the systematic modeling of radio SNe for tens of observed samples to extract the statistical properties of SNe that produces bright radio emissions enough to be detected. We employed the unified method for modeling of radio SNe to exclude the dispersion of the way, and examined several combinations of parameter sets surveyed. We found that, as a overall tendencies, Type II SNe would be characterized by small but increasing mass-loss rate, while stripped-envelope SNe tend to have large but decreasing mass-loss rate with flat ejecta profile. Most of the SN samples prefer soft electron spectrum descibed by $p \gtrsim 3$. The most conservative survey exploring all of the responsible parameters (CSM structure, ejecta gradient, hardness of the electron spectrum, and the efficiencies of electron acceleration and magnetic field amplification) suggests the non-equipartition between the relativistic electrons and magnetic field, but the assumption of the equipartion with appropriate efficiencies ($\epsilon_e = \epsilon_B = 0.05$) can also reproduce good fitting scores, indicating that we can obtain poor information on plasma physics related to micro physics parameters such as ϵ_e and ϵ_B. In addition to such a statistical properties, we proposed some outlier objects that deviates from the overall trends (SN 2016X, SN 2001gd, and several SNe that have multiple solutions for the radio light curve).

We also attempted the investigation on an ultra-stripped SN in terms of its radio emission. An

ultra-stripped SN (USSN) is observationally classified as a rapidly-evolving transient with possibly strong Calcium-rich spectroscopic features, and its short variation timescale implies the small ejecta mass of the explosion itself. In the context of the formation of the binary neutron star, the USSN has been attracted the attention, because it would be a precursor event to the formation of the binary neutron star; the small ejecta mass can avoid the dynamical disruption of the binary system. Optical examinations of candidates for USSNe have succeeded in revealing the explosion properties itself, but they are indeed insensitive to the binary properties. Therefore observational diagnostics for the binary properties of the progenitor of USSNe has been required. We have focused on the mass-loss activity of the USSN progenitors, and analyzed the series of the stellar evolution model of the progenitor proposed by Tauris, Langer, and Podsiadlowski, 2015. We found that for events with small SN ejecta mass the mass-loss rate before the explosion is negatively correlated with the binary separation (Figure 4.2). Particularly we highlighted that some models of the USSN progenitor are characterized by the large mass-loss rate ($\dot{M} \simeq 10^{-2}\,M_{\odot}\,\mathrm{yr}^{-1}$) with small binary separation so that the remnant binary neutron star can make a coalescence within the cosmic age. This indicates the utility of the mass-loss rate inferred for USSNe as diagnostics for the properties of the progenitor binary. Here we have calculated the radio emission from USSNe, and showed that USSNe with bright radio emission can be associated with tight binary systems, proposing the radio observation as a method to infer the binary characteristics of the USSN progenitors. In addition, we have also suggested the observational strategy to practically detect the radio signals from USSNe; $\sim$ 1 month after the explosion for millimeters, or $\sim$ 1 year for centimeters.

Furthermore we have also investigated the subsequent long-term evolution of a USSN as an appearance of a supernova remnant, here termed as an USSNR. The remarkable point is that the progenitor experiences time-dependent mass-loss history driven by the binary interaction. Based on the hydrodynamical simulations we have shown that the CSM structure around the USSNR will be characterized by the non-smooth density distribution with the hot plasma developed at around the boundary between the CSM and the interstellar medium. Employing the constructed CSM model as an initial profile we have continued the hydrodynamical simulation of the expansion of the USSNR. We found that the blastwave in the USSNR will disappear at the collision with the hot plasma due to the rapid decrease in its Mach number as a unique phenomenon. We have also shown that the expected radio emission from USSNR (a light curve and the surface brightness) is fainter than those of typical Galactic SNRs, and possibly can serve as a characteristics of the USSNR. The importance of connecting the detailed mass-loss history of the SN progenitor with the evolution as an SNR has been highlighted in this work.

Appendix A

Variations in definitions of quantities in radio SN modeling

In this appendix section we describe the variations of definitions seen in the quantities used for calculating radio luminosity from SNe. As mentioned in Chapter 3, there is an inconsistent definitions of parameters among the literature of radio SNe. Here we briefly summarize the variations in the definitions of parameters. Readers are referred to Appendix of DeMarchi et al., 2022, for the detailed discussion.

The quantities whose definitions could vary among the studies are enumerated as follows:

1. Shock velocity $V_{\rm sh}$. The popular definition is the self-similar solution defined as $V_{\rm sh} = \frac{dR_{\rm sh}}{dt}$, proposed by Chevalier, 1982a; Chevalier, 1982b. This indicates that the velocity of the forward shock is higher than the head of the ejecta. Another manner is employed for example in Ho et al., 2019, in which the shock velocity is supposed to be $V_{\rm sh} \simeq \frac{R_{\rm sh}}{t}$. This assumption could be valid when the SN shock is plunging into the low-density circumstellar environment, corresponding to free-expansion phase, and also tested numerically in Maeda, 2013a. To consider the variation of the coefficient of the shock velocity, in this chapter we again define the SN shock velocity as

$$V'_{\rm sh} \equiv k_1 V_{\rm sh} = k_1 \frac{n-3}{n-s}\frac{R_{\rm sh}}{t}, \tag{A.1}$$

   where k_1 is a coefficient that can be varied according to the definition of the shock velocity.

2. Magnetic field B. Let us consider defining the energy density of magnetic field as

$$\frac{B'^2}{8\pi} \equiv k_2 \epsilon_B \rho_{\rm CSM} V'^2_{\rm sh}, \tag{A.2}$$

   where k_2 is a variable coefficient adapted to the definition manner of the authors, in a similar way to k_1. In Chapter 2 $\rho_{\rm CSM}$ was supposed to be the unshocked CSM density at the location of the SN shock, equivalent with $k_2 = 1$, and this definition was originally introduced by Chevalier, 1998. In fact, $k_2 = 4, 1/2, 9/8$, and $3/4$ are adopted in Matsuoka and Maeda, 2020, Murase et al., 2019, Petropoulou, Kamble, and Sironi, 2016, and Ho et al., 2019, respectively. The variation may be caused by the idea that the shock compression described by the Rankine-Hugoniot relation should be taken into consideration, or that the energy used for the amplification of the magnetic field should be originally from the "kinetic" energy of the SN shock... etc. The strength of the magnetic field is one of the sensitive quantities in the modeling of radio SNe, so we assess the effect of the choice of the coefficient on the resultant synchrotron characteristic values such as cooling timescales.

3. Synchrotron frequency $\nu_{\rm syn}$. As is known, synchrotron emission is radiation from a relativistic electron experiencing gyro motion around the magnetic field (Rybicki and Lightman,

1979), and the corresponding frequency of the gyration is described as $\omega_{\rm gyro} = \frac{eB}{\gamma m_e c}$. The frequency of photons emitted during the gyro motion suffers the beaming effect and the Doppler effect, resulting in the description of the observed frequency given as $\omega_{\rm syn} \sim \frac{\gamma^2 eB}{m_e c}$. We note that as the Lorentz factor of the electron increases, the gyro frequency decreases while the observed photon frequency increases.

For the differentiation, we denote the critical frequency deduced in equation 2.49 as ν_c, which depends also on the pitch angle. Besides, We define the synchrotron frequency newly as follows:

$$\nu'_{\rm syn} = k_3 \frac{\gamma^2 eB'}{m_e c}, \tag{A.3}$$

where k_3 is also a factor-variable coefficient. The popular choice is $k_3 = 1/(2\pi)$ to be consistent with the description of $\omega_{\rm syn}$. As seen later, this definition leads to the formula of the cooling break frequency commonly used to analyze the observational cooling features of radio SNe (e.g., Horesh et al., 2020). Another quantification is $k_3 \simeq 3/(4\pi)$, that can be compatible with the critical frequency ν_c appearing in the strict solution of the spectrum of the synchrotron emission (equation 2.49. See e.g., van Eerten, Zhang, and MacFadyen, 2010; Ryan et al., 2020). This definition actually involves the dependence of the pitch angle, though often abridged. Furthermore, the equation 36 in Chevalier and Fransson, 2017 defines the critical frequency as $k_3 = 1$, though it is stated that the average over the pitch angle is taken. The discussion in Chapter 2, 3 and 4 relies on this parametrization. Some algebra allows us to deduce the strict solution of the synchrotron emission from the single electron, and one of the confusing points is that the maximum flux of the synchrotron radiation from a single electron takes not at $\nu = \nu'_{\rm syn}$, but around $0.29\nu_{\rm c}$ (Figure 6.6 in Rybicki and Lightman, 1979). Even after taking the average of the pitch angle the tendency does not change (see Figure 13 in Aharonian, Kelner, and Prosekin, 2010). Regardless of this confusing point, $\nu'_{\rm syn}$ is used to convert the γ-dependent cooling timescales into frequency-dependent formulae as a representative of the "observed" synchrotron frequency.

Let us deduce the dependence of k_1, k_2, and k_3 on the critical quantities of radio SNe. We denote the newly defined quantities as Q', in contrast with the original descriptions given in Chapter 2. Equation A.2 deduces the modification of the magnetic field as follows:

$$B' = k_1 k_2^{1/2} B. \tag{A.4}$$

As for the synchrotron frequency, given the Lorentz factor of the electron γ the relation between the original and the newly defined synchrotron frequency can be written as

$$\nu'_{\rm syn} = k_1 k_2^{1/2} k_3 \nu_{\rm syn}. \tag{A.5}$$

If we regard the synchrotron frequency as the observed frequency ν, then we can derive the relationship of the Lorentz factor as follows:

$$\gamma' = k_1^{-1/2} k_2^{-1/4} k_3^{-1/2} \gamma. \tag{A.6}$$

Taking this conversion of the Lorentz factor into consideration, the cooling timescales can be rearranged as follows:

$$t'_{\rm syn} = k_1^{-3/2} k_2^{-3/4} k_3^{1/2} t_{\rm syn}, \tag{A.7}$$

$$t'_{\rm IC} = k_1^{1/2} k_2^{1/4} k_3^{1/2} t_{\rm IC}, \tag{A.8}$$

showing that the variation of the definition seen in equations A.1, A.2, and A.3 results in the variations of cooling timescales by factors. Furthermore, equating $t'_{\rm syn}$ or $t'_{\rm IC}$ with the dynamical timescale t enables us to deduce the modified cooling break frequency shown as follows:

$$\nu'_{\rm syn,break} = k_1^{-3} k_2^{-3/2} k_3 \nu_{\rm syn,break}, \tag{A.9}$$

$$\nu_{\rm IC,break} = k_1 k_2^{1/2} k_3 \nu_{\rm IC,break}. \tag{A.10}$$

Here, if we substitute $k_1 = k_2 = 1$ and $k_3 = 1/(2\pi)$, then the cooling break frequency presented in equation 2.33 would be scaled down by factors of 2π, and matches to the formula used in the other studies (e.g., Horesh et al., 2020). We do not go into the further discussion on the modification of the other quantities such as peak luminosity, but the above discussion would be enough to show that the variation of the definition of the parameters in the model of radio SNe has a risk to lead to the misinterpretation of the observational results by factors.

Appendix B

Derivation of 1σ volumes in N dimensional Gaussian density

In this appendix section we derive the proportion of the volume of the 1σ region in the $N(>2)$ dimensional Gaussian density distribution $F_N(\boldsymbol{x})$, which we define as follows:

$$F_N(\boldsymbol{x}) = \frac{1}{(2\pi\sigma^2)^{N/2}} \exp\left(-\sum_{i=1}^{N} \frac{(x_i-\mu_i)^2}{2\sigma^2}\right), \tag{B.1}$$

where x_i and μ_i denote the ith coordinate in this n dimensional space and its average, respectively. We apply the coordinate transformation from the cartesian to the polar coordinates as follows:

$$\begin{aligned}
x_1-\mu_1 &= r\cos\theta, && \text{(B.2)}\\
x_2-\mu_2 &= r\sin\theta\cos\phi_1, && \text{(B.3)}\\
x_3-\mu_3 &= r\sin\theta\sin\phi_1\cos\phi_2, && \text{(B.4)}\\
&\ldots && \text{(B.5)}\\
x_{N-1}-\mu_{N-1} &= r\prod_{i=1}^{N-2}\sin\phi_i, && \text{(B.6)}\\
x_N-\mu_N &= r\prod_{i=1}^{N-3}\sin\phi_i\cos\phi_{N-2}. && \text{(B.7)}
\end{aligned}$$

By definition $\sum_{i=1}^{N}(x_i-\mu_i)^2 = r^2$ is satisfied. The Jacobean relevant to this transformation is written down as

$$dx_1dx_2...dx_N = r^{N-1}(\sin\theta)^{N-2}\prod_{i=1}^{N-3}(\sin\phi_i)^{N-2-i}drd\theta d\phi_i d\phi_{N-2}. \tag{B.8}$$

We perform the multi-dimensional integration to deduce the volume of the N-dimensional supersphere with its radius R, which we will denote as $\mathcal{V}_N(R)$. The integral can be expressed as follows:

$$\begin{aligned}
\mathcal{V}_N(R) = \int_{r=0}^{R} \quad & \frac{1}{(2\pi\sigma^2)^{N/2}} \exp\left(-\sum_{i=1}^{N}\frac{r^2}{2\sigma^2}\right) r^{N-1}(\sin\theta)^{N-2} \\
\times \quad & \prod_{i=1}^{N-3}(\sin\phi_i)^{N-2-i}drd\theta d\phi_i d\phi_{N-2}. \qquad \text{(B.9)}
\end{aligned}$$

To make the displayed formalism simpler we introduce the normalized variable $y = r/(\sqrt{2}\sigma)$, and we set $R = \sigma$. Then this integral can be solved analytically. For $N = 3$, this can be arranged

into

$$\mathcal{V}_3(\sigma) = \frac{4}{\sqrt{\pi}} \int_0^{1/\sqrt{2}} y^2 e^{-y^2} dy = -\sqrt{\frac{2}{e\pi}} + \mathrm{erf}(1/\sqrt{2}) \approx 0.198, \tag{B.10}$$

where $\mathrm{erf}(x)$ is the error function. For $N = 6$, on the other hand, the integral can be written without using error function as follows:

$$\mathcal{V}_6(\sigma) = \int_0^{1/\sqrt{2}} y^5 e^{-y^2} dy = \left(1 - \frac{13}{8} e^{-1/2}\right) \approx 0.0144. \tag{B.11}$$

The value $\mathcal{V}_3(\sigma)$ and $\mathcal{V}_6(\sigma)$ are used to evaluate the alternative 1σ region around the best-fitted parameter sets shown in Section 3.4.

Appendix C

Physical parameters deduced from MCMC simulations

In this Appendix we leave a record of the deduced medians (termed as MED) and the best-fitted values (BEST) with relevant 1σ errors for each survey framework.

TABLE C.1: Best fitted parameters and medians of log q with 1σ credible intervals.

SN name	BEST in `Usual`	MED in `Usual`	BEST in `Astro`	MED in `Astro`	BEST in `All`	MED in `All`
SN 1983N	$1.65^{+0.288}_{-1.31}$	$0.778^{+0.556}_{-0.303}$	$0.811^{+0.0787}_{-0.0684}$	$0.809^{+0.134}_{-0.117}$	$-0.127^{+0.967}_{-0.134}$	$0.926^{+0.769}_{-0.753}$
SN 1987A	$-1.99^{+0.105}_{-0.00654}$	$-1.8^{+0.303}_{-0.202}$	$-1.48^{+0.0214}_{-0.0183}$	$-1.46^{+0.284}_{-0.234}$	$-0.462^{+0.204}_{-0.201}$	$-0.562^{+0.301}_{-0.318}$
SN 1990B	$1.7^{+0.0712}_{-0.0658}$	$1.64^{+0.101}_{-0.101}$	$-1.64^{+0.13}_{-0.126}$	$-1.6^{+0.318}_{-0.234}$	$0.877^{+0.282}_{-0.539}$	$0.375^{+0.602}_{-1.24}$
SN 1993J	$3.0^{+2.21e-06}_{-0.00116}$	$2.9^{+0.0505}_{-0.0505}$	$2.13^{+0.0078}_{-0.00736}$	$2.11^{+0.0167}_{-0.0167}$	$3.0^{+0.000217}_{-0.0117}$	$2.97^{+0.0167}_{-0.0334}$
SN 1998bw	$-1.21^{+0.0174}_{-0.0211}$	$-1.24^{+0.0505}_{-0.0505}$	$-1.18^{+0.0864}_{-0.116}$	$-1.21^{+0.117}_{-0.117}$	$-1.15^{+0.081}_{-0.111}$	$-1.18^{+0.1}_{-0.1}$
SN 2001gd	$2.33^{+0.164}_{-0.15}$	$2.29^{+0.152}_{-0.152}$	$2.26^{+0.0509}_{-0.0496}$	$2.25^{+0.0669}_{-0.0502}$	$3.0^{+0.00481}_{-0.0592}$	$2.87^{+0.0836}_{-0.184}$
SN 2001ig	$0.646^{+0.0594}_{-0.038}$	$0.626^{+0.0505}_{-0.0505}$	$1.34^{+0.0253}_{-0.0231}$	$1.33^{+0.0502}_{-0.0502}$	$0.382^{+0.0348}_{-0.0302}$	$0.408^{+0.0669}_{-0.0669}$
SN 2002ap	$0.42^{+0.251}_{-0.253}$	$0.525^{+0.253}_{-0.253}$	$-1.06^{+0.0914}_{-0.0939}$	$-1.01^{+0.87}_{-0.318}$	$0.962^{+0.621}_{-0.122}$	$0.926^{+0.936}_{-1.24}$
SN 2003L	$2.24^{+0.0377}_{-0.0395}$	$2.09^{+0.152}_{-0.96}$	$0.897^{+0.046}_{-0.0476}$	$0.876^{+0.0669}_{-0.0669}$	$0.351^{+0.224}_{-0.197}$	$1.04^{+0.184}_{-0.719}$
SN 2003bg	$1.43^{+0.00554}_{-0.00461}$	$1.38^{+0.101}_{-0.0505}$	$1.12^{+0.0223}_{-0.0247}$	$1.11^{+0.0334}_{-0.0502}$	$0.611^{+0.0262}_{-0.018}$	$0.625^{+0.452}_{-0.0502}$
SN 2004C	$2.24^{+0.111}_{-0.0996}$	$2.19^{+0.152}_{-0.101}$	$3.0^{+0.000635}_{-0.0298}$	$1.56^{+1.35}_{-0.268}$	$3.0^{+9.77e-05}_{-0.0105}$	$2.97^{+0.0167}_{-0.0334}$
SN 2004cc	$2.08^{+0.0862}_{-0.0846}$	$2.04^{+0.101}_{-0.152}$	$2.08^{+0.0084}_{-0.0102}$	$2.06^{+0.0502}_{-0.0669}$	$1.31^{+0.126}_{-0.144}$	$1.39^{+0.251}_{-0.268}$
SN 2004dj	$0.598^{+0.0846}_{-0.0764}$	$0.576^{+0.101}_{-0.101}$	$1.38^{+0.0306}_{-0.0358}$	$1.36^{+0.1}_{-0.1}$	$1.29^{+0.475}_{-0.172}$	$1.75^{+0.585}_{-0.468}$
SN 2004dk	$1.1^{+0.11}_{-0.113}$	$1.08^{+0.101}_{-0.152}$	$-0.345^{+0.0522}_{-0.0479}$	$-0.361^{+0.0669}_{-0.0502}$	$1.38^{+0.109}_{-0.286}$	$1.16^{+0.284}_{-0.351}$
SN 2004gq	$0.428^{+0.0157}_{-0.00962}$	$0.424^{+1.41}_{-0.101}$	$0.625^{+0.0375}_{-0.041}$	$0.609^{+0.0836}_{-0.0836}$	$2.55^{+0.0882}_{-0.595}$	$0.492^{+1.3}_{-0.769}$
SN 2007bg	$3.0^{+0.0}_{-1.7}$	$1.33^{+1.21}_{-0.152}$	$-1.4^{+0.687}_{-0.0486}$	$-0.746^{+0.234}_{-0.201}$	$2.99^{+0.0122}_{-0.193}$	$2.77^{+0.134}_{-0.251}$
SN 2007gr	$3.0^{+0.000206}_{-0.0175}$	$2.9^{+0.0505}_{-0.101}$	$-0.344^{+0.0464}_{-0.0492}$	$-0.278^{+2.93}_{-0.284}$	$0.378^{+0.204}_{-0.407}$	$0.191^{+0.485}_{-0.635}$
SN 2007uy	$3.0^{+0.000197}_{-0.02}$	$2.9^{+0.0505}_{-0.0505}$	$0.941^{+0.0545}_{-0.0603}$	$0.91^{+0.0836}_{-0.134}$	$2.98^{+0.0128}_{-1.14}$	$1.76^{+0.803}_{-0.819}$
SN 2008D	$0.294^{+0.0356}_{-0.00799}$	$0.273^{+0.101}_{-0.101}$	$0.453^{+0.0268}_{-0.0251}$	$0.441^{+0.0669}_{-0.0669}$	$1.78^{+0.0264}_{-0.139}$	$1.68^{+0.117}_{-0.184}$
SN 2008ax	$-0.282^{+0.0392}_{-0.0324}$	$-0.333^{+0.0505}_{-0.0505}$	$0.441^{+0.025}_{-0.0238}$	$0.425^{+0.1}_{-0.0836}$	$-0.567^{+0.0871}_{-0.0338}$	$-0.311^{+0.535}_{-0.251}$
SN 2009bb	$1.32^{+0.0364}_{-0.0371}$	$1.23^{+0.101}_{-0.0505}$	$-1.67^{+0.103}_{-0.1}$	$-1.62^{+0.385}_{-0.234}$	$-1.95^{+0.191}_{-0.0462}$	$-1.7^{+0.485}_{-0.201}$
PTF11qcj	$1.6^{+0.163}_{-0.156}$	$1.54^{+0.152}_{-0.152}$	$-0.645^{+0.103}_{-0.0885}$	$-0.662^{+0.1}_{-0.117}$	$1.25^{+0.101}_{-0.125}$	$1.21^{+0.134}_{-0.151}$
SN 2011dh	$0.333^{+0.0131}_{-0.0145}$	$0.273^{+0.0505}_{-0.0505}$	$0.939^{+0.0164}_{-0.0172}$	$0.926^{+0.0334}_{-0.0334}$	$0.0106^{+0.138}_{-0.0147}$	$0.124^{+0.151}_{-0.1}$
SN 2011ei	$3.0^{+0.00131}_{-0.0695}$	$2.8^{+0.101}_{-2.17}$	$0.336^{+0.0466}_{-0.0514}$	$0.324^{+0.134}_{-0.117}$	$-0.475^{+0.245}_{-0.105}$	$-0.294^{+0.468}_{-0.251}$
SN 2011hs	$0.422^{+0.071}_{-0.0135}$	$0.424^{+0.101}_{-0.0505}$	$1.31^{+0.0554}_{-0.0446}$	$1.29^{+0.1}_{-0.0669}$	$1.76^{+0.196}_{-0.165}$	$1.75^{+0.167}_{-0.184}$
SN 2012ap	$2.0^{+0.0393}_{-0.0572}$	$1.89^{+0.101}_{-0.101}$	$-0.515^{+0.111}_{-0.108}$	$-0.528^{+0.117}_{-0.117}$	$0.912^{+0.134}_{-0.56}$	$0.559^{+0.502}_{-0.836}$
SN 2012au	$2.29^{+0.124}_{-1.87}$	$0.424^{+1.57}_{-0.101}$	$-0.129^{+0.0738}_{-0.0756}$	$-0.144^{+0.184}_{-0.151}$	$2.23^{+0.153}_{-1.15}$	$1.21^{+0.803}_{-0.987}$
SN 2012aw	$0.908^{+0.147}_{-0.142}$	$0.879^{+0.152}_{-0.152}$	$1.22^{+0.0239}_{-0.0231}$	$1.21^{+0.0502}_{-0.0669}$	$0.736^{+0.624}_{-0.318}$	$1.11^{+0.535}_{-0.485}$
SN 2013df	$2.99^{+0.00617}_{-0.0426}$	$2.9^{+0.0505}_{-0.0505}$	$1.52^{+0.0269}_{-0.0246}$	$1.49^{+0.0502}_{-0.0334}$	$3.0^{+0.00452}_{-0.0747}$	$2.92^{+0.0502}_{-0.117}$
AT2014ge	$2.65^{+0.0623}_{-0.0728}$	$2.55^{+0.152}_{-1.57}$	$0.397^{+0.0406}_{-0.0382}$	$0.391^{+0.0502}_{-0.0669}$	$0.459^{+0.426}_{-0.684}$	$1.01^{+0.452}_{-0.769}$
SN 2016X	$0.557^{+0.0473}_{-0.0411}$	$0.525^{+0.0505}_{-0.0505}$	$1.48^{+0.0343}_{-0.037}$	$1.46^{+0.0836}_{-0.0836}$	$2.99^{+0.0123}_{-1.44}$	$2.03^{+0.585}_{-0.836}$
SN 2016coi	$1.21^{+0.0408}_{-0.0345}$	$1.18^{+0.101}_{-0.101}$	$0.978^{+0.0482}_{-0.0567}$	$0.96^{+0.117}_{-0.1}$	$1.81^{+0.465}_{-0.304}$	$1.76^{+0.452}_{-0.468}$
SN 2016gkg	$2.7^{+0.0541}_{-0.0517}$	$2.65^{+0.0505}_{-0.101}$	$1.03^{+0.0248}_{-0.0257}$	$1.01^{+0.0334}_{-0.0334}$	$0.117^{+0.0526}_{-0.0419}$	$0.174^{+0.1}_{-0.0836}$
SN 2020oi	$1.05^{+0.085}_{-0.0886}$	$0.98^{+0.101}_{-0.0505}$	$0.731^{+0.0351}_{-0.0304}$	$0.726^{+0.0334}_{-0.0502}$	$0.179^{+0.0903}_{-0.0709}$	$1.95^{+0.217}_{-1.61}$

TABLE C.2: Best fitted parameters and medians of log ϵ_e with 1σ credible intervals.

SN name	BEST in `Usual`	MED in `Usual`	BEST in `Plasma`	MED in `Plasma`	BEST in `All`	MED in `All`
SN 1983N	$-0.571^{+0.16}_{-1.83}$	$-1.97^{+1.06}_{-0.354}$	$-1.6^{+0.0399}_{-0.0812}$	$-1.67^{+0.0505}_{-0.101}$	$-0.952^{+0.24}_{-0.0902}$	$-1.52^{+0.819}_{-1.82}$
SN 1987A	$-0.00676^{+0.00194}_{-0.0402}$	$-0.202^{+0.101}_{-0.808}$	$-0.185^{+0.181}_{-1.37}$	$-1.46^{+0.505}_{-0.303}$	$-0.0339^{+0.0317}_{-0.239}$	$-0.351^{+0.234}_{-0.502}$
SN 1990B	$-0.201^{+0.028}_{-0.0302}$	$-0.253^{+0.0505}_{-0.101}$	$-0.00115^{+0.000839}_{-0.0773}$	$-0.152^{+0.0505}_{-0.101}$	$-1.57^{+0.167}_{-0.534}$	$-1.57^{+0.97}_{-0.518}$
SN 1993J	$-1.65^{+0.0185}_{-0.0167}$	$-1.72^{+0.0505}_{-0.0505}$	$-2.43^{+0.0172}_{-0.0185}$	$-2.47^{+0.0505}_{-0.0505}$	$-0.414^{+0.0771}_{-0.0836}$	$-0.435^{+0.0669}_{-0.0836}$
SN 1998bw	$-0.117^{+0.00752}_{-0.00907}$	$-0.152^{+0.0505}_{-0.0505}$	$-0.00969^{+0.000837}_{-0.00137}$	$-5.0^{+4.95}_{-0.0}$	$-0.108^{+0.0316}_{-0.036}$	$-0.134^{+0.0334}_{-0.0334}$
SN 2001gd	$-0.73^{+0.0932}_{-0.108}$	$-0.808^{+0.101}_{-0.101}$	$-1.38^{+0.148}_{-0.112}$	$-1.41^{+0.152}_{-0.152}$	$-0.558^{+0.113}_{-0.0997}$	$-0.569^{+0.184}_{-0.184}$
SN 2001ig	$-0.056^{+0.0127}_{-0.0117}$	$-0.101^{+0.0505}_{-0.0505}$	$-0.000111^{+1.37e-05}_{-0.00239}$	$-0.101^{+0.0505}_{-0.0}$	$-0.847^{+0.0403}_{-0.0125}$	$-0.836^{+0.0669}_{-0.0502}$
SN 2002ap	$-5.0^{+0.195}_{-0.0021}$	$-4.8^{+0.404}_{-0.152}$	$-3.44^{+0.821}_{-1.47}$	$-4.6^{+0.505}_{-0.303}$	$-4.73^{+0.895}_{-0.27}$	$-4.23^{+1.4}_{-0.552}$
SN 2003L	$-0.000555^{+2.91e-05}_{-0.00296}$	$-0.808^{+0.707}_{-0.152}$	$-0.53^{+0.028}_{-0.0245}$	$-0.606^{+0.0505}_{-0.0}$	$-0.459^{+0.0727}_{-0.0763}$	$-1.47^{+0.987}_{-0.585}$
SN 2003bg	$-1.4^{+0.00171}_{-0.00445}$	$-1.46^{+0.101}_{-0.0505}$	$-1.12^{+0.0147}_{-0.0168}$	$-1.16^{+0.0505}_{-0.0505}$	$-1.49^{+0.0118}_{-0.00792}$	$-1.49^{+0.1}_{-0.0836}$
SN 2004C	$-0.834^{+0.0279}_{-0.0253}$	$-0.859^{+0.0505}_{-0.0505}$	$-0.108^{+0.0139}_{-1.11}$	$-0.758^{+0.253}_{-0.101}$	$-0.000269^{+0.000252}_{-0.0031}$	$-0.0502^{+0.0167}_{-0.0502}$
SN 2004cc	$-3.24^{+0.0788}_{-0.082}$	$-3.28^{+0.101}_{-0.152}$	$-1.19^{+0.85}_{-0.749}$	$-1.57^{+0.556}_{-0.455}$	$-1.12^{+0.141}_{-0.093}$	$-1.2^{+0.167}_{-0.167}$
SN 2004dj	$-1.62^{+0.126}_{-0.133}$	$-1.67^{+0.101}_{-0.101}$	$-2.14^{+0.13}_{-0.124}$	$-2.17^{+0.101}_{-0.152}$	$-3.24^{+0.42}_{-0.495}$	$-3.63^{+0.635}_{-0.669}$
SN 2004dk	$-1.1^{+0.0622}_{-0.0463}$	$-1.11^{+0.0505}_{-0.101}$	$-1.75^{+0.0582}_{-0.0395}$	$-1.77^{+0.0505}_{-0.101}$	$-1.31^{+0.0338}_{-1.74}$	$-2.94^{+0.669}_{-0.452}$
SN 2004gq	$-1.54^{+0.00747}_{-0.0147}$	$-1.57^{+0.152}_{-0.101}$	$-1.63^{+0.0334}_{-0.0233}$	$-1.67^{+0.0505}_{-0.0505}$	$-0.62^{+0.0628}_{-0.249}$	$-0.552^{+0.301}_{-0.936}$
SN 2007bg	$-1.47^{+0.0517}_{-0.045}$	$-1.46^{+1.11}_{-0.101}$	$-0.639^{+0.0672}_{-0.0771}$	$-0.707^{+0.0505}_{-0.0505}$	$-0.611^{+0.426}_{-1.24}$	$-1.84^{+0.552}_{-0.401}$
SN 2007gr	$-3.11^{+0.0186}_{-0.115}$	$-3.23^{+0.101}_{-0.152}$	$-2.92^{+0.752}_{-1.37}$	$-4.14^{+0.556}_{-0.404}$	$-4.98^{+0.934}_{-0.0179}$	$-3.61^{+1.3}_{-1.0}$
SN 2007uy	$-2.76^{+0.136}_{-0.127}$	$-2.83^{+0.101}_{-0.152}$	$-1.8^{+0.763}_{-0.794}$	$-2.42^{+0.505}_{-0.404}$	$-2.27^{+1.16}_{-0.266}$	$-1.12^{+0.702}_{-0.786}$
SN 2008D	$-1.92^{+0.0146}_{-0.0144}$	$-1.97^{+0.101}_{-0.0505}$	$-1.95^{+0.0192}_{-0.00754}$	$-2.02^{+0.0505}_{-0.0}$	$-4.03^{+0.302}_{-0.015}$	$-3.88^{+0.268}_{-0.184}$
SN 2008ax	$-0.0848^{+0.0151}_{-0.017}$	$-0.152^{+0.0505}_{-0.0505}$	$-0.000104^{+7.22e-06}_{-0.00151}$	$-0.101^{+0.0505}_{-0.0505}$	$-0.92^{+0.0199}_{-0.0335}$	$-1.14^{+0.284}_{-0.853}$
SN 2009bb	$-0.0409^{+0.0168}_{-0.0166}$	$-0.101^{+0.0505}_{-0.0505}$	$-1.21^{+0.0474}_{-0.0402}$	$-1.26^{+0.0505}_{-0.0505}$	$-0.0615^{+0.0358}_{-0.218}$	$-0.251^{+0.151}_{-0.251}$
PTF11qcj	$-0.4^{+0.132}_{-0.124}$	$-0.455^{+0.152}_{-0.152}$	$-0.853^{+0.00684}_{-0.00789}$	$-0.909^{+0.0505}_{-0.0505}$	$-0.0433^{+0.037}_{-0.326}$	$-0.418^{+0.268}_{-0.301}$
SN 2011dh	$-0.765^{+0.021}_{-0.0189}$	$-0.808^{+0.0505}_{-0.0505}$	$-0.00016^{+0.000118}_{-0.00432}$	$-0.101^{+0.0505}_{-0.0}$	$-1.03^{+0.0368}_{-0.0917}$	$-1.1^{+0.0836}_{-0.151}$
SN 2011ei	$-0.937^{+0.0964}_{-0.0457}$	$-1.01^{+0.152}_{-0.859}$	$-0.154^{+0.15}_{-1.71}$	$-1.82^{+0.556}_{-0.404}$	$-1.05^{+0.0599}_{-0.0185}$	$-0.97^{+0.134}_{-0.167}$
SN 2011hs	$-0.62^{+0.0181}_{-0.0121}$	$-0.657^{+0.0505}_{-0.0505}$	$-0.224^{+0.0193}_{-0.00808}$	$-0.253^{+0.0505}_{-0.0505}$	$-3.17^{+0.274}_{-0.192}$	$-3.16^{+0.268}_{-0.217}$
SN 2012ap	$-0.467^{+0.0153}_{-0.0515}$	$-0.556^{+0.0505}_{-0.152}$	$-2.11^{+0.0292}_{-0.0372}$	$-2.17^{+0.0505}_{-0.0505}$	$-4.22^{+1.76}_{-0.0325}$	$-2.42^{+1.0}_{-1.14}$
SN 2012au	$-0.336^{+0.0447}_{-1.77}$	$-2.12^{+1.52}_{-0.101}$	$-2.16^{+0.0123}_{-0.0415}$	$-2.22^{+0.0505}_{-0.0505}$	$-0.342^{+0.338}_{-0.186}$	$-0.368^{+0.217}_{-0.368}$
SN 2012aw	$-0.277^{+0.103}_{-0.0977}$	$-0.354^{+0.152}_{-0.101}$	$-0.804^{+0.161}_{-0.177}$	$-0.859^{+0.152}_{-0.202}$	$-0.0135^{+0.0104}_{-0.19}$	$-0.234^{+0.151}_{-0.268}$
SN 2013df	$-3.44^{+0.0281}_{-0.0192}$	$-3.48^{+0.0505}_{-0.0}$	$-2.05^{+0.572}_{-0.598}$	$-2.47^{+0.404}_{-0.354}$	$-2.42^{+0.28}_{-0.277}$	$-2.49^{+0.268}_{-0.268}$
AT2014ge	$-0.535^{+0.0416}_{-0.0297}$	$-0.657^{+0.202}_{-1.92}$	$-2.23^{+0.0613}_{-0.0393}$	$-2.27^{+0.0505}_{-0.0505}$	$-0.00413^{+0.0}_{-0.248}$	$-1.0^{+0.234}_{-0.368}$
SN 2016X	$-0.0667^{+0.0129}_{-0.0148}$	$-0.101^{+0.0505}_{-0.0505}$	$-0.0162^{+0.000921}_{-0.00246}$	$-0.101^{+0.0505}_{-0.0505}$	$-4.13^{+1.3}_{-0.565}$	$-2.86^{+1.49}_{-1.12}$
SN 2016coi	$-2.12^{+0.0424}_{-0.0313}$	$-2.12^{+0.0505}_{-0.101}$	$-1.75^{+1.1}_{-1.06}$	$-2.58^{+0.556}_{-0.404}$	$-2.43^{+0.624}_{-0.157}$	$-2.12^{+0.552}_{-0.619}$
SN 2016gkg	$-0.000111^{+4.08e-05}_{-0.0111}$	$-0.101^{+0.0505}_{-0.0}$	$-0.000147^{+6.49e-05}_{-0.00604}$	$-0.101^{+0.0505}_{-0.0}$	$-0.897^{+0.0783}_{-0.0413}$	$-0.886^{+0.1}_{-0.1}$
SN 2020oi	$-2.3^{+0.0825}_{-0.0834}$	$-2.37^{+0.101}_{-0.0505}$	$-2.05^{+0.018}_{-0.028}$	$-2.12^{+0.0505}_{-0.0505}$	$-1.58^{+0.0537}_{-0.0228}$	$-3.53^{+1.81}_{-0.284}$

TABLE C.3: Best fitted parameters and medians of log ϵ_B with 1σ credible intervals.

SN name	BEST in `Usual`	MED in `Usual`	BEST in `Plasma`	MED in `Plasma`	BEST in `All`	MED in `All`
SN 1983N	$-3.48^{+3.48}_{-0.551}$	$-1.01^{+0.606}_{-1.87}$	$-0.0115^{+0.00218}_{-0.0369}$	$-0.101^{+0.0505}_{-0.0505}$	$-0.165^{+0.103}_{-1.73}$	$-1.04^{+0.686}_{-1.1}$
SN 1987A	$-1.81^{+0.087}_{-0.156}$	$-1.87^{+0.152}_{-0.202}$	$-5.0^{+0.038}_{-0.000612}$	$-5.0^{+0.0505}_{-0.0}$	$-4.99^{+0.33}_{-0.0129}$	$-4.62^{+0.569}_{-0.268}$
SN 1990B	$-5.0^{+0.0243}_{-0.000241}$	$-4.95^{+0.101}_{-0.0505}$	$-3.08^{+0.268}_{-0.242}$	$-3.08^{+0.253}_{-0.202}$	$-4.98^{+0.842}_{-0.0105}$	$-3.7^{+1.52}_{-0.87}$
SN 1993J	$-2.12^{+0.021}_{-0.0214}$	$-2.17^{+0.101}_{-0.101}$	$-0.00163^{+5.48e-05}_{-0.000723}$	$-0.101^{+0.0505}_{-0.0505}$	$-3.35^{+0.0312}_{-0.0334}$	$-3.34^{+0.0502}_{-0.0502}$
SN 1998bw	$-0.625^{+0.0279}_{-0.0252}$	$-0.657^{+0.0505}_{-0.0505}$	$-1.66^{+0.0337}_{-0.0386}$	$-1.72^{+0.0505}_{-0.0505}$	$-0.659^{+0.107}_{-0.136}$	$-0.702^{+0.117}_{-0.134}$
SN 2001gd	$-2.16^{+0.286}_{-0.294}$	$-2.22^{+0.354}_{-0.253}$	$-1.51^{+0.0988}_{-0.0937}$	$-1.57^{+0.101}_{-0.101}$	$-3.26^{+0.0857}_{-0.0928}$	$-3.16^{+0.234}_{-0.184}$
SN 2001ig	$-0.917^{+0.0758}_{-0.105}$	$-0.96^{+0.0505}_{-0.101}$	$-3.61^{+0.0877}_{-0.0605}$	$-3.64^{+0.0505}_{-0.101}$	$-0.0671^{+0.00209}_{-0.0534}$	$-0.184^{+0.1}_{-0.184}$
SN 2002ap	$-0.473^{+0.347}_{-0.446}$	$-0.909^{+0.455}_{-0.657}$	$-0.004^{+0.00395}_{-0.113}$	$-0.152^{+0.0505}_{-0.152}$	$-2.37^{+0.556}_{-1.5}$	$-2.26^{+1.49}_{-1.64}$
SN 2003L	$-2.9^{+0.0328}_{-0.0289}$	$-2.83^{+2.58}_{-0.253}$	$-0.152^{+0.00984}_{-0.0123}$	$-0.202^{+0.0505}_{-0.0505}$	$-1.78^{+0.484}_{-0.26}$	$-1.32^{+0.686}_{-0.518}$
SN 2003bg	$-0.0175^{+0.00023}_{-0.00277}$	$-0.202^{+0.101}_{-0.152}$	$-0.0339^{+0.00133}_{-0.00122}$	$-0.101^{+0.0505}_{-4.9}$	$-0.016^{+0.00178}_{-0.0249}$	$-0.201^{+0.134}_{-2.96}$
SN 2004C	$-0.558^{+0.168}_{-0.192}$	$-0.657^{+0.202}_{-0.202}$	$-0.667^{+0.133}_{-0.144}$	$-0.303^{+0.152}_{-0.556}$	$-4.42^{+0.0387}_{-0.0305}$	$-4.4^{+0.0669}_{-0.0669}$
SN 2004cc	$-1.04^{+0.196}_{-0.185}$	$-1.11^{+0.253}_{-0.202}$	$-0.0307^{+0.0243}_{-0.256}$	$-0.253^{+0.152}_{-0.404}$	$-0.0968^{+0.0604}_{-0.149}$	$-0.268^{+0.151}_{-0.268}$
SN 2004dj	$-0.0106^{+0.00246}_{-0.0361}$	$-0.101^{+0.0505}_{-0.0505}$	$-0.261^{+0.0945}_{-0.0927}$	$-0.303^{+0.101}_{-0.101}$	$-0.01^{+0.00894}_{-0.468}$	$-0.552^{+0.368}_{-0.552}$
SN 2004dk	$-2.04^{+0.191}_{-0.212}$	$-2.17^{+0.253}_{-0.202}$	$-0.00813^{+0.000829}_{-0.007}$	$-0.101^{+0.0505}_{-0.0505}$	$-2.17^{+0.501}_{-0.192}$	$-1.92^{+0.569}_{-0.468}$
SN 2004gq	$-0.0138^{+0.00138}_{-0.0241}$	$-0.354^{+0.202}_{-4.09}$	$-0.0103^{+0.000484}_{-0.00267}$	$-0.101^{+0.0505}_{-0.0505}$	$-4.91^{+1.12}_{-0.0862}$	$-2.01^{+1.4}_{-1.99}$
SN 2007bg	$-0.0155^{+0.000995}_{-0.0415}$	$-0.404^{+0.253}_{-4.09}$	$-0.113^{+0.0205}_{-0.0223}$	$-0.152^{+0.0505}_{-0.0505}$	$-4.99^{+0.0846}_{-0.00637}$	$-4.88^{+0.201}_{-0.0836}$
SN 2007gr	$-5.0^{+0.117}_{-0.00142}$	$-4.9^{+0.202}_{-0.101}$	$-0.000526^{+0.00049}_{-0.0142}$	$-0.101^{+0.0505}_{-0.0}$	$-0.00302^{+0.00253}_{-0.463}$	$-0.585^{+0.401}_{-0.836}$
SN 2007uy	$-3.76^{+0.137}_{-0.146}$	$-3.74^{+0.152}_{-0.152}$	$-0.00697^{+0.00583}_{-0.038}$	$-0.152^{+0.101}_{-0.0505}$	$-4.27^{+1.17}_{-0.141}$	$-3.09^{+1.05}_{-0.903}$
SN 2008D	$-0.00569^{+0.000499}_{-0.0672}$	$-0.202^{+0.101}_{-0.101}$	$-0.00488^{+8.99e-05}_{-0.000896}$	$-0.101^{+0.0505}_{-0.101}$	$-0.000131^{+0.0}_{-0.0217}$	$-0.117^{+0.0669}_{-0.117}$
SN 2008ax	$-0.751^{+0.0712}_{-0.0778}$	$-0.808^{+0.101}_{-0.0505}$	$-3.64^{+0.0097}_{-0.0148}$	$-3.69^{+0.0505}_{-0.0505}$	$-0.0567^{+0.00456}_{-0.112}$	$-0.284^{+0.167}_{-0.452}$
SN 2009bb	$-5.0^{+0.0228}_{-0.000193}$	$-4.95^{+0.0505}_{-0.0505}$	$-1.42^{+0.07}_{-0.0824}$	$-1.46^{+0.101}_{-0.101}$	$-1.02^{+0.186}_{-0.372}$	$-1.22^{+0.385}_{-0.585}$
PTF11qcj	$-1.94^{+0.398}_{-0.418}$	$-1.97^{+0.404}_{-0.455}$	$-0.0656^{+0.00123}_{-0.00125}$	$-0.101^{+0.0505}_{-0.101}$	$-2.95^{+0.247}_{-0.155}$	$-2.89^{+0.201}_{-0.234}$
SN 2011dh	$-0.0818^{+0.00347}_{-0.0164}$	$-0.152^{+0.0505}_{-0.101}$	$-4.02^{+0.0221}_{-0.00925}$	$-4.04^{+0.0505}_{-0.0505}$	$-0.052^{+0.0158}_{-0.227}$	$-0.251^{+0.151}_{-0.234}$
SN 2011ei	$-5.0^{+0.0485}_{-0.0015}$	$-4.8^{+4.19}_{-0.152}$	$-2.75^{+0.16}_{-0.158}$	$-2.78^{+0.101}_{-0.152}$	$-0.199^{+0.152}_{-0.401}$	$-0.569^{+0.368}_{-0.602}$
SN 2011hs	$-0.127^{+0.00995}_{-0.139}$	$-0.303^{+0.152}_{-0.202}$	$-3.08^{+0.068}_{-0.0624}$	$-3.13^{+0.101}_{-0.101}$	$-0.00191^{+0.00168}_{-0.0365}$	$-0.1^{+0.0669}_{-0.0836}$
SN 2012ap	$-5.0^{+0.131}_{-0.000616}$	$-4.8^{+0.303}_{-0.152}$	$-0.00345^{+0.000318}_{-0.0112}$	$-0.101^{+0.0505}_{-0.0}$	$-0.0448^{+0.0341}_{-1.45}$	$-1.24^{+0.819}_{-1.62}$
SN 2012au	$-5.0^{+5.0}_{-0.000916}$	$-0.303^{+0.152}_{-4.19}$	$-0.00302^{+0.000274}_{-0.00735}$	$-0.101^{+0.0505}_{-0.0}$	$-4.82^{+1.45}_{-0.18}$	$-3.51^{+1.71}_{-1.02}$
SN 2012aw	$-1.42^{+0.233}_{-0.249}$	$-1.46^{+0.253}_{-0.253}$	$-1.43^{+0.104}_{-0.0963}$	$-1.46^{+0.101}_{-0.101}$	$-1.61^{+0.536}_{-1.05}$	$-2.14^{+0.803}_{-0.886}$
SN 2013df	$-0.0218^{+0.0217}_{-0.0873}$	$-0.101^{+0.0505}_{-0.101}$	$-0.004^{+0.00293}_{-0.0122}$	$-0.101^{+0.0505}_{-0.0}$	$-2.43^{+0.208}_{-0.244}$	$-2.34^{+0.268}_{-0.234}$
AT2014ge	$-4.36^{+0.118}_{-0.111}$	$-4.34^{+0.606}_{-0.354}$	$-0.00264^{+0.000233}_{-0.00463}$	$-0.101^{+0.0505}_{-0.0}$	$-2.59^{+1.0}_{-0.618}$	$-2.69^{+1.27}_{-0.702}$
SN 2016X	$-0.847^{+0.0797}_{-0.087}$	$-0.909^{+0.101}_{-0.0505}$	$-1.44^{+0.0152}_{-0.0228}$	$-1.52^{+0.0505}_{-0.0505}$	$-1.36^{+1.24}_{-0.382}$	$-1.04^{+0.652}_{-0.953}$
SN 2016coi	$-0.00368^{+0.000314}_{-0.0906}$	$-0.152^{+0.0505}_{-0.152}$	$-0.00834^{+0.00766}_{-0.126}$	$-0.152^{+0.0505}_{-0.152}$	$-1.79^{+0.505}_{-1.06}$	$-1.84^{+0.92}_{-1.02}$
SN 2016gkg	$-3.86^{+0.0793}_{-0.0748}$	$-3.84^{+0.152}_{-0.152}$	$-3.71^{+0.0433}_{-0.0426}$	$-3.74^{+0.0505}_{-0.0505}$	$-0.0616^{+0.00765}_{-0.0769}$	$-0.201^{+0.1}_{-0.217}$
SN 2020oi	$-0.939^{+0.184}_{-0.177}$	$-1.01^{+0.202}_{-0.152}$	$-0.00388^{+0.000237}_{-0.00168}$	$-0.101^{+0.0505}_{-0.0}$	$-0.0388^{+0.0261}_{-0.164}$	$-1.49^{+1.04}_{-0.334}$

TABLE C.4: Best fitted parameters and medians of p with 1σ credible intervals.

SN name	BEST in `Plasma`	MED in `Plasma`	BEST in `All`	MED in `All`
SN 1983N	$3.1^{+0.000179}_{-0.059}$	$3.04^{+0.0333}_{-0.0556}$	$3.04^{+0.0567}_{-0.0822}$	$3.0^{+0.0625}_{-0.0957}$
SN 1987A	$2.0^{+0.0488}_{-0.000622}$	$2.02^{+0.0556}_{-0.0222}$	$2.07^{+0.0814}_{-0.0393}$	$2.11^{+0.114}_{-0.0662}$
SN 1990B	$2.03^{+0.0197}_{-0.0127}$	$2.02^{+0.0222}_{-0.0111}$	$2.88^{+0.2}_{-0.093}$	$2.86^{+0.125}_{-0.14}$
SN 1993J	$2.58^{+0.0178}_{-0.0196}$	$2.57^{+0.0222}_{-0.0222}$	$2.82^{+0.0342}_{-0.0435}$	$2.81^{+0.0331}_{-0.0368}$
SN 1998bw	$2.58^{+0.0623}_{-0.0492}$	$2.57^{+0.0556}_{-0.0444}$	$2.18^{+0.0372}_{-0.0233}$	$2.18^{+0.0294}_{-0.0294}$
SN 2001gd	$2.64^{+0.0746}_{-0.0561}$	$2.63^{+0.0778}_{-0.0667}$	$2.54^{+0.0635}_{-0.0768}$	$2.54^{+0.103}_{-0.0846}$
SN 2001ig	$2.55^{+0.0483}_{-0.0329}$	$2.53^{+0.0333}_{-0.0444}$	$2.81^{+0.024}_{-0.0712}$	$2.78^{+0.0515}_{-0.0552}$
SN 2002ap	$2.0^{+0.0541}_{-0.00137}$	$2.02^{+0.0333}_{-0.0222}$	$2.0^{+0.00247}_{-0.000451}$	$2.04^{+0.0662}_{-0.0294}$
SN 2003L	$2.11^{+0.00925}_{-0.00821}$	$2.1^{+0.0111}_{-0.0111}$	$2.92^{+0.0687}_{-0.101}$	$2.67^{+0.217}_{-0.177}$
SN 2003bg	$2.16^{+0.0146}_{-0.0109}$	$2.16^{+0.0222}_{-0.0333}$	$2.75^{+0.0214}_{-0.0244}$	$2.75^{+0.0662}_{-0.0294}$
SN 2004C	$2.0^{+0.0548}_{-0.000196}$	$2.97^{+0.0889}_{-0.911}$	$2.23^{+0.0237}_{-0.0249}$	$2.22^{+0.0294}_{-0.0258}$
SN 2004cc	$2.0^{+0.0118}_{-0.00204}$	$2.0^{+0.0111}_{-0.0}$	$3.1^{+0.000144}_{-0.0104}$	$3.04^{+0.0405}_{-0.103}$
SN 2004dj	$2.89^{+0.0761}_{-0.0716}$	$2.88^{+0.0778}_{-0.0778}$	$2.67^{+0.103}_{-0.0434}$	$2.75^{+0.158}_{-0.118}$
SN 2004dk	$2.92^{+0.0613}_{-0.0326}$	$2.91^{+0.0444}_{-0.0444}$	$2.0^{+0.0139}_{-0.0}$	$2.02^{+0.0294}_{-0.0184}$
SN 2004gq	$2.5^{+0.0319}_{-0.022}$	$2.5^{+0.0222}_{-0.0222}$	$2.47^{+0.13}_{-0.0718}$	$2.68^{+0.092}_{-0.125}$
SN 2007bg	$2.05^{+0.00951}_{-0.00655}$	$2.03^{+0.0111}_{-0.0111}$	$2.0^{+0.0171}_{-0.000596}$	$2.01^{+0.0258}_{-0.011}$
SN 2007gr	$2.0^{+0.0244}_{-0.000832}$	$2.01^{+0.0222}_{-0.0111}$	$2.9^{+0.196}_{-0.216}$	$2.86^{+0.155}_{-0.202}$
SN 2007uy	$2.0^{+0.00739}_{-0.00113}$	$2.0^{+0.0111}_{-0.0}$	$2.11^{+0.137}_{-0.0955}$	$2.14^{+0.125}_{-0.0846}$
SN 2008D	$2.72^{+0.0193}_{-0.00935}$	$2.71^{+0.0222}_{-0.0222}$	$2.14^{+0.0546}_{-0.0846}$	$2.15^{+0.0883}_{-0.0736}$
SN 2008ax	$3.1^{+6.8e-05}_{-0.00687}$	$3.07^{+0.0111}_{-0.0222}$	$2.92^{+0.127}_{-0.0978}$	$2.82^{+0.14}_{-0.136}$
SN 2009bb	$2.39^{+0.0385}_{-0.0356}$	$2.38^{+0.0444}_{-0.0333}$	$3.1^{+0.00369}_{-0.0296}$	$3.05^{+0.0331}_{-0.0625}$
PTF11qcj	$3.1^{+0.000162}_{-0.00366}$	$3.07^{+0.0111}_{-0.0333}$	$2.0^{+0.0025}_{-0.00106}$	$2.0^{+0.011}_{-0.00368}$
SN 2011dh	$2.61^{+0.014}_{-0.00508}$	$2.61^{+0.0111}_{-0.0111}$	$2.74^{+0.0533}_{-0.037}$	$2.75^{+0.0478}_{-0.0515}$
SN 2011ei	$2.0^{+0.0148}_{-0.000121}$	$2.01^{+0.0111}_{-0.0111}$	$3.05^{+0.0517}_{-0.0598}$	$2.97^{+0.0773}_{-0.147}$
SN 2011hs	$3.0^{+0.0358}_{-0.0306}$	$2.99^{+0.0444}_{-0.0444}$	$3.1^{+0.000636}_{-0.0186}$	$3.08^{+0.011}_{-0.0258}$
SN 2012ap	$2.8^{+0.091}_{-0.112}$	$2.79^{+0.0889}_{-0.0889}$	$2.25^{+0.57}_{-0.0476}$	$2.64^{+0.221}_{-0.258}$
SN 2012au	$2.57^{+0.015}_{-0.0333}$	$2.54^{+0.0222}_{-0.0444}$	$2.68^{+0.193}_{-0.0977}$	$2.84^{+0.158}_{-0.177}$
SN 2012aw	$2.72^{+0.0717}_{-0.0786}$	$2.7^{+0.0889}_{-0.0778}$	$2.49^{+0.108}_{-0.16}$	$2.46^{+0.121}_{-0.121}$
SN 2013df	$2.0^{+0.0127}_{-0.00296}$	$2.0^{+0.0111}_{-0.0}$	$2.84^{+0.12}_{-0.151}$	$2.79^{+0.136}_{-0.143}$
AT2014ge	$2.36^{+0.0647}_{-0.0521}$	$2.36^{+0.0444}_{-0.0556}$	$2.71^{+0.0821}_{-0.0327}$	$2.74^{+0.0552}_{-0.0552}$
SN 2016X	$3.1^{+0.000144}_{-0.0133}$	$3.07^{+0.0222}_{-0.0111}$	$3.0^{+0.0867}_{-0.356}$	$2.77^{+0.188}_{-0.228}$
SN 2016coi	$2.0^{+0.0237}_{-0.00191}$	$2.01^{+0.0222}_{-0.0111}$	$2.44^{+0.148}_{-0.123}$	$2.45^{+0.173}_{-0.173}$
SN 2016gkg	$2.49^{+0.0247}_{-0.0237}$	$2.48^{+0.0222}_{-0.0222}$	$2.91^{+0.0498}_{-0.0413}$	$2.91^{+0.0478}_{-0.0552}$
SN 2020oi	$2.87^{+0.0183}_{-0.0275}$	$2.86^{+0.0222}_{-0.0333}$	$3.1^{+0.00118}_{-0.0366}$	$3.0^{+0.0625}_{-0.103}$

TABLE C.5: Best fitted parameters and medians of s with 1σ credible intervals.

SN name	BEST in `Astro`	MED in `Astro`	BEST in `All`	MED in `All`
SN 1983N	$2.08^{+0.0417}_{-0.0424}$	$2.08^{+0.0903}_{-0.1}$	$1.99^{+0.0694}_{-0.147}$	$2.01^{+0.0803}_{-0.1}$
SN 1987A	$2.47^{+0.085}_{-0.0787}$	$2.47^{+0.11}_{-0.1}$	$2.19^{+0.0864}_{-0.0549}$	$2.14^{+0.1}_{-0.11}$
SN 1990B	$0.567^{+0.0763}_{-0.0726}$	$0.552^{+0.0903}_{-0.0903}$	$0.0817^{+0.627}_{-0.0792}$	$0.763^{+0.401}_{-0.472}$
SN 1993J	$1.85^{+0.0069}_{-0.00653}$	$1.84^{+0.01}_{-0.01}$	$2.17^{+0.00957}_{-0.00935}$	$2.16^{+0.0201}_{-0.01}$
SN 1998bw	$1.44^{+0.061}_{-0.087}$	$1.41^{+0.0803}_{-0.0803}$	$2.01^{+0.0237}_{-0.0426}$	$2.0^{+0.0301}_{-0.0401}$
SN 2001gd	$2.09^{+0.0282}_{-0.0278}$	$2.09^{+0.0401}_{-0.0502}$	$2.37^{+0.0255}_{-0.0223}$	$2.34^{+0.0903}_{-0.12}$
SN 2001ig	$1.81^{+0.016}_{-0.0152}$	$1.8^{+0.0602}_{-0.0602}$	$1.93^{+0.0338}_{-0.0106}$	$1.93^{+0.0401}_{-0.0301}$
SN 2002ap	$1.81^{+0.0569}_{-0.0543}$	$1.78^{+0.151}_{-0.301}$	$0.0378^{+0.784}_{-0.0341}$	$1.7^{+0.251}_{-0.993}$
SN 2003L	$1.02^{+0.0282}_{-0.0296}$	$1.0^{+0.0401}_{-0.0502}$	$0.921^{+0.162}_{-0.0758}$	$1.25^{+0.14}_{-0.261}$
SN 2003bg	$1.45^{+0.0112}_{-0.0127}$	$1.43^{+0.0201}_{-0.01}$	$1.7^{+0.0173}_{-0.0141}$	$1.69^{+0.0201}_{-0.171}$
SN 2004C	$1.99^{+0.00467}_{-0.0176}$	$1.89^{+0.13}_{-0.773}$	$1.96^{+0.02}_{-0.0131}$	$1.95^{+0.0502}_{-0.0401}$
SN 2004cc	$2.97^{+0.00107}_{-0.00212}$	$2.94^{+0.0301}_{-0.0401}$	$2.99^{+0.00235}_{-0.00377}$	$2.89^{+0.0702}_{-0.622}$
SN 2004dj	$2.25^{+0.0248}_{-0.0263}$	$2.24^{+0.0502}_{-0.0602}$	$2.09^{+0.0279}_{-0.0454}$	$2.04^{+0.0803}_{-0.11}$
SN 2004dk	$1.01^{+0.0284}_{-0.0255}$	$1.0^{+0.0401}_{-0.0301}$	$0.907^{+0.0793}_{-0.101}$	$0.943^{+0.171}_{-0.12}$
SN 2004gq	$1.69^{+0.0219}_{-0.0248}$	$1.68^{+0.0602}_{-0.0502}$	$1.98^{+0.0771}_{-0.099}$	$1.84^{+0.0803}_{-0.0903}$
SN 2007bg	$0.000307^{+0.257}_{-0.000255}$	$0.0903^{+0.1}_{-0.0702}$	$0.756^{+0.0345}_{-0.123}$	$0.662^{+0.0803}_{-0.11}$
SN 2007gr	$1.87^{+0.0259}_{-0.026}$	$1.83^{+0.161}_{-1.66}$	$1.68^{+0.0469}_{-0.0563}$	$1.72^{+0.12}_{-0.1}$
SN 2007uy	$2.1^{+0.031}_{-0.0334}$	$2.08^{+0.0702}_{-0.191}$	$2.33^{+0.0681}_{-0.0675}$	$2.34^{+0.0702}_{-0.0803}$
SN 2008D	$1.68^{+0.0266}_{-0.0237}$	$1.67^{+0.0502}_{-0.0502}$	$2.52^{+0.0375}_{-0.0455}$	$2.48^{+0.0602}_{-0.0602}$
SN 2008ax	$1.86^{+0.0244}_{-0.0223}$	$1.86^{+0.0602}_{-0.0702}$	$1.83^{+0.0624}_{-0.0834}$	$1.88^{+0.0903}_{-0.1}$
SN 2009bb	$1.06^{+0.0545}_{-0.0529}$	$1.03^{+0.0803}_{-0.12}$	$1.62^{+0.0284}_{-0.0751}$	$1.57^{+0.0803}_{-0.0903}$
PTF11qcj	$0.294^{+0.0608}_{-0.0508}$	$0.281^{+0.0702}_{-0.0702}$	$0.803^{+0.0761}_{-0.0752}$	$0.793^{+0.1}_{-0.0903}$
SN 2011dh	$1.74^{+0.0157}_{-0.0198}$	$1.73^{+0.0201}_{-0.0201}$	$1.85^{+0.0257}_{-0.0202}$	$1.84^{+0.0301}_{-0.0301}$
SN 2011ei	$1.53^{+0.0299}_{-0.0315}$	$1.52^{+0.0602}_{-0.0803}$	$1.49^{+0.0357}_{-0.0377}$	$1.51^{+0.0803}_{-0.0803}$
SN 2011hs	$1.87^{+0.0452}_{-0.0423}$	$1.86^{+0.0803}_{-0.1}$	$1.94^{+0.0952}_{-0.0686}$	$1.93^{+0.0702}_{-0.0702}$
SN 2012ap	$1.34^{+0.0905}_{-0.0873}$	$1.33^{+0.1}_{-0.0903}$	$1.71^{+0.131}_{-0.217}$	$1.49^{+0.191}_{-0.231}$
SN 2012au	$1.43^{+0.0484}_{-0.0529}$	$1.41^{+0.0803}_{-0.0903}$	$2.2^{+0.199}_{-0.207}$	$2.0^{+0.211}_{-0.221}$
SN 2012aw	$1.88^{+0.023}_{-0.02}$	$1.87^{+0.0401}_{-0.0301}$	$2.17^{+0.0839}_{-0.0645}$	$2.17^{+0.0803}_{-0.0803}$
SN 2013df	$1.65^{+0.0261}_{-0.0213}$	$1.64^{+0.0301}_{-0.0301}$	$1.93^{+0.0488}_{-0.0471}$	$1.91^{+0.0502}_{-0.0502}$
AT2014ge	$1.64^{+0.019}_{-0.0196}$	$1.64^{+0.0301}_{-0.0401}$	$1.83^{+0.0135}_{-0.114}$	$1.74^{+0.0602}_{-0.0602}$
SN 2016X	$2.39^{+0.0485}_{-0.0501}$	$2.38^{+0.0702}_{-0.0702}$	$2.45^{+0.238}_{-0.145}$	$2.44^{+0.181}_{-0.14}$
SN 2016coi	$1.6^{+0.0323}_{-0.0364}$	$1.59^{+0.0803}_{-0.0803}$	$1.8^{+0.0687}_{-0.051}$	$1.82^{+0.0803}_{-0.0702}$
SN 2016gkg	$1.56^{+0.0154}_{-0.016}$	$1.56^{+0.0201}_{-0.0201}$	$1.67^{+0.0173}_{-0.0173}$	$1.66^{+0.0201}_{-0.0301}$
SN 2020oi	$1.94^{+0.0294}_{-0.0293}$	$1.94^{+0.0301}_{-0.0301}$	$1.95^{+0.0227}_{-0.0571}$	$1.72^{+0.191}_{-0.151}$

TABLE C.6: Best fitted parameters and medians of n with 1σ credible intervals.

SN name	BEST in `Astro`	MED in `Astro`	BEST in `All`	MED in `All`
SN 1983N	$7.25^{+0.15}_{-0.118}$	$7.26^{+0.334}_{-0.334}$	$8.14^{+0.286}_{-0.654}$	$7.09^{+0.92}_{-1.17}$
SN 1987A	$9.68^{+0.136}_{-0.122}$	$9.68^{+1.09}_{-0.753}$	$10.3^{+0.207}_{-0.34}$	$10.1^{+0.334}_{-0.502}$
SN 1990B	$7.55^{+0.0397}_{-0.0384}$	$7.59^{+1.0}_{-0.753}$	$5.4^{+0.421}_{-0.0501}$	$6.09^{+2.01}_{-0.585}$
SN 1993J	$13.7^{+0.0783}_{-0.0836}$	$13.6^{+0.0836}_{-0.0836}$	$30.0^{+0.00642}_{-0.137}$	$29.7^{+0.0836}_{-0.251}$
SN 1998bw	$5.43^{+0.0144}_{-0.011}$	$5.33^{+0.0836}_{-0.0836}$	$5.96^{+0.0542}_{-0.0369}$	$5.92^{+0.0}_{-0.0836}$
SN 2001gd	$8.76^{+0.258}_{-0.212}$	$8.68^{+0.502}_{-0.334}$	$24.1^{+5.88}_{-5.68}$	$23.1^{+4.43}_{-6.35}$
SN 2001ig	$7.02^{+0.0326}_{-0.0325}$	$6.92^{+0.251}_{-0.167}$	$8.23^{+0.165}_{-0.0684}$	$8.18^{+0.251}_{-0.167}$
SN 2002ap	$11.1^{+0.264}_{-0.253}$	$11.4^{+15.6}_{-1.51}$	$5.17^{+0.258}_{-0.0759}$	$6.84^{+1.42}_{-1.34}$
SN 2003L	$5.85^{+0.0153}_{-0.0133}$	$5.75^{+0.251}_{-0.251}$	$7.21^{+0.167}_{-0.0587}$	$6.0^{+1.17}_{-0.334}$
SN 2003bg	$6.58^{+0.0125}_{-0.0133}$	$6.51^{+0.167}_{-0.167}$	$7.02^{+0.046}_{-0.0356}$	$6.92^{+1.0}_{-0.0836}$
SN 2004C	$8.08^{+0.102}_{-0.116}$	$7.84^{+0.251}_{-0.92}$	$11.3^{+0.41}_{-0.382}$	$11.3^{+0.502}_{-0.502}$
SN 2004cc	$5.34^{+0.141}_{-0.114}$	$5.33^{+0.167}_{-0.167}$	$5.37^{+0.405}_{-0.27}$	$5.59^{+0.669}_{-0.418}$
SN 2004dj	$11.8^{+0.238}_{-0.252}$	$11.7^{+0.334}_{-0.334}$	$9.57^{+0.53}_{-1.03}$	$8.43^{+1.17}_{-1.42}$
SN 2004dk	$7.57^{+0.0376}_{-0.0332}$	$7.51^{+0.167}_{-0.167}$	$6.11^{+0.121}_{-0.0415}$	$6.09^{+0.334}_{-0.0836}$
SN 2004gq	$6.8^{+0.0236}_{-0.0185}$	$6.76^{+0.167}_{-0.167}$	$6.02^{+0.38}_{-0.157}$	$7.68^{+0.753}_{-1.25}$
SN 2007bg	$7.06^{+4.11}_{-0.14}$	$10.9^{+0.669}_{-0.753}$	$16.2^{+1.1}_{-0.986}$	$15.6^{+1.25}_{-1.34}$
SN 2007gr	$11.2^{+0.245}_{-0.23}$	$11.5^{+7.78}_{-0.92}$	$7.65^{+0.728}_{-0.143}$	$8.6^{+1.92}_{-0.92}$
SN 2007uy	$12.2^{+0.24}_{-0.222}$	$12.1^{+0.418}_{-0.585}$	$10.5^{+6.07}_{-0.814}$	$16.7^{+5.52}_{-4.77}$
SN 2008D	$7.42^{+0.0141}_{-0.0157}$	$7.34^{+0.502}_{-0.502}$	$5.37^{+0.208}_{-0.0571}$	$5.5^{+0.334}_{-0.334}$
SN 2008ax	$7.39^{+0.0281}_{-0.0289}$	$7.34^{+0.669}_{-0.585}$	$8.27^{+0.0612}_{-0.122}$	$7.93^{+0.334}_{-0.669}$
SN 2009bb	$7.08^{+0.019}_{-0.0188}$	$7.01^{+0.0836}_{-0.251}$	$9.03^{+0.0603}_{-0.294}$	$8.6^{+0.502}_{-0.669}$
PTF11qcj	$5.88^{+0.022}_{-0.0236}$	$5.75^{+0.334}_{-0.251}$	$5.32^{+0.067}_{-0.0232}$	$5.5^{+0.585}_{-0.418}$
SN 2011dh	$8.18^{+0.0301}_{-0.0279}$	$8.09^{+0.251}_{-0.167}$	$9.34^{+0.0937}_{-0.155}$	$9.1^{+0.334}_{-0.334}$
SN 2011ei	$11.1^{+0.202}_{-0.199}$	$10.9^{+0.334}_{-0.334}$	$11.7^{+0.325}_{-0.221}$	$12.0^{+0.669}_{-0.585}$
SN 2011hs	$8.61^{+0.139}_{-0.0997}$	$8.6^{+0.585}_{-0.502}$	$6.27^{+0.351}_{-0.32}$	$6.25^{+0.418}_{-0.334}$
SN 2012ap	$7.88^{+0.0372}_{-0.0404}$	$7.84^{+0.167}_{-0.251}$	$5.53^{+0.922}_{-0.0736}$	$6.42^{+1.17}_{-0.753}$
SN 2012au	$7.85^{+0.0424}_{-0.0388}$	$7.76^{+0.334}_{-0.167}$	$7.37^{+1.35}_{-0.418}$	$8.01^{+1.09}_{-0.92}$
SN 2012aw	$10.7^{+0.101}_{-0.111}$	$10.6^{+0.251}_{-0.251}$	$14.0^{+0.411}_{-0.49}$	$13.4^{+0.585}_{-0.753}$
SN 2013df	$30.0^{+0.00358}_{-0.887}$	$29.1^{+0.502}_{-1.17}$	$29.9^{+0.0546}_{-1.28}$	$28.6^{+0.92}_{-1.84}$
AT2014ge	$7.34^{+0.0536}_{-0.0468}$	$7.26^{+0.251}_{-0.251}$	$9.66^{+0.431}_{-0.734}$	$7.42^{+0.502}_{-0.418}$
SN 2016X	$8.82^{+0.112}_{-0.105}$	$8.76^{+0.251}_{-0.334}$	$5.77^{+2.03}_{-0.429}$	$7.26^{+1.51}_{-1.17}$
SN 2016coi	$8.01^{+0.05}_{-0.042}$	$7.93^{+0.418}_{-0.251}$	$7.15^{+0.48}_{-0.214}$	$7.17^{+0.669}_{-0.502}$
SN 2016gkg	$7.69^{+0.0432}_{-0.0417}$	$7.59^{+0.251}_{-0.167}$	$8.62^{+0.173}_{-0.131}$	$8.51^{+0.334}_{-0.251}$
SN 2020oi	$8.14^{+0.0353}_{-0.0169}$	$8.09^{+0.0836}_{-0.167}$	$8.05^{+0.14}_{-0.077}$	$5.33^{+2.51}_{-0.251}$

Appendix D

Derivation of $\rho_{\rm CE}$

In the simulation of the CSM formation, the value of $\rho_{\rm CE}$ must be specified to determine the initial density profile. We consider a CE component with a total mass $M_{\rm CE} = 10 M_\odot$ ejected into a static uniform ISM. The required condition is

$$\int_0^{R_\infty} 4\pi r^2 (\rho(r) - \rho_{\rm ism}) dr = M_{\rm CE}, \tag{D.1}$$

where $R_\infty = 3 \times 10^{21}$ cm is the outermost radius of the simulation domain. For the case $\rho(r) = \rho_{\rm CE} \exp(-r/R_{\rm CE}) + \rho_{\rm ism}$, this can be analytically integrated, so that

$$\rho_{\rm CE} \simeq \frac{M_{\rm CE}}{8\pi R_{\rm CE}^3} = 7.96 \times 10^{-22}\,{\rm g cm^{-3}} \tag{D.2}$$

can be derived.

Appendix E

Tests for the numerical code

The numerical simulation code for the hydrodynamics employed in this study is verified in this section. Figure E.1 shows the result of the shock tube problem with an adiabatic index $\gamma = 5/3$. At $t = 0$, a static ($v = 0$) gas is put into the simulation box, with a step function profile for its density and pressure centered at $x = 0$ as follows; $\rho_L = 1.0, v_L = 0.0, p_L = 1.0, \rho_R = 0.125, v_R = 0.0, p_R = 0.1$ (the subscripts L and R denote $x < 0$ and $x \geq 0$, respectively). The numerical solution successfully reproduces the profiles given by the exact solution. Furthermore, Figure E.2 displays the Sedov solution at $t = 1.0$ second in which an explosion energy $E_{\rm sedov} = 1$ erg is deposited into a uniform medium with $\rho_{\rm sedov} = 1.0 \times 10^{-24}$ g cm^{-3} (Sedov, 1959). The results are again in a good agreement with the analytical solutions for the density, velocity, and pressure profiles, as well as a good match of the shock radius given by $R = 1.15(E_{\rm sedov} t^2/\rho_{\rm sedov})^{0.2}$. These two experiments assure us a good accuracy of our numerical code.

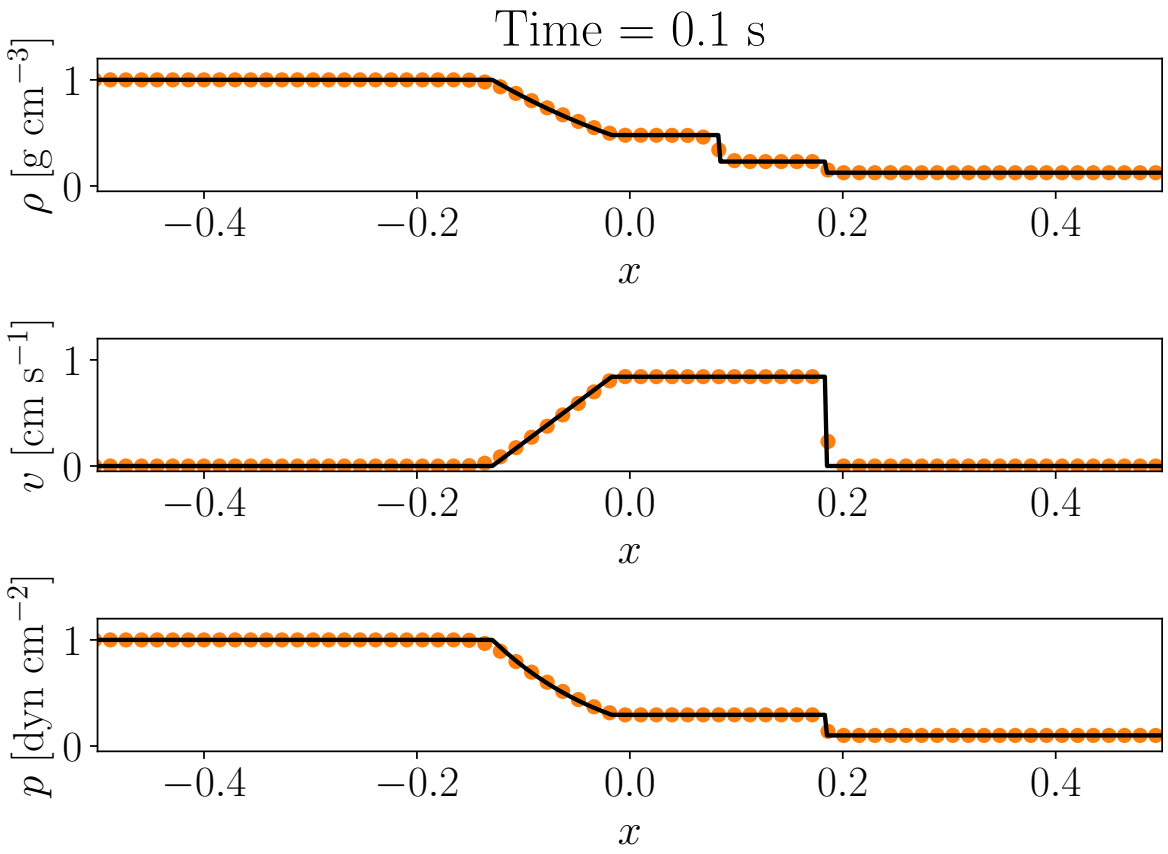

FIGURE E.1: The shock tube test. Black lines and orange circles show the exact solution and numerical solution derived by our code, respectively.

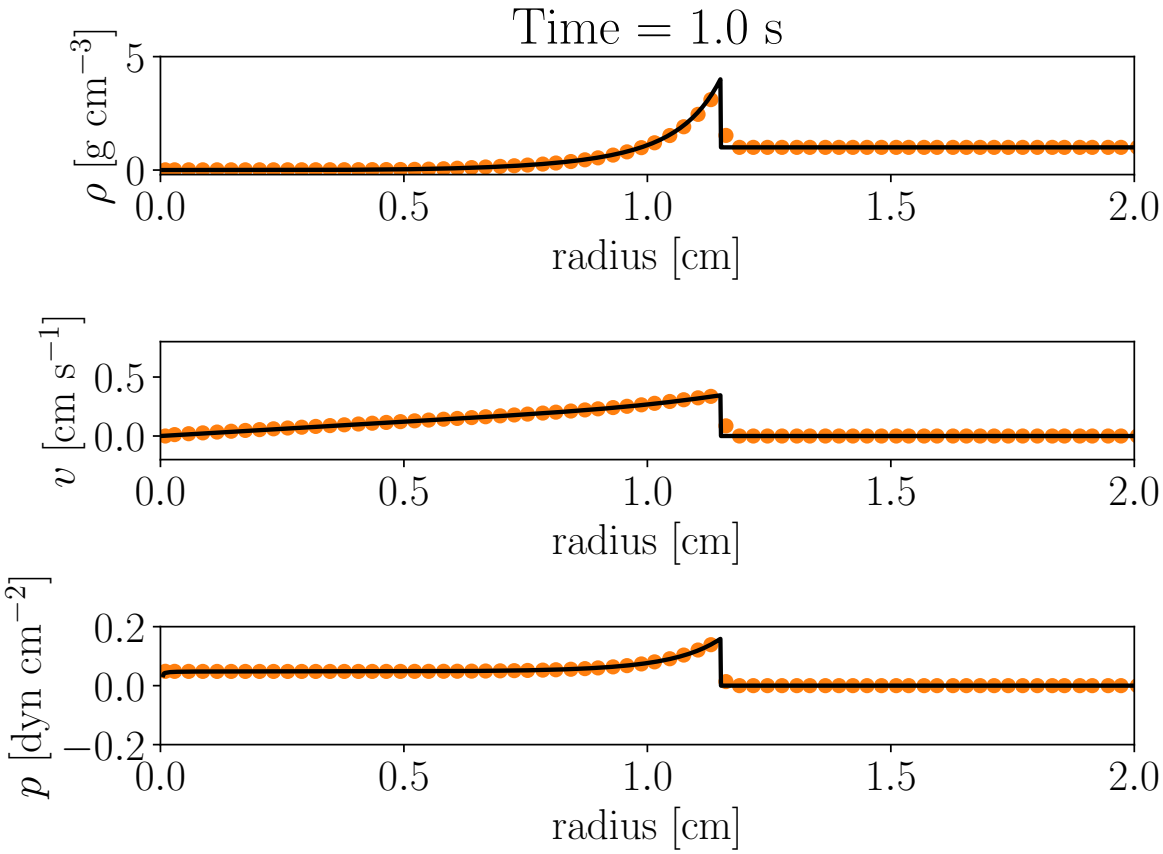

FIGURE E.2: The Sedov explosion test. The line and symbol have the same meaning as in Figure E.1.

Bibliography

Abbott, B. P., R. Abbott, T. D. Abbott, et al. (2017a). "Gravitational Waves and Gamma-rays from a Binary Neutron Star Merger: GW170817 and GRB 170817A". In: *Astrophys. J.* 848.2, p. L13. DOI: 10.3847/2041-8213/aa920c. arXiv: 1710.05834 [astro-ph.HE].

— (2017b). "GW170817: Observation of Gravitational Waves from a Binary Neutron Star Inspiral". In: *Phys. Rev. Lett.* 119.16, p. 161101. DOI: 10.1103/PhysRevLett.119.161101. arXiv: 1710.05832 [gr-qc].

— (2017c). "Multi-messenger Observations of a Binary Neutron Star Merger". In: *Astrophys. J.* 848.2, p. L12. DOI: 10.3847/2041-8213/aa91c9. arXiv: 1710.05833 [astro-ph.HE].

Abbott, R. et al. (Sept. 2020). "GW190521: A Binary Black Hole Merger with a Total Mass of 150 $M_\odot$". In: *Phys. Rev. Lett.* 125.10, 101102, p. 101102. DOI: 10.1103/PhysRevLett.125.101102. arXiv: 2009.01075 [gr-qc].

Abdikamalov, Ernazar, Giulia Pagliaroli, and David Radice (Oct. 2020). "Gravitational Waves from Core-Collapse Supernovae". In: *arXiv e-prints*, arXiv:2010.04356, arXiv:2010.04356. arXiv: 2010.04356 [astro-ph.SR].

Ackermann, M. et al. (Feb. 2013). "Detection of the Characteristic Pion-Decay Signature in Supernova Remnants". In: *Science* 339.6121, pp. 807–811. DOI: 10.1126/science.1231160. arXiv: 1302.3307 [astro-ph.HE].

Aharonian, F. A., S. R. Kelner, and A. Y. Prosekin (Aug. 2010). "Angular, spectral, and time distributions of highest energy protons and associated secondary gamma rays and neutrinos propagating through extragalactic magnetic and radiation fields". In: *Phys. Rev. D* 82.4, 043002, p. 043002. DOI: 10.1103/PhysRevD.82.043002. arXiv: 1006.1045 [astro-ph.HE].

Alexander, Kate D., Alicia M. Soderberg, and Laura B. Chomiuk (June 2015). "A New Model for the Radio Emission from SN 1994I and an Associated Search for Radio Transients in M51". In: *ApJ* 806.1, 106, p. 106. DOI: 10.1088/0004-637X/806/1/106. arXiv: 1405.0228 [astro-ph.HE].

Allen, G. E. et al. (Jan. 2015). "On the Expansion Rate, Age, and Distance of the Supernova Remnant G266.2-1.2 (Vela Jr.)" In: *ApJ* 798.2, 82, p. 82. DOI: 10.1088/0004-637X/798/2/82. arXiv: 1410.7435 [astro-ph.HE].

Ambrocio-Cruz, P. et al. (Nov. 2017). "Kinematic study at the H α line in the north-eastern region of the Galactic supernova remnant IC 443". In: *MNRAS* 472.1, pp. 51–54. DOI: 10.1093/mnras/stx1936.

Anderson, J. P. (Aug. 2019). "A meta-analysis of core-collapse supernova ^{56}Ni masses". In: *A&A* 628, A7, A7. DOI: 10.1051/0004-6361/201935027. arXiv: 1906.00761 [astro-ph.HE].

Anderson, J. P. et al. (May 2014). "Characterizing the V-band Light-curves of Hydrogen-rich Type II Supernovae". In: *ApJ* 786, 67, p. 67. DOI: 10.1088/0004-637X/786/1/67. arXiv: 1403.7091 [astro-ph.HE].

Arcavi, Iair et al. (2012). "Caltech Core-Collapse Project (CCCP) Observations of Type II Supernovae: Evidence for Three Distinct Photometric Subtypes". In: *ApJ* 756.2, L30, p. L30. DOI: 10.1088/2041-8205/756/2/L30. arXiv: 1206.2029 [astro-ph.CO].

Arnett, David (1996). *Supernovae and Nucleosynthesis: An Investigation of the History of Matter from the Big Bang to the Present*.

Arnett, W. D. (1982). "Type I supernovae. I - Analytic solutions for the early part of the light curve". In: *ApJ* 253, pp. 785–797. DOI: 10.1086/159681.

Arnett, W. David (Oct. 1969). "A Possible Model of Supernovae: Detonation of ^{12}C". In: *Ap&SS* 5.2, pp. 180–212. DOI: 10.1007/BF00650291.

Barbon, R., F. Ciatti, and L. Rosino (1979). "Photometric properties of type II supernovae." In: *A&A* 72, pp. 287–292.

Barkana, R. and A. Loeb (July 2001). "In the beginning: the first sources of light and the reionization of the universe". In: *Phys. Rep.* 349.2, pp. 125–238. DOI: 10.1016/S0370-1573(01)00019-9. arXiv: astro-ph/0010468 [astro-ph].

Barniol Duran, R. (Aug. 2014). "Constraining the magnetic field in GRB relativistic collisionless shocks using radio data". In: *MNRAS* 442.4, pp. 3147–3154. DOI: 10.1093/mnras/stu1070. arXiv: 1311.1216 [astro-ph.HE].

Bartel, N. et al. (Apr. 1994). "The shape, expansion rate and distance of supernova 1993J from VLBI measurements". In: *Nature* 368.6472, pp. 610–613. DOI: 10.1038/368610a0.

Bell, A. R. (Jan. 1978). "The acceleration of cosmic rays in shock fronts. I". In: *MNRAS* 182, pp. 147–156. DOI: 10.1093/mnras/182.2.147.

Bellm, Eric C. et al. (2019). "The Zwicky Transient Facility: System Overview, Performance, and First Results". In: *PASP* 131.995, p. 018002. DOI: 10.1088/1538-3873/aaecbe. arXiv: 1902.01932 [astro-ph.IM].

Beniamini, Paz and Alexander J. van der Horst (Dec. 2017). "Electrons' energy in GRB afterglows implied by radio peaks". In: *MNRAS* 472.3, pp. 3161–3168. DOI: 10.1093/mnras/stx2203. arXiv: 1706.07817 [astro-ph.HE].

Berger, E., S. R. Kulkarni, and R. A. Chevalier (Sept. 2002). "The Radio Evolution of the Ordinary Type Ic Supernova SN 2002ap". In: *ApJ* 577.1, pp. L5–L8. DOI: 10.1086/344045. arXiv: astro-ph/0206183 [astro-ph].

Berkhuijsen, E. M. and A. Fletcher (Oct. 2008). "Density probability distribution functions of diffuse gas in the Milky Way". In: *MNRAS* 390.1, pp. L19–L23. DOI: 10.1111/j.1745-3933.2008.00526.x. arXiv: 0806.4316 [astro-ph].

Bersten, M. C. et al. (Feb. 2018). "A surge of light at the birth of a supernova". In: *Nature* 554.7693, pp. 497–499. DOI: 10.1038/nature25151. arXiv: 1802.09360 [astro-ph.HE].

Bersten, Melina C. et al. (Sept. 2012). "The Type IIb Supernova 2011dh from a Supergiant Progenitor". In: *ApJ* 757.1, 31, p. 31. DOI: 10.1088/0004-637X/757/1/31. arXiv: 1207.5975 [astro-ph.HE].

Bhattacharya, D. and E. P. J. van den Heuvel (1991). "Formation and evolution of binary and millisecond radio pulsars". In: *Phys. Rep.* 203.1-2, pp. 1–124. DOI: 10.1016/0370-1573(91)90064-S.

Bietenholz, M. F. et al. (Feb. 2021). "The Radio Luminosity-risetime Function of Core-collapse Supernovae". In: *ApJ* 908.1, 75, p. 75. DOI: 10.3847/1538-4357/abccd9. arXiv: 2011.11737 [astro-ph.HE].

Björnsson, C. I. (Sept. 2022). "Radio Spectra of SN 2020oi: Effects of Radiative Cooling on the Deduced Source Properties". In: *ApJ* 936.2, 98, p. 98. DOI: 10.3847/1538-4357/ac87aa. arXiv: 2209.03057 [astro-ph.HE].

Björnsson, Claes-Ingvar and Claes Fransson (Apr. 2004). "The X-Ray and Radio Emission from SN 2002ap: The Importance of Compton Scattering". In: *ApJ* 605.2, pp. 823–829. DOI: 10.1086/382584. arXiv: astro-ph/0401196 [astro-ph].

Blinnikov, S. I. and O. S. Bartunov (1993). "Non-equilibrium radiative transfer in supernova theory : models of linear type II supernovae." In: *A&A* 273, pp. 106–122.

Blinnikov, Sergei et al. (Apr. 2000). "Radiation Hydrodynamics of SN 1987A. I. Global Analysis of the Light Curve for the First 4 Months". In: *ApJ* 532.2, pp. 1132–1149. DOI: 10.1086/308588. arXiv: astro-ph/9911205 [astro-ph].

Bock, G. et al. (Jan. 2016). "ASASSN-16at: Discovery of A Probable Nearby Supernova in UGC 08041". In: *The Astronomer's Telegram* 8566, p. 1.

Bollig, Robert et al. (July 2021). "Self-consistent 3D Supernova Models From -7 Minutes to +7 s: A 1-bethe Explosion of a 19 $M_\odot$ Progenitor". In: *ApJ* 915.1, 28, p. 28. DOI: 10.3847/1538-4357/abf82e. arXiv: 2010.10506 [astro-ph.HE].

Book, D. L. (July 1994). "The Sedov self-similar point blast solutions in nonuniform media". In: *Shock Waves* 4, pp. 1–10. DOI: 10.1007/BF01414626. URL: https://doi.org/10.1007/BF01414626.

Botteon, A. et al. (Feb. 2020). "Shock acceleration efficiency in radio relics". In: *A&A* 634, A64, A64. DOI: 10.1051/0004-6361/201936216. arXiv: 1907.00966 [astro-ph.HE].

Braun, Robert et al. (Dec. 2019). "Anticipated Performance of the Square Kilometre Array – Phase 1 (SKA1)". In: *arXiv e-prints*, arXiv:1912.12699, arXiv:1912.12699. arXiv: 1912.12699 [astro-ph.IM].

Brouillette, Martin (Jan. 2002). "The richtmyer-meshkov instability". In: *Annual Review of Fluid Mechanics* 34.34, pp. 445–468. DOI: 10.1146/annurev.fluid.34.090101.162238.

Bufano, F. et al. (Apr. 2014). "SN 2011hs: a fast and faint Type IIb supernova from a supergiant progenitor". In: *MNRAS* 439.2, pp. 1807–1828. DOI: 10.1093/mnras/stu065. arXiv: 1401.2368 [astro-ph.SR].

Burgay, M. et al. (2003). "An increased estimate of the merger rate of double neutron stars from observations of a highly relativistic system". In: *Nature* 426.6966, pp. 531–533. DOI: 10.1038/nature02124. arXiv: astro-ph/0312071 [astro-ph].

Camenzind, Max (2007). *Compact objects in astrophysics : white dwarfs, neutron stars, and black holes*. DOI: 10.1007/978-3-540-49912-1.

Caprioli, D., A.-R. Pop, and A. Spitkovsky (Jan. 2015). "Simulations and Theory of Ion Injection at Non-relativistic Collisionless Shocks". In: *ApJ* 798, L28, p. L28. DOI: 10.1088/2041-8205/798/2/L28. arXiv: 1409.8291 [astro-ph.HE].

Caprioli, D. and A. Spitkovsky (Mar. 2014a). "Simulations of Ion Acceleration at Non-relativistic Shocks. I. Acceleration Efficiency". In: *ApJ* 783.2, 91, p. 91. DOI: 10.1088/0004-637X/783/2/91. arXiv: 1310.2943 [astro-ph.HE].

— (Oct. 2014b). "Simulations of Ion Acceleration at Non-relativistic Shocks. II. Magnetic Field Amplification". In: *ApJ* 794.1, 46, p. 46. DOI: 10.1088/0004-637X/794/1/46. arXiv: 1401.7679 [astro-ph.HE].

Catalán, S. et al. (July 2008). "The initial-final mass relationship of white dwarfs revisited: effect on the luminosity function and mass distribution". In: *MNRAS* 387.4, pp. 1693–1706. DOI: 10.1111/j.1365-2966.2008.13356.x. arXiv: 0804.3034 [astro-ph].

Chakraborti, Sayan et al. (June 2015). "A Missing-link in the Supernova-GRB Connection: The Case of SN 2012ap". In: *ApJ* 805.2, 187, p. 187. DOI: 10.1088/0004-637X/805/2/187. arXiv: 1402.6336 [astro-ph.HE].

Chandra, Poonam et al. (Jan. 2009). "Eleven Years of Radio Monitoring of the type IIn Supernova SN 1995N". In: *ApJ* 690.2, pp. 1839–1846. DOI: 10.1088/0004-637X/690/2/1839. arXiv: 0809.2810 [astro-ph].

Chandra, Poonam et al. (2012). "Radio and X-Ray Observations of SN 2006jd: Another Strongly Interacting Type IIn Supernova". In: *ApJ* 755.2, 110, p. 110. DOI: 10.1088/0004-637X/755/2/110. arXiv: 1205.0250 [astro-ph.HE].

Chandra, Poonam et al. (2015). "X-Ray and Radio Emission from Type IIn Supernova SN 2010jl". In: *ApJ* 810.1, 32, p. 32. DOI: 10.1088/0004-637X/810/1/32. arXiv: 1507.06059 [astro-ph.HE].

Chandra, Poonam et al. (June 2019). "Type Ib Supernova Master OT J120451.50+265946.6: Radio-emitting Shock with Inhomogeneities Crossing through a Dense Shell". In: *ApJ* 877.2, 79, p. 79. DOI: 10.3847/1538-4357/ab1900. arXiv: 1904.06392 [astro-ph.HE].

Chandra, Poonam et al. (Oct. 2020). "Supernova Interaction with a Dense Detached Shell in SN 2001em". In: *ApJ* 902.1, 55, p. 55. DOI: 10.3847/1538-4357/abb460. arXiv: 2008.13724 [astro-ph.HE].

Chashkina, Anna et al. (2019). "Super-Eddington accretion discs with advection and outflows around magnetized neutron stars". In: *A&A* 626, A18, A18. DOI: 10.1051/0004-6361/201834414. arXiv: 1902.04609 [astro-ph.HE].

Chevalier, R. A. (July 1982a). "Self-similar solutions for the interaction of stellar ejecta with an external medium". In: *ApJ* 258, pp. 790–797. DOI: 10.1086/160126.

— (Aug. 1982b). "The radio and X-ray emission from type II supernovae". In: *ApJ* 259, pp. 302–310. DOI: 10.1086/160167.

— (May 1998). "Synchrotron Self-Absorption in Radio Supernovae". In: *ApJ* 499, pp. 810–819. DOI: 10.1086/305676.

Chevalier, R. A. and C. Fransson (Nov. 2006). "Circumstellar Emission from Type Ib and Ic Supernovae". In: *ApJ* 651, pp. 381–391. DOI: 10.1086/507606. eprint: astro-ph/0607196.

Chevalier, R. A., C. Fransson, and T. K. Nymark (Apr. 2006). "Radio and X-Ray Emission as Probes of Type IIP Supernovae and Red Supergiant Mass Loss". In: *ApJ* 641, pp. 1029–1038. DOI: 10.1086/500528. eprint: astro-ph/0509468.

Chevalier, Roger A. and Claes Fransson (Jan. 1994). "Emission from Circumstellar Interaction in Normal Type II Supernovae". In: *ApJ* 420, p. 268. DOI: 10.1086/173557.

— (2017). "Thermal and Non-thermal Emission from Circumstellar Interaction". In: *Handbook of Supernovae*. Ed. by Athem W. Alsabti and Paul Murdin, p. 875. DOI: 10.1007/978-3-319-21846-5_34.

Chomiuk, Laura (2013). "SN 2011fe: A Laboratory for Testing Models of Type Ia Supernovae". In: *Publ. Astron. Soc. Australia* 30, e046, e046. DOI: 10.1017/pasa.2013.24. arXiv: 1307.2721 [astro-ph.HE].

Chugai, N. N. and I. J. Danziger (May 1994). "SN 1988Z: low-mass ejecta colliding with the clumpy wind?" In: *MNRAS* 268, pp. 173–180. DOI: 10.1093/mnras/268.1.173.

Cioffi, Denis F., Christopher F. McKee, and Edmund Bertschinger (Nov. 1988). "Dynamics of Radiative Supernova Remnants". In: *ApJ* 334, p. 252. DOI: 10.1086/166834.

Corsi, A. et al. (Feb. 2014). "A Multi-wavelength Investigation of the Radio-loud Supernova PTF11qcj and its Circumstellar Environment". In: *ApJ* 782.1, 42, p. 42. DOI: 10.1088/0004-637X/782/1/42. arXiv: 1307.2366 [astro-ph.HE].

Cowperthwaite, P. S. et al. (2017). "The Electromagnetic Counterpart of the Binary Neutron Star Merger LIGO/Virgo GW170817. II. UV, Optical, and Near-infrared Light Curves and Comparison to Kilonova Models". In: *ApJ* 848.2, L17, p. L17. DOI: 10.3847/2041-8213/aa8fc7. arXiv: 1710.05840 [astro-ph.HE].

Dall'Ora, M. et al. (June 2014). "The Type IIP Supernova 2012aw in M95: Hydrodynamical Modeling of the Photospheric Phase from Accurate Spectrophotometric Monitoring". In: *ApJ* 787.2, 139, p. 139. DOI: 10.1088/0004-637X/787/2/139. arXiv: 1404.1294 [astro-ph.SR].

Davies, Ben and Emma R. Beasor (July 2020a). "'On the red supergiant problem': a rebuttal, and a consensus on the upper mass cut-off for II-P progenitors". In: *MNRAS* 496.1, pp. L142–L146. DOI: 10.1093/mnrasl/slaa102. arXiv: 2005.13855 [astro-ph.SR].

— (Mar. 2020b). "The 'red supergiant problem': the upper luminosity boundary of Type II supernova progenitors". In: *MNRAS* 493.1, pp. 468–476. DOI: 10.1093/mnras/staa174. arXiv: 2001.06020 [astro-ph.SR].

De, K. et al. (2018). "A hot and fast ultra-stripped supernova that likely formed a compact neutron star binary". In: *Science* 362.6411, pp. 201–206. DOI: 10.1126/science.aas8693. arXiv: 1810.05181 [astro-ph.HE].

DeLaney, Tracey and Lawrence Rudnick (June 2003). "The First Measurement of Cassiopeia A's Forward Shock Expansion Rate". In: *ApJ* 589.2, pp. 818–826. DOI: 10.1086/374813. arXiv: astro-ph/0303399 [astro-ph].

DeMarchi, Lindsay et al. (Oct. 2022). "Radio Analysis of SN2004C Reveals an Unusual CSM Density Profile as a Harbinger of Core Collapse". In: *The Astrophysical Journal* 938.1, 84, p. 84. DOI: 10.3847/1538-4357/ac8c26. arXiv: 2203.07388 [astro-ph.HE].

Dessart, Luc et al. (May 2016). "Inferring supernova IIb/Ib/Ic ejecta properties from light curves and spectra: correlations from radiative-transfer models". In: *MNRAS* 458.2, pp. 1618–1635. DOI: 10.1093/mnras/stw418. arXiv: 1602.06280 [astro-ph.SR].

Draine, Bruce T. (2010). *Physics of the Interstellar and Intergalactic Medium*. Princeton University Press. ISBN: 9781400839087. DOI: doi:10.1515/9781400839087. URL: https://doi.org/10.1515/9781400839087.

Drout, M. R. et al. (2013). "The Fast and Furious Decay of the Peculiar Type Ic Supernova 2005ek". In: *ApJ* 774.1, 58, p. 58. DOI: 10.1088/0004-637X/774/1/58. arXiv: 1306.2337 [astro-ph.HE].

Drury, L. O. (Aug. 1983). "An introduction to the theory of diffusive shock acceleration of energetic particles in tenuous plasmas". In: *Reports on Progress in Physics* 46, pp. 973–1027. DOI: 10.1088/0034-4885/46/8/002.

Dubner, Gloria and Elsa Giacani (Sept. 2015). "Radio emission from supernova remnants". In: *A&ARv* 23, 3, p. 3. DOI: 10.1007/s00159-015-0083-5. arXiv: 1508.07294 [astro-ph.HE].

Duncan, Ruby A., Alexander J. van der Horst, and Paz Beniamini (Jan. 2023). "Constraints on electron acceleration in gamma-ray bursts afterglows from radio peaks". In: *MNRAS* 518.1, pp. 1522–1530. DOI: 10.1093/mnras/stac3172. arXiv: 2211.00686 [astro-ph.HE].

Dwarkadas, Vikram V. (Sept. 2005). "The Evolution of Supernovae in Circumstellar Wind-Blown Bubbles. I. Introduction and One-Dimensional Calculations". In: *ApJ* 630.2, pp. 892–910. DOI: 10.1086/432109. arXiv: astro-ph/0410464 [astro-ph].

— (Sept. 2007). "The Evolution of Supernovae in Circumstellar Wind Bubbles. II. Case of a Wolf-Rayet Star". In: *ApJ* 667.1, pp. 226–247. DOI: 10.1086/520670. arXiv: 0706.1049 [astro-ph].

Eichler, David and Eli Waxman (July 2005). "The Efficiency of Electron Acceleration in Collisionless Shocks and Gamma-Ray Burst Energetics". In: *ApJ* 627.2, pp. 861–867. DOI: 10.1086/430596. arXiv: astro-ph/0502070 [astro-ph].

Eldridge, John J. et al. (2013). "The death of massive stars - II. Observational constraints on the progenitors of Type Ibc supernovae". In: *MNRAS* 436.1, pp. 774–795. DOI: 10.1093/mnras/stt1612. arXiv: 1301.1975 [astro-ph.SR].

Ellison, Donald C., Patrick Slane, and Bryan M. Gaensler (Dec. 2001). "Broadband Observations and Modeling of the Shell-Type Supernova Remnant G347.3-0.5". In: *ApJ* 563.1, pp. 191–201. DOI: 10.1086/323687. arXiv: astro-ph/0106257 [astro-ph].

Ensman, Lisa M. and S. E. Woosley (1988). "Explosions in Wolf-Rayet Stars and Type Ib Supernovae. I. Light Curves". In: *ApJ* 333, p. 754. DOI: 10.1086/166785.

Fang, Qiliang et al. (2019). "A hybrid envelope-stripping mechanism for massive stars from supernova nebular spectroscopy". In: *Nature Astronomy* 3, pp. 434–439. DOI: 10.1038/s41550-019-0710-6. URL: https://www.nature.com/articles/s41550-019-0710-6.

Faran, T. et al. (2014). "A sample of Type II-L supernovae". In: *MNRAS* 445.1, pp. 554–569. DOI: 10.1093/mnras/stu1760. arXiv: 1409.1536 [astro-ph.HE].

Fermi, E. (Apr. 1949). "On the Origin of the Cosmic Radiation". In: *Physical Review* 75, pp. 1169–1174. DOI: 10.1103/PhysRev.75.1169.

Ferrand, Gilles, Anne Decourchelle, and Samar Safi-Harb (July 2014). "Three-dimensional Simulations of the Non-thermal Broadband Emission from Young Supernova Remnants Including Efficient Particle Acceleration". In: *ApJ* 789.1, 49, p. 49. DOI: 10.1088/0004-637X/789/1/49. arXiv: 1405.0614 [astro-ph.HE].

Filippenko, A. V. (1997). "Optical Spectra of Supernovae". In: *ARA&A* 35, pp. 309–355. DOI: 10.1146/annurev.astro.35.1.309.

Filippenko, Alexei V. et al. (Jan. 1992a). "The Peculiar Type IA SN 1991T: Detonation of a White Dwarf?" In: *ApJ* 384, p. L15. DOI: 10.1086/186252.

Filippenko, Alexei V. et al. (1992b). "The Subluminous, Spectroscopically Peculiar Type 1a Supernova 1991bg in the Elliptical Galaxy NGC 4374". In: *AJ* 104, p. 1543. DOI: 10.1086/116339.

Fink, M. et al. (May 2010). "Double-detonation sub-Chandrasekhar supernovae: can minimum helium shell masses detonate the core?" In: *A&A* 514, A53, A53. DOI: 10.1051/0004-6361/200913892. arXiv: 1002.2173 [astro-ph.SR].

Foley, Ryan J. et al. (Apr. 2013). "Type Iax Supernovae: A New Class of Stellar Explosion". In: *ApJ* 767.1, 57, p. 57. DOI: 10.1088/0004-637X/767/1/57. arXiv: 1212.2209 [astro-ph.SR].

Foreman-Mackey, Daniel (June 2016). "corner.py: Scatterplot matrices in Python". In: *The Journal of Open Source Software* 1, p. 24. DOI: 10.21105/joss.00024.

Foreman-Mackey, Daniel et al. (Mar. 2013). "emcee: The MCMC Hammer". In: *PASP* 125.925, p. 306. DOI: 10.1086/670067. arXiv: 1202.3665 [astro-ph.IM].

Forster, F. et al. (Aug. 2018). "The delay of shock breakout due to circumstellar material evident in most type II supernovae." In: *Nature Astronomy* 2, pp. 808–818. arXiv: 1809.06379 [astro-ph.HE].

Fransson, C. and C.-I. Björnsson (Dec. 1998). "Radio Emission and Particle Acceleration in SN 1993J". In: *ApJ* 509, pp. 861–878. DOI: 10.1086/306531. eprint: astro-ph/9807030.

Fransson, Claes, Peter Lundqvist, and Roger A. Chevalier (Apr. 1996). "Circumstellar Interaction in SN 1993J". In: *ApJ* 461, p. 993. DOI: 10.1086/177119.

Fransson, Claes et al. (Dec. 2014). "High-density Circumstellar Interaction in the Luminous Type IIn SN 2010jl: The First 1100 Days". In: *ApJ* 797.2, 118, p. 118. DOI: 10.1088/0004-637X/797/2/118. arXiv: 1312.6617 [astro-ph.HE].

Fukui, Yasuo et al. (Oct. 2003). "Discovery of Interacting Molecular Gas toward the TeV Gamma-Ray Peak of the SNR G 347.3–0.5". In: *PASJ* 55, pp. L61–L64. DOI: 10.1093/pasj/55.5.L61.

Gaensler, B. M., A. J. Green, and R. N. Manchester (Sept. 1998). "G309.2-00.6 and jets in supernova remnants". In: *MNRAS* 299.3, pp. 812–824. DOI: 10.1046/j.1365-8711.1998.01814.x. arXiv: astro-ph/9805163 [astro-ph].

Gaensler, B. M. and B. J. Wallace (Sept. 2003). "A Multifrequency Radio Study of Supernova Remnant G292.0+1.8 and Its Pulsar Wind Nebula". In: *ApJ* 594.1, pp. 326–339. DOI: 10.1086/376861. arXiv: astro-ph/0305168 [astro-ph].

Gagliano, Alexander et al. (Jan. 2022). "An Early-time Optical and Ultraviolet Excess in the Type-Ic SN 2020oi". In: *ApJ* 924.2, 55, p. 55. DOI: 10.3847/1538-4357/ac35ec. arXiv: 2105.09963 [astro-ph.HE].

Gal-Yam, Avishay et al. (2007). "On the Progenitor of SN 2005gl and the Nature of Type IIn Supernovae". In: *ApJ* 656.1, pp. 372–381. DOI: 10.1086/510523. arXiv: astro-ph/0608029 [astro-ph].

Galama, T. J. et al. (Oct. 1998). "An unusual supernova in the error box of the γ-ray burst of 25 April 1998". In: *Nature* 395.6703, pp. 670–672. DOI: 10.1038/27150. arXiv: astro-ph/9806175 [astro-ph].

Ganeshalingam, Mohan et al. (June 2012). "The Low-velocity, Rapidly Fading Type Ia Supernova 2002es". In: *ApJ* 751.2, 142, p. 142. DOI: 10.1088/0004-637X/751/2/142. arXiv: 1202.3140 [astro-ph.CO].

Gerke, J. R., C. S. Kochanek, and K. Z. Stanek (July 2015). "The search for failed supernovae with the Large Binocular Telescope: first candidates". In: *MNRAS* 450.3, pp. 3289–3305. DOI: 10.1093/mnras/stv776. arXiv: 1411.1761 [astro-ph.SR].

Gök, F. and A. Sezer (Jan. 2012). "Ejecta detection in the middle-aged Galactic supernova remnant G296.1-0.5 observed with Suzaku". In: *MNRAS* 419.2, pp. 1603–1609. DOI: 10.1111/j.1365-2966.2011.19822.x. arXiv: 1109.3971 [astro-ph.HE].

Graham, Matthew J. et al. (2019). "The Zwicky Transient Facility: Science Objectives". In: *PASP* 131.1001, p. 078001. DOI: 10.1088/1538-3873/ab006c. arXiv: 1902.01945 [astro-ph.IM].

Granot, Jonathan and Re'em Sari (Apr. 2002). "The Shape of Spectral Breaks in Gamma-Ray Burst Afterglows". In: *ApJ* 568.2, pp. 820–829. DOI: 10.1086/338966. arXiv: astro-ph/0108027 [astro-ph].

Green, D. A. (June 2017). "VizieR Online Data Catalog: A Catalogue of Galactic Supernova Remnants (Green 2017)". In: *VizieR Online Data Catalog*, VII/278, pp. VII/278.

— (Aug. 2019). "A revised catalogue of 294 Galactic supernova remnants". In: *Journal of Astrophysics and Astronomy* 40.4, 36, p. 36. DOI: 10.1007/s12036-019-9601-6. arXiv: 1907.02638 [astro-ph.GA].

Groh, Jose H., Cyril Georgy, and Sylvia Ekström (2013). "Progenitors of supernova Ibc: a single Wolf-Rayet star as the possible progenitor of the SN Ib iPTF13bvn". In: *A&A* 558, L1, p. L1. DOI: 10.1051/0004-6361/201322369. arXiv: 1307.8434 [astro-ph.SR].

Ha, Ji-Hoon et al. (Sept. 2018). "Proton Acceleration in Weak Quasi-parallel Intracluster Shocks: Injection and Early Acceleration". In: *ApJ* 864.2, 105, p. 105. DOI: 10.3847/1538-4357/aad634. arXiv: 1807.09403 [astro-ph.HE].

Harten, Ami and James M. Hyman (May 1983). "Self-Adjusting Grid Methods for One-Dimensional Hyperbolic Conservation Laws". In: *Journal of Computational Physics* 50.2, pp. 235–269. DOI: 10.1016/0021-9991(83)90066-9.

Haynie, Annastasia and Anthony L. Piro (Apr. 2021). "Shock Breakout in Dense Circumstellar Material with Application to PS1-13arp". In: *ApJ* 910.2, 128, p. 128. DOI: 10.3847/1538-4357/abe938. arXiv: 2011.01937 [astro-ph.HE].

Heger, A. and S. E. Woosley (Mar. 2002). "The Nucleosynthetic Signature of Population III". In: *ApJ* 567.1, pp. 532–543. DOI: 10.1086/338487. arXiv: astro-ph/0107037 [astro-ph].

Hendry, M. A. et al. (2005). "A study of the Type II-P supernova 2003gd in M74". In: *MNRAS* 359.3, pp. 906–926. DOI: 10.1111/j.1365-2966.2005.08928.x. arXiv: astro-ph/0501341 [astro-ph].

Hijikawa, Kotaro et al. (2019). "The Rate of iPTF 14gqr like Ultra-stripped Supernovae and Binary Evolution Leading to Double Neutron Star Formation". In: *ApJ* 882.2, 93, p. 93. DOI: 10.3847/1538-4357/ab321c. arXiv: 1903.07575 [astro-ph.HE].

Hillebrandt, Wolfgang and Jens C. Niemeyer (2000). "Type IA Supernova Explosion Models". In: *ARA&A* 38, pp. 191–230. DOI: 10.1146/annurev.astro.38.1.191. arXiv: astro-ph/0006305 [astro-ph].

Hiramatsu, Daichi et al. (June 2021). "The electron-capture origin of supernova 2018zd". In: *Nature Astronomy* 5, pp. 903–910. DOI: 10.1038/s41550-021-01384-2. arXiv: 2011.02176 [astro-ph.HE].

Ho, Anna Y. Q. et al. (2019). "AT2018cow: A Luminous Millimeter Transient". In: *ApJ* 871.1, 73, p. 73. DOI: 10.3847/1538-4357/aaf473. arXiv: 1810.10880 [astro-ph.HE].

Höflich, Peter, J. Craig Wheeler, and Lifan Wang (Aug. 1999). "Aspherical Explosion Models for SN 1998BW/GRB-980425". In: *ApJ* 521.1, pp. 179–189. DOI: 10.1086/307521. arXiv: astro-ph/9808086 [astro-ph].

Horesh, Assaf et al. (Nov. 2020). "A Non-equipartition Shock Wave Traveling in a Dense Circumstellar Environment around SN 2020oi". In: *ApJ* 903.2, 132, p. 132. DOI: 10.3847/1538-4357/abbd38. arXiv: 2006.13952 [astro-ph.HE].

Hotokezaka, Kenta et al. (Nov. 2013). "Progenitor Models of the Electromagnetic Transient Associated with the Short Gamma Ray Burst 130603B". In: *ApJ* 778.1, L16, p. L16. DOI: 10.1088/2041-8205/778/1/L16. arXiv: 1310.1623 [astro-ph.HE].

Howell, D. Andrew et al. (Sept. 2006). "The type Ia supernova SNLS-03D3bb from a super-Chandrasekhar-mass white dwarf star". In: *Nature* 443.7109, pp. 308–311. DOI: 10.1038/nature05103. arXiv: astro-ph/0609616 [astro-ph].

Huang, F. et al. (Apr. 2018). "SN 2016X: a type II-P supernova with a signature of shock breakout from explosion of a massive red supergiant". In: *MNRAS* 475.3, pp. 3959–3973. DOI: 10.1093/mnras/sty066. arXiv: 1801.03167 [astro-ph.HE].

Hui, C. Y. and W. Becker (Feb. 2009). "Exploring the X-ray emission properties of the supernova remnant G67.7+1.8 and its central X-ray sources". In: *A&A* 494.3, pp. 1005–1012. DOI: 10.1051/0004-6361:200810789. arXiv: 0812.2186 [astro-ph].

Hunter, D. J. et al. (Dec. 2009). "Extensive optical and near-infrared observations of the nearby, narrow-lined type Ic <ASTROBJ>SN 2007gr</ASTROBJ>: days 5 to 415". In: *A&A* 508.1, pp. 371–389. DOI: 10.1051/0004-6361/200912896. arXiv: 0909.3780 [astro-ph.SR].

Iaconi, Roberto et al. (Nov. 2019). "Properties of the post-inspiral common envelope ejecta - I. Dynamical and thermal evolution". In: *MNRAS* 489.3, pp. 3334–3350. DOI: 10.1093/mnras/stz2312. arXiv: 1907.03980 [astro-ph.SR].

Iben I., Jr. and A. V. Tutukov (1984). "Supernovae of type I as end products of the evolution of binaries with components of moderate initial mass." In: *ApJS* 54, pp. 335–372. DOI: 10.1086/190932.

Imasheva, Liliya, Hans-Thomas Janka, and Achim Weiss (Jan. 2023). "Parametrizations of thermal bomb explosions for core-collapse supernovae and ^{56}Ni production". In: *MNRAS* 518.2, pp. 1818–1839. DOI: 10.1093/mnras/stac3239. arXiv: 2209.10989 [astro-ph.HE].

Ivanova, N. et al. (Feb. 2013). "Common envelope evolution: where we stand and how we can move forward". In: *A&ARv* 21, 59, p. 59. DOI: 10.1007/s00159-013-0059-2. arXiv: 1209.4302 [astro-ph.HE].

Iwamoto, Koichi et al. (Dec. 1999). "Nucleosynthesis in Chandrasekhar Mass Models for Type IA Supernovae and Constraints on Progenitor Systems and Burning-Front Propagation". In: *ApJS* 125.2, pp. 439–462. DOI: 10.1086/313278. arXiv: astro-ph/0002337 [astro-ph].

Izzo, L. et al. (Jan. 2019). "Signatures of a jet cocoon in early spectra of a supernova associated with a γ-ray burst". In: *Nature* 565.7739, pp. 324–327. DOI: 10.1038/s41586-018-0826-3. arXiv: 1901.05500 [astro-ph.HE].

Jacobson-Galán, Wynn V. et al. (Aug. 2020). "SN 2019ehk: A Double-peaked Ca-rich Transient with Luminous X-Ray Emission and Shock-ionized Spectral Features". In: *ApJ* 898.2, 166, p. 166. DOI: 10.3847/1538-4357/ab9e66. arXiv: 2005.01782 [astro-ph.HE].

Janka, Hans-Thomas (2012). "Explosion Mechanisms of Core-Collapse Supernovae". In: *Annual Review of Nuclear and Particle Science* 62.1, pp. 407–451. DOI: 10.1146/annurev-nucl-102711-094901. arXiv: 1206.2503 [astro-ph.SR].

Janka, Hans-Thomas (2017). "Neutrino-Driven Explosions". In: *Handbook of Supernovae*. Ed. by Athem W. Alsabti and Paul Murdin. Cham: Springer International Publishing, pp. 1095–1150. ISBN: 978-3-319-21846-5. DOI: 10.1007/978-3-319-21846-5_109. URL: https://doi.org/10.1007/978-3-319-21846-5_109.

Jones, S. et al. (Aug. 2013). "Advanced Burning Stages and Fate of 8-10 M $_\odot$ Stars". In: *ApJ* 772.2, 150, p. 150. DOI: 10.1088/0004-637X/772/2/150. arXiv: 1306.2030 [astro-ph.SR].

Kalogera, Vassiliki and Gordon Baym (Oct. 1996). "The Maximum Mass of a Neutron Star". In: *ApJ* 470, p. L61. DOI: 10.1086/310296. arXiv: astro-ph/9608059 [astro-ph].

Kamble, Atish et al. (Dec. 2014). "Radio Observations Reveal a Smooth Circumstellar Environment Around the Extraordinary Type Ib Supernova 2012au". In: *ApJ* 797.1, 2, p. 2. DOI: 10.1088/0004-637X/797/1/2.

Kamble, Atish et al. (Feb. 2016). "Progenitors of Type IIB Supernovae in the Light of Radio and X-Rays from SN 2013DF". In: *ApJ* 818.2, 111, p. 111. DOI: 10.3847/0004-637X/818/2/111. arXiv: 1504.07988 [astro-ph.HE].

Kasen, Daniel and Peter E. Nugent (2013). "The Supernova in the Pinwheel Galaxy". In: *Annual Review of Nuclear and Particle Science* 63, pp. 153–174. DOI: 10.1146/annurev-nucl-102212-170624.

Kasen, Daniel and S. E. Woosley (2009). "Type II Supernovae: Model Light Curves and Standard Candle Relationships". In: *ApJ* 703.2, pp. 2205–2216. DOI: 10.1088/0004-637X/703/2/2205. arXiv: 0910.1590 [astro-ph.CO].

Kashiyama, Kazumi, Kenta Hotokezaka, and Kohta Murase (Aug. 2018). "Radio transients from newborn black holes". In: *MNRAS* 478.2, pp. 2281–2290. DOI: 10.1093/mnras/sty1145. arXiv: 1710.10765 [astro-ph.HE].

Kasliwal, Mansi M. et al. (2010). "Rapidly Decaying Supernova 2010X: A Candidate ".Ia" Explosion". In: *ApJ* 723.1, pp. L98–L102. DOI: 10.1088/2041-8205/723/1/L98. arXiv: 1009.0960 [astro-ph.HE].

Katsuda, S. et al. (Dec. 2016). "Two Distinct-absorption X-Ray Components from Type IIn Supernovae: Evidence for Asphericity in the Circumstellar Medium". In: *ApJ* 832, 194, p. 194. DOI: 10.3847/0004-637X/832/2/194. arXiv: 1609.09093 [astro-ph.HE].

Khatami, David K. and Daniel N. Kasen (June 2019). "Physics of Luminous Transient Light Curves: A New Relation between Peak Time and Luminosity". In: *ApJ* 878.1, 56, p. 56. DOI: 10.3847/1538-4357/ab1f09. arXiv: 1812.06522 [astro-ph.HE].

Kiewe, Michael et al. (Jan. 2012). "Caltech Core-Collapse Project (CCCP) Observations of Type IIn Supernovae: Typical Properties and Implications for Their Progenitor Stars". In: *ApJ* 744.1, 10, p. 10. DOI: 10.1088/0004-637X/744/1/10. arXiv: 1010.2689 [astro-ph.CO].

Kilpatrick, Charles D. et al. (Mar. 2017). "On the progenitor of the Type IIb supernova 2016gkg". In: *MNRAS* 465.4, pp. 4650–4657. DOI: 10.1093/mnras/stw3082. arXiv: 1610.04587 [astro-ph.SR].

Kilpatrick, Charles D. et al. (Sept. 2022). "Updated Photometry of the Yellow Supergiant Progenitor and Late-time Observations of the Type IIb Supernova SN 2016gkg". In: *ApJ* 936.2, 111, p. 111. DOI: 10.3847/1538-4357/ac8a4c. arXiv: 2112.03308 [astro-ph.HE].

Kippenhahn, Rudolf, Alfred Weigert, and Achim Weiss (2013). *Stellar Structure and Evolution*. DOI: 10.1007/978-3-642-30304-3.

Kitaura, F. S., H. Th. Janka, and W. Hillebrandt (Apr. 2006). "Explosions of O-Ne-Mg cores, the Crab supernova, and subluminous type II-P supernovae". In: *A&A* 450.1, pp. 345–350. DOI: 10.1051/0004-6361:20054703. arXiv: astro-ph/0512065 [astro-ph].

Kochanek, C. S. (Apr. 2020). "On the red supergiant problem". In: *MNRAS* 493.4, pp. 4945–4949. DOI: 10.1093/mnras/staa605. arXiv: 2001.07216 [astro-ph.SR].

Krauss, M. I. et al. (May 2012). "Expanded Very Large Array Observations of the Radio Evolution of SN 2011dh". In: *ApJ* 750.2, L40, p. L40. DOI: 10.1088/2041-8205/750/2/L40. arXiv: 1201.0770 [astro-ph.HE].

Kulkarni, S. R. et al. (Oct. 1998). "Radio emission from the unusual supernova 1998bw and its association with the γ-ray burst of 25 April 1998". In: *Nature* 395.6703, pp. 663–669. DOI: 10.1038/27139.

Kumar, Brajesh et al. (Sept. 2019). "On the observational behaviour of the highly polarized Type IIn supernova SN 2017hcc". In: *MNRAS* 488.3, pp. 3089–3099. DOI: 10.1093/mnras/stz1914. arXiv: 1907.03160 [astro-ph.HE].

Kurfürst, P. and J. Krtička (May 2019). "Modeling of interactions between supernovae ejecta and aspherical circumstellar environments". In: *A&A* 625, A24, A24. DOI: 10.1051/0004-6361/201833429. arXiv: 1904.01312 [astro-ph.SR].

Lacy, M. et al. (Mar. 2020). "The Karl G. Jansky Very Large Array Sky Survey (VLASS). Science Case and Survey Design". In: *PASP* 132.1009, 035001, p. 035001. DOI: 10.1088/1538-3873/ab63eb. arXiv: 1907.01981 [astro-ph.IM].

Lau, Mike Y. M. et al. (June 2022). "Common envelopes in massive stars: towards the role of radiation pressure and recombination energy in ejecting red supergiant envelopes". In: *MNRAS* 512.4, pp. 5462–5480. DOI: 10.1093/mnras/stac049. arXiv: 2111.00923 [astro-ph.SR].

Law-Smith, Jamie A. P. et al. (Nov. 2020). "Successful Common Envelope Ejection and Binary Neutron Star Formation in 3D Hydrodynamics". In: *arXiv e-prints*, arXiv:2011.06630, arXiv:2011.06630. arXiv: 2011.06630 [astro-ph.HE].

Lee, S.-H., D. C. Ellison, and S. Nagataki (May 2012). "A Generalized Model of Nonlinear Diffusive Shock Acceleration Coupled to an Evolving Supernova Remnant". In: *ApJ* 750, 156, p. 156. DOI: 10.1088/0004-637X/750/2/156. arXiv: 1203.3614 [astro-ph.HE].

Li, Weidong et al. (Feb. 2005). "On the Progenitor of the Type II Supernova 2004et in NGC 6946". In: *PASP* 117.828, pp. 121–131. DOI: 10.1086/428278. arXiv: astro-ph/0412487 [astro-ph].

Lovchinsky, I. et al. (Apr. 2011). "A Chandra Observation of Supernova Remnant G350.1-0.3 and Its Central Compact Object". In: *ApJ* 731.1, 70, p. 70. DOI: 10.1088/0004-637X/731/1/70. arXiv: 1102.5333 [astro-ph.HE].

Lundqvist, P. and C. Fransson (1988). "Circumstellar absorption of UV and radio emission from supernovae." In: *A&A* 192, pp. 221–233.

Lyman, J. D. et al. (Mar. 2016). "Bolometric light curves and explosion parameters of 38 stripped-envelope core-collapse supernovae". In: *MNRAS* 457.1, pp. 328–350. DOI: 10.1093/mnras/stv2983. arXiv: 1406.3667 [astro-ph.SR].

Madau, Piero and Mark Dickinson (Aug. 2014). "Cosmic Star-Formation History". In: *ARA&A* 52, pp. 415–486. DOI: 10.1146/annurev-astro-081811-125615. arXiv: 1403.0007 [astro-ph.CO].

Maeda, K. (Oct. 2012). "Injection and Acceleration of Electrons at a Strong Shock: Radio and X-Ray Study of Young Supernova 2011dh". In: *ApJ* 758, 81, p. 81. DOI: 10.1088/0004-637X/758/2/81. arXiv: 1209.1466 [astro-ph.HE].

Maeda, K. et al. (July 2015). "Type IIb Supernova 2013df Entering into an Interaction Phase: A Link between the Progenitor and the Mass Loss". In: *ApJ* 807.1, 35, p. 35. DOI: 10.1088/0004-637X/807/1/35. arXiv: 1504.06668 [astro-ph.SR].

Maeda, Keiichi (2013a). "Probing Shock Breakout and Progenitors of Stripped-envelope Supernovae through their Early Radio Emissions". In: *ApJ* 762.1, 14, p. 14. DOI: 10.1088/0004-637X/762/1/14. arXiv: 1209.1904 [astro-ph.HE].

— (Jan. 2013b). "Young Supernovae as Experimental Sites for Studying the Electron Acceleration Mechanism". In: *ApJ* 762.2, L24, p. L24. DOI: 10.1088/2041-8205/762/2/L24. arXiv: 1211.5835 [astro-ph.HE].

Maeda, Keiichi and Yukikatsu Terada (July 2016). "Progenitors of type Ia supernovae". In: *International Journal of Modern Physics D* 25.10, 1630024, p. 1630024. DOI: 10.1142/S021827181630024X. arXiv: 1609.03639 [astro-ph.SR].

Maeda, Keiichi et al. (Sept. 2021). "The Final Months of Massive Star Evolution from the Circumstellar Environment around SN Ic 2020oi". In: *ApJ* 918.1, 34, p. 34. DOI: 10.3847/1538-4357/ac0dbc. arXiv: 2106.11618 [astro-ph.HE].

Maeda, Keiichi et al. (Nov. 2022). "A Multi-Wavelength View on the Rapidly-Evolving Supernova 2018ivc: An Analog of SN IIb 1993J but Powered Primarily by Circumstellar Interaction". In: *arXiv e-prints*, arXiv:2211.04808, arXiv:2211.04808. arXiv: 2211.04808 [astro-ph.HE].

Maoz, Dan, Filippo Mannucci, and Gijs Nelemans (2014). "Observational Clues to the Progenitors of Type Ia Supernovae". In: *ARA&A* 52, pp. 107–170. DOI: 10.1146/annurev-astro-082812-141031. arXiv: 1312.0628 [astro-ph.CO].

Margalit, Ben (July 2022). "Analytic Light Curves of Dense CSM Shock Breakout and Cooling". In: *ApJ* 933.2, 238, p. 238. DOI: 10.3847/1538-4357/ac771a. arXiv: 2107.04048 [astro-ph.HE].

Margalit, Ben and Brian D. Metzger (Dec. 2017). "Constraining the Maximum Mass of Neutron Stars from Multi-messenger Observations of GW170817". In: *ApJ* 850.2, L19, p. L19. DOI: 10.3847/2041-8213/aa991c. arXiv: 1710.05938 [astro-ph.HE].

Margutti, R. et al. (2014). "Relativistic Supernovae have Shorter-lived Central Engines or More Extended Progenitors: The Case of SN 2012ap". In: *ApJ* 797.2, 107, p. 107. DOI: 10.1088/0004-637X/797/2/107. arXiv: 1402.6344 [astro-ph.HE].

Margutti, R. et al. (Feb. 2019). "An Embedded X-Ray Source Shines through the Aspherical AT 2018cow: Revealing the Inner Workings of the Most Luminous Fast-evolving Optical Transients". In: *ApJ* 872.1, 18, p. 18. DOI: 10.3847/1538-4357/aafa01. arXiv: 1810.10720 [astro-ph.HE].

Margutti, Raffaella et al. (Feb. 2017). "Ejection of the Massive Hydrogen-rich Envelope Timed with the Collapse of the Stripped SN 2014C". In: *ApJ* 835.2, 140, p. 140. DOI: 10.3847/1538-4357/835/2/140. arXiv: 1601.06806 [astro-ph.HE].

Martí-Vidal, I. et al. (Feb. 2011). "Radio emission of SN1993J: the complete picture. II. Simultaneous fit of expansion and radio light curves". In: *A&A* 526, A143, A143. DOI: 10.1051/0004-6361/201014517. arXiv: 1007.1224 [astro-ph.HE].

Matsuoka, Tomoki and Keiichi Maeda (Aug. 2020). "Radio Emission from Ultra-stripped Supernovae as Diagnostics for Properties of the Remnant Double Neutron Star Binaries". In: *ApJ* 898.2, 158, p. 158. DOI: 10.3847/1538-4357/ab9c1b. arXiv: 2006.06689 [astro-ph.HE].

Matsuoka, Tomoki et al. (2019). "Radio Emission from Supernovae in the Very Early Phase: Implications for the Dynamical Mass Loss of Massive Stars". In: *ApJ* 885.1, 41, p. 41. DOI: 10.3847/1538-4357/ab4421.

Matsuoka, Tomoki et al. (May 2022). "Long-term Evolution of a Supernova Remnant Hosting a Double Neutron Star Binary". In: *ApJ* 930.2, 143, p. 143. DOI: 10.3847/1538-4357/ac67a4. arXiv: 2204.06706 [astro-ph.HE].

Matzner, Christopher D. and Christopher F. McKee (1999). "The Expulsion of Stellar Envelopes in Core-Collapse Supernovae". In: *ApJ* 510.1, pp. 379–403. DOI: 10.1086/306571. arXiv: astro-ph/9807046 [astro-ph].

Maund, J. R. et al. (Oct. 2011). "The Yellow Supergiant Progenitor of the Type II Supernova 2011dh in M51". In: *ApJ* 739.2, L37, p. L37. DOI: 10.1088/2041-8205/739/2/L37. arXiv: 1106.2565 [astro-ph.SR].

Maund, Justyn R. et al. (Jan. 2004). "The massive binary companion star to the progenitor of supernova 1993J". In: *Nature* 427.6970, pp. 129–131. DOI: 10.1038/nature02161. arXiv: astro-ph/0401090 [astro-ph].

Mazzali, P. A. et al. (June 2002). "The Type Ic Hypernova SN 2002ap". In: *ApJ* 572.1, pp. L61–L65. DOI: 10.1086/341504.

Mazzali, Paolo A. et al. (Oct. 2009). "SN 2003bg: A Broad-Lined Type IIb Supernova with Hydrogen". In: *ApJ* 703.2, pp. 1624–1634. DOI: 10.1088/0004-637X/703/2/1624. arXiv: 0908.1773 [astro-ph.HE].

McKee, C. F. and J. P. Ostriker (Nov. 1977). "A theory of the interstellar medium: three components regulated by supernova explosions in an inhomogeneous substrate." In: *ApJ* 218, pp. 148–169. DOI: 10.1086/155667.

McWilliam, Andrew (Jan. 1997). "Abundance Ratios and Galactic Chemical Evolution". In: *ARA&A* 35, pp. 503–556. DOI: 10.1146/annurev.astro.35.1.503.

Meza, N. and J. P. Anderson (Sept. 2020). "Stripped-envelope core-collapse supernova ^{56}Ni masses. Persistently larger values than supernovae type II". In: *A&A* 641, A177, A177. DOI: 10.1051/0004-6361/201937113. arXiv: 2002.01015 [astro-ph.HE].

Milisavljevic, D. et al. (Jan. 2015). "The Broad-lined Type Ic SN 2012ap and the Nature of Relativistic Supernovae Lacking a Gamma-Ray Burst Detection". In: *ApJ* 799.1, 51, p. 51. DOI: 10.1088/0004-637X/799/1/51. arXiv: 1408.1606 [astro-ph.HE].

Milisavljevic, Dan et al. (Apr. 2013a). "Multi-wavelength Observations of Supernova 2011ei: Time-dependent Classification of Type IIb and Ib Supernovae and Implications for Their Progenitors". In: *ApJ* 767.1, 71, p. 71. DOI: 10.1088/0004-637X/767/1/71. arXiv: 1207.2152 [astro-ph.HE].

Milisavljevic, Dan et al. (June 2013b). "SN 2012au: A Golden Link between Superluminous Supernovae and Their Lower-luminosity Counterparts". In: *ApJ* 770.2, L38, p. L38. DOI: 10.1088/2041-8205/770/2/L38. arXiv: 1304.0095 [astro-ph.HE].

Miller, J. M. et al. (2016). "An Ultra-fast X-Ray Disk Wind in the Neutron Star Binary GX 340+0". In: *ApJ* 822.1, L18, p. L18. DOI: 10.3847/2041-8205/822/1/L18. arXiv: 1604.03329 [astro-ph.HE].

Moffett, David A. and Stephen P. Reynolds (Dec. 1994). "Multifrequency Studies of Bright Radio Supernova Remnants. II. W49B". In: *ApJ* 437, p. 705. DOI: 10.1086/175033.

Morales-Garoffolo, A. et al. (Dec. 2014). "SN 2013df, a double-peaked IIb supernova from a compact progenitor and an extended H envelope". In: *MNRAS* 445.2, pp. 1647–1662. DOI: 10.1093/mnras/stu1837. arXiv: 1409.2784 [astro-ph.SR].

Moriya, T. J. et al. (July 2017a). "Immediate dense circumstellar environment of supernova progenitors caused by wind acceleration: its effect on supernova light curves". In: *MNRAS* 469, pp. L108–L112. DOI: 10.1093/mnrasl/slx056. arXiv: 1703.03084 [astro-ph.HE].

Moriya, Takashi J. et al. (Apr. 2014). "Mass-loss histories of Type IIn supernova progenitors within decades before their explosion". In: *MNRAS* 439.3, pp. 2917–2926. DOI: 10.1093/mnras/stu163. arXiv: 1401.4893 [astro-ph.SR].

Moriya, Takashi J. et al. (2016). "On the nature of rapidly fading Type II supernovae". In: *MNRAS* 455.1, pp. 423–430. DOI: 10.1093/mnras/stv2336. arXiv: 1510.01656 [astro-ph.HE].

Moriya, Takashi J. et al. (2017b). "Light-curve and spectral properties of ultrastripped core-collapse supernovae leading to binary neutron stars". In: *MNRAS* 466.2, pp. 2085–2098. DOI: 10.1093/mnras/stw3225. arXiv: 1612.02882 [astro-ph.HE].

Morozova, V. et al. (Nov. 2015). "Light Curves of Core-collapse Supernovae with Substantial Mass Loss Using the New Open-source SuperNova Explosion Code (SNEC)". In: *ApJ* 814, 63, p. 63. DOI: 10.1088/0004-637X/814/1/63. arXiv: 1505.06746 [astro-ph.HE].

Morozova, Viktoriya et al. (Mar. 2020). "The Influence of Late-stage Nuclear Burning on Red Supergiant Supernova Light Curves". In: *ApJ* 891.2, L32, p. L32. DOI: 10.3847/2041-8213/ab77c8. arXiv: 1912.10050 [astro-ph.HE].

Müller, B. (2016). "The Status of Multi-Dimensional Core-Collapse Supernova Models". In: *Publ. Astron. Soc. Australia* 33, e048, e048. DOI: 10.1017/pasa.2016.40. arXiv: 1608.03274 [astro-ph.SR].

Müller, Bernhard et al. (2018). "Multidimensional simulations of ultrastripped supernovae to shock breakout". In: *MNRAS* 479.3, pp. 3675–3689. DOI: 10.1093/mnras/sty1683. arXiv: 1803.03388 [astro-ph.SR].

Murase, K. et al. (Mar. 2019). "High-energy Emission from Interacting Supernovae: New Constraints on Cosmic-Ray Acceleration in Dense Circumstellar Environments". In: *ApJ* 874, 80, p. 80. DOI: 10.3847/1538-4357/ab0422. arXiv: 1807.01460 [astro-ph.HE].

Murase, Kohta, Todd A. Thompson, and Eran O. Ofek (2014). "Probing cosmic ray ion acceleration with radio-submm and gamma-ray emission from interaction-powered supernovae". In: *MNRAS* 440.3, pp. 2528–2543. DOI: 10.1093/mnras/stu384. arXiv: 1311.6778 [astro-ph.HE].

Nakamura, Ko et al. (2014). "Impacts of Rotation on Three-dimensional Hydrodynamics of Core-collapse Supernovae". In: *ApJ* 793.1, 45, p. 45. DOI: 10.1088/0004-637X/793/1/45. arXiv: 1403.7290 [astro-ph.HE].

Nakaoka, Tatsuya et al. (May 2021). "Calcium-rich Transient SN 2019ehk in a Star-forming Environment: Yet Another Candidate for a Precursor of a Double Neutron-star Binary". In: *ApJ* 912.1, 30, p. 30. DOI: 10.3847/1538-4357/abe765. arXiv: 2005.02992 [astro-ph.HE].

Nayana, A. J., Poonam Chandra, and Alak K. Ray (Aug. 2018). "Long-term Behavior of a Type IIP Supernova SN 2004dj in the Radio Bands". In: *ApJ* 863.2, 163, p. 163. DOI: 10.3847/1538-4357/aad17a.

Nayana, A. J. et al. (Aug. 2022). "Radio Evolution of a Type IIb Supernova SN 2016gkg". In: *ApJ* 934.2, 186, p. 186. DOI: 10.3847/1538-4357/ac7c1e. arXiv: 2206.12103 [astro-ph.HE].

Nugis, T. and H. J. G. L. M. Lamers (2000). "Mass-loss rates of Wolf-Rayet stars as a function of stellar parameters". In: *A&A* 360, pp. 227–244.

Ofek, E. O. et al. (Apr. 2007). "SN 2006gy: An Extremely Luminous Supernova in the Galaxy NGC 1260". In: *ApJ* 659.1, pp. L13–L16. DOI: 10.1086/516749. arXiv: astro-ph/0612408 [astro-ph].

Orlando, S. et al. (Feb. 2011). "Effects of non-uniform interstellar magnetic field on synchrotron X-ray and inverse-Compton γ-ray morphology of supernova remnants". In: *A&A* 526, A129, A129. DOI: 10.1051/0004-6361/201015505. arXiv: 1011.1847 [astro-ph.HE].

Ouchi, Ryoma and Keiichi Maeda (2017). "Radii and Mass-loss Rates of Type IIb Supernova Progenitors". In: *ApJ* 840.2, 90, p. 90. DOI: 10.3847/1538-4357/aa6ea9. arXiv: 1705.02430 [astro-ph.HE].

Ouchi, Ryoma et al. (Dec. 2021). "Are Stripped Envelope Supernovae Really Deficient in ^{56}Ni?" In: *ApJ* 922.2, 141, p. 141. DOI: 10.3847/1538-4357/ac2306. arXiv: 2109.00603 [astro-ph.HE].

Park, Jaehong, Damiano Caprioli, and Anatoly Spitkovsky (2015). "Simultaneous Acceleration of Protons and Electrons at Nonrelativistic Quasiparallel Collisionless Shocks". In: *Phys. Rev. Lett.*

114 (8), p. 085003. DOI: 10.1103/PhysRevLett.114.085003. URL: https://link.aps.org/doi/10.1103/PhysRevLett.114.085003.

Pastorello, A. et al. (Sept. 2008). "The Type IIb SN 2008ax: spectral and light curve evolution". In: *MNRAS* 389.2, pp. 955–966. DOI: 10.1111/j.1365-2966.2008.13618.x. arXiv: 0805.1914 [astro-ph].

Patat, F. et al. (Mar. 2011). "Asymmetries in the type IIn SN 2010jl". In: *A&A* 527, L6, p. L6. DOI: 10.1051/0004-6361/201016217. arXiv: 1011.5926.

Patat, Ferdinando et al. (July 2001). "The Metamorphosis of SN 1998bw". In: *ApJ* 555.2, pp. 900–917. DOI: 10.1086/321526. arXiv: astro-ph/0103111 [astro-ph].

Pavlović, M. Z. et al. (Jan. 2013). "The Radio Surface-brightness-to-Diameter Relation for Galactic Supernova Remnants: Sample Selection and Robust Analysis with Various Fitting Offsets". In: *ApJS* 204.1, 4, p. 4. DOI: 10.1088/0067-0049/204/1/4. arXiv: 1210.4602 [astro-ph.GA].

Paxton, B. et al. (Jan. 2011). "Modules for Experiments in Stellar Astrophysics (MESA)". In: *ApJS* 192, 3, p. 3. DOI: 10.1088/0067-0049/192/1/3. arXiv: 1009.1622 [astro-ph.SR].

Paxton, B. et al. (Sept. 2013). "Modules for Experiments in Stellar Astrophysics (MESA): Planets, Oscillations, Rotation, and Massive Stars". In: *ApJS* 208, 4, p. 4. DOI: 10.1088/0067-0049/208/1/4. arXiv: 1301.0319 [astro-ph.SR].

Paxton, B. et al. (Sept. 2015). "Modules for Experiments in Stellar Astrophysics (MESA): Binaries, Pulsations, and Explosions". In: *ApJS* 220, 15, p. 15. DOI: 10.1088/0067-0049/220/1/15. arXiv: 1506.03146 [astro-ph.SR].

Paxton, B. et al. (Feb. 2018). "Modules for Experiments in Stellar Astrophysics (MESA): Convective Boundaries, Element Diffusion, and Massive Star Explosions". In: *ApJS* 234, 34, p. 34. DOI: 10.3847/1538-4365/aaa5a8. arXiv: 1710.08424 [astro-ph.SR].

Pedregosa, F. et al. (2011). "Scikit-learn: Machine Learning in Python". In: *Journal of Machine Learning Research* 12, pp. 2825–2830.

Pereira, R. et al. (June 2013). "Spectrophotometric time series of SN 2011fe from the Nearby Supernova Factory". In: *A&A* 554, A27, A27. DOI: 10.1051/0004-6361/201221008. arXiv: 1302.1292 [astro-ph.CO].

Perley, Daniel A. et al. (Mar. 2019). "The fast, luminous ultraviolet transient AT2018cow: extreme supernova, or disruption of a star by an intermediate-mass black hole?" In: *MNRAS* 484.1, pp. 1031–1049. DOI: 10.1093/mnras/sty3420. arXiv: 1808.00969 [astro-ph.HE].

Petropoulou, M., A. Kamble, and L. Sironi (July 2016). "Radio synchrotron emission from secondary electrons in interaction-powered supernovae". In: *MNRAS* 460, pp. 44–66. DOI: 10.1093/mnras/stw920. arXiv: 1603.00891 [astro-ph.HE].

Phillips, M. M. (Aug. 1993). "The Absolute Magnitudes of Type IA Supernovae". In: *ApJ* 413, p. L105. DOI: 10.1086/186970.

Phillips, M. M. et al. (Oct. 1999). "The Reddening-Free Decline Rate Versus Luminosity Relationship for Type IA Supernovae". In: *AJ* 118.4, pp. 1766–1776. DOI: 10.1086/301032. arXiv: astro-ph/9907052 [astro-ph].

Pignata, Giuliano et al. (Feb. 2011). "SN 2009bb: A Peculiar Broad-lined Type Ic Supernova". In: *ApJ* 728.1, 14, p. 14. DOI: 10.1088/0004-637X/728/1/14. arXiv: 1011.6126 [astro-ph.SR].

Piro, Anthony L. and Wenbin Lu (May 2020). "Wind-reprocessed Transients". In: *ApJ* 894.1, 2, p. 2. DOI: 10.3847/1538-4357/ab83f6. arXiv: 2001.08770 [astro-ph.HE].

Podsiadlowski, Ph., P. C. Joss, and J. J. L. Hsu (1992). "Presupernova Evolution in Massive Interacting Binaries". In: *ApJ* 391, p. 246. DOI: 10.1086/171341.

Podsiadlowski, Ph. et al. (Aug. 2005). "The double pulsar J0737-3039: testing the neutron star equation of state". In: *MNRAS* 361.4, pp. 1243–1249. DOI: 10.1111/j.1365-2966.2005.09253.x. arXiv: astro-ph/0506566 [astro-ph].

Podsiadlowski, Philipp (1992). "The progenitor of SN 1987 A". In: *Publications of the Astronomical Society of the Pacific* 104, p. 717. DOI: 10.1086/133043. URL: https://doi.org/10.1086%2F133043.

Poveda, A. and L. Woltjer (Mar. 1968). "Supernovae and Supernova Remnants". In: *AJ* 73, p. 65. DOI: 10.1086/110600.

Prakash, M., T. L. Ainsworth, and J. M. Lattimer (Nov. 1988). "Equation of state and the maximum mass of neutron stars". In: *Phys. Rev. Lett.* 61.22, pp. 2518–2521. DOI: 10.1103/PhysRevLett.61.2518.

Prentice, S. J. et al. (Aug. 2018). "SN 2016coi/ASASSN-16fp: an example of residual helium in a typeIc supernova?" In: *MNRAS* 478.3, pp. 4162–4192. DOI: 10.1093/mnras/sty1223. arXiv: 1709.03593 [astro-ph.HE].

Prentice, S. J. et al. (May 2019). "Investigating the properties of stripped-envelope supernovae; what are the implications for their progenitors?" In: *MNRAS* 485.2, pp. 1559–1578. DOI: 10.1093/mnras/sty3399. arXiv: 1812.03716 [astro-ph.HE].

Prinz, T. and W. Becker (Aug. 2012). "Exploring the supernova remnant G308.4-1.4". In: *A&A* 544, A7, A7. DOI: 10.1051/0004-6361/201219086. arXiv: 1202.4677 [astro-ph.HE].

Rakowski, Cara E., John P. Hughes, and Patrick Slane (Feb. 2001). "Two New Ejecta-dominated Galactic Supernova Remnants: G337.2-0.7 and G309.2-0.6". In: *ApJ* 548.1, pp. 258–268. DOI: 10.1086/318680. arXiv: astro-ph/0010091 [astro-ph].

Renzo, M. et al. (Aug. 2020). "Predictions for the hydrogen-free ejecta of pulsational pair-instability supernovae". In: *A&A* 640, A56, A56. DOI: 10.1051/0004-6361/202037710. arXiv: 2002.05077 [astro-ph.SR].

Reynolds, S. P. (Sept. 2008). "Supernova remnants at high energy." In: *ARA&A* 46, pp. 89–126. DOI: 10.1146/annurev.astro.46.060407.145237.

Reynolds, Stephen P. (Jan. 1998). "Models of Synchrotron X-Rays from Shell Supernova Remnants". In: *ApJ* 493.1, pp. 375–396. DOI: 10.1086/305103.

Reynoso, E. M., S. Cichowolski, and A. J. Walsh (Jan. 2017). "A high-resolution H I study towards the supernova remnant Puppis A and its environments". In: *MNRAS* 464.3, pp. 3029–3039. DOI: 10.1093/mnras/stw2219. arXiv: 1609.01779 [astro-ph.GA].

Reynoso, E. M. and A. J. Walsh (Aug. 2015). "Radio spectral characteristics of the supernova remnant Puppis A and nearby sources". In: *MNRAS* 451.3, pp. 3044–3054. DOI: 10.1093/mnras/stv1147. arXiv: 1506.03801 [astro-ph.GA].

Rho, J. et al. (Feb. 2021). "Near-infrared and Optical Observations of Type Ic SN 2020oi and Broad-lined Type Ic SN 2020bvc: Carbon Monoxide, Dust, and High-velocity Supernova Ejecta". In: *ApJ* 908.2, 232, p. 232. DOI: 10.3847/1538-4357/abd850. arXiv: 2010.00662 [astro-ph.SR].

Riess, Adam G. et al. (1998). "Observational Evidence from Supernovae for an Accelerating Universe and a Cosmological Constant". In: *AJ* 116.3, pp. 1009–1038. DOI: 10.1086/300499. arXiv: astro-ph/9805201 [astro-ph].

Roger, R. S. et al. (Apr. 1986). "G 291.0-0.1, a centrally bright supernova remnant, in Carina." In: *MNRAS* 219, pp. 815–822. DOI: 10.1093/mnras/219.4.815.

Roming, P. W. A. et al. (Oct. 2009). "Multi-Wavelength Properties of the Type IIb SN 2008ax". In: *ApJ* 704.2, pp. L118–L123. DOI: 10.1088/0004-637X/704/2/L118. arXiv: 0909.0967 [astro-ph.HE].

Röpke, F. K. and J. C. Niemeyer (Mar. 2007). "Delayed detonations in full-star models of type Ia supernova explosions". In: *A&A* 464.2, pp. 683–686. DOI: 10.1051/0004-6361:20066585. arXiv: astro-ph/0703378 [astro-ph].

Roy, Rupak et al. (Sept. 2013). "SN 2007uy - metamorphosis of an aspheric Type Ib explosion". In: *MNRAS* 434.3, pp. 2032–2050. DOI: 10.1093/mnras/stt1148. arXiv: 1306.5389 [astro-ph.HE].

Ruiz-Carmona, R., I. Sfaradi, and A. Horesh (Oct. 2022). "Type IIP supernova SN2016X in radio frequencies". In: *A&A* 666, A82, A82. DOI: 10.1051/0004-6361/202142024. arXiv: 2205.11032 [astro-ph.HE].

Ryan, Geoffrey et al. (June 2020). "Gamma-Ray Burst Afterglows in the Multimessenger Era: Numerical Models and Closure Relations". In: *ApJ* 896.2, 166, p. 166. DOI: 10.3847/1538-4357/ab93cf. arXiv: 1909.11691 [astro-ph.HE].

Rybicki, G. B. and A. P. Lightman (1979). *Radiative processes in astrophysics*. A wiley-Interscience Publication.

Ryder, Stuart D. et al. (Apr. 2004). "Modulations in the radio light curve of the Type IIb supernova 2001ig: evidence for a Wolf-Rayet binary progenitor?" In: *MNRAS* 349.3, pp. 1093–1100. DOI: 10.1111/j.1365-2966.2004.07589.x. arXiv: astro-ph/0401135 [astro-ph].

Sahu, D. K. et al. (Nov. 2006). "Photometric and spectroscopic evolution of the Type IIP supernova SN 2004et". In: *MNRAS* 372.3, pp. 1315–1324. DOI: 10.1111/j.1365-2966.2006.10937.x. arXiv: astro-ph/0608432 [astro-ph].

Saito, Sei et al. (June 2022). "Constraints on the Explosion Timescale of Core-collapse Supernovae Based on Systematic Analysis of Light Curves". In: *ApJ* 931.2, 153, p. 153. DOI: 10.3847/1538-4357/ac6bec. arXiv: 2205.00624 [astro-ph.HE].

Salas, P. et al. (Jan. 2013). "SN 2007bg: the complex circumstellar medium around one of the most radio-luminous broad-lined Type Ic supernovae". In: *MNRAS* 428.2, pp. 1207–1217. DOI: 10.1093/mnras/sts104. arXiv: 1208.3455 [astro-ph.HE].

Salpeter, Edwin E. (Jan. 1955). "The Luminosity Function and Stellar Evolution." In: *ApJ* 121, p. 161. DOI: 10.1086/145971.

Sano, H. et al. (July 2022). "An Expanding Shell of Neutral Hydrogen Associated with SN 1006: Hints for the Single-degenerate Origin and Faint Hadronic Gamma-Rays". In: *ApJ* 933.2, 157, p. 157. DOI: 10.3847/1538-4357/ac7465. arXiv: 2205.13712 [astro-ph.HE].

Sasaki, Manami et al. (Sept. 2018). "Infrared and X-ray study of the Galactic SNR G15.9+0.2". In: *MNRAS* 479.3, pp. 3033–3041. DOI: 10.1093/mnras/sty1596. arXiv: 1806.11365 [astro-ph.HE].

Sato, Yuri et al. (July 2021). "Off-axis jet scenario for early afterglow emission of low-luminosity gamma-ray burst GRB 190829A". In: *MNRAS* 504.4, pp. 5647–5655. DOI: 10.1093/mnras/stab1273. arXiv: 2101.10581 [astro-ph.HE].

Sawada, Ryo and Keiichi Maeda (2019). "Nucleosynthesis Constraints on the Energy Growth Timescale of a Core-collapse Supernova Explosion". In: *ApJ* 886.1, 47, p. 47. DOI: 10.3847/1538-4357/ab4da3. arXiv: 1910.06972 [astro-ph.HE].

Sedov, L. I. (1959). *Similarity and Dimensional Methods in Mechanics*.

Shigeyama, Toshikazu et al. (Sept. 1990). "Low-Mass Helium Star Models for Type Ib Supernovae: Light Curves, Mixing, and Nucleosynthesis". In: *ApJ* 361, p. L23. DOI: 10.1086/185818.

Shigeyama, Toshikazu et al. (Jan. 1994). "Theoretical Light Curves of Type IIb Supernova 1993J". In: *ApJ* 420, p. 341. DOI: 10.1086/173564.

Silverman, Jeffrey M. et al. (July 2013). "Type Ia Supernovae Strongly Interacting with Their Circumstellar Medium". In: *ApJS* 207.1, 3, p. 3. DOI: 10.1088/0067-0049/207/1/3. arXiv: 1304.0763 [astro-ph.CO].

Sironi, Lorenzo and Dimitrios Giannios (Dec. 2013). "A Late-time Flattening of Light Curves in Gamma-Ray Burst Afterglows". In: *ApJ* 778.2, 107, p. 107. DOI: 10.1088/0004-637X/778/2/107. arXiv: 1307.3250 [astro-ph.HE].

Sironi, Lorenzo and Anatoly Spitkovsky (Jan. 2011). "Particle Acceleration in Relativistic Magnetized Collisionless Electron-Ion Shocks". In: *ApJ* 726.2, 75, p. 75. DOI: 10.1088/0004-637X/726/2/75. arXiv: 1009.0024 [astro-ph.HE].

Smartt, S. J. et al. (2009). "The death of massive stars - I. Observational constraints on the progenitors of Type II-P supernovae". In: *MNRAS* 395.3, pp. 1409–1437. DOI: 10.1111/j.1365-2966.2009.14506.x. arXiv: 0809.0403 [astro-ph].

Smartt, Stephen J. (2009). "Progenitors of Core-Collapse Supernovae". In: *ARA&A* 47.1, pp. 63–106. DOI: 10.1146/annurev-astro-082708-101737. arXiv: 0908.0700 [astro-ph.SR].

Smartt, Stephen J. et al. (2004). "Detection of a Red Supergiant Progenitor Star of a Type II-Plateau Supernova". In: *Science* 303.5657, pp. 499–503. DOI: 10.1126/science.1092967. arXiv: astro-ph/0401235 [astro-ph].

Soderberg, A. M. et al. (Mar. 2005). "The Radio and X-Ray-Luminous Type Ibc Supernova 2003L". In: *ApJ* 621.2, pp. 908–920. DOI: 10.1086/427649. arXiv: astro-ph/0410163 [astro-ph].

Soderberg, A. M. et al. (Nov. 2006). "The Radio and X-Ray Luminous SN 2003bg and the Circumstellar Density Variations around Radio Supernovae". In: *ApJ* 651.2, pp. 1005–1018. DOI: 10.1086/507571. arXiv: astro-ph/0512413 [astro-ph].

Soderberg, A. M. et al. (May 2008). "An extremely luminous X-ray outburst at the birth of a supernova". In: *Nature* 453.7194, pp. 469–474. DOI: 10.1038/nature06997. arXiv: 0802.1712 [astro-ph].

Soderberg, A. M. et al. (Jan. 2010a). "A relativistic type Ibc supernova without a detected γ-ray burst". In: *Nature* 463.7280, pp. 513–515. DOI: 10.1038/nature08714. arXiv: 0908.2817 [astro-ph.HE].

Soderberg, A. M. et al. (Dec. 2010b). "Radio and X-ray Observations of the Type Ic SN 2007gr Reveal an Ordinary, Non-relativistic Explosion". In: *ApJ* 725.1, pp. 922–930. DOI: 10.1088/0004-637X/725/1/922. arXiv: 1005.1932 [astro-ph.CO].

Soderberg, A. M. et al. (June 2012). "Panchromatic Observations of SN 2011dh Point to a Compact Progenitor Star". In: *ApJ* 752.2, 78, p. 78. DOI: 10.1088/0004-637X/752/2/78. arXiv: 1107.1876 [astro-ph.HE].

Spitkovsky, Anatoly (2008). "Particle Acceleration in Relativistic Collisionless Shocks: Fermi Process at Last?" In: *ApJ* 682.1, p. L5. DOI: 10.1086/590248. arXiv: 0802.3216 [astro-ph].

Srivastav, Shubham et al. (Mar. 2016). "Optical and NIR observations of the nearby type Ia supernova SN 2014J". In: *MNRAS* 457.1, pp. 1000–1014. DOI: 10.1093/mnras/stw039. arXiv: 1601.00805 [astro-ph.SR].

Stockdale, Christopher J. et al. (Dec. 2007). "The Radio Evolution of SN 2001gd". In: *ApJ* 671.1, pp. 689–694. DOI: 10.1086/522584. arXiv: 0708.1026 [astro-ph].

Sukhbold, Tuguldur, S. E. Woosley, and Alexander Heger (June 2018). "A High-resolution Study of Presupernova Core Structure". In: *ApJ* 860.2, 93, p. 93. DOI: 10.3847/1538-4357/aac2da. arXiv: 1710.03243 [astro-ph.HE].

Suntzeff, Nicholas B. and Patrice Bouchet (Feb. 1990). "The Bolometric Light Curve of SN 1987A. I. Results from ESO and CTIO U to Q0 Photometry". In: *AJ* 99, p. 650. DOI: 10.1086/115358.

Sutherland, Ralph S. and M. A. Dopita (Sept. 1993). "Cooling Functions for Low-Density Astrophysical Plasmas". In: *ApJS* 88, p. 253. DOI: 10.1086/191823.

Suwa, Yudai, Nozomu Tominaga, and Keiichi Maeda (2019). "Importance of ^{56}Ni production on diagnosing explosion mechanism of core-collapse supernova". In: *MNRAS* 483.3, pp. 3607–3617. DOI: 10.1093/mnras/sty3309. arXiv: 1704.04780 [astro-ph.HE].

Suwa, Yudai et al. (2010). "Explosion Geometry of a Rotating 13M Star Driven by the SASI-Aided Neutrino-Heating Supernova Mechanism". In: *PASJ* 62.6, pp. L49–L53. DOI: 10.1093/pasj/62.6.L49. arXiv: 0912.1157 [astro-ph.HE].

Suwa, Yudai et al. (2015). "Neutrino-driven explosions of ultra-stripped Type Ic supernovae generating binary neutron stars". In: *MNRAS* 454.3, pp. 3073–3081. DOI: 10.1093/mnras/stv2195. arXiv: 1506.08827 [astro-ph.HE].

Suwa, Yudai et al. (July 2022). "Observing Supernova Neutrino Light Curves with Super-Kamiokande. III. Extraction of Mass and Radius of Neutron Stars from Synthetic Data". In: *ApJ* 934.1, 15, p. 15. DOI: 10.3847/1538-4357/ac795e. arXiv: 2204.08363 [astro-ph.HE].

Suzuki, A. and K. Maeda (July 2018). "Broad-band emission properties of central engine-powered supernova ejecta interacting with a circumstellar medium". In: *MNRAS* 478, pp. 110–125. DOI: 10.1093/mnras/sty999. arXiv: 1804.05397 [astro-ph.HE].

Suzuki, Akihiro, Takashi J. Moriya, and Tomoya Takiwaki (Dec. 2019). "Supernova Ejecta Interacting with a Circumstellar Disk. I. Two-dimensional Radiation-hydrodynamic Simulations". In: *ApJ* 887.2, 249, p. 249. DOI: 10.3847/1538-4357/ab5a83. arXiv: 1911.09261 [astro-ph.HE].

Suzuki, Tomoharu et al. (Dec. 1993). "Hydrodynamical Models for X-Ray Emissions from SN 1993J in M81". In: *ApJ* 419, p. L73. DOI: 10.1086/187140.

Swiggum, J. K. et al. (2015). "PSR J1930-1852: a Pulsar in the Widest Known Orbit around Another Neutron Star". In: *ApJ* 805.2, 156, p. 156. DOI: 10.1088/0004-637X/805/2/156. arXiv: 1503.06276 [astro-ph.HE].

Taddia, F. et al. (Jan. 2019). "Analysis of broad-lined Type Ic supernovae from the (intermediate) Palomar Transient Factory". In: *A&A* 621, A71, A71. DOI: 10.1051/0004-6361/201834429. arXiv: 1811.09544 [astro-ph.HE].

Takiwaki, Tomoya, Kei Kotake, and Yudai Suwa (2014). "A Comparison of Two- and Three-dimensional Neutrino-hydrodynamics Simulations of Core-collapse Supernovae". In: *ApJ* 786.2, 83, p. 83. DOI: 10.1088/0004-637X/786/2/83. arXiv: 1308.5755 [astro-ph.SR].

— (2016). "Three-dimensional simulations of rapidly rotating core-collapse supernovae: finding a neutrino-powered explosion aided by non-axisymmetric flows". In: *MNRAS* 461.1, pp. L112–L116. DOI: 10.1093/mnrasl/slw105. arXiv: 1602.06759 [astro-ph.HE].

Tanaka, Masaomi and Kenta Hotokezaka (Oct. 2013). "Radiative Transfer Simulations of Neutron Star Merger Ejecta". In: *ApJ* 775.2, 113, p. 113. DOI: 10.1088/0004-637X/775/2/113. arXiv: 1306.3742 [astro-ph.HE].

Tanaka, Masaomi et al. (Feb. 2009). "Type Ib Supernova 2008D Associated With the Luminous X-Ray Transient 080109: An Energetic Explosion of a Massive Helium Star". In: *ApJ* 692.2, pp. 1131–1142. DOI: 10.1088/0004-637X/692/2/1131. arXiv: 0807.1674 [astro-ph].

Tanaka, Masaomi et al. (2017). "Kilonova from post-merger ejecta as an optical and near-Infrared counterpart of GW170817". In: *PASJ* 69.6, 102, p. 102. DOI: 10.1093/pasj/psx121. arXiv: 1710.05850 [astro-ph.HE].

Tanaka, Takaaki et al. (Jan. 2021). "Rapid Deceleration of Blast Waves Witnessed in Tycho's Supernova Remnant". In: *ApJ* 906.1, L3, p. L3. DOI: 10.3847/2041-8213/abd6cf. arXiv: 2012.13622 [astro-ph.HE].

Tanvir, N. R. et al. (Aug. 2013). "A 'kilonova' associated with the short-duration γ-ray burst GRB 130603B". In: *Nature* 500.7464, pp. 547–549. DOI: 10.1038/nature12505. arXiv: 1306.4971 [astro-ph.HE].

Taubenberger, Stefan (2017). "The Extremes of Thermonuclear Supernovae". In: *Handbook of Supernovae*. Ed. by Athem W. Alsabti and Paul Murdin, p. 317. DOI: 10.1007/978-3-319-21846-5_37.

Tauris, T. M. et al. (2013). "Ultra-stripped Type Ic Supernovae from Close Binary Evolution". In: *ApJ* 778.2, L23, p. L23. DOI: 10.1088/2041-8205/778/2/L23. arXiv: 1310.6356 [astro-ph.SR].

Tauris, T. M. et al. (2017). "Formation of Double Neutron Star Systems". In: *ApJ* 846.2, 170, p. 170. DOI: 10.3847/1538-4357/aa7e89. arXiv: 1706.09438 [astro-ph.HE].

Tauris, Thomas M., Norbert Langer, and Philipp Podsiadlowski (2015). "Ultra-stripped supernovae: progenitors and fate". In: *MNRAS* 451.2, pp. 2123–2144. DOI: 10.1093/mnras/stv990. arXiv: 1505.00270 [astro-ph.SR].

Tenorio-Tagle, G. et al. (June 1990). "On the evolution of supernova remnants. I. Explosions inside pre-existing wind-driven bubbles." In: *MNRAS* 244, p. 563.

Tenorio-Tagle, G. et al. (July 1991). "On the evolution of supernova remnants - II. Two-dimensional calculationsof explosions inside pre-existing wind-driven bubbles." In: *MNRAS* 251, p. 318. DOI: 10.1093/mnras/251.2.318.

Terreran, G. et al. (2019). "SN 2016coi (ASASSN-16fp): An Energetic H-stripped Core-collapse Supernova from a Massive Stellar Progenitor with Large Mass Loss". In: *ApJ* 883.2, 147, p. 147. DOI: 10.3847/1538-4357/ab3e37. arXiv: 1905.02226 [astro-ph.HE].

Timmes, F. X. and S. E. Woosley (Sept. 1992). "The Conductive Propagation of Nuclear Flames. I. Degenerate C + O and O + NE + MG White Dwarfs". In: *ApJ* 396, p. 649. DOI: 10.1086/171746.

Tominaga, Nozomu, Sergei I. Blinnikov, and Ken'ichi Nomoto (July 2013). "Supernova Explosions of Super-asymptotic Giant Branch Stars: Multicolor Light Curves of Electron-capture Supernovae". In: *ApJ* 771.1, L12, p. L12. DOI: 10.1088/2041-8205/771/1/L12. arXiv: 1305.6813 [astro-ph.HE].

Truelove, J. Kelly and Christopher F. McKee (Feb. 1999). "Evolution of Nonradiative Supernova Remnants". In: *ApJS* 120.2, pp. 299–326. DOI: 10.1086/313176.

Tsuna, Daichi, Kazumi Kashiyama, and Toshikazu Shigeyama (Dec. 2021). "AT 2018lqh: Black Hole Born from a Rotating Star?" In: *ApJ* 922.2, L34, p. L34. DOI: 10.3847/2041-8213/ac3997. arXiv: 2110.07164 [astro-ph.HE].

Turtle, A. J. et al. (May 1987). "A prompt radio burst from supernova 1987A in the Large Magellanic Cloud". In: *Nature* 327.6117, pp. 38–40. DOI: 10.1038/327038a0.

Uchida, Hiroyuki et al. (Dec. 2012). "Recombining Plasma and Hard X-Ray Filament in the Mixed-Morphology Supernova Remnant W 44". In: *PASJ* 64, 141, p. 141. DOI: 10.1093/pasj/64.6.141. arXiv: 1208.0113 [astro-ph.HE].

Uno, Kohki and Keiichi Maeda (July 2020). "A Wind-driven Model: Application to Peculiar Transients AT2018cow and iPTF14hls". In: *ApJ* 897.2, 156, p. 156. DOI: 10.3847/1538-4357/ab9632. arXiv: 2003.05795 [astro-ph.HE].

Utrobin, V. P. and N. N. Chugai (Dec. 2019). "Resolving the puzzle of type IIP SN 2016X". In: *MNRAS* 490.2, pp. 2042–2049. DOI: 10.1093/mnras/stz2716. arXiv: 1909.13138 [astro-ph.HE].

Valenti, S. et al. (2015). "Supernova 2013by: a Type IIL supernova with a IIP-like light-curve drop*". In: *MNRAS* 448.3, pp. 2608–2616. DOI: 10.1093/mnras/stv208. arXiv: 1501.06491 [astro-ph.HE].

van der Horst, A. J. et al. (Jan. 2011). "Detailed Radio View on Two Stellar Explosions and Their Host Galaxy: XRF 080109/SN 2008D and SN 2007uy in NGC 2770". In: *ApJ* 726.2, 99, p. 99. DOI: 10.1088/0004-637X/726/2/99. arXiv: 1011.2521 [astro-ph.HE].

van Dyk, Schuyler D. et al. (May 1993). "The Radio Emission from the Type IC Supernova SN 1990B". In: *ApJ* 409, p. 162. DOI: 10.1086/172652.

Van Dyk, Schuyler D. et al. (Feb. 2014). "The Type IIb Supernova 2013df and its Cool Supergiant Progenitor". In: *AJ* 147.2, 37, p. 37. DOI: 10.1088/0004-6256/147/2/37. arXiv: 1312.3984 [astro-ph.SR].

van Eerten, Hendrik, Weiqun Zhang, and Andrew MacFadyen (Oct. 2010). "Off-axis Gamma-ray Burst Afterglow Modeling Based on a Two-dimensional Axisymmetric Hydrodynamics Simulation". In: *ApJ* 722.1, pp. 235–247. DOI: 10.1088/0004-637X/722/1/235. arXiv: 1006.5125 [astro-ph.HE].

Vigna-Gómez, Alejandro et al. (Apr. 2022). "Stellar response after stripping as a model for common-envelope outcomes". In: *MNRAS* 511.2, pp. 2326–2338. DOI: 10.1093/mnras/stac237. arXiv: 2107.14526 [astro-ph.HE].

Vink, Jacco (2020). *Physics and Evolution of Supernova Remnants*. DOI: 10.1007/978-3-030-55231-2.

Vink, Jacco et al. (Sept. 2006). "The X-Ray Synchrotron Emission of RCW 86 and the Implications for Its Age". In: *ApJ* 648.1, pp. L33–L37. DOI: 10.1086/507628. arXiv: astro-ph/0607307 [astro-ph].

Walborn, Nolan R. et al. (1987). "The Composite Image of Sanduleak -69 degrees 202, Candidate Precursor to Supernova 1978A in the Large Magellanic Cloud". In: *ApJ* 321, p. L41. DOI: 10.1086/185002.

Wang, Bo and Zhanwen Han (2012). "Progenitors of type Ia supernovae". In: *New Astron. Rev.* 56.4, pp. 122–141. DOI: 10.1016/j.newar.2012.04.001. arXiv: 1204.1155 [astro-ph.SR].

Waxman, Eli and Boaz Katz (2017). "Shock Breakout Theory". In: *Handbook of Supernovae*. Ed. by Athem W. Alsabti and Paul Murdin, p. 967. DOI: 10.1007/978-3-319-21846-5_33.

Weaver, R. et al. (Dec. 1977). "Interstellar bubbles. II. Structure and evolution." In: *ApJ* 218, pp. 377–395. DOI: 10.1086/155692.

Weiler, K. W. et al. (Feb. 1986). "Radio Supernovae". In: *ApJ* 301, p. 790. DOI: 10.1086/163944.

Weiler, Kurt W. et al. (Dec. 2007). "Long-Term Radio Monitoring of SN 1993J". In: *ApJ* 671.2, pp. 1959–1980. DOI: 10.1086/523258. arXiv: 0709.1136 [astro-ph].

Wellons, Sarah, Alicia M. Soderberg, and Roger A. Chevalier (June 2012). "Radio Observations Reveal Unusual Circumstellar Environments for Some Type Ibc Supernova Progenitors". In: *ApJ* 752.1, 17, p. 17. DOI: 10.1088/0004-637X/752/1/17. arXiv: 1201.5120 [astro-ph.HE].

Wheeler, J. C. and R. Levreault (1985). "The peculiar type I supernova in NGC 991." In: *ApJ* 294, pp. L17–L20. DOI: 10.1086/184500.

Whelan, John and Jr. Iben Icko (1973). "Binaries and Supernovae of Type I". In: *ApJ* 186, pp. 1007–1014. DOI: 10.1086/152565.

Whiteoak, J. B. Z. and A. J. Green (Aug. 1996). "The MOST supernova remnant catalogue (MSC)." In: *A&AS* 118, pp. 329–380.

Woosley, S. E. (Feb. 2017). "Pulsational Pair-instability Supernovae". In: *ApJ* 836.2, 244, p. 244. DOI: 10.3847/1538-4357/836/2/244. arXiv: 1608.08939 [astro-ph.HE].

Woosley, S. E., S. Blinnikov, and Alexander Heger (Nov. 2007). "Pulsational pair instability as an explanation for the most luminous supernovae". In: *Nature* 450.7168, pp. 390–392. DOI: 10.1038/nature06333. arXiv: 0710.3314 [astro-ph].

Woosley, S. E. and J. S. Bloom (Sept. 2006). "The Supernova Gamma-Ray Burst Connection". In: *ARA&A* 44.1, pp. 507–556. DOI: 10.1146/annurev.astro.43.072103.150558. arXiv: astro-ph/0609142 [astro-ph].

Woosley, S. E. and A. Heger (Feb. 2006). "The Progenitor Stars of Gamma-Ray Bursts". In: *ApJ* 637.2, pp. 914–921. DOI: 10.1086/498500. arXiv: astro-ph/0508175 [astro-ph].

Woosley, S. E., A. Heger, and T. A. Weaver (2002). "The evolution and explosion of massive stars". In: *Rev. Mod. Phys.* 74 (4), pp. 1015–1071. DOI: 10.1103/RevModPhys.74.1015. URL: https://link.aps.org/doi/10.1103/RevModPhys.74.1015.

Woosley, S. E., R. E. Taam, and T. A. Weaver (Feb. 1986). "Models for Type I Supernova. I. Detonations in White Dwarfs". In: *ApJ* 301, p. 601. DOI: 10.1086/163926.

Woosley, Stan and Thomas Janka (Dec. 2005). "The physics of core-collapse supernovae". In: *Nature Physics* 1.3, pp. 147–154. DOI: 10.1038/nphys172. arXiv: astro-ph/0601261 [astro-ph].

Yadav, Naveen et al. (Feb. 2014). "Electron Cooling in a Young Radio Supernova: SN 2012aw". In: *ApJ* 782.1, 30, p. 30. DOI: 10.1088/0004-637X/782/1/30. arXiv: 1311.3568 [astro-ph.HE].

Yadav, Naveen et al. (Feb. 2020). "Large-scale Mixing in a Violent Oxygen-Neon Shell Merger Prior to a Core-collapse Supernova". In: *ApJ* 890.2, 94, p. 94. DOI: 10.3847/1538-4357/ab66bb. arXiv: 1905.04378 [astro-ph.HE].

Yadlapalli, Nitika, Vikram Ravi, and Anna Y. Q. Ho (July 2022). "Models of Millimeter and Radio Emission from Interacting Supernovae". In: *ApJ* 934.1, 5, p. 5. DOI: 10.3847/1538-4357/ac771f. arXiv: 2206.03518 [astro-ph.HE].

Yao, Yuhan et al. (Sept. 2020). "SN2019dge: A Helium-rich Ultra-stripped Envelope Supernova". In: *ApJ* 900.1, 46, p. 46. DOI: 10.3847/1538-4357/abaa3d. arXiv: 2005.12922 [astro-ph.HE].

Yaron, O. et al. (Feb. 2017). "Confined dense circumstellar material surrounding a regular type II supernova". In: *Nature Physics* 13, pp. 510–517. DOI: 10.1038/nphys4025. arXiv: 1701.02596 [astro-ph.HE].

Yasuda, H. and S.-H. Lee (May 2019). "Time Evolution of Broadband Nonthermal Emission from Supernova Remnants in Different Circumstellar Environments". In: *ApJ* 876, 27, p. 27. DOI: 10.3847/1538-4357/ab13ab. arXiv: 1903.10226 [astro-ph.HE].

Yasuda, Haruo, Shiu-Hang Lee, and Keiichi Maeda (Oct. 2021). "Dark Age of Type II Supernova Remnants". In: *ApJ* 919.2, L16, p. L16. DOI: 10.3847/2041-8213/ac24ac. arXiv: 2109.04032 [astro-ph.HE].

— (Feb. 2022). "Resurrection of Nonthermal Emissions from Type Ib/c Supernova Remnants". In: *ApJ* 925.2, 193, p. 193. DOI: 10.3847/1538-4357/ac3b49. arXiv: 2111.09534 [astro-ph.HE].

Yoon, S. C., S. E. Woosley, and N. Langer (2010). "Type Ib/c Supernovae in Binary Systems. I. Evolution and Properties of the Progenitor Stars". In: *ApJ* 725.1, pp. 940–954. DOI: 10.1088/0004-637X/725/1/940. arXiv: 1004.0843 [astro-ph.SR].

Yoon, Sung-Chul (Apr. 2015). "Evolutionary Models for Type Ib/c Supernova Progenitors". In: *Publ. Astron. Soc. Australia* 32, e015, e015. DOI: 10.1017/pasa.2015.16. arXiv: 1504.01205 [astro-ph.SR].

Yoshida, Takashi et al. (Nov. 2017). "Explosive nucleosynthesis of ultra-stripped Type Ic supernovae: application to light trans-iron elements". In: *MNRAS* 471.4, pp. 4275–4285. DOI: 10.1093/mnras/stx1738. arXiv: 1707.02685 [astro-ph.HE].

Young, D. R. et al. (Mar. 2010). "Two type Ic supernovae in low-metallicity, dwarf galaxies: diversity of explosions". In: *A&A* 512, A70, A70. DOI: 10.1051/0004-6361/200913004. arXiv: 0910.2248 [astro-ph.CO].

Young, Timothy R. and David Branch (1989). "Absolute Light Curves of Type II Supernovae". In: *ApJ* 342, p. L79. DOI: 10.1086/185489.

Zhang, Tianmeng et al. (Apr. 2006). "Optical Photometry of the Type II-P Supernova 2004dj in NGC 2403". In: *AJ* 131.4, pp. 2245–2255. DOI: 10.1086/500972. arXiv: astro-ph/0512526 [astro-ph].

Zhu, H., W. W. Tian, and P. Zuo (Oct. 2014). "Supernova Remnant W49B and Its Environment". In: *ApJ* 793.2, 95, p. 95. DOI: 10.1088/0004-637X/793/2/95. arXiv: 1407.8260 [astro-ph.SR].

Zirakashvili, Vladimir N. and Vladimir S. Ptuskin (Dec. 2008). "The influence of the Alfvénic drift on the shape of cosmic ray spectra in SNRs". In: *American Institute of Physics Conference Series*. Ed. by Felix A. Aharonian, Werner Hofmann, and Frank Rieger. Vol. 1085. American Institute of Physics Conference Series, pp. 336–339. DOI: 10.1063/1.3076675. arXiv: 0807.2754 [astro-ph].